SYNTHESIS, STRUCTURE, MAGNETISM, AND COORDINATION CHEMISTRY OF SOME SELF ASSEMBLED POLYNUCLEAR CLUSTERS AND GRIDS OF FIRST ROW TRANSITION METAL IONS DERIVED FROM POLYTOPIC HYDRAZONE LIGANDS

S.M. TAREQUE ABEDIN

Your file Votre référence
ISBN: 978-0-494-33466-9
Our file Notre référence
ISBN: 978-0-494-33466-9

Synthesis, Structure, Magnetism, and Coordination Chemistry of Some Self assembled Polynuclear Clusters and Grids of First Row Transition Metal Ions Derived from Polytopic Hydrazone Ligands

By

S. M. Tareque Abedin, B. Sc. (Honors), M. Sc.

This thesis is submitted to
the School of Graduate Studies
in partial fulfillment of the requirement for the
degree of Doctor of Philosophy

Department of Chemistry
Memorial University of Newfoundland

August, 2007

St. John's **Newfoundland and Labrador** **Canada**

Abstract

A collection of hydrazone based ligands ranging from simple ditopic to pentatopic have been synthesized and allowed to react with different transition metals ions (e.g. Mn(II), Cu(II)). The ligands varied in terms of their coordination capability (ditopic vs. tritopic), terminal functional group (e.g. $-NH_2$, vs. $-CH_3$), and overall ligand flexibility (e.g. rigid pyridine vs. –NH central piece). The ditopic ligand (e.g. pomp) gave tetranuclear $M(II)_4$ (M = Mn(II), Cu(II)) complexes when treated with Mn(II) and Cu(II) metal salts. In all of the tetranuclear complexes, metal ions were hydrazone oxygen bridged except for the copper case where Cu(II) centers were bridged by a mixture of N-N diazine and hydrazone oxygen groups. Intramolecular antiferromagnetism was observed in all cases. Tritopic ligands with a flexible secondary *–NH* central piece yielded mostly trinuclear linear complexes with Cu(II) and trinuclear nonlinear complexes with Mn(II) ions. The inability of this class of ligands to form nonanuclear grids was attributed to the unusual flexible nature of the ligands which is unsuitable for grid formation. Intramolecular antiferromagnetism was observed in all of the trinuclear complexes. Tritopic ligands with pyridine as a relatively rigid center piece (e.g. 2pomp) yielded [3 x 3] nonanuclear $Mn(II)_9$ grids when reacted with Mn(II). However, with Cu(II) ions this ligand yielded octanuclear $Cu(II)_8$ pinwheel clusters. All of the $Mn(II)_9$ grids showed intramolecular antiferromagnetism whereas pinwheels were found to show ferromagnetism, which is relatively rare in this class of polynuclear complexes. Changing the choice to two different donor functional groupings gave two unprecedented outcomes. An oxalic acid dihydrazide based ditopic ligand yielded an inorganic [2] catenane, with mixed oxidation

states when reacted with Co(II) ions. This is the first example of an inorganic cobalt catenane. However, due to large metal separations, no magnetic exchange coupling was observed in the complex. In another instance, an extended tritopic ligand formed an enormous $Cu(II)_{36}$ cluster using the extra coordination capability of the oxime substituents at two ends of the ligand. The cluster showed intramolecular antiferromagnetism. A logical and symmetric extension of the tritopic ligand led to a pentatopic ligand which gave a [5 x 5] square $Mn(II)_{25}$ cluster. STM imaging techniques were employed to explore the structure of the cluster. Topographic images clearly showed the [5 x 5] square grid-like array on a HOPG surface.

Acknowledgement

I would like to sincerely thank my supervisor Prof. Laurence K. Thompson, and offer my utmost gratitude for all his guidance and support that he has given me over the course of my graduate studies. Magnetism would not have been such an interesting study for me without him. I owe to him what I know in this area.

I would also like to thank my supervisory committee members, Dr. C. R. Lucas, and Dr. N. Gogan, for their help and valuable suggestions. I want to thank them for their time and painstaking effort to review my thesis and fine tune it to make it better.

I would like to acknowledge the effort and contribution of Dr. R. McDonald (University of Alberta) and David O. Miller for x-ray structural data collection and solutions. I also acknowledge Mr. M. S. Alam and Prof. Dr. P. Müller (Physikalisches Institut III, Universität Erlangen-Nürnberg, Germany) for STS and CITS images. I would like to thank Julie Collins, C-CART, for NMR data and solving one structure. I also thank Linda Winsor, C-CART, for help and assistance characterizing the ligands with LCMS. I especially thank Kai Zhang, former member of C-CART, for being so cooperative and helping me out with IR and NMR spectra. I also thank Dr. Yuming Zhao and Amit Kudale for their help in explaining some NMR spectra. Thanks are also due to former Lab. colleagues Stewart Parsons, Timothy Kelly, and Subrata K. Dey who obtained MALDI TOF spectra of some complexes.

I would like to thank former members of the Thompson Research group, Liang Zhao, Zhiqiang Xu, Steve DeGrace, Virginie Niel, Hilde Grove and Matin Lemiare for being so cooperative and for creating a nice and friendly environment in the Lab. I learned a lot from them especially Zhiqiang Xu, whose wizardry in Chemistry I will never forget. No less deserving of thanks are the latter members of the group, Louise N. Dawe, who solved one crystal structure and calls me 'SQUIDDY', Peter Blanchard, Randy Royle, and especially Victoria Milway for her enormous support and understanding and largely for her friendship.

Thanks are also due to my past and present friends and well wishers for their support. Thanks to my mother for being there for me, and for her understanding and unwavering support. I thank my brothers Nazmul Abedin and Mahbub Zamil for their love and support. Most of all, I recall my father, who would have been the happiest person to see this accomplishment.

Finally, I would like to acknowledge the Department of Chemistry and the School of Graduate Studies at Memorial University, and NSERC for financial support.

Table of Contents

List of Schemes

List of Figures

List of Tables

List of symbols and abbreviations

AF	antiferromagnetic
APCI	atmospheric pressure chemical ionization
B	magnetic induction
BVS	bond valence sum
bipy	bipyridine
C	Curie constant
CCD	charge coupled device
c	velocity of light
CHCA	α-cyano-4-hydroxycinnamic acid
CITS	current image tunnelling spectroscopy
CNT	carbon nanotube
dca	dicyanamide
DFT	density functional theory
DMF	dimethylformamide
DMSO	dimethylsulfoxide
DNA	deoxyribonucleic acid
e	electronic charge
EI	electronic ionization
E(S')	energy of total spin quantum numbers
FMD	full matrix diagonalization
FT-IR	Fourier transformed-infra red

GOF	goodness of fit
g	Landé splitting factor
H	external magnetic field
h	Planck's constant
H_{ex}	exchange Hamiltonian
HOPG	highly ordered pyrolytic graphite
HOMO	highest occupied molecular orbital
I	intensity of magnetization
IR	infrared
ITO	irreducible tensor operators
J	exchange integral
k	Boltzmann constant
kJ	kilo joule
LC / MSD	liquid chromatography mass spectrometric device
LFSE	ligand field stabilization energy
M	molar mass
M / H	magnetization versus field
MALDI TOF	matrix assisted laser desorption of ionization with time of flight
Mp	melting point
M_s	saturation magnetization
N	Avogadro's number
Nα	correction term for temperature independent paramagnetism

NMR	nuclear magnetic resonance
NLR	non-linear regression
Oe	Oersted
P	magnetic permeability
PC	personal computer
Py	pyridine
QCA	quantum dot cellular automata
R	residual factor
Qubits	quantum bits
RAM	random access memory
S	spin quantum number
S'	total spin quantum numbers
SADABS	siemens area detector absorption
SAMS	self-assembled monolayers
SMMS	single molecule magnets
SQUID	superconducting quantum interference device
STM	scanning tunnelling microscope
STS	scanning tunnelling spectroscopy
SIE	single ion effect
K	temperature in Kelvins
TIP	temperature independent paramagnetism
TMS	tetramethylsilane

THF	tetrahydrofuran
TMV	tobacco mosaic virus
UV	ultra-violet
VC	vector coupling
Vis	visible
ZFS	zero-field splitting
α	fraction of paramagnetic impurity
β	Bohr magnetons
θ / Θ	Weiss (or Weiss-like) constant
κ	volume susceptibility
μ_{eff}	effective magnetic moment
μ_{mol}	magnetic moment per mole
ρ	paramagnetic impurity fraction
χ'_m	corrected molar susceptibility
χ_g	mass susceptibility
χ_m	molar susceptibility
$\Omega(S')$	degeneracy function

CHAPTER 1

General introduction to supramolecular chemistry - Self assembly through self recognition

1.1 General introduction

1.1.1 Supramolecular Chemistry

The field of supramolecular chemistry is defined as the "Chemistry beyond the molecule" [1]. Despite the fact that the synthesis of even small organic molecules by conventional methods is often tedious and time consuming, the success of making large and complicated molecules has come a long way since the first synthesis of urea by Friedrich Wöhler in 1928 [2]. Systematic, controlled, and step by step methodologies have enabled us to construct very large and complex molecular structures such as polynucleotides with a single DNA strand [3]. Inorganic synthesis has made a parallel progress in approaches to making large architectures containing large numbers of metal centers. The building of such large inorganic polynuclear complexes is largely based on non-covalent interactions. A number of such interactions which play a major role in building supramolecular blocks are: a) electrostatic interactions (ion-ion, ion-dipole, and dipole-dipole), b) hydrogen bonding, c) π-π stacking, and d) van der Waals interactions (weakest).

Energy wise, non-covalent interactions are very weak compared to any covalent bond even though their combined effect is dramatic. The average energy of a covalent

bond is around 350 kJ mol^{-1} which can rise to 942 kJ mol^{-1} in case of the stable triple bond in N_2. In comparison the ion-ion interaction energies are the strongest among the non-covalent interactions with values around 250 kJ mol^{-1}. van der Waals interactions are the weakest with energies around 2 kJ mol^{-1}. However, such weak interactions can have dramatic results when they influence the interplay between a pair of host and guest or a receptor and a substrate with the correct magnitude of complementarity and under certain favorable conditions [1].

1.1.2 Self-assembly and self recognition

Lehn has distinguished and defined a hierarchical order of the terms; 'Templating', 'Self-assembly' and 'Self Organization'. Together these terms cover the process that enables preprogrammed molecular components called 'Tectons' to come together spontaneously in a well defined way to give one, two, or three dimensional assemblies [4]. The term 'Self-assembly' is very broad in sense. It implies the formation of a molecular or multi molecular architecture through spontaneous connection of a few or many components resulting in entities at either the covalent molecular or non-covalent supramolecular level [5]. So, within the self-assembly context, 'Supramolecular self-assembly' is the recognition directed reversible and spontaneous association of a limited number of components (e.g. ligands, metals), under relatively labile non-covalent interactions and should not be confused with 'Molecular self-assembly' which concerns the formation of covalent bonds as part of a special synthetic route [4]. This will not be discussed within the scope of this thesis.

The formation of curved spheroidal fullerenes (e.g. C_{60}, C_{70}) [6] and carbon nanotubes (CNT) [7] in the high temperature regime is an excellent example of covalent self-assembly. Lehn et al. found that, if poly bipyridine strands containing two, three, four or five bipyridine units are mixed in the presence of copper(I) ions, only helices containing two strands of the same length would form. Lehn called it self-assembly through 'Self recognition' [8-10]. Being a hierarchical assembly of several steps, self-assembly requires some degree of reversibility of the connecting events e.g. kinetic lability and weak bonding [5]. As a result of reversibility of the process, any errors that may have occurred during assembly can be corrected provided the reversibility is rapid [1].

1.1.3 Self-assembly in biological systems

Supramolecular species formed by self-assembly have well defined structural, conformational, thermodynamic, kinetic, and dynamic properties. In general, they are thermodynamically less stable, kinetically more labile and dynamically more flexible than covalent molecules [5]. Self-assembly has been found to be a very powerful methodology, which acts as a driving force to combine all these non-covalent interactions together, and encourage them to contribute to the construction of supramolecular systems [11]. Nature uses self-assembly ubiquitously to construct complex functional structures with utmost precision [12-15]. Biologically self-assembled structures are built from simple and ordinary subunits so that a minimum amount of information is required for a particular ensemble. Many notable examples exist. The self-assembly of the Tobacco

Mosaic Virus (TMV) and the ensemble of DNA double helices from the complementary deoxyribonucleic acid strands are two striking examples [16].

1.1.4 Types of self-assembly

1.1.4.1 Thermodynamic self-assembly

Thermodynamic self-assembly is the most widely used technique in coordination chemistry. It stands on kinetic reversibility of bond formation leading to a thermodynamic equilibrium in the system. As a result of this process, the energetically most stable product is formed in greater proportion. The individual coordinate bonds need not be formed in the desired manner every time because the equilibrium is reversible, instead 'incorrect' bonds become undone and associate 'correctly' under a thermodynamic impetus. The following example can be considered for illustration. When similar ditopic and tritopic ligands are mixed and allowed to react with metal ions such as Ag(I), rectangular [2 x 3] Ag_6 grids are formed as the major product by virtue of self recognition which might be the most thermodynamically stable product. As a result of the reversible nature of this assembly, some assemblies can disassemble and reassemble again which results in small amount of homoligand [2 x 2] Ag_4 and [3 x 3] Ag_9 grids as well [17].

1.1.4.2 Strict self-assembly

In strict self-assembly the final product is produced entirely spontaneously when the components are mixed together in the correct ratio under a given set of conditions e.g.

pH, temperature. In this case all the necessary information for the assembly to occur is encoded in the constituent parts, and the system approaches the one destined product, which has the thermodynamic minimum. The best example of strict self-assembly is the generation of [m x n] grid type complexes from ligands developed by rational design. A large family of grid type complexes has been synthesized by Lehn and co-workers. Square [2 x 2], [3 x 3] grids by using similar type of ligands, and [2 x 3] ladder type complexes using two different types of ligands, were developed with a variety of transition metals [18-22]. Scheme 1.1 shows a tritopic ligand and the formation of a [3 x 3] grid through strict self-assembly.

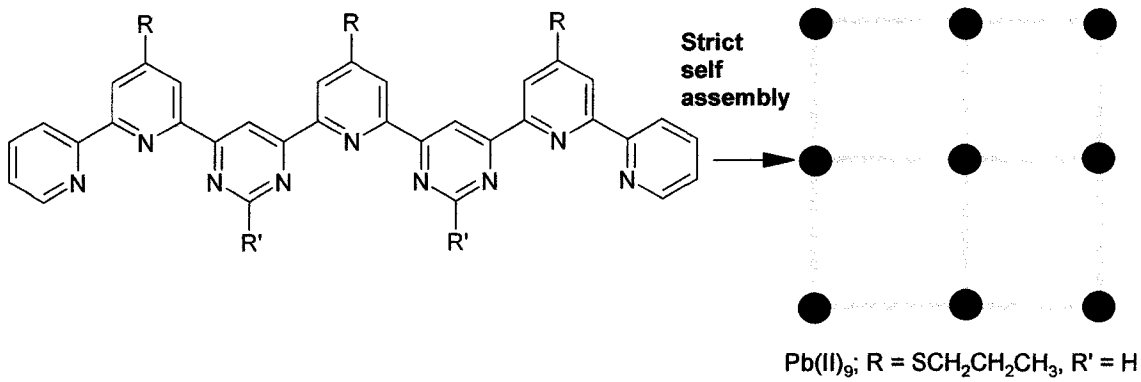

Scheme 1.1 Strict self-assembly.

The use of transition metal ions to direct molecular self assemblies has two major advantages:

a) Metal ligand dative bonds are thermodynamically strong interactions, but have varying degrees of lability; they can therefore provide stabilization energy for a large number of different structures.

b) Due to ligand field effects, transition metals often have very specific geometric requirements in their coordination sphere. This gives the metal ions the ability to control the geometry of the molecular assembly very precisely [4].

A great diversity of polynuclear metal clusters has been synthesized so far by self-assembly, with increasing ability to control and predict the structural outcome of the final ensemble from two or more complementary components.

The general concept about the complementarity is the construction of the host, in this case the ligand, such that it exactly matches both sterically and electronically the requirement of the guest, the metal used. Thus the 'host' and 'guest' are called complementary to each other [4]. Sterically the host must be able to fit physically around the guest without being too large or too small. That is, the binding site at the donor pockets of a ligand backbone should be appropriately positioned to hold and bind the transition metal of a particular ionic size. As summed up by Cram et al. "To complex, the host must have binding sites which cooperatively contact and attract the binding site of the guest without generating strong non-bonded repulsions" [23 (a)].

For large transition metal assemblies, we basically rely on two approaches for the assembly processes. Namely, 'designed assembly', and 'serendipitous assembly'. 'Designed assembly' includes the use of 'pre-designed ligands'. Lego™ chemical components which will be used to build the ligand are carefully chosen. Generally, they are commercially available chemicals. Usually, rigid organic ligands bearing linearly and conveniently oriented coordination pockets within the ligand backbone are synthesized. When reacted with a suitable metal ion, these ligands can give rise to targeted metal clusters with desired topology (e.g. squares, rectangles). In some cases, a simple metal complex is synthesized which is used as the precursor.

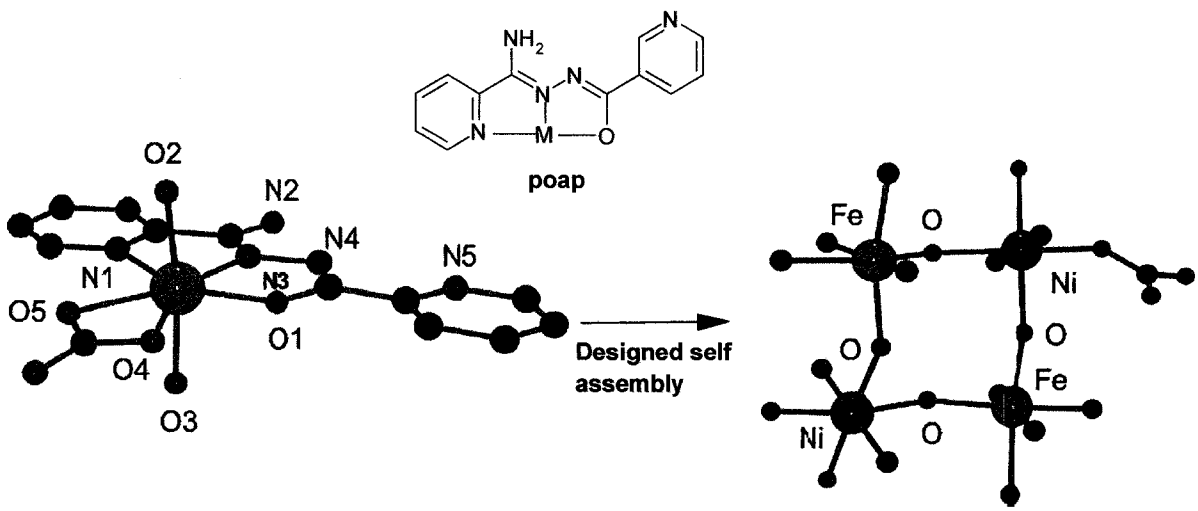

Fig. 1.1 Designed self-assembly; formation of heteronuclear [2 x 2] grid; Blue = N, Magenta = Fe(III), Green = Ni(II), Red = O, Black = C.

An excellent example of 'designed self-assembly' using a metal complex as precursor is the generation of a heterometallic square [2 x 2][$Fe^{III}_2Ni^{II}_2$] grid from a preformed mononuclear Fe(III) complex derived from the ditopic ligand 'poap' (Fig. 1.1) [23(b)].

Depending on the number and relative 'bite' size of the coordination pockets available within the ligand, the type of transition metal used, counter anion, sol vent polarity, and pH, each of these organic ligands may result in metal clusters with different nuclearity.

As described by Lehn, the self-assembly of specific supramolecular architectures from a set of organic ligands and metal ions results from the processing of the structural information stored in the ligands by the metal ions operating through the algorithm defined by their coordination geometry [5]. So, the nuclearity of these clusters is clearly based on the polytopic nature of the ligand and the ability of the metal to read and interpret the coordination options presented by the ligand in the most efficient way, depending on its own coordination algorithm [24, 25]. It was furthermore shown that the reading of the same ligand information with different sets of metal ions yields different inorganic architectures as outputs [26, 27]. This is of particular interest, since it indicates that the information contained in a molecular entity does not necessarily code for a single species only, but may generate different outputs depending on how it is read and processed.

Rational design of ligand plays a crucial role in designed self-assembly. A well designed ligand not only helps to control the topology of the resultant complex, but it also determines the overall stability of the complex. Ligands designed with relatively rigid functional groups in the center of the ligand are generally more suitable for the formation of n^n type grids. A central rigid group restricts the ligand from bending. Thereby,

adoption of other conformations of the ligand which could lead to different topologies than grids, is limited. Moreover, if the ligand contains suitably embedded donor groupings, such that metal ions are chelated due to coordination forming five or six membered rings in each donor pocket, such coordination increases the overall stability of the complex. Chapter 2 will discuss the ligand design strategies in detail.

1.2 Polynuclear complexes derived from designed assembly

1.2.1 Dinuclear complexes - rotational versus flexible coordination conformation

Polynucleating ligands have structural attributes that allow combining separate coordination pockets in a contiguous fashion. This provides a unique way to bind and link different metal ions sitting in those pockets in such close proximity that the spins can 'talk' and communicate. This assembly often requires the help of exogenous or endogenous ligands. Conjugated aromatic heterocycles with N-N diazine bridges are good bridging platforms to create such an environment. 1,2-Diazine ligands based on aromatic heterocycles, such as pyridazine and phthalazine effectively fix the relative coordination position of the donor sites, and limit the flexibility of the dinuclear center dimensions. Nonetheless, these conjugated aromatic heterocyclic ligands bring the two metal centers into such close proximity that dinuclear complexes form where the two metal centers can generate relatively strong antiferromagnetic intramolecular exchange ($-2J$ = 700 - 900 cm^{-1}) through the π system of the heterocycle. In cases where the two nitrogen donor sites in the heterocycle are situated 1,3 as in pyrimidine or 1,4 as in pyrazine ring positions, weak antiferromagnetic exchange ($-2J$ = less than 50 cm^{-1}) is

observed. The magnitude of exchange varies with the nature of the diazine ligands and also on the nature of the exogenous bridging ligand. Extensive studies have been carried out on spin coupled dinuclear Cu(II) complexes of 1,2 diazine ligands (Scheme 1.2) over the past few decades [28-54].

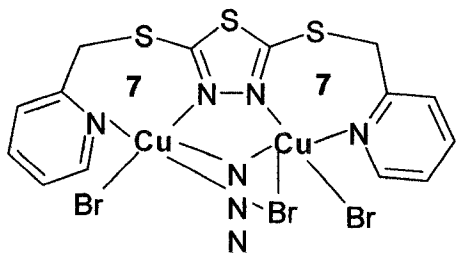

DMPTD dicopper complex

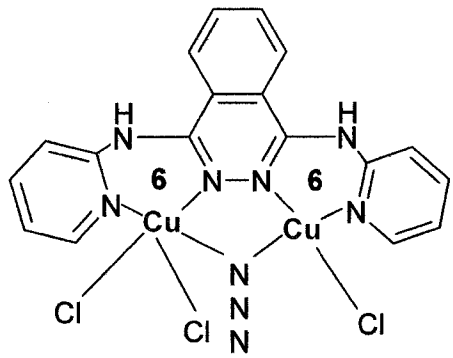

PAP dicopper complex

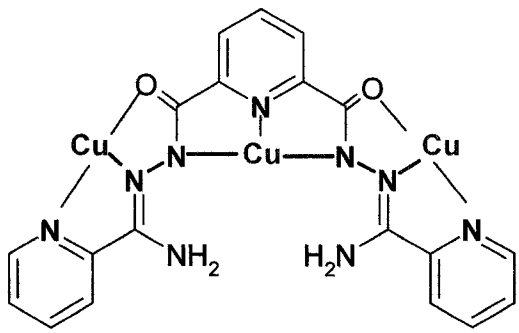

2poap tricopper complex

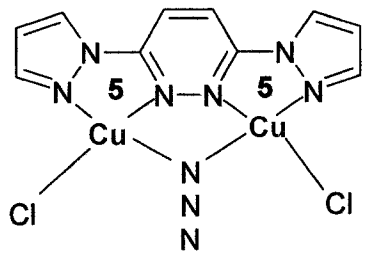

PPD3Me dicopper complex

Scheme 1.2 Copper complexes with chelating ligands with varying chelate ring size.

The effect of exogenous bridging ligands (X) on exchange parameters has also been studied using various groups for X (X = Cl, Br, OH, IO_3^-, SO_4^{2-}, and N_3^-). It was

possible to show that by using ligands like DMPTD [50] (Scheme 1.2) which contains the common N-N diazine backbone, it is possible to vary chelate ring size (5, 6, and 7) at the metal coordination sites of the dicopper complexes which leads to the situation where the metal-metal distances progressively become shorter. This causes the bridge angle to become gradually smaller and eventually a transition is observed from antiferromagnetic exchange interaction observed at large bridge angles to ferromagnetic exchange observed at smaller bridge angles.

Open chain diazine ligands on the other hand allow considerable rotational flexibility around the metal magnetic planes, which leads to unique exchange situations. Reaction of PAHAP (Scheme 1.3) with copper generally yielded dinuclear complexes where the two copper centers are moderately antiferromagnetically coupled when the twist angle between the two metal magnetic planes is fairly large (>100°). One exception is a bromide analogue where a bromide bridge essentially locked the two magnetic planes 75° apart leading to a weak ferromagnetic exchange (a metal magnetic plane is defined in terms of the ground state atomic orbital where the valence electron usually resides) [55]. For Cu(II) (d^1) it is the d_{x2-y2} orbital. Other analogues with different transition metals e.g. Fe(II), Fe(III), Co(II), Ni(II) and Mn(II) were also synthesized, which were M_2L_3 spiral complexes with antiferromagnetic exchange prevailing between metal ions [56].

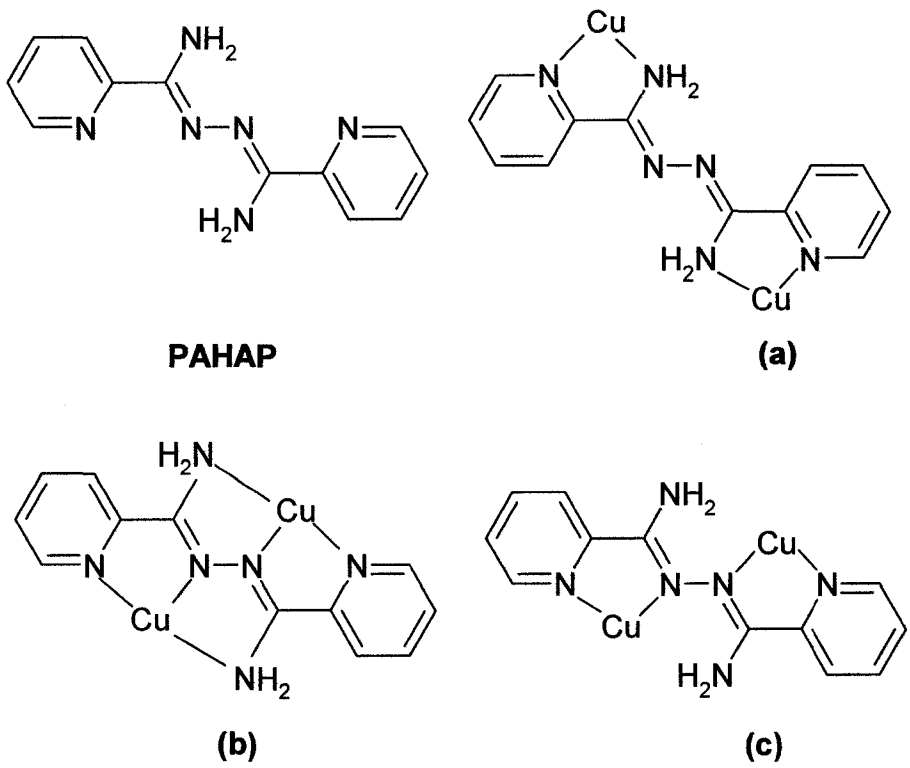

Scheme 1.3 Picolinamide azine type ligand PAHAP and its coordination modes.

1.2.2 Trinuclear complexes with tritopic ligands

The relative bite size of the coordination pockets and flexibility of the overall ligand backbone has a profound effect on the structure and nuclearity of the final outcome. Ideally, for a trinuclear linear complex to form, the ligand should have three coordination pockets arranged in a linear fashion with appropriate bridging atoms to encourage spin communication between metals. The 2,6-picolinic dihydrazone based ligand 2poap (Scheme 1.2) and its various analogues have linear, contiguous arrangements of coordination pockets, and can form trinuclear copper complexes when

reacted with Cu(II) [57] using poorly coordinating groups as anions. The magnetic interaction can be pictured as a model where the central copper atom is bridged by N-N groups to two external copper atoms with a large torsional angle between the copper magnetic planes leading to moderate antiferromagnetic coupling among the three metal centers.

1.2.3 Tetranuclear [2 x 2] grid and pentanuclear cluster complexes - partial versus complete occupancy of the coordination sites

Ditopic ligands (e.g. poap and its analogues) with a tridentate and a bidentate donor coordination pocket arranged in a linear fashion can self-assemble in the presence of transition metals to give high yields of heteroleptic [2 x 2] grid like complexes. Examples of [2 x 2] square grid structures with Mn(II), Co(II), Ni(II), Cu(II), and Zn(II) have been produced [58, 59]. Depending on the identity of the metal, each metal center in the tetranuclear square complex can be either six coordinate (for Mn, Co, Ni, and Zn) or a mixture of five and six coordinate (e.g. for Cu(II)). The metal coordination sites in the tetranuclear square grids are only partially filled by the ligand donor sites. The extra coordination sites of metals are taken up by solvent molecules. In comparison, in a homoleptic pentanuclear cluster, all the coordination requirements are completely filled by the ligand donors leading to a L_6M_5 (M = Mn(II)) stoichiometry for the complex. All the tetranuclear copper complexes have a $[Cu_4(\mu\text{-}O)_4]$ core and are dominated by ferromagnetism. For other $M(II)_4$ [2 x 2] (M = Mn(II), Ni(II)) square grids,

antiferromagnetism is observed with varying magnitude of coupling depending on the M-O-M bridge angles. A spin coupled heterometallic $[Cu(II)_3Fe(III)_3]$ square grid was synthesized from mononuclear precursors and showed overall ferrimagnetism [60]. The use of strongly coordinating anions encourages the formation of heteroleptic tetranuclear square grids. However, when weakly coordinating anions (e.g. ClO_4^-) are used, it favors the formation of homoleptic pentanuclear clusters as the dominant product. This was shown true for the ditopic ligand poap with Mn(II), Co(II), and Zn(II) [61, 62]. Antiferromagnetic exchange coupling was detected in all of the pentanuclear clusters. A detailed discussion about tetranuclear and pentanuclear clusters is given in Chapter 4.

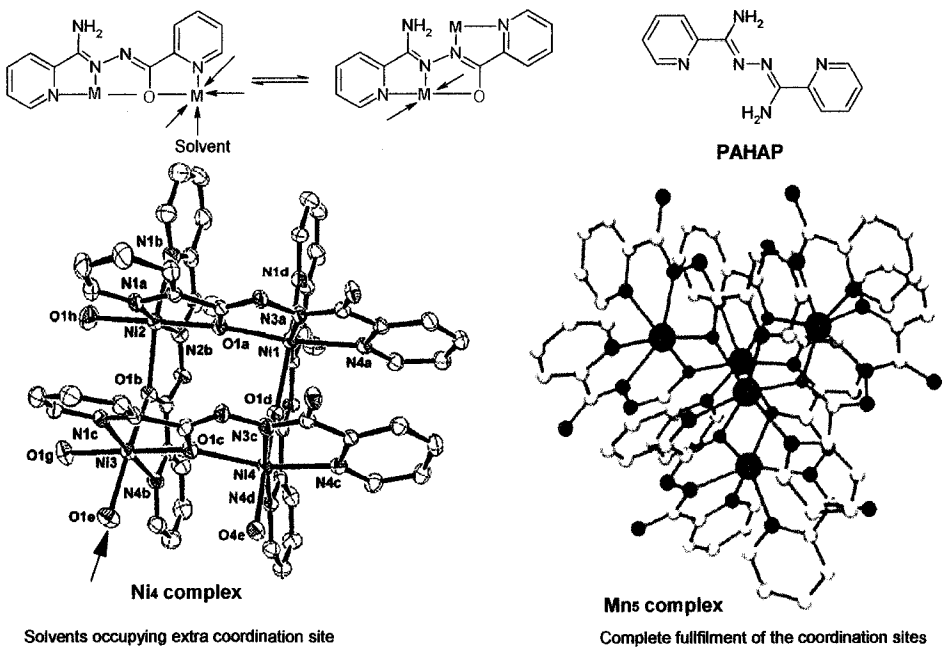

Fig. 1.2 Partial and complete filling of coordination sites in a tetranuclear and pentanuclear cluster respectively.

Tetranuclear [2 x 2] grid structures using relatively rigid ditopic diamide type ligands, where the center of the ligand contains a pyrazine moiety, have been reported by Brooker and co-workers. Fig. 1.3 shows a ligand and a schematic view of the tetranuclear copper complex obtained by self-assembly [63]. The adjacent copper centers are bridged by the aromatic pyrazine ring. The complex contains a large cavity in the center. In some cases, the central cavity of a self assembled cluster contains anion molecules which have a stabilization effect on the overall formation of the complex. Dunbar and co-workers showed that the ring size of the resultant cluster can be controlled and strategically altered in a reversible way by the suitable choice of the anion size. 3,6-Bis(2-pyridyl)-1,2,4,5-tetrazine (bptz) (Fig. 1.3 (b)) forms preferentially [2 x 2] square tetranuclear grids when reacted with solvated Ni(II) ions in the presence of small anions (e.g. ClO_4^-).

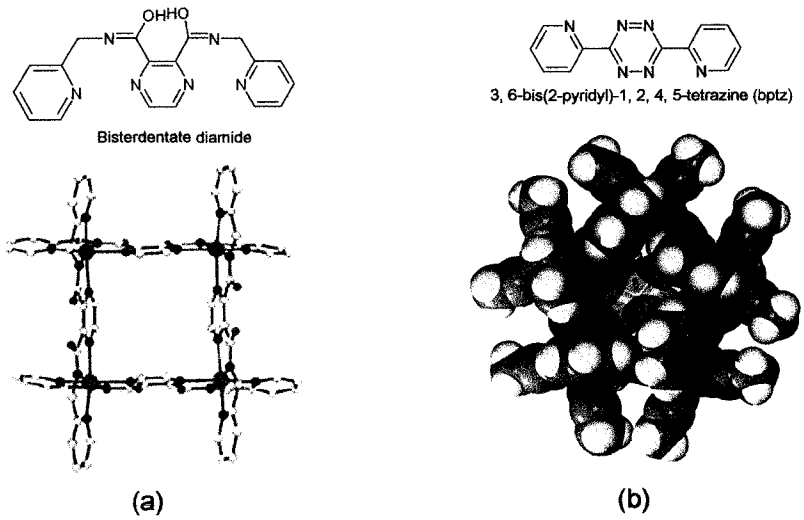

Fig. 1.3 (a) Schematic representation of the [2 x 2] Cu_4 grid; (b) Space filling diagram of the pentagon in $[(bptz)_5Ni_5]^{9+}$ cation.

However, larger anions (e.g. SbF_6^-) favor the formation of pentagons. The molecular pentagon can easily be converted back to the square by addition of excess small anions [64].

1.2.4 Octanuclear and Nonanuclear grids - higher homologues made by self-assembly

2,6-Pyridine based tritopic ligands which have two open chain diazine groups in their backbone (e.g. 2poap and its analogues), have been exploited successfully to give homoleptic square [3 x 3] nonanuclear grids in high yield when reacted with transition metal ions M (M = Fe(III), Mn(II), Co(II), Ni(II), Cu(II), and Zn(II)) [65]. Two sets, each having three heptadentate ligands, sandwich nine metals from above and below the plane of the grid to form the molecule creating a central $[M_9(\mu\text{-}O)_{12}]$ core. All of the nonanuclear clusters exhibit overall antiferromagnetic interactions between the metal centers due to a large angle at the hydrazone oxygen bridge, except for the $Cu(II)_9$ grids, where ferromagnetic coupling is observed [66].

A second unusual class of $Cu(II)_8$ octanuclear pinwheel clusters was formed when tritopic ligands such as '2poap' reacted with Cu(II) metal ions in solvents such as MeOH, or CH_3CN at low temperature. The first incidental discovery of this class of compounds was observed when the ligand 2poap was reacted with $Cu(NO_3)_2.3H_2O$ in the presence of $Gd(NO_3)_3$ [67]. Gd(III) ion was initially thought to have a precoordination effect in the self-assembly process. More pinwheel clusters were synthesized with similar

classes of ligands e.g. Cl2poap, Cl2pomp, without the presence of $Gd(III)(NO_3)_3$ [68]. The important structural features of this class of clusters include a $[Cu_4(\mu\text{-}O)_4]$ central square core, where four Cu(II) centers are bridged by hydrazone oxygen atoms. Another four Cu(II) centers are held by four appended arms of the ligand on the periphery of the complex core with oxygen or N-N diazine bridges. This forms a 'pinwheel' type structure. The orthogonal arrangement of the metal magnetic orbitals revealed from the alternative short and long connections between adjacent copper centers leads to a unique situation of ferromagnetic exchange coupling between the Cu(II) centers.

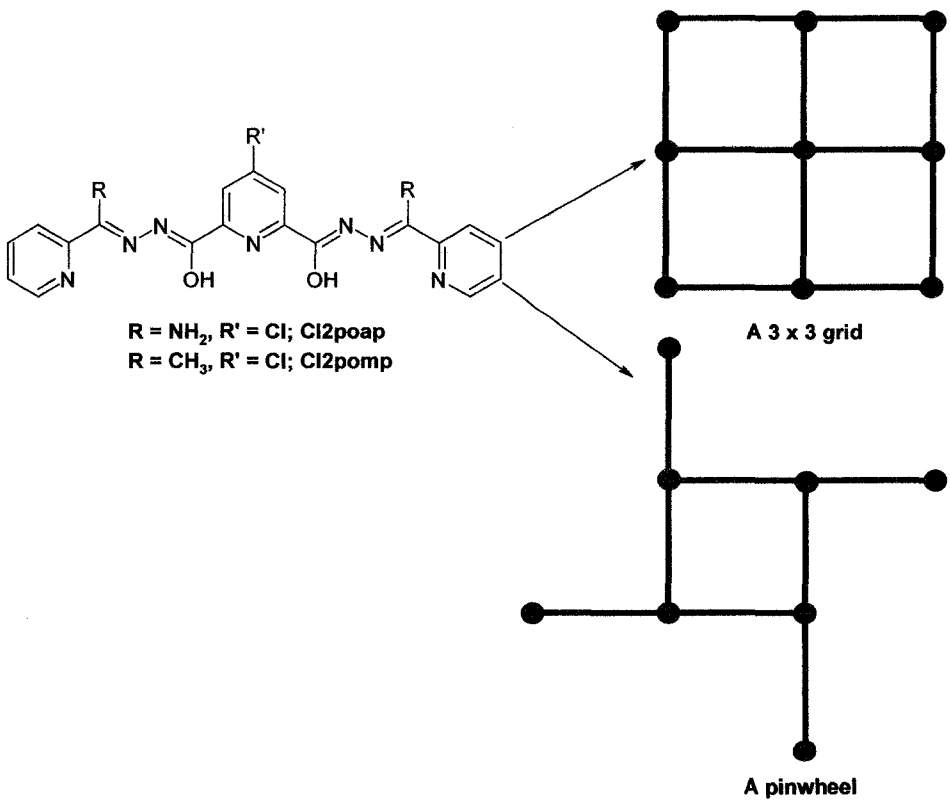

Scheme 1.4 A 3 x 3 grid and a pinwheel cluster.

1.2.5 Polynuclear rings - serendipitous assembly:

Introducing rigid ligands which have strict binding preferences into the self-assembly process and then inviting transition metals for coordination has evolved as a successful way of making polymetallic arrays, with some degree of predictability and control. We can call it 'designed self-assembly'. This requires a similar coordination environment to be maintained at each metal site. The disadvantage of 'designed self-assembly' is that it restricts access to many unpredictable structures.

The use of less well behaved ligands or modifying an existing symmetric ligand and letting them self-assemble in the presence of transition metals could result in unpredictable and novel polymetallic structures by serendipity. Once the possibility of the formation of fairly rigid five and six membered chelate rings is excluded, the coordinative flexibility of any polydentate ligand increases enormously. This in turn allows the stabilization of many unpredictable structures with the help of additional ligands such as alkoxide or hydroxide. This was termed as 'serendipitous assembly' [69]. The oxalic dihydrazide based ligand 'pttp' (Fig. 1.4), which can exist in S-*cis* or S-*trans* conformations, has the ability to bind metals terminally and also by secondary coordination through the oxalic hydrazide group itself. When reacted with metals like Co(II), Fe(II) it gives [2 x 2] tetranuclear square complexes [70]. A slight terminal modification of the ligand (ppttp; Fig. 1.4) gave a unique octanuclear $Ni(II)_8$ cluster when reacted with $Ni(BF_4)_2$. $6H_2O$. The unique feature of the structure is that it contains a group of eight Ni(II) centers at the periphery of an octanuclear ring with Ni(II) ions

arranged at the external ligand pockets [71]. Each pair of adjacent Ni(II) centers in the cluster is bridged by an N-N diazine group in a *trans-* fashion. Variable temperature magnetism suggests that strong antiferromagnetic exchange coupling exists within the octanuclear cluster.

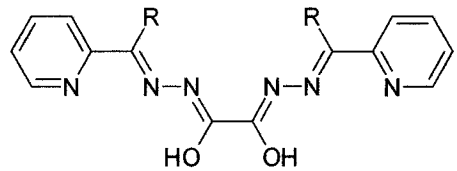

R = NH_2; pttp; R = Ph, ppttp

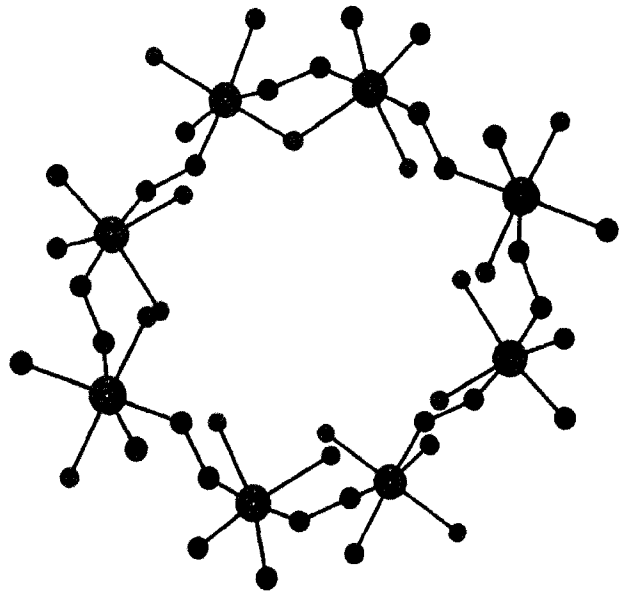

Ni(II)$_8$

Fig. 1.4 'pttp' type ditopic ligand and **POVRAY** representation of the octanuclear Ni_8 cluster.

Exploitation of the coordination chemistry of simple molecules like pyridonate and halogen substituted pyridonates with simple acetates has enabled the synthesis of

beautiful yet complicated molecules, by the route of 'serendipitous assembly' which would be otherwise difficult to synthesize in any thoughtfully designed way. Dodecanuclear $Ni(II)_{12}$ [72, 73] and $Co(II)_{12}$ [74], and larger $Cu(II)_{36}$ and $Cu(II)_{44}$ clusters by Powell and co-workers [75, 76] are important to mention in this context and were synthesized using very simple organic aminocarboxylic acids such as nitrilotripropionic acid (H_3ntp). Three of the largest cyclic structures in this class which have been so far reported, comprising exclusively 3-d transition metals are the Fe_{18} wheel reported by Lippard and his co-workers [77], the $Ni(II)_{24}$ cluster reported by Winpenny and his group [78] and the enormous manganese ring $Mn(II)_{84}$ by Christou [79]. They were synthesized following the same strategy. The tetraicosanuclear $Ni(II)_{24}$ cage is an octamer of repeating trinuclear subunits bridged by acetate and mpo ligand (mpo = 3-methyl-3-pyrazolin-5-one). The magnetic behavior is dominated by antiferromagnetic exchange between Ni(II) centers [78].

1.3 Introduction to magnetic behavior of inorganic polynuclear assemblies

1.3.1 Basics of Magnetism

The fundamental aspects of magnetism continued to be elusive until quantum mechanics led to the revelation that the key ingredient of magnetic behavior is the interplay of the spins of electrons [80]. All substances are affected in some ways in the presence of a magnetic field. When a substance is placed in a magnetic field H (Oe), the

magnetic induction B that the substance experiences is the sum of the field applied and an additional component contributed by the substance itself.

$$B = H + 4\pi I \qquad [1.1]$$

Where I = Intensity of magnetization.

Dividing both sides with field strength H gives intensity per unit field strength which is known as the volume susceptibility (κ). The quantity B/H is called the magnetic permeability P.

$$B/H = 1 + 4\pi I/H \qquad [1.2]$$

$$\kappa = I/H \qquad [1.3]$$

But the general practice is to express susceptibility per unit mass. So the gram susceptibility χ_g can be related to the volume susceptibility by the following equation

$$\chi_g = \kappa/\rho \qquad [1.4]$$

Where ρ is the density and χ_g is the susceptibility per gram. Gram susceptibility can be converted to molar susceptibility by the following equation 1.5.

$$\chi_M = \chi_g M \qquad [1.5]$$

In the above equation, M is the molecular weight of the material.

In principle, the total susceptibility of a substance is the algebraic sum of two contributions, diamagnetic χ^D and paramagnetic χ^P susceptibilities.

$$\chi^T = \chi^D + \chi^P \qquad [1.6]$$

In one case, the substance can produce a flux which opposes the applied field causing a reduction in density of the lines of magnetic force passing through it. Such substances are called '*Diamagnetic*' substances. Diamagnetic samples are therefore repelled by the applied field. This effect is independent of temperature. In the other case the substance may produce a flux which enhances the density of magnetic lines of force passing through it. In other words, the sample will tend to move to the regions of highest field strength. Those samples are said to be '*Paramagnetic*' and paramagnetic substances are attracted by the applied field. This effect is temperature dependent.

Diamagnetism is an underlying property of all matter. Quantum mechanically said, it is due to the interaction of the magnetic field with the motion of the bonding and non-bonding paired electrons in their orbitals [80]. χ^D is independent of both the temperature and the strength of the applied field. It can be calculated from the so called 'Pascal's constants' and is effectively a positive quantity in equation 1.6. Paramagnetic susceptibility χ^P is generally distinctly larger than diamagnetic χ^D, except in cases where compounds with large molecular weight (e. g. proteins with a single ion active site) contain only a few paramagnetic centers. In such cases the additive method does not

work and direct study of the diamagnetic susceptibility is necessary [81]. It is important to remember that as diamagnetism is associated with paired electrons, all matter possesses a diamagnetic component. So, when magnetic properties of a paramagnetic substance are measured, it is necessary to add a correction for its diamagnetic component.

1.3.2 Temperature dependence of the paramagnetic substances - The Curie law

As mentioned earlier, the magnetic moments of paramagnetic substances are affected by changes of temperature, although the number and proximity of the individual spin centers, and coupling between the spin centers determine the overall magnetic behavior of a substance in a magnetic field. For an isolated spin system, paramagnetic susceptibility is inversely proportional to the absolute temperature. This is the well known Curie law (Equation 1.7). C is the Curie constant.

$$\chi = C/T \qquad [1.7]$$

This law holds true for the compounds where individual spin centers are magnetically well separated (dilute). A different way of presenting the Curie law is shown in equation 1.8, where the Curie constant C is expressed in terms of N, g, μ_B, k and spin quantum number S of the particular ion [82].

$$\chi = N\mu_B^2/3kT\{g^2 S(S+1)\} \qquad [1.8]$$

Where N is Avogadro's number, g is the Landé factor, μ_B is the magnetic moment expressed in Bohr Magnetons, S is the spin quantum number (e. g. 1/2, 1 etc.), k is Boltzmann's constant, and T is temperature in degrees Kelvin.

The property of a paramagnetic substance is frequently and more conveniently expressed in terms of "effective magnetic moment" μ_{eff} where the moment is expressed in Bohr magnetons. This is related to the atomic susceptibility of the paramagnetic center by the following equation

$$\chi_A = N\mu_{eff}^2 / 3k_B T.\beta^2 \qquad [1.9]$$

where β is the Bohr magneton.

$$\beta = \frac{eh}{4\pi mc} = 0.927x10^{-1} erg.gauss^{-1} \qquad [1.10]$$

Substituting the values for N = 6.023 x 10^{23}, Boltzmann constant k_B = 1.381 x 10^{-16} erg / deg, T is the absolute temperature in Kelvin, β being the Bohr magneton = 0.9273 x 10^{-20} erg / gauss, the above equation gives a general form

$$\mu_e = 2.828\sqrt{\chi_M T} \qquad [1.11]$$

This is known as the Langevin formula for calculating spin only values. χ_M is the molar susceptibility after correction for any diamagnetic component.

1.3.3 Ferromagnetism vs Anti ferromagnetism - Curie-Weiss correction

Interaction between paramagnetic centers gives rise to two more divisions in magnetic properties, antiferromagnetism and ferromagnetism. In compounds where the molecular or the crystal structure is such that it brings the paramagnetic spin centers sufficiently close, or there is actually a bridging bond between the spin centers, the spin centers will most likely interact. In cases where at lower temperature the spins oppose each other leading to a reduced total susceptibility compared with the sum of the individual spins, the interaction is said to be antiferromagnetic. This happens in many synthetic and natural dinuclear and polynuclear complexes. In relatively rare cases, spin alignment enhances the susceptibility with respect to that from the sum of the independent spins, and this is called ferromagnetic coupling. Both the behavior of an isolated paramagnetic spin and magnetically coupled spins can be modeled with the Curie-Weiss Law (Equation 1.12) and can be schematically represented (Fig. 1.5).

$$\chi = C/(T + \theta) \qquad [1.12]$$

Where C = Curie constant, θ = Curie–Weiss constant. The Curie-Weiss law is applicable for a system where the individual spin centers are in such close proximity that spin interaction is possible. If however, individual spin centers are coordinated with large ligands or are heavily solvated, the non-interacting spin centers can be considered as isolated and equation 1.7 applies.

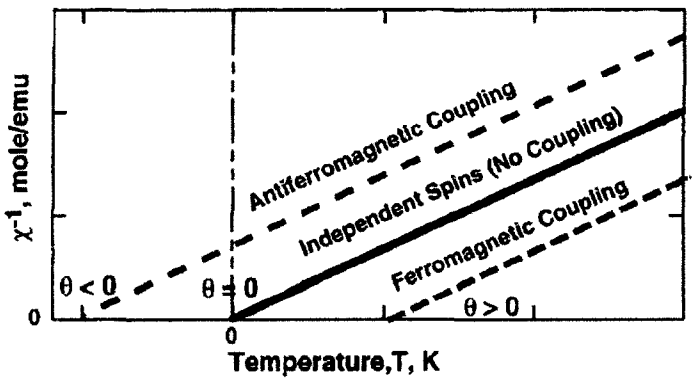

Fig. 1.5 Representation of the magnetic behavior of two interacting spins with variable temperature.

A plot of $1/\chi$ against T clearly shows these two behaviors schematically. For ferromagnetic substances the intercept is positive (+ ve θ value). Curie discovered that for ferromagnetic substances there is a temperature above which normal paramagnetism sets in. This is known as the Curie temperature Tc. In some cases this is equal to the value of the intercept on the temperature axis. θ is sometimes referred to as the Curie temperature. Similarly, for antiferromagnetic substances, the temperature has to be below zero to observe the antiferromagnetic effect. The - ve intercept on the temperature axis is called the Néel temperature T_N.

A much more idealized representation of these three types of paramagnetic substance can be illustrated by a plot of χ against temperature such as that given in Fig. 1.6. For simple non interacting paramagnetic centers, at high temperature (T) thermal energy is sufficient to randomize the spins of the sample. Upon cooling, spin alignment

overcomes the randomization energy and thus the susceptibility increases with the lowering of the temperature. For ferromagnetic compounds, the behavior of the sample in the magnetic field is analogous to that of a simple paramagnet at temperatures above Tc. At the Curie temperature the individual spins acquire a tendency to become *parallel* which becomes dominant and overcomes the thermal randomization. So continued cooling below Tc thereby yields an increase in χ, greater than that expected for a simple paramagnet. Conversely, for antiferromagnetic compounds, randomization of spins by thermal energy happens above the Néel temperature T_N. Thermal cooling below the Néel temperature helps *antiparallel* alignment of the spins which overcomes the randomization. Accordingly, a maximum in χ is observed in the χ versus T profile.

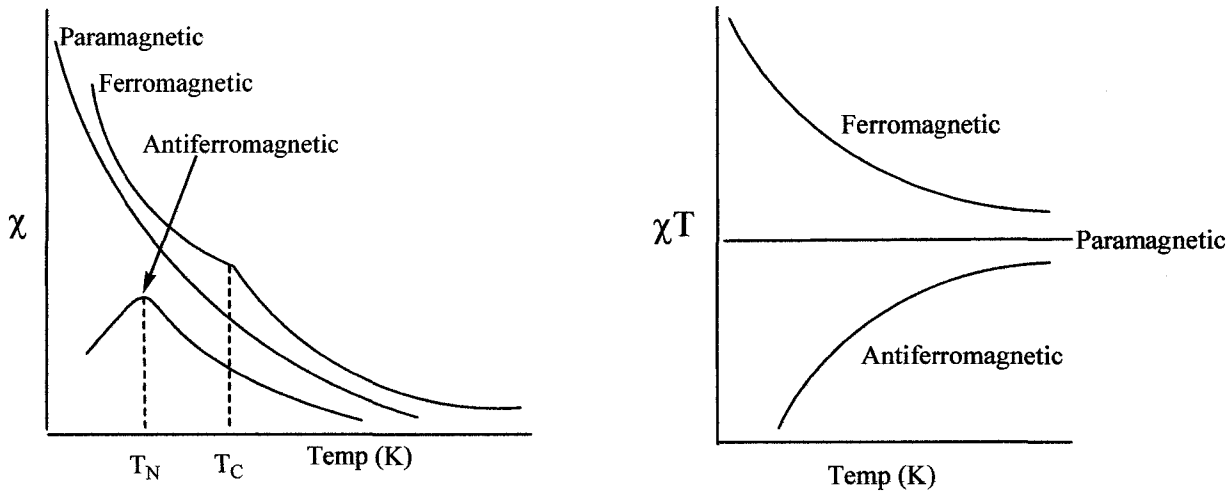

Fig. 1.6 Representation of three types of magnetism showing χ vs Temperature and χT vs Temperature profile.

The molar susceptibility further decreases on continued cooling. In practice it is common not to observe a discontinuity in the χ versus temperature profile of a ferromagnetic complex. For this reason, a plot of χT versus T is sometimes utilized. Such a plot yields a clear distinction between all three types of magnetism (Fig. 1.6).

1.4 Exchange coupling in a dinuclear complex with a single atom bridge - Molecular magnetism

To further illustrate the two types of magnetism discussed earlier, let us consider a dinuclear complex containing two paramagnetic centers A and B. The two spin centers interact, usually via bridging ligand groups. This is called a 'Superexchange process'. If we ignore the orbital contribution, the isotropic magnetic spin exchange between the metal centers can be given by the Heisenberg-Dirac-Van Vleck Hamiltonian

$$H_{ex} = -2J\{\hat{S}_A \cdot \hat{S}_B\} \qquad [1.13]$$

Here S_A and S_B are the local spin quantum numbers of the interacting ions, and 2J is the exchange integral between the two centers. If 2J is negative, the lowest state is that with a maximum number of spins paired.

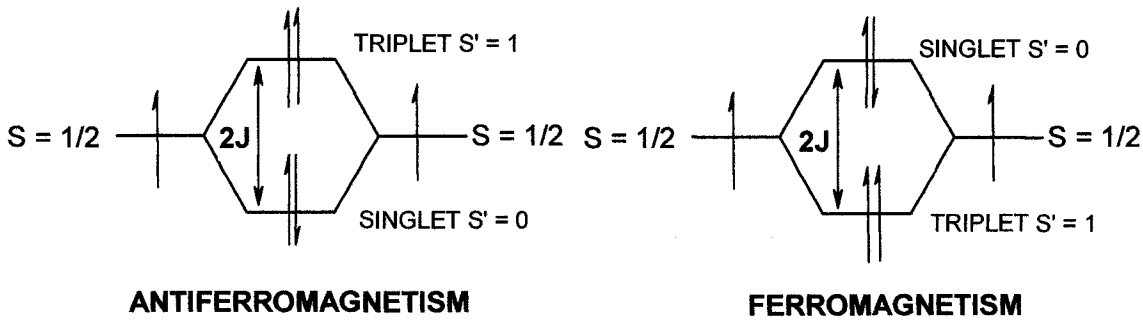

Scheme 1.5 Energy separation diagram for antiferromagnetism and ferromagnetism for a dinuclear system.

This results in antiferromagnetism. If on the other hand 2J is positive, the lowest state has spins aligned or parallel. This is called ferromagnetism. In general antiferromagnetism is very common in nature compared to ferromagnetism. A schematic diagram (Scheme 1.5) clearly shows the phenomenon in terms of an energy level scheme.

For an antiferromagnet, high temperatures will cause most of the electrons to occupy the triplet energy state and so the system will behave similar to a Curie-Weiss paramagnet. χ values will be low due to the thermal spin randomization effect. The electrons will drop to the lower energy singlet state at temperatures close to 2J which is accompanied by a dramatic drop in χ . For the ferromagnetic case, at high temperatures the system again behaves like a Curie-Weiss paramagnet even though a significant population of electrons remains in the singlet state. As the temperature is lowered,

electrons populate the triplet state more and consequently the χ increases. Scheme 1.6 shows how the 2J value corresponds with the variation of temperature.

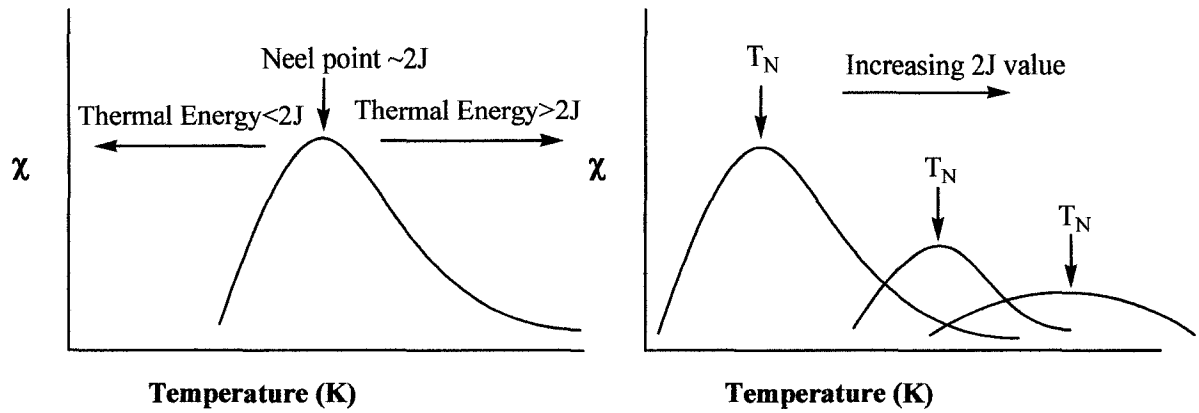

Scheme 1.6 The Néel point temperature at which the maximum occurs is closely related to 2J.

There are mainly two types of antiferromagnetic behavior observed. In 'intermolecular' antiferromagnetism, the interaction extends throughout the whole crystal network, and generally it is weak in magnitude. In 'intramolecular' antiferromagnets, the exchange coupling is only considered within the molecule which is much stronger compared to any long range interactions. The exchange equation in 1.13 is valid for both ferromagnetism and antiferromagnetism. The exchange coupling between the coupled centers in antiferromagnets is associated with the ligands bridging between the two interacting atoms. In cases where the spin interaction is very direct or very strong, covalent bonding results e.g. $Fe_2(CO)_9$, $Mn(CO)_{10}$. The metal-metal bonds in these complexes can be regarded as extreme cases of antiferromagnetic coupling and they appear diamagnetic.

1.5 Isotropic spin interaction between metal centers in metal complexes

1.5.1 Molar magnetic susceptibility-the Van Vleck equation

The magnitude of interaction of a metal complex with an external magnetic field in classical terms is given by its degree of magnetization

$$M = -\partial E/\partial H \qquad [1.14]$$

Where E is the energy and H is the magnetic field. Using the quantum mechanical terms, the bulk molar magnetization can be expressed as

$$M = \frac{N\sum_N(\partial E_n/\partial H)\exp(E_n/kT)}{\sum_n \exp(-E_n/kT)} \qquad [1.15]$$

The difficulty about this thermodynamic expression is that it is not very user friendly to ordinary users and besides one has to know all the E_n values as a function of Field strength to calculate the derivatives. A much more convenient expression for calculating molar magnetic susceptibility is the Van Vleck equation [83].

$$\chi_M = \frac{N\sum_n (E_n^{(1)2}/kT - 2E_n^{(2)2})\exp^{E_n^{(0)}/kT}}{\exp^{E_n^{(0)}/kT}} \qquad [1.16]$$

Where $E_n^{(0)}$ is the energy of the nth level in absence of the magnetic field. And $E_n^{(1)}$ and $E_n^{(2)}$ are the coefficients of the first and second order Zeeman effects respectively.

The different atomic or molecular energy levels of a paramagnetic sample (monoatomic or polyatomic) are altered when placed in a magnetic field due to interaction with the external magnetic field. Depending on the magnitude of the field strength and the temperature of the system, electrons populate various energy levels leading to different total spin state combinations. Therefore, it is necessary to calculate the different spin state combinations and their related energies and relate them to the susceptibility in order to understand the overall bulk magnetic behavior. In a zero magnetic field electrons retain their orbital degeneracy. But when a paramagnetic sample is placed in a magnetic field, the first order Zeeman effect, which accounts for the splitting of the energy states in a magnetic field, splits each level symmetrically into 2S' +1 component levels having energies ranging from $g\beta JH$ to $-g\beta JH$. The separation between two adjacent energy levels is $g\beta H$. An illustration of such splitting and removal of degeneracy is given in Scheme 1.7. A second order Zeeman effect however results from mixing between the ground state and some excited energy states. When the energy separation of these states is >> kT, population of the higher energy levels does not occur, but rather it accounts for an additional contribution to the susceptibility known as Temperature Independent Paramagnetism (TIP). A small term ($N\alpha$) is included with the modified Van Vleck equation which also takes account of the small underlying diamagnetism as well (Equation 1.18).

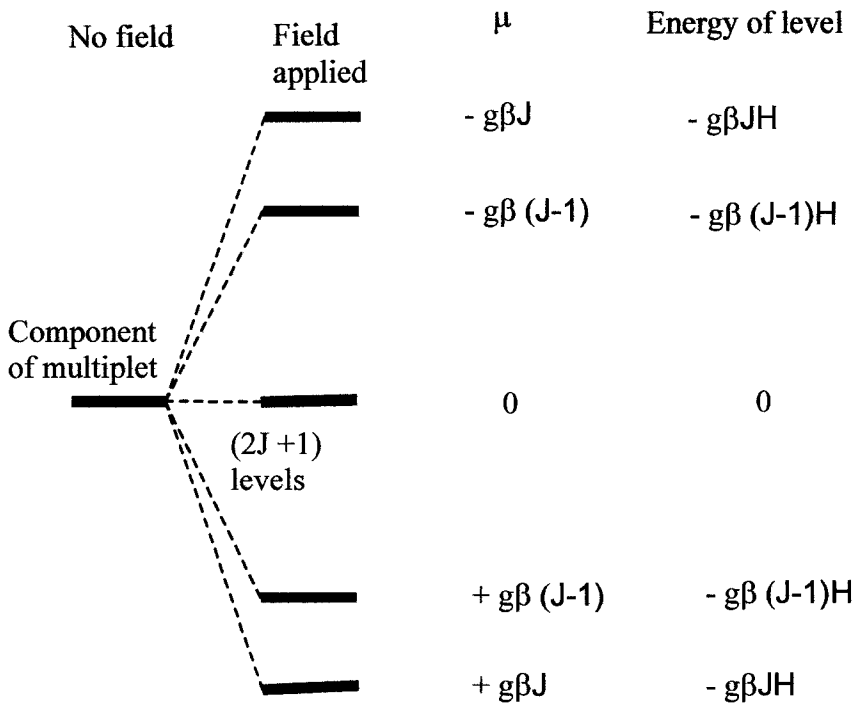

Scheme 1.7 Removal of degeneracy by application of magnetic field and energy separation between the multiplet.

In an ideal system the energy expression using the Heisenberg spin Hamiltonian includes the interaction between the paramagnetic centers, ligand field effects and Zeeman effect (Equation 1.17]

$$H = -\sum_{i<j} J_{ij} \cdot S_i \cdot S_j + \sum_i S_i \cdot D_i \cdot S_i + \sum_i S_i \cdot g_i \cdot B \qquad [1.17]$$

However, the above Hamiltonian can be simplified by ignoring the ligand field effects (2nd term), and the Zeeman effect (last term; g represents the Landé splitting factor). This simplification leaves the evaluation of the total energy in terms of the spin quantum numbers (S) of the paramagnetic centers and the exchange integral between them. If the total spin quantum number combinations (S′) and their corresponding energy terms are substituted into the Van Vleck equation, the molar susceptibility of a substance can be calculated in its simplest form, equation 1.18.

$$\chi_M = \frac{N g^2 \beta^2}{3kT}\left(\frac{\sum S'(S'+1)(2S'+1)\Omega \exp(-E(S')/kT)}{\sum (2S'+1)\Omega \exp(-E(S')/kT)}\right) + N\alpha \qquad [1.18]$$

Here χ_M is the molar susceptibility, N is Avogadro's number, g is the Landé splitting term, S′ is the total spin quantum number (e. g. S1 = S2 = ½, S′ = 0, 1), E(S′) energy of a state for a particular spin combination, β = Bohr magnetons, k = Botzmann constant, T is temperature in Kelvins, Ω is the degeneracy factor and Nα is the correction term for temperature independent paramagnetism (TIP).

1.5.2 Application of Van Vleck equation for homodinuclear copper complexes- Modified Bleaney-Bowers equation

To illustrate the way the above equation is applied, we have to make some simplifying assumptions. Each ion has a spin angular momentum specified by the quantum number S. Then the total angular momentum is given by S′ such that S′ can

have values 0 to 2S with a total of (2S+1) values. Each of these values corresponds to a particular energy level given by J[S'(S'+1)]. Each level has a multiplicity of (2S'+1). Here J is the exchange coupling constant.

For an antiferromagnetic interaction (-2J), S' = 0 defines the ground level and S' = 2S defines the highest. On the other hand if the interaction is ferromagnetic (+2J), S' = 2S defines the ground state. For S = ½ (Cu(II) ion), S' can have values S' = 0, 1 with energies 0, and 2J. Substituting these values into the equation 1.18 we get

$$\chi_M = \frac{N g^2 \beta^2}{3kT}\left[\frac{6\exp(-2J/kT)}{1+3\exp(-2J/kT)}\right] + N\alpha \qquad [1.19]$$

Susceptibility per metal χ_A can then be calculated by replacing $\chi_A = 1/2\chi_M$. So the above equation takes the form

$$\chi_A = \frac{N g^2 \beta^2}{3kT}\left[\frac{1}{3+\exp(-2J/kT)}\right] + N\alpha \qquad [1.20]$$

For Cu(II) complexes, we have to consider two more things. Cu(II) and other paramagnetic polynuclear metal complexes normally contain a small amount of paramagnetic impurity and also non-localized intermolecular interactions are observed.

$$\chi_A = \frac{Ng^2\beta^2}{3k(T-\theta)}\left[\frac{1}{3+\exp(-2J/kT)}\right](1-\rho)+\left(\frac{Ng^2\beta^2}{4kT}\right)\rho+N\alpha \qquad [1.21]$$

ρ is the fraction of paramagnetic impurity, θ is the Weiss like correction term which accounts for the intermolecular interactions. This equation is well known as the modified Bleaney-Bowers equation [84]. This equation is a different and specific form of the Van Vleck equation 1.18 adopted for (S1 = S2 = ½) dinuclear Cu(II) complexes. The middle term ($Ng^2\beta^2/4kT$) is the contribution of the paramagnetic impurity towards the total susceptibility.

Putting exp (-2J/kT) = X, and $K = Ng^2\beta^2/3k$ (= $0.1251g^2$), equation 1.21 can be expressed in another form as equation 1.22. Similar expressions can be derived in the same way for S = 1, 3/2, 2, 5/2 etc. For S = 1/2

$$\chi_A = \frac{3K}{T}\left[\frac{1}{3+x^2}\right]+N\alpha \qquad [1.22]$$

For S =3/2

$$\chi_A = \frac{3K}{T}\left[\frac{14+5x^6+x^{10}}{7+5x^6+3x^{10}+x^{12}}\right]+N\alpha \qquad [1.23]$$

For S = 5/2

$$\chi_A = \frac{3K}{T}\left[\frac{55+30x^{10}+14x^{18}+5x^{24}+x^{28}}{11+9x^{10}+7x^{18}+5x^{24}+3x^{28}+x^{30}}\right]+N\alpha \qquad [1.24]$$

If nα is neglected, and the exchange integral 2J is set to zero, we can calculate the susceptibility for one Cu(II) ion at 300K which is $1.251\text{x}10^{-3}$ emu per metal. Putting this value in the Langevin formula (equation 1.11) gives us the spin only moment for one Cu(II) metal ion which is $\sqrt{3} = 1.73\ \mu_B$.

Three mathematical methodologies are available for the calculation of different spin states and magnetic susceptibility of a substance with interacting spin centers. Vector coupling (**VC**) is the easiest among them to understand, set up and use. This was developed by Kambe [85]. The main drawback with this method is that it works only with certain symmetries. And also the calculation of different spin combinations becomes very complicated and non trivial where large numbers of spins are involved.

The second method is full matrix diagonalization (FMD) [86]. It is very powerful and allows the calculation of spin states for a large variety of systems. The major disadvantage of this method lies in the fact that the dimension of the Hamiltonian matrix increases dramatically with increase of the number of paramagnetic centers. So, for large matrices, the diagonalization time becomes very long which results in longer total computation time. Also, for a very large total number of unpaired electrons,

diagonalization goes beyond the capabilities of normal PC systems. Symmetry reduction techniques then become necessary. MAGMUN 4.1 software, which was used in all cases in this thesis to fit the variable temperature magnetic data, uses this method. The third and last is the irreducible Tensor operator method (ITO). This method reduces the size of the matrices required for the calculation and thereby reduces the computation time but it is very difficult and requires sophisticated mathematics to set up in the first place. Besides, it is difficult to include terms like single ion effect (SIE) and zero field splitting (ZFS) in ITO.

1.6 MAGMUN 4.1

MAGMUN 4.1 is a windows based software package written in Visual Basic. It was developed to provide a convenient platform to model the variable temperature magnetic properties for a wide variety of polynuclear clusters having both simple and complex topology [87]. This program is useful especially for complex topologies where deriving an exchange equation or defining the eigenstates of the exchange is non trivial. The program contains two components. The OW01.ini which is the input file, and has to be created by the user. OW01.exe is the executable file, which reads the input file. The input file OW01.ini contains all the necessary information about the complex regarding nuclearity, the coupling scheme and the relative strength of coupling between the metal centers.

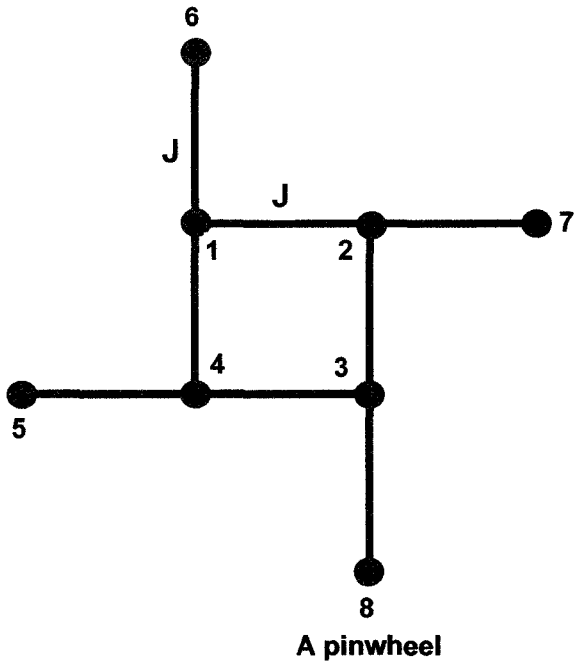

Fig. 1.7 A spin model for regular octanuclear pinwheel.

In order to create the OW01.ini file one has to draw a model of the complex with appropriate and logical numbering. For example, a simple octanuclear pinwheel complex can be considered. The atom numbering and the coupling constants are shown in Fig. 1.7.

The numbers of unpaired electrons for each of the spin centers are entered in the first line of the OW01.ini file. Any number can be entered depending on the identity of the transition metal. Also, it is not necessary for the spin quantum numbers to be same (e.g. 1 2 for Cu(II)-Ni(II) heterodinuclear system). The coupling scheme is entered in the second line showing the connectivity between coupled atoms with pairs of atom numbers (12 23 to show the coupling between atoms 1-2 and 2-3). Fig. 1.8 shows an example of OW01.ini file for the above octanuclear $Cu(II)_8$ pinwheel.

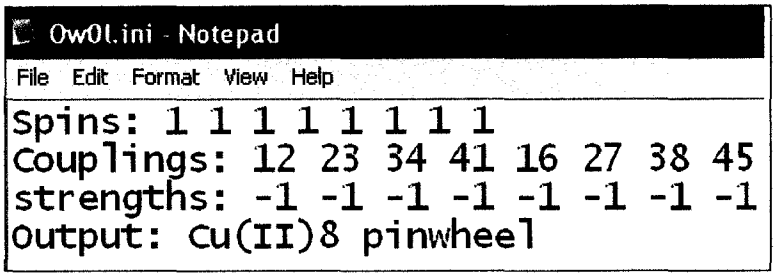

Fig. 1.8 MAGMUN 4.1 OW01.ini input file for a $Cu(II)_8$ octanuclear pinwheel.

The relative strengths of coupling are entered in the 3rd line. In a system as above where all the 'J' values are considered the same or equivalent due to direct symmetry, or imposed symmetry for simplification, '-1' (meaning -1 cm^{-1}) is a convenient number which can be translated readily into the non-linear regression analysis (NLR) of the experimental data. However, any value with positive or negative signs will work. Fitting procedures and conditions of the experimental data with non-linear regression for each class of complexes are discussed in the respective chapters. So, the best value of 'J' determined by NLR will be a multiple of unity. In such cases, the calculated 'J' value should be multiplied by the coupling strength to determine the actual coupling constant of the system. A -1 cm^{-1} will mean antiferromagnetic coupling while positive 1 cm^{-1} will mean a ferromagnetic coupling in the system. The name of the output file is entered in the 4th line and the file is saved with the desired file name.

The current package of MAGMUN 4.1 is limited to numerical inputs of J and individual 'J' values cannot be evaluated directly. However, for systems with different 'J'

values, the second coupling constant can be represented as an appropriate ratio of the first one. An example will illustrate the point. If a system has two different couplings, both ferromagnetic, the coupling strengths can be entered as 1 and 0.1. Such that after non linear regression of the experimental data, the absolute 'J' value (fitted value) should be multiplied by the input ratios of the coupling strength. So, in the above case the two J values will be related to each other by a ratio 10:1 (J1 = 10 x J2). A system with different coupling constants and also different exchange (ferromagnetic and antiferromagnetic) can also be treated in a similar way by putting appropriate signs before coupling strengths (e. g. -1 and 0.1 for antiferromagnetic and ferromagnetic respectively). Application of MAGMUN 4.1 is not limited to 2D complexes, 3D polyhedral complexes can also be treated in the same way.

After the OW01.ini file is created and saved, the program OW01.exe is used. The OW01.exe program calculates the spin states and energies of the system and generates two output files as **.spk and **.eig. A detailed description of MAGMUN 4.1 on how to handle several simple dinuclear, trinuclear, and tetranuclear spin models has been published [87]. The treatment of larger polynuclear spin models such as octanuclear pinwheel complexes and nonanuclear complexes has been discussed [88]. The discussion of magnetism of pinwheel complexes is included in chapter 5 and the corresponding **.spk files are included in the appendices. The **.spk file contains all of the vector coupled spin states of the system and their energies and is read into the MAGMUN 4.1 program and processed. Within the menu driven built-in subroutine of the software, the

**.spk file can be processed to simulate the magnetic profile and fit the experimental data by non linear regression. The fitted results can be saved and exported to any spreadsheet (e.g. Microsoft Excel). The **.eig file also contains all the energy terms from different spin state combinations but in a different format that cannot be fed into MAGMUN 4.1 directly. However, it is easier to use **.spk file in MAGMUN 4.1 for fitting purposes.

MAGMUN 4.1 is also capable of generating simulated graphical presentations of magnetization against variable field using the standard Brillouin function (equation 1.25).

$$M_S = Ng\beta SBs(y) \qquad [1.25]$$

At very low temperature (2K) and very high magnetic field, the magnetization approaches the maximum value close to the saturation magnetization M_S. The equation reduces to:

$$M_S = Ng\beta S \qquad [1.26]$$

Magnetization data are useful in understanding the magnetic ground state of a system. In the ground state, the resultant spin is obtained due to the summation of exchange effects. A simulated graphical representation generated by MAGMUN 4.1 showing several magnetization profiles for different spin ground states S = 1/2-5/2 for g = 2.0 at 2K is presented in Fig. 1.9.

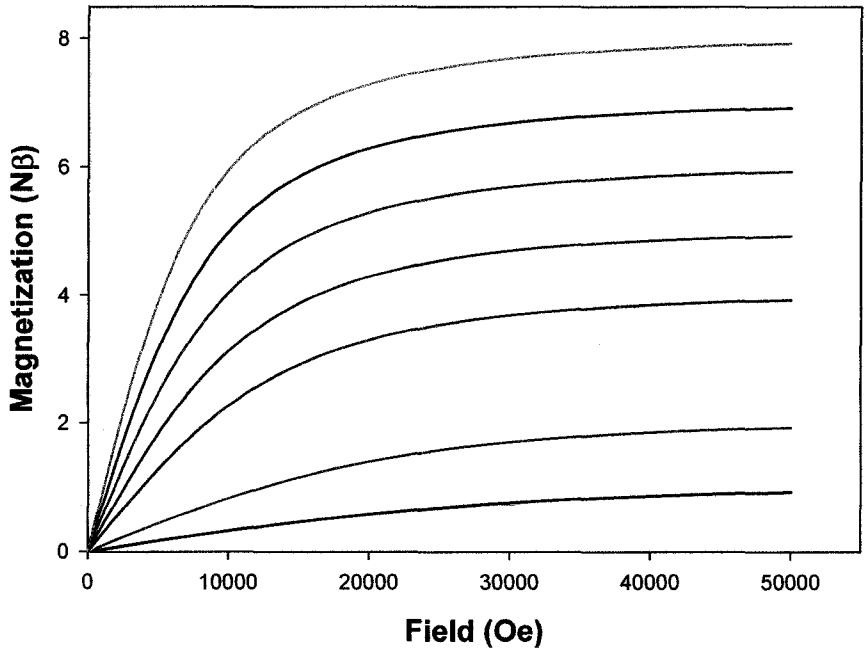

Fig. 1.9 Magnetization versus field plots for S = ½ (black), S = 1 (pink), S = 3/2 (yellow), S = 2 (red), S = 5/2 (purple), S = 3 (green), S = 7/2 (blue), S = 4 (orange) at 2 K for g = 2.0.

1.7 Scope of this thesis

This thesis will present a study on the coordination chemistry of some polynuclear complexes of first row transition metal ions and will focus on their structures and magnetic properties. A series of open chain N-N diazine-based ditopic and tritopic ligands with both flexible (e.g. -NH-) and rigid (e.g. pyridine-N) backbones were synthesized and their polynuclear transition metal complexes were prepared. Metal complexes are arranged according to their nuclearity. The initial chapters are devoted to

complexes with lower nuclearity and their magnetism while the later chapters will deal with higher nuclearity complexes such as a triakontahexanuclear copper cluster and their magnetism.

In Chapter 2, ligand synthesis and the extension of ligands are described. The synthesis of the N-N open chain diazine based ligand 'pomp' and a series of tritopic ligands derived from a diester of a secondary amine are presented as well. The importance of the presence of a rigid group in the ligand backbone for forming [n x n] grid complexes is emphasized. A specific strategy for a logical extension of the tritopic ligands towards tetratopic and pentatopic ligands with the use of different extender groups is also described. Structures of some unexpected intermediates are highlighted to emphasize the hydrolytic instability of such ligand extension procedures and other barriers to such organic synthesis.

In Chapter 3, trinuclear complexes of an open chain N-N diazine based ligand with flexible secondary amine (-NH-) backbones are presented. Both trinuclear Cu(II) and Mn(II) complexes are included and their magnetic properties studied. The metal centers in the trinuclear complexes are bridged by single N-N bonds. The ligands used were 'tritopic' and they did not form any [3x3] grids (e.g. as in the case of 2poap). This is explained in terms of the structural attribute relating to the secondary amine group present as the backbone in this class of ligands.

In Chapter 4, some tetranuclear and pentanuclear Mn(II) clusters are included and their magnetism studied. All the $Cu(II)_4$, $Mn(II)_4$, and $Mn(II)_5$ complexes reported in this chapter are synthesized using the ligand 'pomp' which is a $-CH_3$ analogue of poap. The tetranuclear copper complexes showed ferromagnetism. Both tetra and pentanuclear Mn(II) complexes were found to exhibit antiferromagnetism. The magnetism of these complexes was explained in terms of their hydrazone oxygen and N-N bridge angles.

Chapter 5 includes some examples of octanuclear copper 'pinwheels'. The ligand used to synthesize these complexes is '2pomp' which is again a $-CH_3$ analogue of 2poap. Octanuclear pinwheel clusters were found to lead to an overall ferromagnetic exchange in the cluster. In a unique case '2pomp' formed a 2D network of pinwheel clusters with $CuBr_2$. In the network each of the pinwheels was connected to four other pinwheels by an external copper(II) site.

Chapter 6 includes some nonanuclear [3 x 3] square grids derived from the same tritopic ligand '2pomp'. The nonanuclear grids contain a $[Mn_9(\mu\text{-}O)_{12}]$ core where adjacent Mn(II) centers are bridged by hydrazone oxygen with large Mn-O-Mn bridge angles, leading to a global antiferromagnetism in the grids.

In Chapter 7, one unique example of an inorganic cobalt catenane is included. Catenanes are interesting not only because of their topological beauty but also for the fact that they form by an intricate molecular self-assembly. The oxalic dihydrazide based

ligand 'pttp' was used. 'pttp' can have both *cis* and *trans* conformations and can form tetranuclear $M(II)_4$ clusters. A mechanistic explanation is given to suggest that the catenane was formed from a preformed tetranuclear $Co(II)_4$ ring, followed by 'ring opening' and 'ring closure' steps.

Chapter 8 includes a unique example of a $Cu(II)_{36}$ cluster, presented along with its magnetism. The terminally modified oxime ligand 'dpocco' yielded the cluster when reacted with $Cu(OAc)_2$. The cluster consists of an octamer of eight trinuclear subunits plus twelve other Cu(II) ions bridged between the trinuclear subunits. The adjacent Cu(II) centers within the subunit are bridged by oxime N-O groups and μ_3-OH. Overall antiferromagnetism was observed within the cluster.

Chapter 9 includes CITS (Current Imaging Tunneling Spectroscopy) imaging and magnetism of a [5x5] grid complex derived from the pentatopic ligand '4popap'. This ligand is a symmetric extension of the tritopic type ligands (e.g. 2poap). CITS has been developed for use with scanning tunneling spectroscopy (STS) of a sample surface and involves the measurement of the current-voltage (I-V) characteristics at each pixel of a normal STM topography. This allows the imaging of the metal centers in a complex applied to a surface as a result of selective tunneling through the metal 'd' orbitals. Overall anti-ferromagnetism was observed within the [5 x 5] grid which is correlated with the putative structural features.

CHAPTER 2

Self-assembly and ligand design - synthesis and strategic extension of ligands

2.1 Introduction

2.1.1 Design principle and predictability

The structures of metallo-supramolecular architectures made from the spontaneous self-assembly of organic ligands and metal ions can be controlled by making full use of the structural and coordination features of both of the participating components. By careful design of the ligand and specific choice of the transition metal, a supramolecular metal cluster of desired nuclearity can be synthesized. Transition metal ions have special properties which when incorporated in the self-assembly process can affect the overall outcome. They are:

a) Strict coordination geometry

b) Binding strength from weak to very strong

c) Formation and dissociation kinetics from labile to inert

A well designed ligand with an appropriate arrangement of donor atoms with their relative orientations in the binding sites under a set of particular pH and temperature conditions can give rise to fascinating metallo-supramolecular architectures. Most supramolecular structures, based on any directional interaction can be divided into two sub-categories; polymeric species and discrete aggregates.

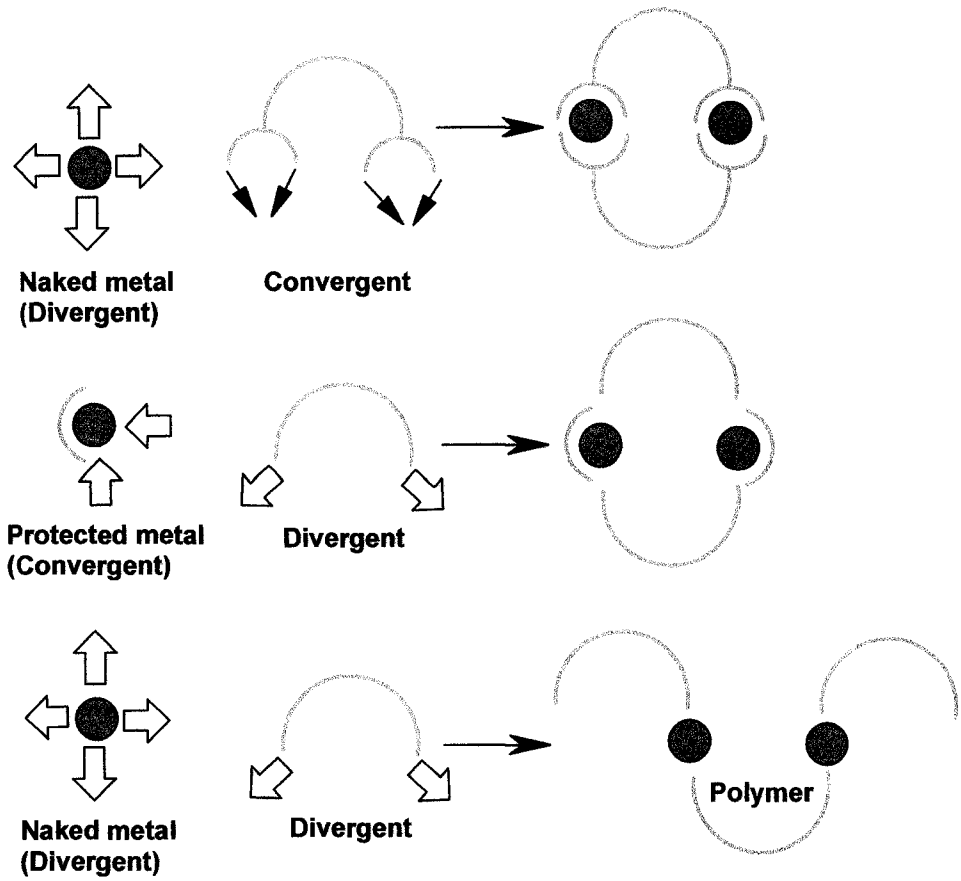

Scheme 2.1 Dependency of self-assembly on convergent or divergent nature of the ligand.

Fujita [89] pointed out that the type of aggregate produced is sometimes predictable and controllable by the nature and design of the building blocks forming the assembly; more precisely, the divergent or convergent nature of the host (in this case ligand). A host-guest type metal-ligand complex will be nonpolymeric and discrete if the ligand is convergent. Scheme 2.1 clarifies the concept. The host will envelop the divergent guest. If the convergent host cannot completely envelop the guest, a larger discrete aggregate

will be formed until the host is able to do so. This in turn leads to an expansion of the assembly size and dimension and nuclearity of the final complex. On the other hand, if a divergent ligand is used, a discrete complex can only be made if the metal center is protected by making it convergent using blocking ligands. However, in the case of both being divergent, a polymeric species would result [89].

2.1.2 Bipyridine type ligands

Polytopic bipyridine type ligands were developed by Lehn and co-workers. The compartmental nature of the ligand was successfully deployed to make a two layered cylindrical polynuclear assembly with Cu(I) by multiple component self-assembly (Fig. 2.1). An additional auxiliary ligand formed multi-layers within the assembly. Applying the same technique, analogous cylindrical architectures were also produced [90]. Flatter grid-like inorganic structures were also produced with the n-topic (n = di, tri, tetra) ligands shown in Scheme 2.2 which are constructed from repetitive terpyridine type coordination building blocks. [2 x 2] square grids from Co(II), Zn(II) [18, 91], Ni(II) [92], Cu(II) [93], a [3 x 3] square $Pb(II)_9$ grid and a [4 x 4] square $Pb(II)_{16}$ grid [22] were produced by self- assembly. In these self-assembled polynuclear clusters, the metal ion fits nicely into the coordination pockets constructed by pairs of pyridine and pyrimidine substituents creating an N_3 coordination environment. The pyrimidine group serves as the bridging unit between adjacent metal centers. This leads to intramolecular antiferromagnetic exchange interactions in such grids, despite comparatively larger metal separation (~ 6.5 Å for Co grid) [22] than the intermetallic distances (~ 4 Å) in other

analogous [2 x 2] square grids with hydrazone ligands developed by Thompson and co-workers [59].

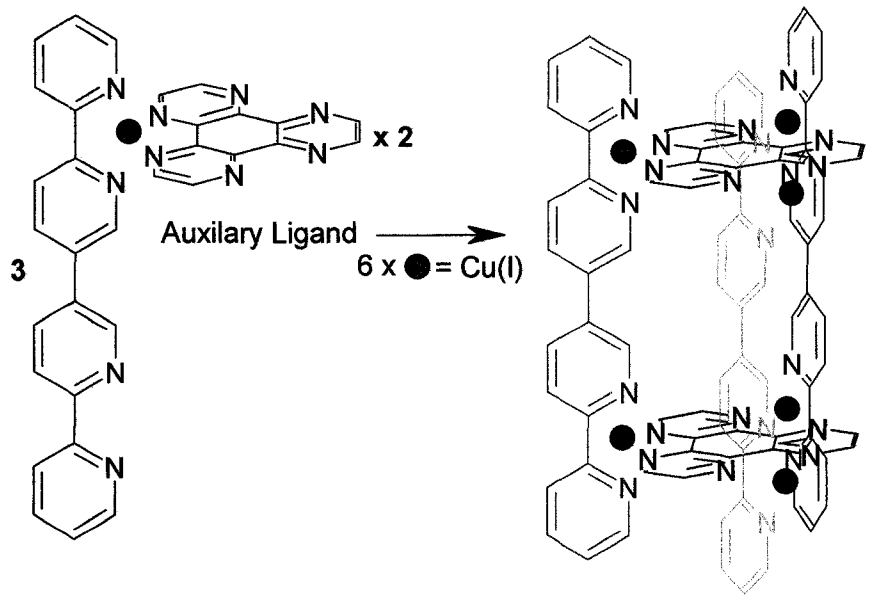

Fig. 2.1 Self-assembly of a two layered cylinder from a bipyridine type ligand.

Possessing an entirely aromatic nature, the bipyridine type ligands are planar. Each of the metal coordination sites in these ligands is constructed from three N-coordinations from the pyridine and pyrimidine groups (scheme 2.2). This gives a chelating nature to the ligands and they bind more strongly to the metal ions. Consequently, this inhibits ligand twisting or ligand bending during the course of the reaction.

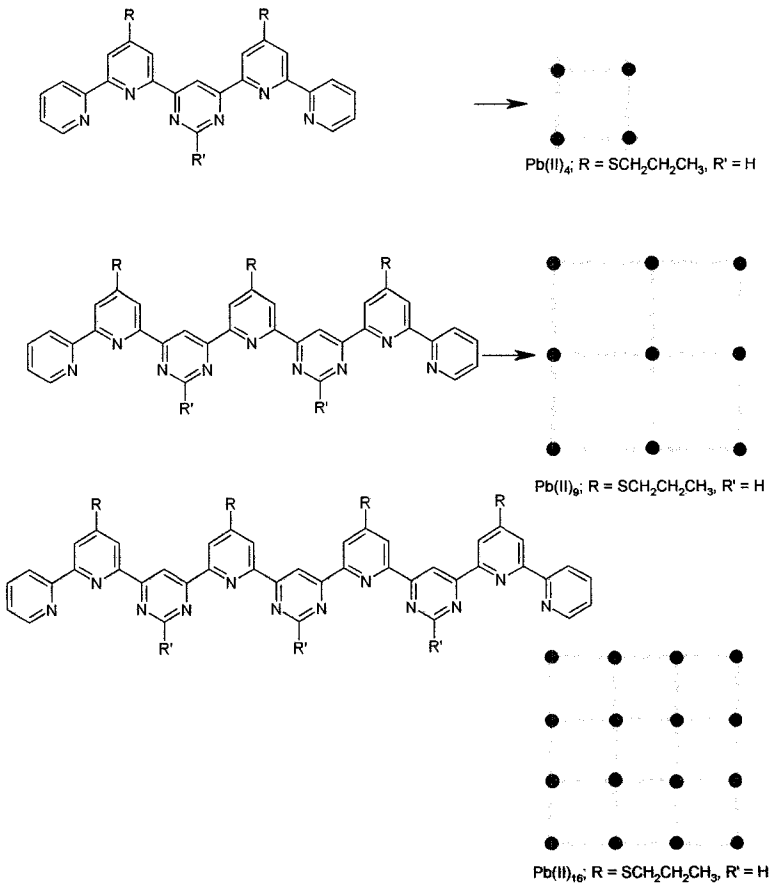

Scheme 2.2 [2 x 2], [3 x 3] and [4 x 4] grid formation from terpyridine type ligands.

As a result, the possibilities of having unexpected results are eliminated. Also, the chance of having variety in this class of polymetallic complexes is limited as well. However, there are other consequences too. Each of the coordination pockets in these ligands only fulfills half of the coordination requirement of a *mer*-octahedral metal cation (e.g. Mn(II), Ni(II)). This ensures the complete filling of the coordination requirement of metal ions from another similar ligand. It also conveys a directional property to the second incoming ligand such that, due to *mer*- arrangement of the metal ions, the second ligand must be

oriented perpendicular to the first in order for proper alignment of the ligands for grid formation. A similar mechanism is continued until the grid is complete. Scheme 2.2 shows the formation of [2 x 2], [3 x 3] and [4 x 4] grids from the terpyridine type ligand.

2.1.3 Hydrazone ligand with a flexible backbone

A tritopic ligand was synthesized with a secondary NH group as the central piece. Reaction of diethyl iminodiacetate with hydrazine gave the corresponding iminodiacetic dihydrazone in good yield. The syntheses of the ligand (**L1**) was completed by adding the appropriate end piece to form an amidrazone type linkage (from 2-cyanopyridine). Scheme 2.3 shows the synthetic route for such an imino-N based ligand. The principal feature of this class of ligands is that they contain contiguous, linearly arranged five membered chelate rings when coordinated, which are ideal templates towards the formation of grids. However, the introduction of a less rigid functional group in the core of the ligand has had some bearing on the overall stability of the clusters formed by self-assembly. Three different coordination modes were observed with the ligand '2noap' (Fig. 2.2). Linear trinuclear complexes (with Cu(II); mode (a) in Fig. 2.2) and triangular trinuclear complexes (with Mn(II); mode (b) in Fig. 2.2) were formed as major products when reacted with transition metals such as Cu(II) and Mn(II) respectively (Chapter 3). In another case, a dinuclear complex with distant metal centers (mode (c) in Fig. 2.2) was found to result when reacted with $Ni(BF_4)_2.xH_2O$. This is clearly a consequence of the overall ligand flexibility, which allows different coordination modes to occur. Such ligand orientations are clearly not suitable for the formation of a grid. Instability of this

ligand due to hydrolytic attack in aqueous solvents also became apparent, which will be discussed in following sections.

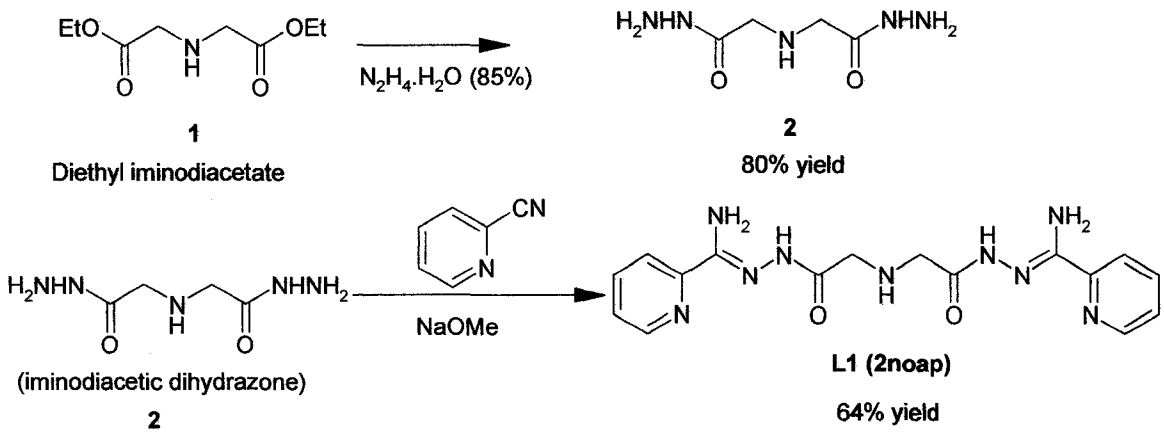

Scheme 2.3 Synthetic route for 2noap (**L1**).

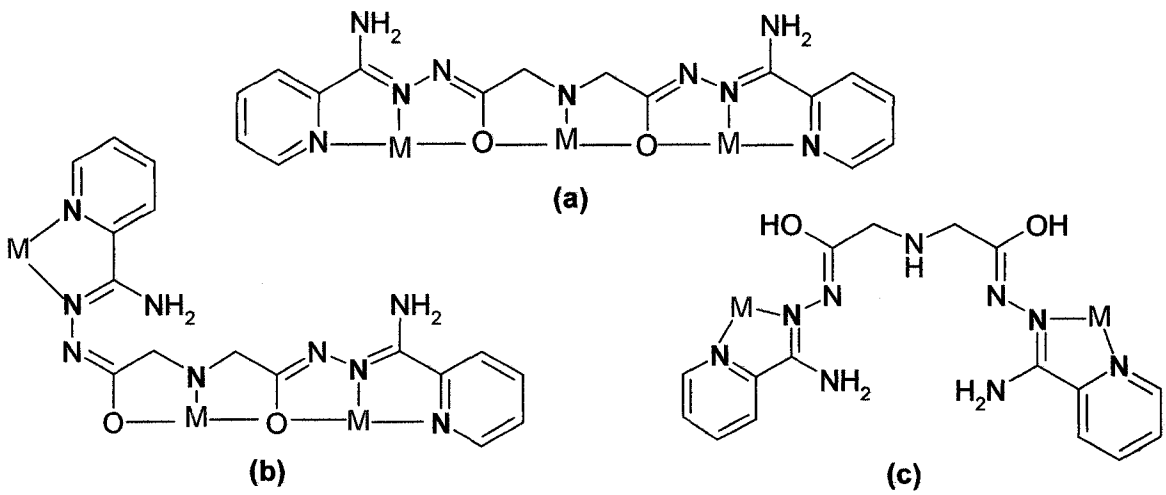

Fig. 2.2 Three coordination modes of the ligand '2noap' (**L1**).

2.1.4 Polytopic hydrazone ligands with more rigid backbones

Linear picolinic based di- and tri-topic ligands, where the coordination compartments are built around single atoms such as a hydrazone oxygen, offer a better situation for producing n-topic grids. Such ligands have several advantages over the previous class of ligands. In general these ligands are less flexible, limiting the number of different conformations, and the aromatic rings align readily in parallel fashion when the grids form.

The ditopic ligand 'pomp' (**L2**) was synthesized by reaction of 2-picolinic hydrazone and 2-acetylpyridine (Scheme 2.4). The ligand contains two coordination pockets built around a single hydrazone oxygen atom. When reacted with transition metal ions (e.g. Mn(II)), it formed a [2 x 2] square $Mn(II)_4$ heteroleptic grid and a $Mn(II)_5$ homoleptic trigonal bipyramidal cluster (Chapter 4). The coordination pockets involve two different types of donor atom arrangement; NO (incomplete metal coordination number) and N_2O (complete metal coordination number) respectively (Fig. 2.3). In the case of the [2 x 2] grids, two mutually parallel pairs of ligands self-assemble in a perpendicular fashion on the two faces of the square grid. Extra ligands (e. g. solvents or anions) fill the corner metal sites of the grid where two ligands with coordination sites having 'insufficient donor atoms' meet. In the homoleptic $Mn(II)_5$ clusters, however, all the coordination requirements of the metals are satisfied by the ligand donor sites only.

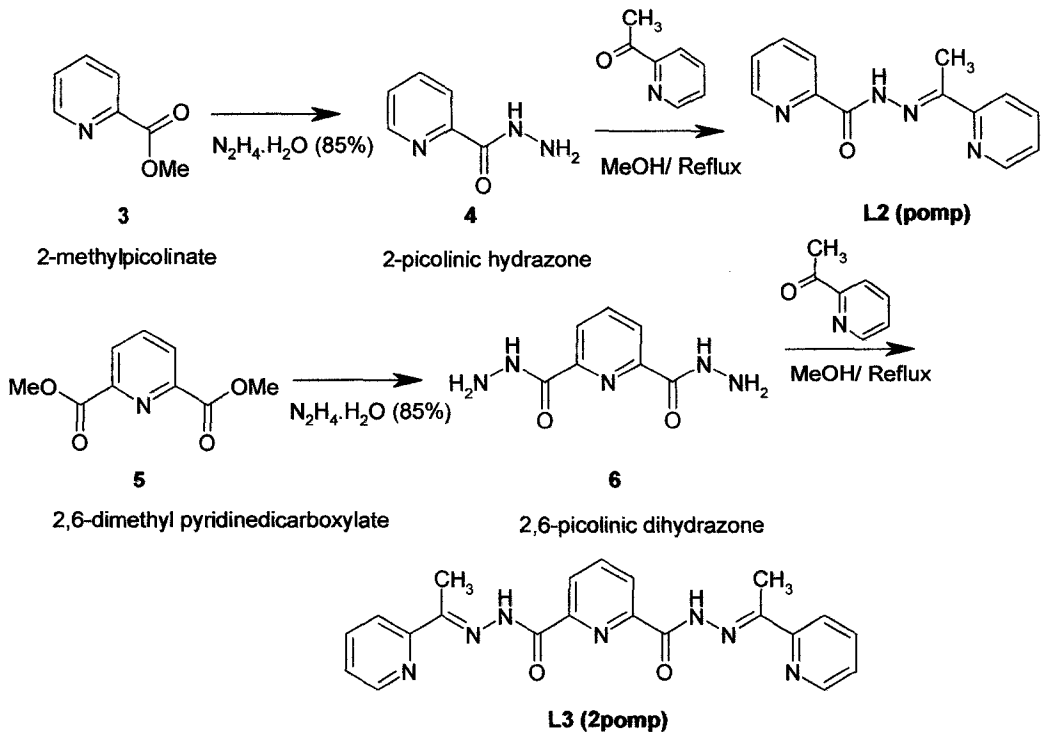

Scheme 2.4 Synthetic route for pomp (**L2**) and 2pomp (**L3**)

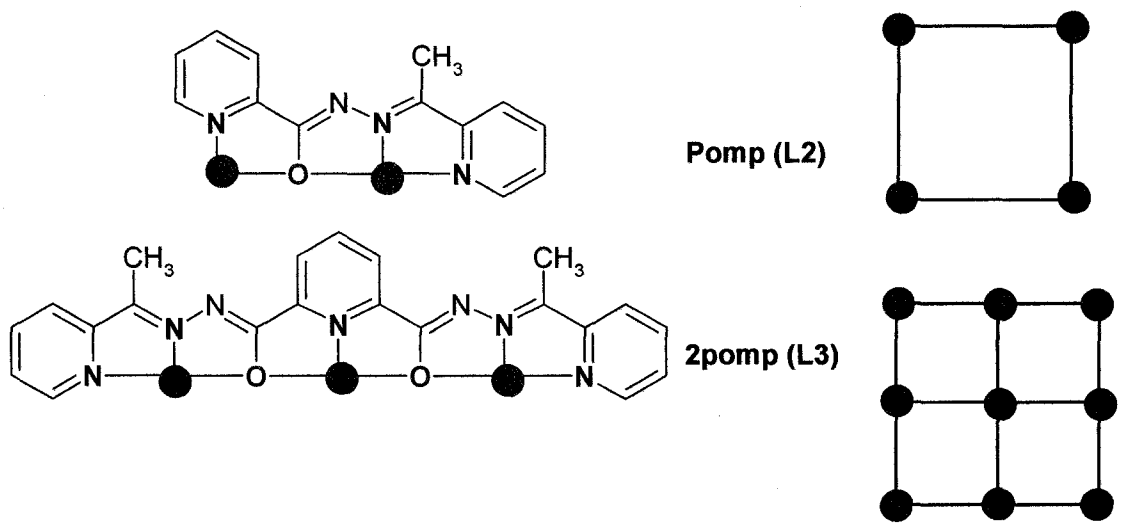

Fig. 2.3 Two and three coordination pockets in ditopic and tritopic ligands **L2** and **L3**.

The tritopic ligand '2pomp' (**L3**) is an extended version of the ditopic ligand 'pomp' (**L2**) with an added extra coordination pocket. The ligand was synthesized following a similar synthetic strategy (Scheme 2.4) from 2,6-picolinic dihydrazone and 2-acetyl pyridine. The ligand contains three coordination compartments created with NO_2 donor atoms for the central and N_2O donor atoms for the terminal coordination groups. Each of these groups satisfies only half of the coordination requirement of an octahedral M(II) cation. It again encourages the rest of the coordination sites of the metal cation to be filled by a second incoming ligand. The *mer-* arrangement of the donors in each pocket dictates and ensures the orientation of the second ligand to be perpendicular in order to coordinate the metal. As a result self-assembly creates [3 x 3] nonanuclear homoleptic $Mn(II)_9$ grid molecules with this ligand (Chapter 6).

Six ligands self-assemble with nine octahedral Mn(II) ions to form the grid, where adjacent metal ions are bridged by hydrazone oxygen atoms. The hydrazone oxygen atoms mediate the magnetic exchange interactions between bridged metal centers. The ligand also contains a diazine N-N group from the hydrazone fragment that links the central coordination compartment to the external sites. The presence of hydrazone as a linker group has some important consequences on the properties as well as the nuclearity of the complexes. In a normal coordination mode where each of the three donor sites of the ligand hosts one metal ion in a linear fashion, the hydrazone-N does not take part in coordination and remains free. In an event of single bond rotation around the C_{py}-C_{co} bond, the hydrazone-N swings in and coordinates to the central metal ion making all the

coordination sites equivalent with N_2O donor atoms (Fig. 2.4). When reacted with Cu(II) ions, four 2pomp ligands with such a twisted arrangement self- assemble with eight Cu(II) ions giving a new class of 'pinwheel' clusters (Chapter 5). In the pinwheel clusters, the coordination requirements of the metal ions at the external sites are only partially filled by the ligand.

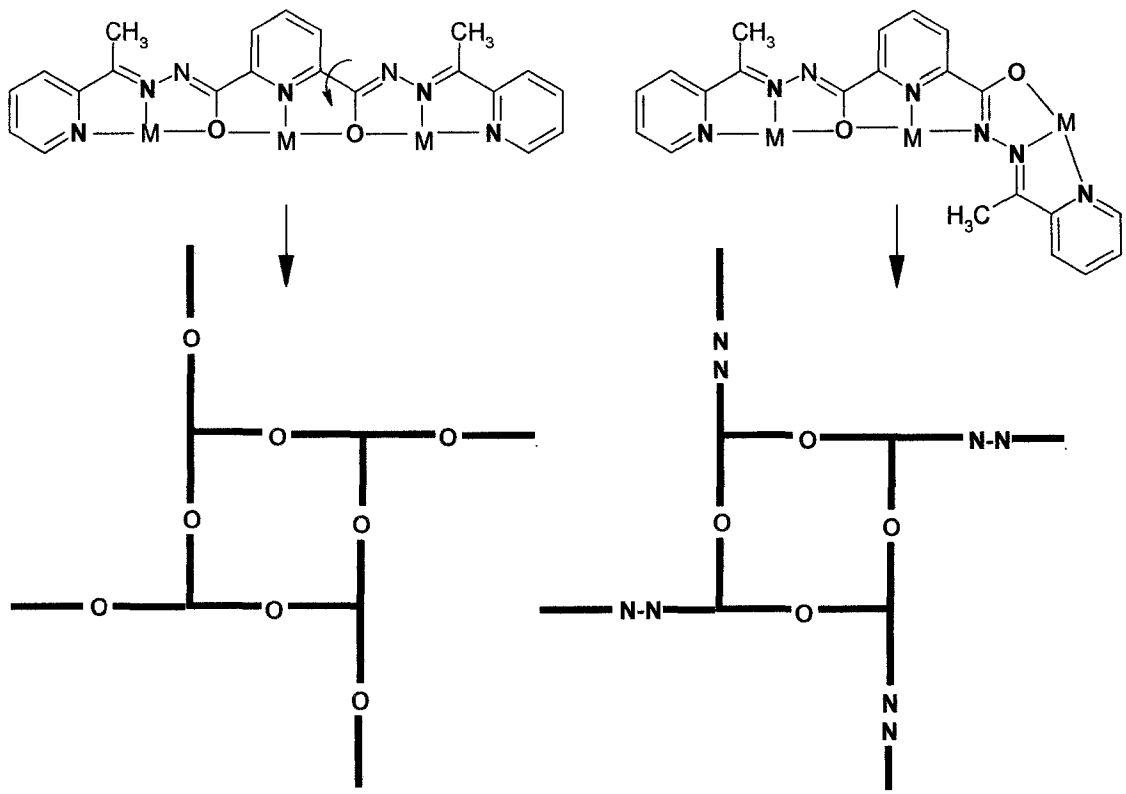

Fig. 2.4 Formation of pinwheel cluster with two types of peripheral bonding

So, the remaining coordination requirements are satisfied by coordinating solvent molecules (e.g. H_2O) or donor anions (e.g. NO_3^-). In both types of complexes, the shorter hydrazone oxygen and diazine bridges ensure good overlap of the metal magnetic orbitals and thus result in more efficient spin communication.

2.1.5 Ditopic ligand with four coordination pockets

The oxalic dihydrazide based polydentate ligand 'pttp' (**L4**) was synthesized according to a previously published procedure [70]. The schematic presentation of the synthesis is shown in Scheme 2.5. This class of ligands contains two terminal hydrazone fragments with N_2O donor sites which are linked by a flexible oxalic C-C single bond. Rotation around the single bond leads to two different conformations of the ligand (*cis* and *trans*).

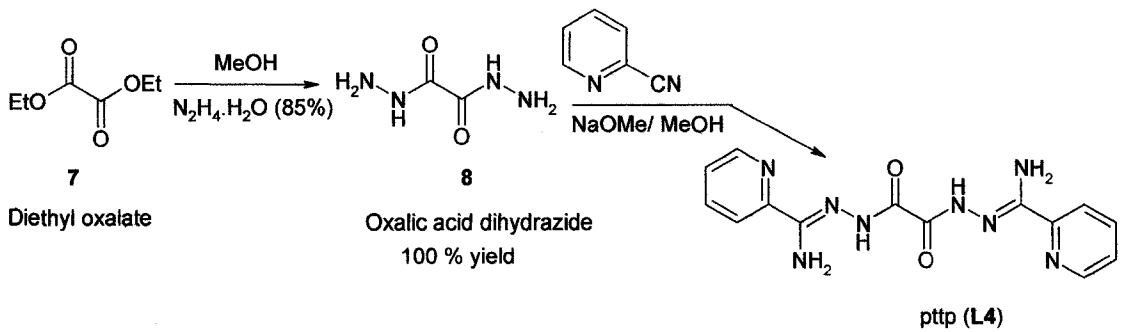

Scheme 2.5 Synthetic route for pttp **(L4)**

A detailed study of an octanuclear mixed oxidation $[Co(II)_4Co(III)_4]$ complex obtained from this ligand along with some other tetranuclear complexes is discussed in Chapter 7.

2.2 Ligand modification and extension-steps towards larger grids

2.2.1 Ligand modification

Addition of a terminal substituent, with the potential for additional bridging interactions on the two ends of a basic ligand framework or increasing the number of coordination sites within the ligand body itself would be a logical approach towards the extension to larger clusters and grids. Hydrazone ligands with suitable coordination pockets positioned along the ligand backbone are effective for generation of grid molecules. However, homoleptic grid molecules are comparatively difficult to create in general because it requires preprogramming of the coordinating elements. Square tetranuclear [2 x 2] grids and [3 x 3] nonanuclear grids had been successfully obtained with ditopic ligands (e.g. poap, Scheme 4.1; Chapter 4) and tritopic ligands (e.g. 2poap, Scheme 6.1, Chapter 6) with $[M_4(\mu\text{-}O)_4]$ and $[M_9(\mu\text{-}O)_{12}]$ grid-like cores (M = Mn(II), Cu(II)) within the cluster respectively. Applying a similar strategy for the creation of larger grids (e.g. M_{16}, M_{25}) appears to be a significant synthetic challenge.

However, changing the terminal substituent of a basic ligand structure turned out to be much easier than expected and large clusters can be created through the extended interaction of the added piece. 'dpocco' and 'Cl-dpocco' (**L5-L6**) are two tritopic ligands derived by extending the hydrazone framework with an oxime fragment. They contain three coordination sites similar to other tritopic ligands such as 2poap. Apart from the normal arrangement of three pockets, the ligand ends bear two oxime-OH groups which are potentially capable of initiating further coordination interactions. The schematic

presentation of the synthesis of the two ligands is given in Scheme 2.6. The precursor oxime for the synthesis of dpocco is a known compound and commercially available. Dpocco was obtained as a powder from a reaction of 2,6-picolinic dihydrazone and butane dionemonoxime. The chloro derivative was obtained in the same way from 4-chloro-2,6-diethylpyridine dicarboxylate. It involves the initial construction of the central pyridine ring with the chloro substitution at the 4-position.

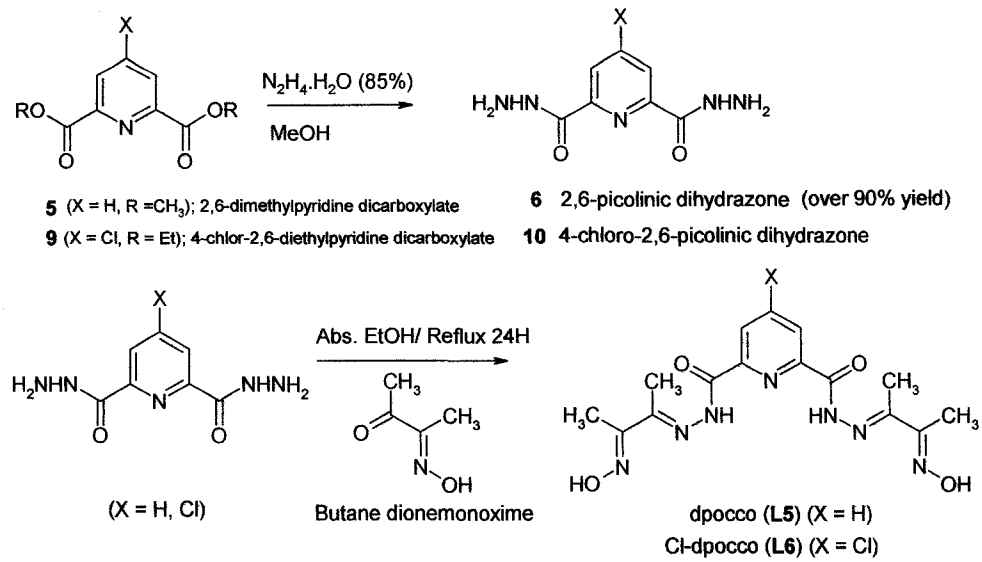

Scheme 2.6 Synthesis of dpocco (**L5**) and Cl-dpocco (**L6**)

This was accomplished via a multi-step synthesis developed by Z. Xu and further modified and optimized by V. A. Milway [88]. The subsequent synthetic steps after esterification are similar in both the syntheses. The chloro substitution on the central pyridine rings of the tritopic ligands in general facilitates further functionalization of the ligands. When reacted with $Cu(OAc)_2 \cdot H_2O$, dpocco formed a $Cu(II)_{36}$ polynuclear

complex, which was structurally characterized.

Most of the novel and large polynuclear clusters are formed by way of serendipitous synthesis and the role played by the ligand cannot be determined beforehand. It can only be ascertained after the reaction is complete and often the synthetic mechanism cannot be rationalized. However, designing the ligand carefully by placing well constructed coordination pockets along the ligand backbone, by positioning suitable donor atoms might reduce the degree of uncertainty and allow some control over the nuclearity of the final outcome. We have seen before that 2poap and other similar tritopic ligands were successfully employed to produce [3 x 3] nonanuclear grid molecules with several transition metal ions (Mn(II), Cu(II) etc). If a similar strategy could be followed, where there are simply more coordination pockets within the ligand body, then tetratopic and pentatopic ligands should theoretically yield [4 x 4] and [5 x 5] square grids under favorable conditions.

2.2.2 Ligand extension

There may be several ways that a tritopic 2poap type ligand can be extended. But one convenient way is extension through the initial acylation of 2,6-picolinic dihydrazone [94]. 2,6-Picolinic dihydrazone can be extended at the hydrazide nitrogen atoms by reaction with a keto-ester to form an extended ester. This can be further functionalized with hydrazine to form an extended hydrazone, which can be terminated as before with e.g. a ketone or an imino ester.

a) Extension using MBF (methyl benzoyl formate)

2-Picolinic hydrazone **4** was obtained by addition of hydrazine hydrate (85%) to a methanolic solution of the ester 2-methylpicolinate **3** [95]. Scheme 2.7 shows a synthetic route for the intermediates **11** and **12**.

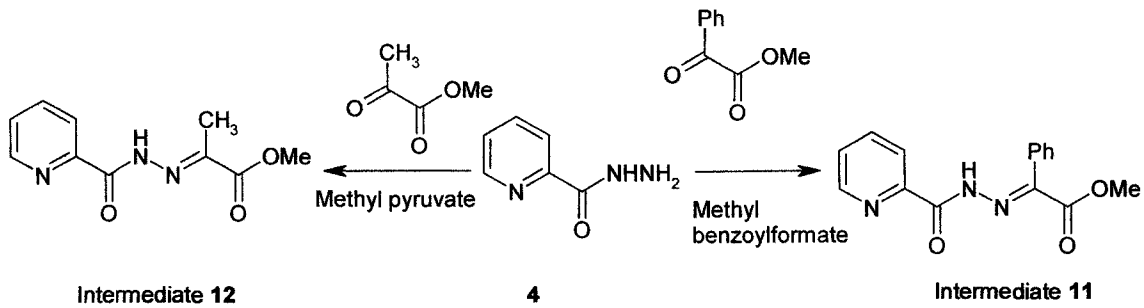

Scheme 2.7 Synthesis of two intermediates **11** and **12**.

The intermediate **11** was synthesized by refluxing a methanolic solution of **4** with methyl benzoyl formate. The product is a white crystalline solid which can be recrystallized from a solvent mixture of $CH_3OH/CHCl_3$. Appropriate synthetic details are given in the experimental section. Good quality crystals suitable for x-ray structure determination were obtained. A detailed description of the structure is provided in the Results and Discussion section 2.8. A CH_3- analogue of the partially extended ester **12** was also obtained earlier in a similar synthetic technique with methyl pyruvate [96]. The success with the partial extension of 2-picolinic hydrazone **4** inspired us to take up similar synthetic steps for the double extension on both sides of the 2,6-picolinic dihydrazone **6**. A solution of 2,6-picolinic dihydrazone in a $CH_3OH/CHCl_3$ solvent mixture was refluxed with methyl benzoyl formate (MBF), which yielded the doubly

extended ester (Intermediate **13**). The reaction conditions and the solvents used are shown in Scheme 2.8. An x-ray structural analysis was carried out on intermediate **13**.

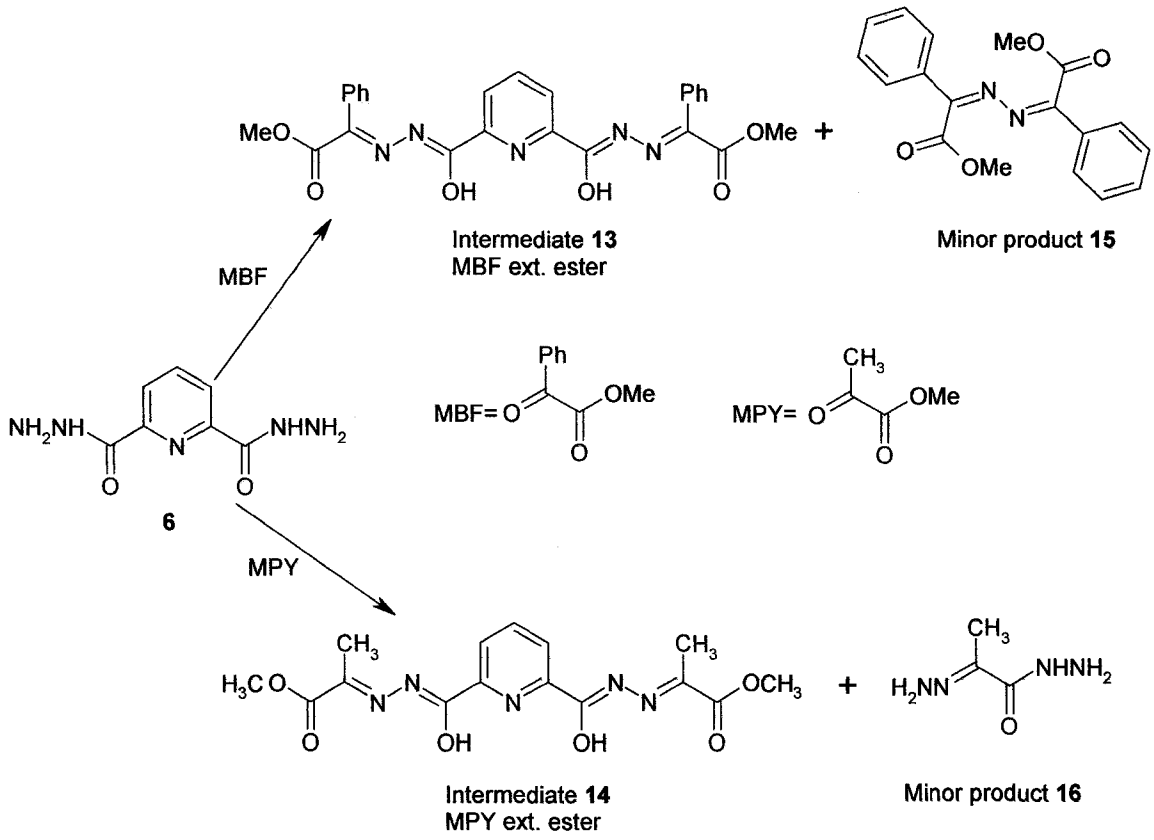

Scheme 2.8 Synthesis of two intermediates **13** and **14**.

b) Extension using MPY (Methyl pyruvate)

A similar strategy was taken to synthesize the extended ester (Intermediate **14**). Methyl pyruvate (MPY) was used at this time as an extender. Compound **6** was suspended in a mixture of methanol / ethanol to which methyl pyruvate (MPY) was

added. The resulting solution was refluxed for a day. Intermediate **14** was obtained in good yield. X-ray quality crystals could be grown from a methanolic solution and a solid state structural study was carried out on **14**. Details are provided in the experimental section while a description of a crystal structure is given in the crystallographic section. The overall yield was fairly good. A description of the synthesis is given in the experimental section. Crystals suitable for x-ray analysis could be obtained by recrystallization from a similar solvent system as before. An x-ray structural analysis was carried out on intermediate **13**. Poor crystal quality and very weak reflections produced a poor data set. However, enough reflections were taken to show the carbon skeleton of the molecule and the presence of different functional groups.

It became evident from the ^{1}H NMR studies of **14** that, this intermediate is a mixture of two isomers which remain in equilibrium in solution. The ^{1}H NMR was recorded in deuterated DMSO at 500 MHz. The *–CH_3* protons of the pyruvate functional group gave two separate singlets close to each other instead of only one singlet which was expected. It signifies that the two methyl groups are chemically non-equivalent. From the peak intensity, it can also be inferred that one isomer has preference over the other with an approximate ratio of 3:2. Similar non-equivalencies were also observed for the signals for the *OCH_3* ester and *OH* hydroxyl groups as well. Intermediate **14** can give rise to a rotational isomer (Rotamer) due to rotation around the C(2)-C(3) single bond in the molecule which is responsible for such behavior in the NMR. The isomers may vary in their relative positions of the –CH_3 and OCH_3 groups. The intermediate then probably

exists in solution as an equilibrium mixture of rotamers, the proportions of which should be temperature dependent. Alternatively, intermediate **14** might have *syn* and *anti* conformations relative to the -CH_3 and - OCH_3 groups. The x-ray crystal structure of **14** then represents probably one of the isomers. Similar behavior has been seen before with the thiosemicarbazone based ligand methyl pyruvate-hydrazinopyruvoyl thiosemicarbazone (H_2mpipt) (Fig. 2.5) [97].

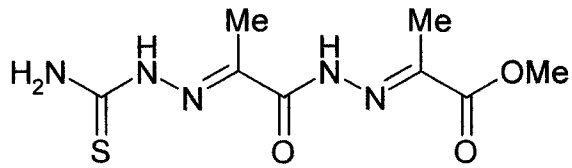

Fig. 2.5 Structure of H_2mpipt

Intermediate **13** has two ester ends, and the carbonyl carbon atoms are again potential targets for nucleophilic attack and so it could still be reactive to further reaction with hydrazine. Hydrazine solution (1.0 M) in THF was added to a solution of the extended ester intermediate **13** in dry THF. The detailed synthetic procedure is provided in the experimental section. Synthesizing the extended dihydrazone turned out to be the most crucial part of the synthesis. A variety of solvents was chosen as the media, but most of the difficulties were encountered using solvents containing even a small amount of water. Even freshly distilled and very dry methanol or ethanol led to a mixture of products, and indications were that a ligand hydrolysis had occurred. However, the use of very dry and freshly distilled THF allowed the synthesis of the extended dihydrazone (Intermediate **17**, Scheme 2.9). The extended MBF dihydrazone (Intermediate **17**,

Scheme 2.9) was characterized spectroscopically. A detailed procedure and characterization particulars are provided in the experimental section. The extended MBF dihydrazone **17** was isolated as a white, air stable solid.

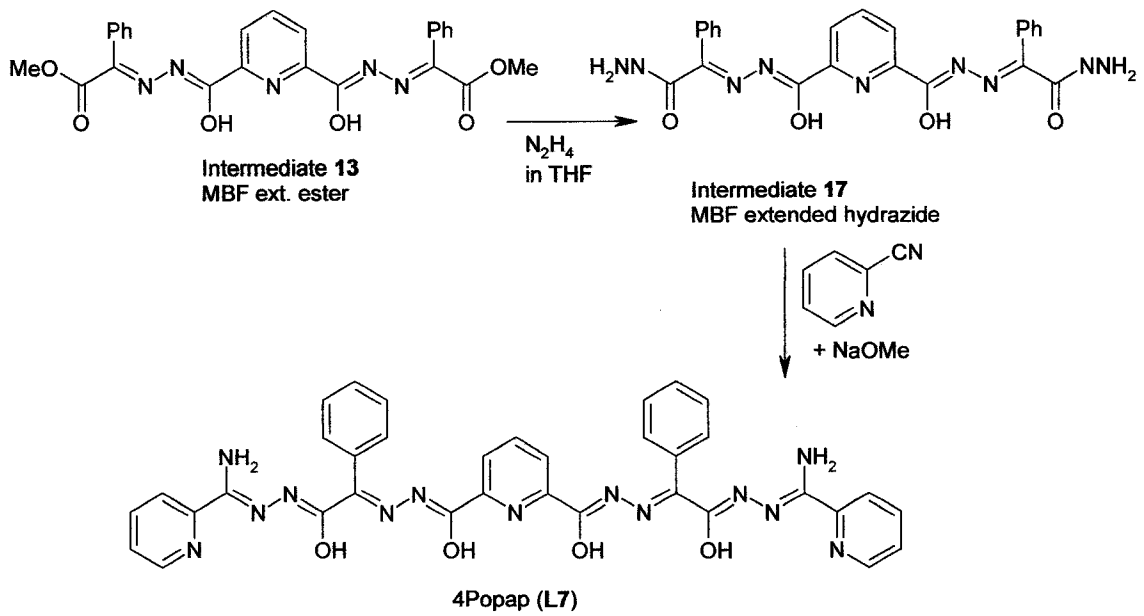

Scheme 2.9 Synthesis of the pentatopic ligands 4popap (**L7**) and through the intermediates **17**

Intermediate **17** was further reacted with the methyl ester of iminopicolinic acid generated *in situ* following a standard procedure from 2-cyanopyridine and sodium in methanol. The pentatopic ligand 4popap (**L7**) (Scheme 2.9) was isolated as a pale yellow powder, which was characterized spectroscopically by infrared, ^{1}H NMR, and mass spectrometry (Experimental section). A 3D representation of the pentatopic ligand **L7**

generated by ACD/3D viewer (Freeware) is provided in Fig. 2.6.

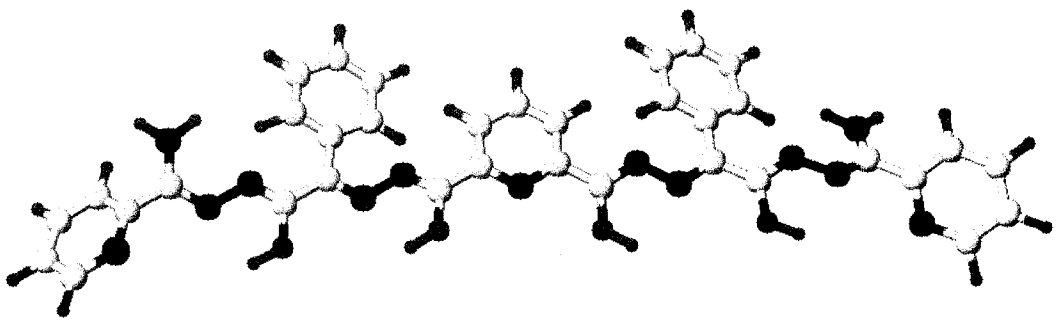

Fig. 2.6 Pentatopic ligand **L7** in one of its stable tautomeric forms; Color code Grey = C, Blue = N, Red = O, Cyan = H

The ligand **L7** was reacted with different transition metal ions and a few metal complexes were isolated. A [5 x 5] $Mn(II)_{25}$ grid was formed when 4popap (**L7**) was reacted with $Mn(ClO_4)_2.6H_2O$, which will be discussed in Chapter 9. Further substantial evidence for the characterization of the ligand **L7** was obtained from mass spectrometry, which clearly showed a peak for the (M+1) ion fragment. Besides this a mononuclear [(**L7**-2H)Mn] complex was isolated and characterized by x-ray crystallography when the ligand was reacted with $Mn(SO_3CF_3).xH_2O$. From the structure of the complex it became evident that the ligand was doubly deprotonated and coordinated to a single octahedral Mn(II) ion. Chapter 9 will highlight a discussion on the nuclearity and magnetism of the complexes synthesized by designed assembly from the pentatopic ligands.

2.2.3 Hydrolytic instability of the hydrazone ligands

Ligands which are derived using a "Lego Chemical" approach, i.e. building blocks of the ligand are extended by condensation reactions involving the elimination of small leaving groups like H_2O, MeOH, are always at a risk of hydrolytic attack in solvents containing even traces of water in the presence of a transition metal ion. In many cases the hydrolysis is encouraged or even catalyzed by the transition metal present [98]. In such cases, the ligand framework can break down, or even rearrange to a new, more stable ligand, which then reacts with the transition metal and gives rise to totally unexpected coordination products in some cases. In one such case, a dinuclear copper complex **22** of the ligand PAHAP was formed by the hydrolysis of the tritopic ligand 2noap (**L1**, Scheme 2.3; see Chapter 3) in an aqueous medium. A possible mechanism for the hydrolysis of the ligand to form PAHAP is given in Schemes 2.10 and 2.11.

This result led us to suspect that a second hydrolytic product of the ligand, which would be a ditopic fragment, might still be present in the solution. In the reaction above a dark black crystalline solid complex was isolated as a second product. The product was analyzed by C, H, N and variable temperature magnetic data were acquired. The details are provided in the experimental section. The CHN data and magnetic data were indicative of a tetranuclear complex with the formula $[L_4Cu(II)_4]$ where L matches the ditopic $[C_{10}H_{13}N_5O_3]$ organic fragment **20** (Scheme 2.10).

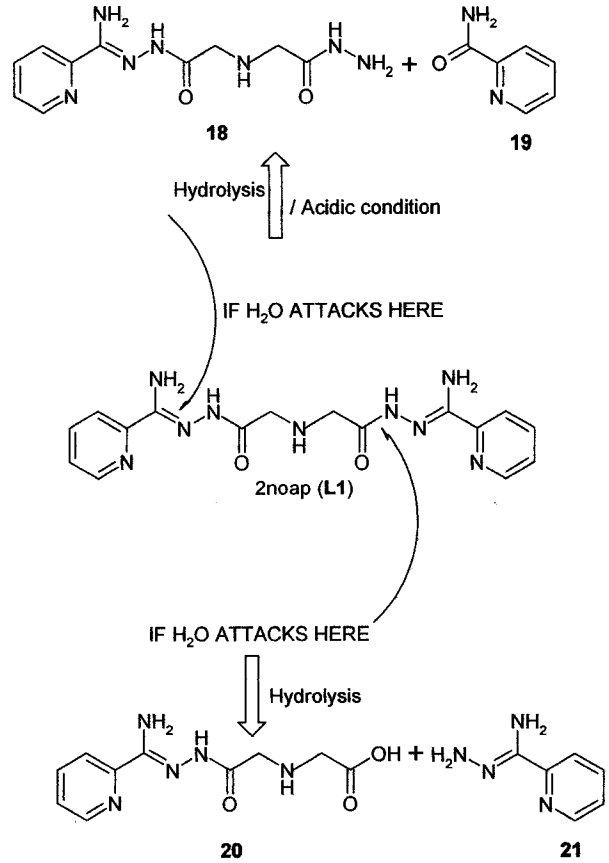

Scheme 2.10 Hydrolysis of the ligand 2noap (**L1**)

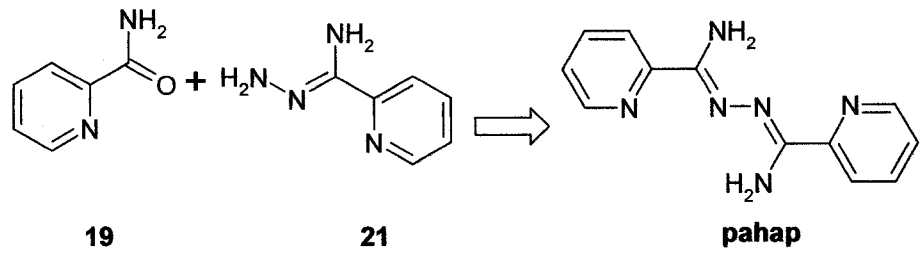

Scheme 2.11 PAHAP formation

Transition metal induced hydrolytic cleavage of the parent organic ligand and subsequent complexation of the reactive metal with the hydrolysis product has been documented before. When methyl pyruvate-hydrazinopyruvoyl thiosemicarbazone (H_2mpipt) (Fig. 2.5) was reacted with $[Cu(PPh_3)Cl]_4$ in the presence of air, a mixture of products was isolated and identified which included a mononuclear Cu-complex of a hydrolysis product H_2ipt (pyruvic acid thiosemicarbazone hydrazide) [97].

The vulnerability of the hydrazone ligands towards hydrolytic attack on reaction with transition metal ions in solvents containing even small amounts of water is well documented in our group. Structures of hydrolyzed ligand fragments and their resulting coordination complexes were reported previously with various hydrazone based ligands [98]. A second and useful piece of evidence for the above mentioned phenomena is the isolation and structural characterization of two unexpected minor products **15** and **16** (Scheme 2.8). **15** was isolated as a minor crystalline product showing two molecules of the ester **13** were hydrolytically cleaved asymmetrically, and two end pieces joined together to form **15**. A single crystal structural study was performed on **15** (see Fig. 2.10 (a) in the crystallography section). An analogous minor product **16** was also isolated in very low yield from the esterification reaction of the 2,6-picolinic dihydrazone with methyl pyruvate (Scheme 2.8). This supports the suggestion that an unsymmetrical hydrolytic cleavage happened in the case of the reaction of **L7** with Cu(II). An x-ray structure of the minor product **16** was obtained as well (see Fig. 2.10 (b) in the crystallographic section).

It is suspected that the water present in the solvents or crystal water from the metal salts causes nucleophilic attack at the C=N site adjacent to a phenyl ring, leading to a hydrolytic cleavage before hydrazine attacks the nucleophilic carbonyl carbon to yield the extended dihydrazone (Scheme 2.9). The hydrolytic cleavage of the C=N bond appeared to be kinetically favored over the reaction with hydrazine. As a result 2,6-picolinic dihydrazone was the major hydrolyzed ligand fragment in all cases where aqueous solvents were used. However, the difficulties with the reaction of hydrazine with the extended esters to produce the extended dihydrazone were finally resolved by using very dry and distilled THF as solvent and anhydrous hydrazine in THF. The details are provided in the experimental section.

2.3 Experimental

2.3.1 Materials

Commercially available solvents and chemicals were used without further purification.

2.4 Physical measurements

2.4.1 UV/ VIS SPECTRA

Electronic spectra were recorded as Nujol mulls and in solution using a Cary 5E spectrometer.

2.4.2 INFRA RED SPECTROSCOPY (IR)

Infra red spectra were recorded as Nujol mulls using a Mattson Polaris FT-IR and a Tensor 27, Bruker single beam FTIR instrument.

2.4.3 MASS SPECTRA

Mass spectra were recorded using a VG Micromass 7070HS spectrometer and an Agilent 1100 Series LC/MSD instrument in both EI and APCI mode.

2.4.4 ELEMENTAL ANALYSIS

C, H, and N analysis on vacuum dried samples was carried out by Canadian Micro- Analytical Service, Delta, BC, Canada.

2.4.5 MELTING POINT

Melting points were recorded on a Fisher–Johns melting point apparatus and are uncorrected.

2.4.6 ^{1}H NMR

^{1}H NMR were recorded on a General Electric 300 NB and Bruker AVANCE 500MHz spectrometer in C-CART (Center for Chemical Analyses, Research and Training, Department of Chemistry, Memorial University), Tetramethylsilane (TMS) was used as internal standard.

2.4.7 MAGNETIC MEASUREMENTS

Room temperature magnetic moments were measured using a Mettler BE 21 Faraday balance. Variable temperature magnetic data (2–300 K) were obtained using a Quantum Design MPMS5S SQUID magnetometer using field strengths in the range 0.1 T to 5T. Samples were prepared in a gelcap or in an aluminum cap and mounted inside a plastic straw, which was then attached to the transport rod. Background corrections for the sample holder assembly and diamagnetic components of the complexes were applied.

2.4.8 X-RAY STRUCTURE DETERMINATION

Data collection for the x-ray structure determination of the complexes reported herein were done either on a Bruker P4/CCD x-ray diffractometer at the University of Alberta, or on a Rigaku AFC6S and Rigaku Saturn AFC8 diffractometer, at C-CART, Department of Chemistry, Memorial University.

2.5 Safety notes

All perchlorate salts are potentially explosive. They were treated carefully and were used only in small quantities. All perchlorate complexes reported herein were tested by controlled mechanical impact to ensure their stability.

2.6 Synthesis of the ligands and some complexes

2.6.1 Synthesis of tritopic ligands

2noap [($C_{16}H_{19}N_9O_2$)] (L1)

The methyl ester of iminopicolinic acid was prepared *in situ* by reaction of 2-cyanopyridine (8.3 g, 80 mmol) with a sodium methoxide solution. The sodium methoxide was produced by dissolving sodium metal (0.23 g, 10 mmol) in dry methanol (~50 ml). Iminodiacetic dihydrazone **2** (3.2 g, 20 mmol) (prepared from the reaction of diethyl iminodiacetate **1** (5.0 g, 26 mmol) with hydrazine hydrate (85%; 3.3 g, 65 mmol) in methanol and diethyl ether (1:1, v/v) was added to the above solution and the mixture was gently refluxed for 1.5 hrs. A yellow precipitate formed, which was separated by filtration, washed with methanol and diethyl ether and dried under vacuum. (Yellow

powder, Yield 64%). Mp. 205-207 °C. IR (Nujol, cm^{-1}): 3420 (ν NH), 3210, 1645, 1610, (ν C=O), 996 (ν py). ^1H NMR (300 MHz, DMSO-d_6, ppm): δ 10.07 (d, 1H), 8.58 (m, 1H), 8.10 (m, 1 H), 7.89 (m, 1 H), 7.47 (m, 1H), 6.67 (dd, 2H), 3.76 (s, 1H), 3.32 (s, 2H). Mass spectrum (Major mass peaks, m/z): 333 (M-$2H_2O$). Anal. Calc. (%) for $C_{16}H_{19}N_9O_2$; C, 52.02; H, 5.18; N, 34.12. Found (%); C, 51.82; H, 5.28; N, 33.97.

Pomp [($C_{13}H_{12}N_4O$)] (L2)

2-acetylpyridine (1.8 g, 15.0 mmol) was added dropwise to a solution of 2-picolinic hydrazone **4** (1.35 g, 10.0 mmol) in 15 mL of methanol. The resulting solution was refluxed for 6 hours. A noticeable cloudiness of the solution was observed within 1 hour. A white precipitate formed, which was separated by filtration, washed with methanol and diethyl ether and vacuum dried (White solid, Yield 83%). Mp. 195 – 197 °C. IR (Nujol, cm^{-1}): 3316 (ν NH), 1701 (ν C=O), 995 (ν py). ^1H NMR (500 MHz, DMSO-d_6, ppm): δ 11.15 (s, 1H), 8.75 (d, 1H, 5 Hz), 8.64 (d, 1H, 4 Hz), 8.16 (m, 2H, 8.5 Hz), 8.11 (dd, 1H, 7.5 Hz), 7.90 (dd, 1H, 7.5 Hz), 7.72 (dd, 1H, 6 Hz), 7.45 (dd, 1H, 6 Hz), 2.5 (s, 3H). Mass spectrum (Major mass peaks, m/z): 241 (M+1). Anal. Calc. (%) for $C_{13}H_{12}N_4O$; C, 64.98; H, 5.03; N, 23.31. Found (%); C, 64.69; H, 5.10; N, 23.07.

2Pomp [($C_{21}H_{19}N_7O_2$)] (L3)

2-acetylpyridine (0.75 g, 6.4 mmol) was added dropwise to a solution of 2,6-picolinic dihydrazone **6** (0.5 g, 2.5 mmol) in 15 mL of methanol. The resulting solution was refluxed overnight. An off white precipitate formed, which was separated by

filtration, washed with methanol and ether, and vacuum dried (Off white solid, Yield 99%). Mp. 313-315 °C. IR (Nujol, cm^{-1}): 3350 (ν NH), 1704, 1695 (ν C=O), 992 (ν py). ^1H NMR (DMSO-d_6, ppm): δ 11.6 (s, 2H), 8.71 (d, 2H, 4.8 Hz), 8.21 (m, 5H), 7.97 (m, 2H), 7.53 (dd, 2H, 5.9 Hz), 2.7 (s, 6H). Mass spectrum (m/z): 401 (M+), 386 (M-CH_3), 323 (M-C_5H_4N). Anal. Calc. (%) for $C_{21}H_{19}N_7O_2$; C, 62.83; H, 4.77; N, 24.42. Found (%); C, 62.47; H, 4.77; N, 24.67.

pttp [($C_{14}H_{14}N_8O_2$)] (L4)

The ligand 'pttp' was synthesized according to the previously published procedure [70].

Dpocco [($C_{15}H_{19}N_7O_4$)] (L5)

i) Synthesis of dimethyl-2,6-pyridinedicarboxylate (5)

2,6-pyridinedicarboxylic acid (4.1 g, 25 mmol) was suspended in 100 mL of methanol and cooled to – 30° C with dry ice and acetone. $SOCl_2$ (5.9 g, 50 mmol) was added slowly to the slurry over a period of 2 hours while maintaining the temperature at – 30° C. While stirring overnight, the temperature of the solution was allowed to rise to room temperature. The total volume of the solution was reduced to one third of the initial using a rotary evaporator. Cooling the mother liquor in an ice bath led to the formation of white crystals of the diester (Yield 76%). Mp. 121-125 °C. IR (Nujol, cm^{-1}): 1742, 1730. ^1H NMR (500 MHz, DMSO-d_6, ppm): δ 8.3 (m, 3H), 3.4 (s, 6H).

ii) Synthesis of 2,6-picolinic dihydrazone (6)

Dimethyl 2,6-pyridinedicarboxylate (3.3 g, 17 mmol) was dissolved in 50 mL of hot methanol. Hydrazine hydrate (85%) (2.2 g, 68 mmol) in methanol (100 mL) was added to the above solution and the resulting mixture was stirred overnight. A white precipitate was collected after 18h (approximately) by filtration and recrystallized from a large volume (~200 mL) of water. (White solid, Yield 95%). Mp. Decomposition at temperature >260 °C. IR (Nujol, cm^{-1}): 3275 (ν NH), 1691, 1636 (ν C=O), 998 (ν py). ^1H NMR (500 MHz, DMSO-d_6, ppm): δ 10.4 (s, 2H), 8.13 (s, 3H), 4.6 (d, 4H).

iii) Synthesis of 4-Chloro-2,6-picolinic dihydrazone (10)

The chloro derivative of 2,6-picolinic dihydrazone was prepared in a similar way to that described in the previous section. However, the synthesis of the ester 4-chloro-2,6-diethylpyridine dicarboxylate (**9**, Scheme 2.6) was accomplished by a multi-step synthetic procedure starting from diethyloxalate [88]. The diethyl-4-chloro-2,6-pyridine dicarboxylate (3.0 g, 11 mmol) ester **9** was dissolved in 30 mL of methanol. The solution was cooled to - 40 °C with dry ice and acetone. A methanolic solution of hydrazine hydrate (85%) (2.2 g, 68 mmol) was added to the above solution and the resulting mixture was stirred overnight. A white precipitate was formed, which was collected by filtration and recrystallized from a large volume of water. (White solid, Yield 88%). Mp. >300 °C. IR (Nujol, cm^{-1}): 3333 (ν NH), 1691, 1657 (ν C=O), 972 (ν py).

iv) Synthesis of dpocco (L5)

2,6-picolinic dihydrazone **6** (5 g, 25 mmol) was added to an ethanolic solution (50 mL) of butanedionemonoxime (7.75 g, 75 mmol) and the resulting solution was refluxed for 24 hours. A white precipitate was formed which was separated by filtration and washed with methanol and ether and dried (White solid, Yield 92%). Mp. >260 °C. IR (Nujol, cm $^{-1}$): 3279 (ν OH), 1692, 1650 (ν C=O), 998 (ν py). ^{1}H NMR (500 MHz, DMSO-d_6, ppm): δ 11.73 (s, 1H), 11.29 (s, 1H), 8.34 (m, 3H), 2.28 (s, 3H), 2.07 (s, 3H). Mass spectrum (m/z): 361 (M+.). Anal. Calc. (%) for $C_{15}H_{19}N_7O_4$; C, 49.85; H, 5.29; N, 27.13. Found; C, 50.40; H, 5.43; N, 26.68.

Cl-dpocco [($C_{15}H_{18}N_7O_4Cl$)] (L6)

4-Chloro-2,6-picolinic dihydrazone **10** (5 g, 22 mmol) was added to an ethanolic solution (50 mL) of butanedionemonoxime (6.8 g, 66 mmol) and the resulting solution was refluxed for 24 hours. A white precipitate was formed which was filtered and washed with methanol and ether and dried (White solid, Yield 90%). Mp. >260 °C. IR (Nujol, cm^{-1}): 3277 (ν OH), 1697, 1653 (ν C=O), 1019 (ν py). ^{1}H NMR (DMSO-d_6, 500 MHz, ppm): δ 11.76 (s, 2H), 11.31 (s, 2H), 8.32 (s, 2H), 2.27 (s, 6H), 2.05 (s, 6H). Mass spectrum (m/z): 395 (M+). Anal. Calc. (%) for $C_{15}H_{18}N_7O_4Cl$; C, 45.51; H, 4.58; N, 24.77. Found; C, 45.75; H, 4.60; N, 24.58.

Intermediate [($C_{15}H_{13}N_3O_3$)] (11)

Methyl benzoyl formate (3.3g, 20 mmol) was added to a methanolic solution (45 mL) of picolinic hydrazone (2.74g, 20mmol) and refluxed overnight. White crystals suitable for x-ray structure (Table 2.1) were collected after standing for 18h at RT, washed with methanol and ether, and dried in air (Yield 91% overall). Mp. 198-200 °C. IR (Nujol, cm^{-1}): 3284 (ν NH), 1706 (ν C=O), 1577, 996 (ν py). Mass spectrum (LCMS, APCI, m/z): 284 (M+1), 224 (M-COOMe). ^1H NMR (500 MHz, $CDCl_3$, ppm): δ 11.32 (s, 1H, *NH*), 8.38 (d, 1H, *Py-H*, 4.5 Hz), 8.28 (d, 1H, *Py-H*, 7 Hz), 7.86 (m, 2H, *Py-H*), 7.58 (m, 3H, *Ar-H*), 7.42 (m, 3H, *Ar-H*), 3.93 (s, 3H, OCH_3).

2.6.2 Extension of the tritopic ligand to a pentatopic ligand

i) Extended MBF ester [($C_{25}H_{21}N_5O_6$)] (13)

Methyl benzoyl formate (10.7 g, 65 mmol) was added to 2,6-picolinic dihydrazone **6** (6.00 g, 31.0 mmol) suspended in a chloroform/methanol mixture (30/20 mL). The mixture was refluxed overnight, and the volume of the resulting pale yellow solution was reduced to ~20 mL. The corresponding extended dibenzoyl ester (**13**) was formed on standing at RT as a white powder after two days. (Yield >95%). Mp. 190-192 °C. Mass spectrum (APCI, m/z): 488 (100%, $M+1)^+$. IR (Nujol, cm^{-1}): 3326, 3240 (ν NH), 1743, 1713 (ν C=O), 999 (ν py). ^1H NMR (500 MHz, $CDCl_3$, ppm): δ 13.49 (s, 2H, *NH*), 8.53 (d, 2H, *Ar-H*, $J = 7.2$ *Hz*), 8.18 (t, 1H, *Ar-H*, $J = 8.1$ *Hz*), 7.79 (d, 4H, *Ar-H*, $J =$ 7 *Hz*), 7.45 (m, 6H, *Ar-H*), 3.91 (s, 6H, OCH_3). Confirmation of the successful extension came from a single crystal x-ray structure (Table 2.1) of a sample of **13** recrystallized

from MeOH/$CHCl_3$. A second product which came out of the mother liquor as white crystals **15** was also isolated in low yield (Scheme 2.8). From x-ray structural determination, this turned out to be a hydrolyzed fragment of the parent ligand (Table 2.4).

ii) Extended MPY ester ($C_{15}H_{17}N_5O_6$) (14)

Methyl pyruvate (3.5g, 86.1 mmol) was added to a slurry of (8.78 g, 41.0 mmol) 2,6-picolinic dihydrazone **6** in (50 mL / 50 mL) methanol/ethanol mixture. The resulting mixture was refluxed for 24 hours. An off white polycrystalline powder was formed the next day, which was isolated and dried in air (Yield > 95%). White crystals suitable for x-ray were obtained by recrystallization from methanol. Mp. 243-245 °C. Mass spectrums (m/z): 363 (M+.), 304, 244, 221, 160, 77. IR (Nujol, cm^{-1}): 3333, 3247 (ν NH), 1720 (C=O), 1694 (ν NH), 995 (py). NMR (500 MHz, DMSO-d_6, ppm): δ 14.01 (s, 1H, *NH*), 10.89 (s, 1H, *NH*), 8.38 (m, 3H, *Ar-H*), 3.82 (s, 3H, OCH_3), 3.81 (s, 3H, OCH_3), 2.37 (s, 3H, $-CH_3$), 2.22 (s, 3H, $-CH_3$). Again confirmation of the successful extension came from a single crystal x-ray structure of a sample of **14** recrystallized from MeOH (Table 2.1). A second product was obtained from the mother liquor as white crystals **16**, which were isolated in low yield (Scheme 2.8). An x-ray structural study on **16** showed it to be a hydrolyzed fragment of the parent ligand (Table 2.4).

iii) Extended MBF dihydrazone ($C_{23}H_{21}N_9O_4$) (17)

The extended diester **13** (4.0g, 8.20 mmol) was dissolved in 50 mL of absolutely dry THF in a 250 mL three necked flask under a N_2 atmosphere. 19.0 mL (18.45 mmol) of 1.0 M solution of hydrazine in THF was added dropwise using a syringe, forming a golden yellow solution, which was cooled with ice water and stirred for two days. A pale yellow precipitate of the bis-hydrazone formed, which was separated by filtration, washed by ether and dried in air (Yield 70%). Mp: 180-195 °C. Mass spectrum (APCI, m/z): 488 $(M+1)^+$, 470 $(M-H_2O)$, 342 (Base 100%). IR (Nujol, cm^{-1}): 3428, 3316, 3224 (ν NH), 1685, 1666, 1619 (ν C=O, CN), 998 (ν py). ^1H NMR (500 MHz, DMSO-d_6, ppm): δ 12.72 (s, 2H, *NH*), 9.94 (s, 2H, *NH*), 8.24 (m, 3H, *Pyr-H*), 7.73 (m, 4H, *Ar-H*), 7.50 (m, 6H, *Ar-H*), 3.16 (s, 4H, NH_2).

4Popap ($C_{35}H_{29}N_{13}O_4$) (L7)

The methyl ester of iminopicolinic acid was prepared in *situ* by reaction of 2-cyanopyridine (0.3 g, 2.88 mmol) with sodium methoxide solution produced by dissolving sodium metal (0.3 g, 13.0 mmol) in very dry methanol (50 mL) under N_2. The crude extended dihydrazone **17** (0.5 g, 1.0 mmol) was added to the above solution, followed by a few drops of glacial acetic acid to neutralize the excess methoxide. The mixture was stirred at room temperature overnight. A light yellow powder (**L7**) was obtained which was separated by filtration and air dried (Light yellow powder, Yield 85%). Mp: 228-230 °C. Mass spectrum (APCI, m/z): 696 $(M+1)^+$, 678 $(M-H_2O)$, 488, 446 (Base 100%). IR (Nujol, cm^{-1}): 3413, 3324, 3243 (ν NH), 3158, 1697, 1666 (ν C=O),

998 (ν py). ^{1}H NMR (500 MHz, DMSO-d_6, ppm): δ 11.82 (s, 2H, *NH*), 9.94 (s, 2H, *NH*), 8.45 (d, 2H, *Ar-H*, 4.8 *Hz*), 8.23 (m, 5H, *Ar-H*), 8.01 (m, 2H, *Ar-H*), 7.85 (m, 4H, *Ar-H*), 7.61 (m, 2H, *Ar-H*), 7.47 (m, 6H, *Ar-H*), 6.84 (s, 4H, NH_2).

[(PAHAP)$Cu_2(H_2O)_6$]$(NO_3)_4$ (22)

1.66 g of **L1** (4.5 mmol) was added to a hot aqueous solution (15 mL) of $CuNO_3 \cdot 3H_2O$ (0.72 g, 3.0 mmol). The resulting green solution was stirred for 1 hour, and filtered and kept for crystallization. A green crystalline compound came out as the first product after several days (Yield 35 %). IR (Nujol, cm^{-1}): 3329, 3171, 1690, 1667, 1600, 1027. Anal. Calc.(%) for $[(C_{12}H_{11}N_6)Cu_2](NO_3)_3 \cdot H_2O$; C, 25.26; H, 2.29; N, 22.10. Found (%); C, 25.33, H, 3.31, N, 21.70. Green crystals of **22** suitable for x-ray structural study were obtained form the mother liquor on standing at RT. Details of the structure is provided in the results and discussion section. The mother liquor was retained. A dark black crystalline solid **23** was isolated in a very low yield as the solvent was reduced. Anal. Calc. (%) for $[(C_{10}H_{13}N_5O_3)(C_{10}H_{12}N_5O_3)_3Cu_4](NO_3)_5 \cdot 6H_2O$ **(23)**; C, 28.69, H, 3.67, N, 20.91. Found; C, 28.72, H, 3.46, N, 20.88.

. The Variable temperature magnetic data for **23** shows a moment of 3.90 μ_B (μ_{SO} for 4Cu(II) ions is 3.46 μ_B at room temperature) at 300 K which then drops down slightly to 3.70 μ_B at 50 K. The magnetic moment then shows a sharp rise to 3.75 μ_B around 30 K. This behavior is consistent with weak ferromagnetic exchange observed in similar square [2x2] Cu_4L_4 grid complexes with orthogonal Cu-O-Cu bridge connections [59].

2.7 Crystallographic data collection and refinement of structures

Colorless prisms and colorless rectangular crystals of intermediates **11** and **14** with approximate dimensions 0.25 x 0.25 x 0.40 and 0.15 x 0.20 x 0.40 mm respectively were mounted on glass fibers. All measurements were done on a Rigaku AFC6S diffractometer with graphite monochromated Mo-Kα radiation. Hydrogen atoms were introduced in difference map positions with isotropic thermal parameters set twenty percent greater than those of their bonding partners at the time of inclusion. They were optimized by positional refinement. The data were collected at 299 K using the ω-2θ scan technique to a maximum 2θ value of 55.1° and 55.2° for **11** and **14** respectively. Omega scans of several intense reflections, made prior to data collection, had an average width at half height of 0.34° for **11** and 0.23° for **14** respectively with a take off angle of 6.0°. Scans were made at speed of 4.0°/min. The weak reflections were rescanned with a maximum of 5 scans and the counts were accumulated to ensure good counting statistics. Stationary background counts were recorded on each side of the reflection. The ratio of peak counting time to background counting time was 2:1 for both cases. The diameter of the incident beam collimator was 1.0 mm and the crystal to detector distance was 400 mm. The detector apertures were 6.0 x 6.0 mm for **11** and 4.5 x 3.0 mm for **14**. The data were corrected for Lorentz and polarization effects. Both the structures were solved by direct methods [99] and expanded using Fourier techniques [100].

All non-hydrogen atoms were refined anisotropically. The hydrogen atoms were refined but their isotropic B's were held fixed. The maximum and minimum peaks on the

final difference Fourier map corresponded to 0.16 and -0.19 e $^-$/Å^3 in case for **11** and 0.24 and -0.24 e$^-$/Å^3 for **14** respectively. Neutral atom scattering factors were taken from the usual source Cromer and Waber [101]. Anomalous dispersion effects were included in F_{calc} [102]. The values for $\Delta f'$ and $\Delta f''$ were those of Creagh and McAuley [103]. The values for the mass attenuation coefficients are those of Creagh and Hubbell [104]. All calculations were performed using the teXsan [105 (a)] crystallographic software package of Molecular Structure Corporation except for refinement, which was performed using SHELXL-97 [99]. Due to poor crystal quality, an inadequate number of unique reflections and overall weak reflections, the structural determination of the intermediate **13** was limited. However, the core skeletal view of the molecule could be obtained which shows the presence of the two benzoyl formate ester groups.

A yellow prism crystal of **15** with approximate dimensions 0.40 x 0.40 x 0.40 mm was mounted on a glass fiber. All other parameters were the same as described previously. Hydrogen atoms were included but not refined. For **16**, a colorless rectangular crystal was used with dimensions 0.20 x 0.10 x 0.40 mm. The data were collected at 299±1 K using the ω-2θ scan technique to a maximum 2θ value of 55.1° for both compounds. A green prism crystal was used for **22**. The approximate dimensions of the crystal were 0.48 x 0.29 x 0.22 mm. The measurements for this complex were done on a Bruker P4/CCD system with graphite monochromated Mo-Kα radiation and a rotating anode generator. The data were collected at 193 ± 1 K. The full hemisphere of data was collected to a maximum 2θ value of 52.8°. The Siemens area detector

absorption routine (SADABS) was used to correct the data. The non-hydrogen atoms were refined anisotropically. Hydrogen atoms were included but not refined. All other parameters such as Neutral atom scattering factor, anomalous dispersion effects, Δf' and Δf" values, and mass attenuation coefficients were taken from their usual sources as before.

2.8 Results and Discussion

2.8.1 Structural details

POVRAY© representations of the structures of **11, 13** and **14** are presented in Fig. 2.7-2.9 respectively. The important C-O distances and N-N distances for **11** and **14** are given in Table 2.2. From the short C-O distances (typical C=O 1.21 Å) in all of the three intermediates, it is apparent that the carbonyl groups are in the C=O form and there is no formal charge on the oxygen atoms. A crystallographic summary for the three intermediate compounds is given in Table 2.1. Compound **11** is an intermediate with single extension having one methyl benzoyl formate group in one side of the molecule. The phenyl and the OCH_3 groups are in an *anti* conformation in its tautomeric form shown in Fig. 2.7.

In compound **13** the two phenyl groups are again *anti* to the ester groups in the tautomeric form of the intermediate shown in Fig. 2.8. In compound **14**, the relative positions of the CH_3 and OCH_3 ester groups are not the same at the two ends. This makes the two methyl groups and the - OMe groups at the two ends of the molecule chemically

non-equivalent. This is consistent with the observation in the solution ^{1}H NMR spectroscopy.

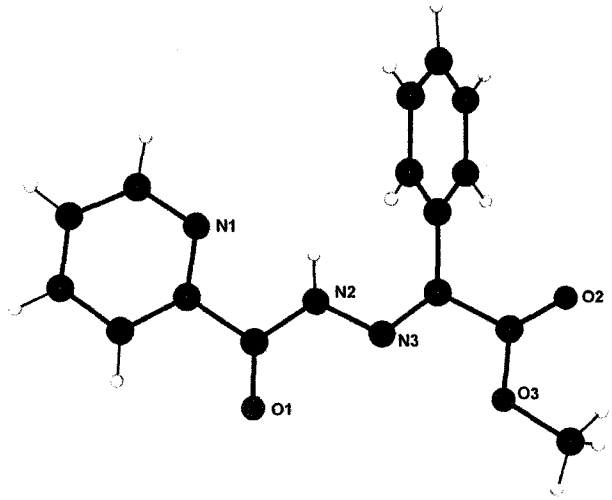

Fig. 2.7 POVRAY© representation of the intermediate **11**; Color code; Grey = H, Black = C, Blue = N, Red = O

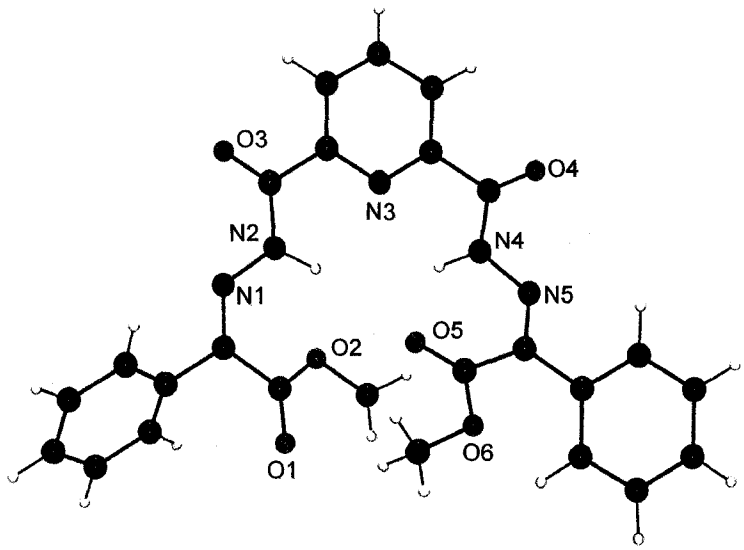

Fig. 2.8 POVRAY© representation of the intermediate **13**; Color code; Grey = H, Black = C, Blue = N, Red = O; the structure was not fully refined.

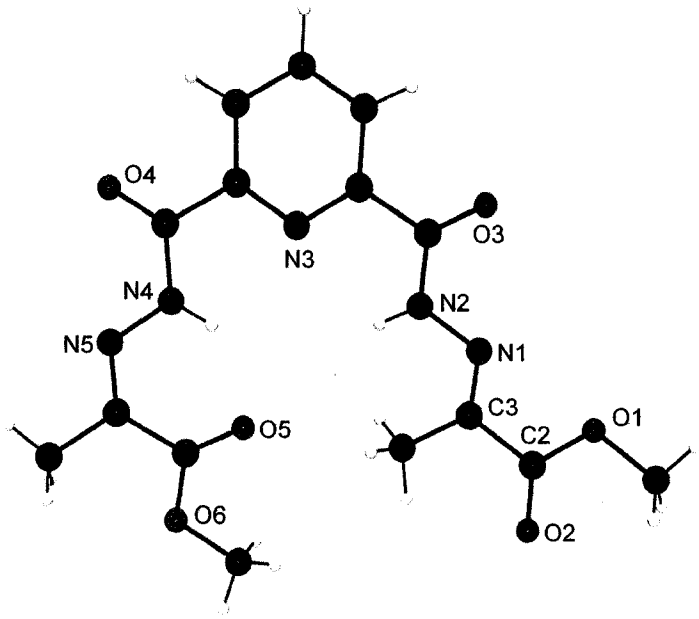

Fig. 2.9 POVRAY© representation of the intermediate **14**; Color code; Grey = H, Black = C, Blue = N, Red = O

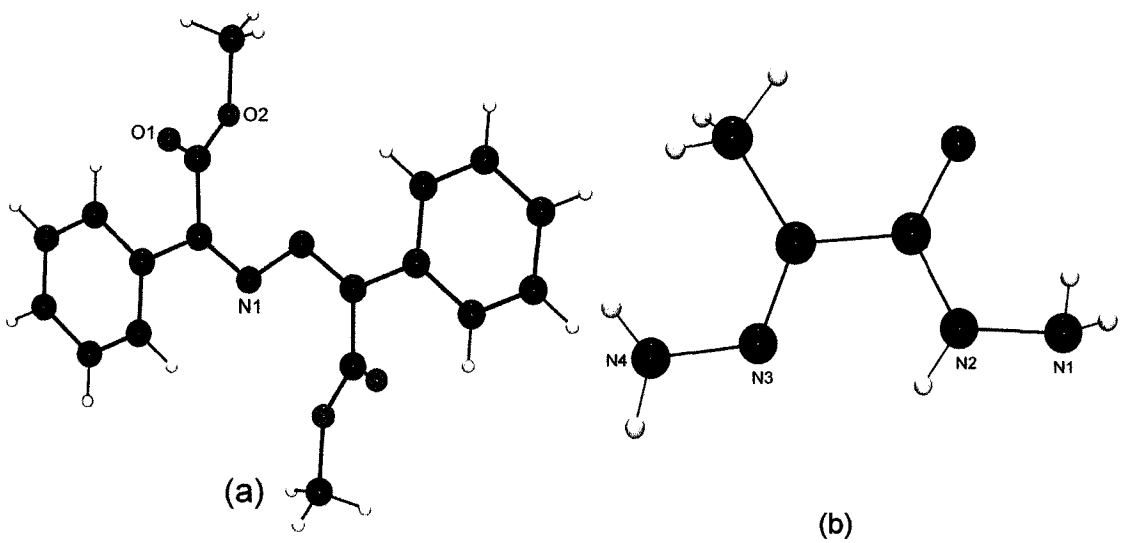

Fig. 2.10 POVRAY© representation of the intermediate **15** (a) and **16** (b); Color code; Grey = H, Black = C, Blue = N, Red = O

Table 2.1 Summary of crystallographic data for **11, 13** and **14**

	11	**13**	**14**
Empirical Formula	$C_{15}H_{13}N_3O_3$	$C_{25}H_{21}N_5O_6$	$C_{15}H_{17}O_6N_5$
Formula Weight	283.29	487.47	363.33
Crystal Color, Habit	Colorless, prism	Colorless	Colorless, Rectangular
Crystal Dimensions	0.25 X 0.25 X 0.40 mm	Not available	0.15 X 0.20 X 0.40 mm
Crystal System	Triclinic	Centric	Monoclinic
Lattice Type	Primitive	Primitive	Primitive
No. of Reflections Used for Unit Cell Determination (2θ range)	20 (29.0 - 37.4 °)	Not available	25 (13.4 – 27.3 °)
Omega Scan Peak Width at Half-height	0.34 °	Not available	0.23 °
Lattice Parameters	a = 9.451(4) Å b = 10.400(3) Å c = 8.315(2) Å α = 108.22(2) ° β = 101.02(3) ° γ = 109.61(3) ° V = 690.0(5) Å^3	a = 9.343(6) Å b = 11.046(7) Å c = 22.411(4) Å β = 90.31(3) ° V = 2313(2) Å^3	a = 9.076(4) Å b = 11.637(3) Å c = 15.840(3) Å β = 94.58(3) ° V = 1667.6(8) Å^3
Space Group	P-1 (#2)	$P2_1/c$	$P2_1/c$ (#14)
Z value	2	4	4
D_{calc}	1.363 g/cm^3	1.400 g/cm^3	1.447 g/cm^3
F_{000}	296.00	Not available	760.00
μ(MoKα)	0.98 cm^{-1}	1.026 cm^{-1}	1.14 cm^{-1}
Temp (K)	299 ± 1	299 ± 1	299
R1	0.044	Not refined	0.054
wR2	0.041	Not refined	0.050

Table 2.2 Important bond distances (Å) for **11**, and **14**

	11			**14**		
C-O	C6	O1	1.211(3)	C5	O3	1.209(4)
				C11	O4	1.216(4)
N-N	N2	N3	1.362(3)	N1	N2	1.373(4)
				N4	N5	1.372(4)

Table 2.3 Important bond distances (Å) and bond angles (°) for **22**

Cu1	O2	1.9517(17)	Cu1	O9	2.4025(19)
Cu1	N2	1.9527(19)	Cu1-N2-N2_2-Cu1_2		91.59
Cu1	O1	1.9798(18)			
Cu1	N1	1.991(2)			

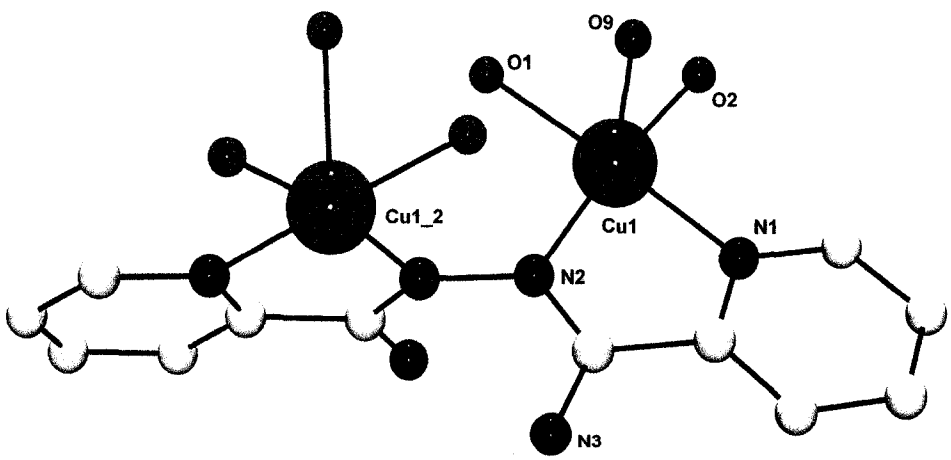

Fig. 2.11 POVRAY© representation of the cation in **22** (color code: Grey = C, blue = N, magenta = Cu(II), red = O)

Table 2.4 Summary of crystallographic data for **15**, **16** and **22**

	15	**16**	**22**
Empirical Formula	$C_{18}H_{16}N_2O_4$	$C_3H_8N_4O$	$C_{12}H_{24}N_{10}O_{18}Cu_2$
Formula Weight	324.34	116.12	723.47
Crystal Color, Habit	Yellow, prism	Colorless, Rectangular	Green, Prism
Crystal Dimensions	0.40 X 0.40 X 0.40 mm	0.20 x 0.10 x 0.40 mm	0.48 X 0.29 X 0.22 mm
Crystal System	Monoclinic	Monoclinic	Monoclinic
Lattice Type	Primitive	Primitive	C-centered
Cell Determination (2θ range)	24 (35.8 – 42.2 °)	22 (20.2-25.5 °)	Not available
Omega Scan Peak Width at Half-height	0.30 °	0.23 °	Not available
Lattice Parameters	a = 8.979(1) Å b = 11.624(1) Å c = 8.099(1) Å β = 101.96(1) ° V = 826.9(2) Å^3	a = 7.678(2) Å b = 7.515(2) Å c = 9.749(2) Å β = 98.54(2) ° V = 556.2(2) Å^3	a = 20.973(4) Å b = 7.322(2) Å c = 16.791(3) Å β = 100.361(3) ° V = 2536.5(8) Å^3
Space Group	$P2_1/c$ (#14)	$P2_1/n$ (#14)	C2/c (#15)
Z value	2	4	4
D_{calc}	1.302 g/cm^3	1.387 g/cm^3	1.894 g/cm^3
F_{000}	340.00	248.00	1472.00
μ(MoKα)	0.93 cm^{-1}	1.08 cm^{-1}	17.81 cm^{-1}
Temp (K)	299 ± 1	299 ± 1	193 ± 1
R1	0.041	0.049	0.047
wR2	0.041	0.051	0.123

The solid state structure of **22** is given in Fig. 2.11 and a summary of crystallographic data is given in Table 2.4. Important bond distances and angles are listed in Table 2.3. Two five coordinate square pyramidal copper ions (τ = 0.03, values for perfect square pyramidal and trigonal bipyramidal copper centers are 0 and 1 respectively [105 (b)]) are bound in two coordination pockets at two ends of the ligand with a twist along the N-N single bond. The N-N bond length of 1.407(3) Å indicates single bond character (typical N-N bond distance in parent PAHAP ligand 1.424(3) Å [55]) . The copper basal planes include two ligand nitrogen atoms and two water molecules. The torsional angle between the two copper magnetic planes is 91.59 °. Axial positions are also occupied by water molecules. The overall structure of **22** is similar to a dinuclear copper complex reported earlier [106].

2.9 Conclusion

Ligands **L1**-**L7** were successfully synthesized. Trinuclear complexes with ligand **L1** will be discussed in Chapter 3. A group of tetranuclear [2 x 2] square grids and pentanuclear complexes derived from ligand **L2** are included in Chapter 4. Their structural characteristics and magnetic behavior will be discussed. The tritopic ligand 2pomp (**L3**) and its octanuclear pinwheel complexes will be addressed in Chapter 5. A group of [3 x 3] nonanuclear grid complexes which are the major class of complexes derived from the tritopic ligand 2pomp will be discussed in Chapter 6. A unique octanuclear mixed metal cobalt catenane complex derived from the ligand **L4** (pttp) and other tetranuclear complexes are included in Chapter 7. Another unique example of a

polynuclear $Cu(II)_{36}$ cluster derived from the ligand **L5** (dpocco) and analogous complexes made from ligand **L6** (Cl-dpocco) are presented in Chapter 8. A [5 x 5] $Mn(II)_{25}$ square grid derived from the ligand 4popap (**L7**), along with a mononuclear Mn(II) complex will be presented in Chapter 9.

Isolation and characterization of hydrolysis products and the complexation of transition metal ions with the hydrolysis products have been reported. The isolation and structural determination of two reaction intermediates **15** and **16** has indicated the vulnerability of hydrazone based ligands towards hydrolytic attack in solvents containing water.

CHAPTER 3

Structure and magnetic properties of dinuclear and trinuclear complexes derived from an imino dihydrazone based ligand with a flexible ligand backbone

3.1 Introduction

Symmetric tritopic ligands e. g. 2poap (Scheme 3.1) and its various analogues, which have a rigid central 2,6-pyridine dihydrazone core have been very successful in producing [3 x 3] nonanuclear $M(II)_9$ square grids in high yield by self-assembly (M = Mn(II), Cu(II), Fe(II), Fe(III), Co(II), Ni(II) [65, 66, 107-113]. Homoleptic nonanuclear grids are formed when metal salts with moderate to weakly coordinating anions (e. g. ClO_4^-, BF_4^-) are used. However, the ultimate outcome is dependent upon the ligand design to a large extent. In designed self-assembly, ligands are designed with suitable coordination pockets as 'ligand components' which host metal ions upon self-assembly. However, the individual components in a ligand do not necessarily always behave in a predictable manner. If the ligand is too flexible, it may not self-assemble to form grids and might prefer to chelate around single metal ions. One way to prevent such chelation is to arrange the donor atoms along the ligand backbone in such a way that rigid five membered chelate rings are produced in each coordination pocket upon coordination. This will override the possibility of chelation around single metal ions and will force the

individual coordination sites to self-assemble to form nonanuclear grids. However, in the presence of potentially coordinating anions such as acetates, or strong donor solvents such as DMF, or DMSO, such formations are inhibited, (e.g. in case of Cu(II)), and simple linear trinuclear complexes are formed. 2poap produced linear trinuclear copper complexes $[(2poap\text{-}2H)Cu_3(CH_3COO)_4]\cdot 3H_2O$ and $[(2poap\text{-}2H)Cu_3(H_2O)(DMF)_3(CH_3OH)_2](BF_4)_4$ where a coordinated acetate group and a DMF solvent molecule acted as competitive ligands respectively [57].

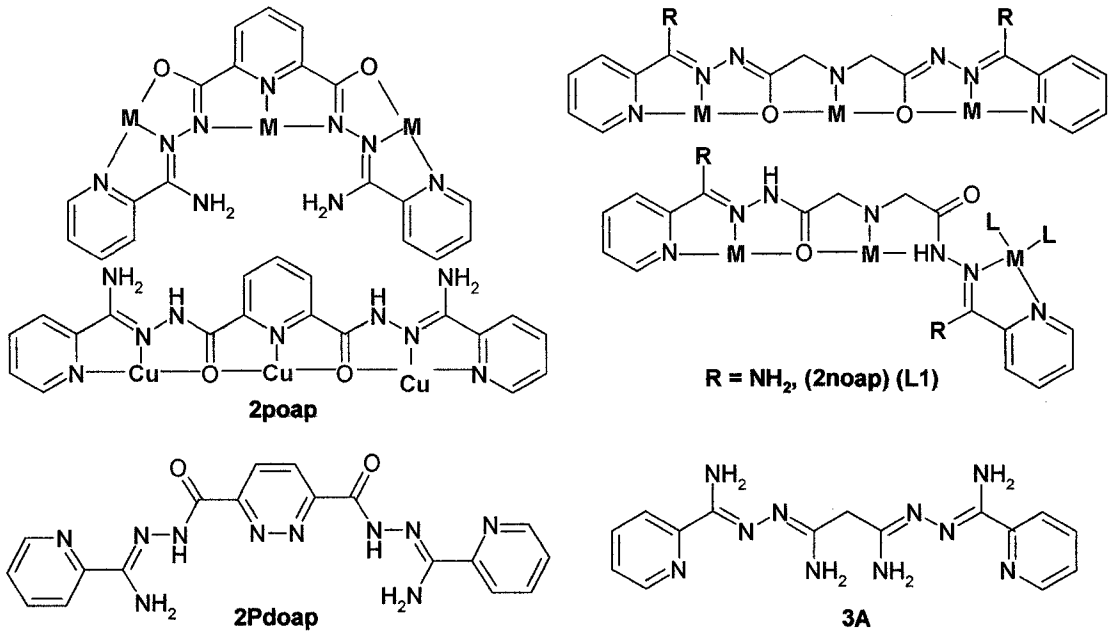

Scheme 3.1 2poap and analogous tritopic ligands with both rigid and flexible backbone

In the homoleptic nonanuclear complexes, the metal coordination requirements are completely fulfilled by the ligands and the hydrazone oxygen atoms act as bridges between the metal centers. Consequently, the magnetic exchange properties are

dependent upon the M-O-M bridge angle. The flexible N-N diazine group does not act as a bridge in these complexes.

The trinuclear copper complexes are different in the sense that the metal ions are bridged by N-N bridging groups and the magnetic coupling is dependent on the torsional angle of the Cu(II) magnetic orbitals around the single N-N diazine bond [55]. The relationship between the torsional angle and the exchange integral is such that ferromagnetic coupling occurs at angles < 80° and antiferromagnetic coupling occurs for angles > 80° [55,106,114]. In the complex $[(2poap\text{-}2H)Cu_3(CH_3COO)_4]\cdot 3H_2O$, the three metal centers are arranged in a roughly linear fashion (Scheme 3.1) and copper magnetic planes are conformationally locked into an almost *trans* N-N disposition with large torsional angles (Cu(2)-N(4)-N(3)-Cu(1) 168.4° and Cu(2)-N(6)-N(7)-Cu(3) 160.7°) (Fig. 3.1) [57].

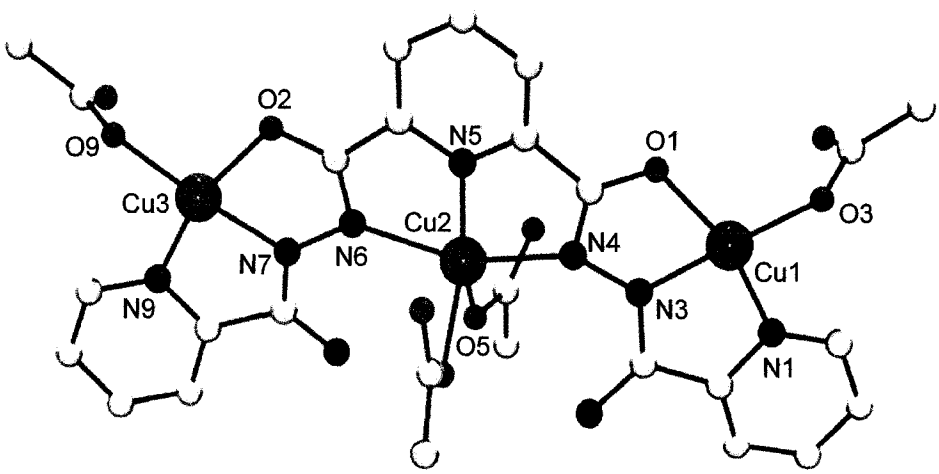

Fig. 3.1 POVRAY© representation of the trinuclear copper(II) complex $[(2poap\text{-}2H)Cu_3(CH_3COO)_4]\cdot 3H_2O$

In the trinuclear Ni(II) complex $[(3A)Ni_3(H_2O)_2](NO_3)_6.8H_2O$ of a ditopic ligand 3A (Scheme 3.1) the N-N single bond is found to propagate magnetic exchange through the Ni–N–N–Ni bond system and again the exchange coupling is torsional angle dependent. In the above complex, a moderate torsional angle (39°- 42°) led to very weak antiferromagnetic exchange (< 1 cm^{-1}) between the metal centers [71]. In one exceptional case of a trinuclear complex $[(2Pdoap\text{-}H)_3Ni_3(H_2O)](NO_3).2H_2O$ with the ligand 2Pdoap (Scheme 3.1), three polytopic ligands bind three octahedral Ni(II) centers and an oxygen atom from a water molecule in such a linear fashion that each of the contiguous coordination pockets of a ligand holds one metal center. Except for the third ligand pocket, which does not contain any metal and it is occupied by a water molecule. Each pair of adjacent Ni(II) centers are bridged by three single N-N diazine groups from the ligands. This makes the complex as a composite of a dinuclear subunit and a third isolated mononuclear Ni(II) center at the forth external ligand pocket with a very long M-M distance of 10.912(3) Å. An average torsional angle of about 40.5° around three N-N single bonds led to moderate antiferromagnetic exchange coupling [115]. Triangular trinuclear complexes of transition metal ions are also known for Fe(II) [116], Co(II) [117] and Mn(II) [118]. Simple carboxylic acids (e.g. pivalic acid) were employed successfully to produce such triangular complexes by self-assembly.

In this chapter, one dinuclear Ni(II) complex and a few trinuclear metal complexes (one Mn(II) and three Cu(II) complexes) will be presented along with their magnetic properties. All of these complexes were derived from an imino dihydrazone

based ligand (Scheme 3.1). The common feature about this class of ligand is the overall flexibility along the ligand backbone. Antiferromagnetic exchange has been observed in all of the complexes, except for the dinuclear Ni(II) complex where significant exchange coupling is absent, due to a large separation between the two metal centers. One trinuclear manganese complex was structurally characterized which showed that the exchange coupling between the Mn(II) centers is mediated through hydrazone oxygen bridges with large bridge angles, while for the trinuclear Cu(II) complexes, the exchange coupling is assumed to be mediated by the N-N diazine bridges.

3.2 Experimental

3.2.1 Materials

Commercially available solvents and chemicals were used without further purification.

3.2.2 Characterization

Analysis, spectroscopic and physical measurements were carried out according to the procedure described in Chapter 2.

3.2.3 Synthesis of the Ligands

Synthesis of the ligand used in this chapter is given in Chapter 2 with spectroscopic details.

3.2.4 Syntheses of the complexes

$[Mn_3(2noap)_2(CH_3CN)_2(H_2O)_2](ClO_4)_6 \cdot 2H_2O$ (1)

2noap (0.1 g, 0.2 mmol) was added to a hot solution of $Mn(ClO_4)_2 \cdot 6H_2O$ (0.21 g, 0.6 mmol) in acetonitrile (~15 mL). The ligand dissolved on stirring. The resulting solution was stirred for 10 minutes to give a bright yellow colored solution which was filtered. Slow evaporation of the solvent at room temperature gave pale yellow crystals suitable for x-ray analysis (Yield 60%). IR (Nujol, cm^{-1}): 3436, 3426, 3352, 3259, 1669 (υ C=N) 1615, 1585, 1084, 1018 (ν ClO_4^-). Anal Calc. (%) for $[(C_{16}H_{19}N_9O_2)_2\ Mn_3]$ $(CH_3CN)_2 \cdot (ClO_4)_6(H_2O)_4$; C, 26.13; H, 3.16; N, 16.93. Found; C, 26.03; H, 3.06; N, 16.76.

$[Cu_3(2noap\text{-}2H)]\ Br_4(CH_3OH) \cdot 0.5CH_3CN$ (2)

A solution of 2noap (0.1 g, 0.3 mmol) in 5 mL of DMF was added dropwise to a methanol solution (~15 mL) of $CuBr_2$ (0.5 g, 2 mmol) at room temperature. The resulting solution was stirred for 0.5 hours. A green-yellow precipitate formed, which was collected by filtration after two days (Yield 80%). IR (Nujol, cm^{-1}): 3245, 1735, 1717, 1655, 1101, 1019, 909. Anal. Calc. (%) for $(C_{16}H_{17}N_9O_2)Cu_3Br_4(CH_3OH)(CH_3CN)_{0.5}$; C, 23.37; H, 2.45; N, 14.39. Found; C, 23.57; H, 2.69; N, 14.30.

$[Cu_3(2noap\text{-}2H)](NO_3)_4 \cdot 4.5H_2O$ (3)

2noap (0.0185 g, 0.5 mmol) was added to a solution of $Cu(NO_3)_2 \cdot 3H_2O$ (0.5 g, 2 mmol) in methanol and dichloromethane (10mL:10mL) at room temperature. The ligand dissolved immediately resulting in a deep blue solution. Slow evaporation of the solvent at room temperature led to the formation of a deep blue crystalline compound, which was isolated by filtration and dried in air (Yield 65%). IR (Nujol, cm^{-1}): 3550 (ν OH), 3400, 3200 (ν NH), 1735 (ν NO_3^-), 1665, 1675 (ν C=O, C=N), 1020 (ν py). UV/vis λ_{max} (nm): 650.18. Anal. Calc. (%) for $[(C_{16}H_{17}N_9O_2)Cu_3](NO_3)_4(H_2O)_{4.5}$; C, 21.66; H, 2.95; N, 20.53. Found; C, 21.86; H, 2.52; N, 20.29.

$[Cu_3(2noap\text{-}2H)](CH_3COO)_4(CH_3OH)_{3.5} \cdot 9.5H_2O$ (4)

2noap (0.0185 g, 0.5 mmol) was added to a solution of $Cu(OAc)_2 \cdot H_2O$ (0.5 g, 2.5 mmol) in methanol (~20 mL) at room temperature. The ligand dissolved immediately to result in a deep blue green clear solution. Slow evaporation of the solvent at room temperature led to the formation of a deep blue crystalline compound, which was isolated by filtration, washed with acetonitrile and dried in air (Yield 48%). IR (Nujol, cm^{-1}): 3474 (ν OH), 3368 (ν NH), 3268, 3177, 1689, 1599 (ν C=O, ν C=N), 1050, 1024 (ν py). Anal. Calc (%) for $[(C_{16}\ H_{17}N_9O_2)Cu_3](CH_3COO)_4(CH_3OH)_{3.5}(H_2O)_{9.5}$; C, 30.65; H, 5.79; N, 11.69. Found; C, 30.45; H, 3.94; N, 11.45.

$[Ni_2(2noap)_3](BF_4)_4 \cdot 14.5H_2O$ (5)

2noap (1.1 g, 3 mmol) was added to a solution of $Ni(BF_4)_2 \cdot 6H_2O$ (0.68 g, 2 mmol) in methanol (~20 mL). The resulting solution was stirred for 30 min, filtered and kept for crystallization. Slow evaporation of the solvent at room temperature gave deep red crystals suitable for a preliminary x-ray determination. (Yield 50%). IR (Nujol, cm^{-1}): 3340, 1675, 1645, 1017. Anal. Calc. (%) for $[(C_{16}\ H_{19}N_9O_2)_3\ Ni_2](BF_4)_4(H_2O)_{14.5}$; C, 31.43; H, 4.72; N, 20.62. Found; C, 31.53; H, 4.27; N, 20.53.

3.3 Crystallographic data collection and refinement of structures

A yellow prismatic crystal of **1** with approximate dimensions 0.44 x 0.34 x 0.10 mm was mounted on a glass fiber. All measurements were done on a Bruker P4/CCD system with graphite monochromated Mo-Kα radiation and a rotating anode generator. Hydrogen atoms were introduced with isotropic thermal parameters set twenty percent greater than those of their bonding partners at the time of their inclusion. They were optimized by positional refinement. The data were collected at a temperature of 193 K. The full hemisphere of data was collected to a maximum 2θ value of 52.8°. The Siemens area detector absorption routine (SADABS) was used to collect the data with maximum and minimum effective transmissions of 0.9094 and 0.6754 respectively. The data were corrected for Lorentz and polarization effects. The structure was solved by direct methods [99] and expanded using Fourier techniques [100]. The non-hydrogen atoms were refined anisotropically. The maximum and minimum peaks on the final difference

Fourier map corresponded to 1.11 and -0.61 $e^-/Å^3$, respectively. Neutral atom scattering factors were taken from the usual source of Cromer and Waber [101]. Anomalous dispersion effects were included in F_{calc} [102]. The values for $\Delta f'$ and $\Delta f''$ were those of Creagh and McAuley [103]. The values for the mass attenuation coefficients are those of Creagh and Hubbell [104]. All calculations were performed using the teXsan [105 (a)] crystallographic software package of Molecular Structure Corporation except for refinement, which was performed using SHELXL-97 [99]. The structural refinement of complex **5** was not possible due to poor diffraction and an inadequate number of reflections and inherent disorder within the crystal. Nevertheless the main metal framework is apparent from the preliminary structure.

3.4 Results and Discussion

3.4.1 Structural details

The structure of **1** is illustrated in Fig. 3.2. Abbreviated crystal data for **1** are given in Table 3.1 and selected important bond angles and bond distances are presented in Table 3.2. The structure comprises three Mn(II) centers creating an isosceles triangle where two Mn(II) centers are oxygen bridged as a $Mn_2(\mu\text{-}O)_2$ subunit, and the third Mn(II) acts as a distant mononuclear center. The two oxygen bridged Mn(II) centers have a distorted pentagonal bipyramidal geometry, while the third Mn(II) is pseudo-octahedral. Protons have been located on N(4), N(5), N(6), and other symmetry related nitrogen atoms. The C-O bond lengths (C(10)-O(2) 1.230 Å) are short and indicate that they have significant C=O character. This means that the two ligands involved in the trinuclear

They are arranged in a bent fashion binding the dinuclear subunit with one end while connecting the mononuclear center with the other end. The central nitrogen atoms N(5) and its symmetry related N(5_2) in the two ligands act as the terminal bond to Mn(2) and Mn(2_2). They also act as the point of bifurcation for both the ligands where the ligand takes a twist and forms one corner of the isosceles triangle.

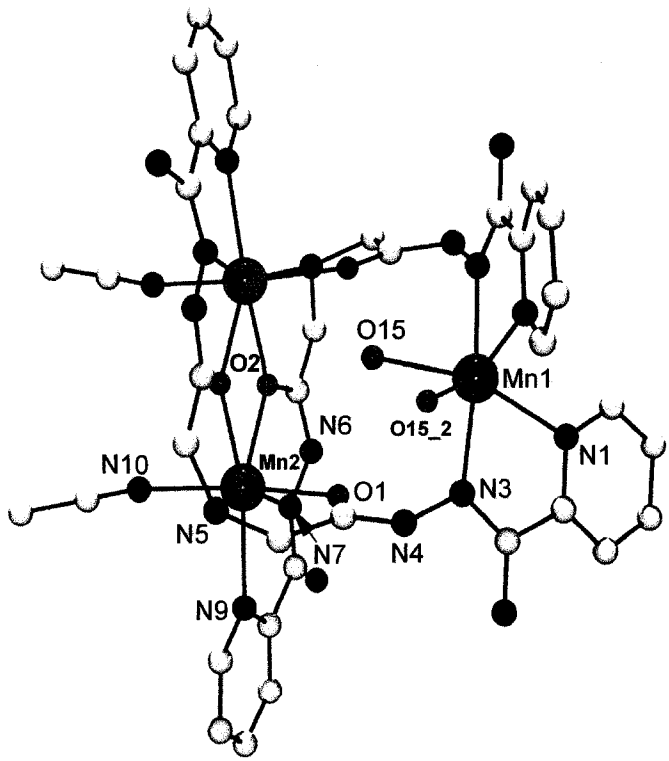

Fig. 3.2 POVRAY© representation of the core structure in complex **1**

The Mn(2) - Mn(2_2) separation is 3.903 Å. An acetonitrile molecule is bonded to each of the oxygen bridged Mn(II) centers in an *axial* position (Mn(2)-N(10) 2.208 Å). The Mn(1)-Mn(2) distance is fairly long (5.315 Å) and two *cis*-coordinated water molecules fill the coordination sphere of Mn(1) with distances of Mn(1)-O(15) 2.247 Å.

Table 3.1 Abbreviated crystal data for **$[Mn_3(2noap)_2(CH_3CN)_2(H_2O)_2](ClO_4)_6 \cdot 2H_2O$ (1)**

Empirical Formula	$C_{36}H_{52}N_{20}O_{32}Cl_6Mn_3$
Formula Weight	1654.45
Crystal Color, Habit	Yellow, prism
Crystal Dimensions	0.44 X 0.34 X 0.10 mm
Crystal System	Monoclinic
Lattice Type	C-centered
Lattice Parameters	a = 14.957 (2) Å b = 21.519 (2) Å c = 19.792 (2) Å β = 103.233 (2) ° V = 6201 (1) $Å^3$
Space Group	C2/c (#15)
Z value	4
D_{calc}	1.772 g/cm^3
F_{000}	3364.00
μ(MoKα)	9.67 cm^{-1}
Temp (K)	193 (±1)
R1	0.060
wR2	0.169

Table 3.2 List of selected bond angles (°) and bond distances (Å) for

$[Mn_3(2noap)_2(CH_3CN)_2(H_2O)_2](ClO_4)_6 \cdot 2H_2O$ (1)

Mn1	N3	2.161(3)
Mn1	N3	2.161(3)
Mn1	N1	2.231(3)
Mn1	N1	2.231(3)
Mn1	O15	2.247(3)
Mn1	O15	2.247(3)
Mn2	O1	2.167(3)
Mn2	N10	2.209(4)
Mn2	O2	2.235(3)
Mn2	N7	2.244(4)
Mn2	N9	2.334(4)
Mn2	O2	2.356(3)
Mn2	N5	2.490(4)
O2	C10	1.230(5)

Mn2	O2	Mn2	116.44(12)

In order to compensate for the neutral nature of the ligands and large Mn(2)-Mn(2_2) separation, the Mn-O distances to the bridging oxygen atoms are quite long (2.235 Å for Mn(2)-O(2) and 2.356 Å for Mn(2)-O(2_2)) which in turn leads to a very large oxygen bridge angle of Mn(2)-O(2)-Mn(2_2) 116.44°. The other Mn(II)-L distances fall within the range 2.161-2.231 Å around Mn(1) and 2.167-2.490 Å around Mn(2) and they are typical for Mn(II) [112].

The structural data set for complex **5** was not good enough to support a full anisotropic refinement of the model, primarily due to very weak diffraction and subsequent low percentage of observed data. However, a preliminary structure of the complex shows the three ligands and the two Ni(II) ions.

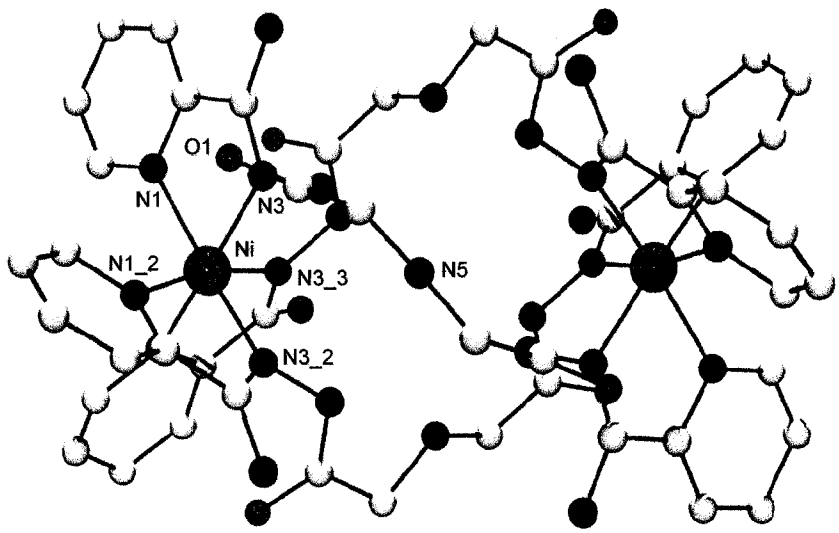

Fig. 3.3 POVRAY© representation of the cationic framework of complex **5** resulting from preliminary x-ray data (structure not fully refined).

Each ligand coordinates through the two ends only, leaving the carbonyl oxygen and imino nitrogen (N(5) and its symmetry related atoms) free and uncoordinated. The three ligands bind two Ni(II) centers by their ends in a twisted fashion. A pictorial representation of the cationic framework from the preliminary structural solution is given in Fig. 3.3.

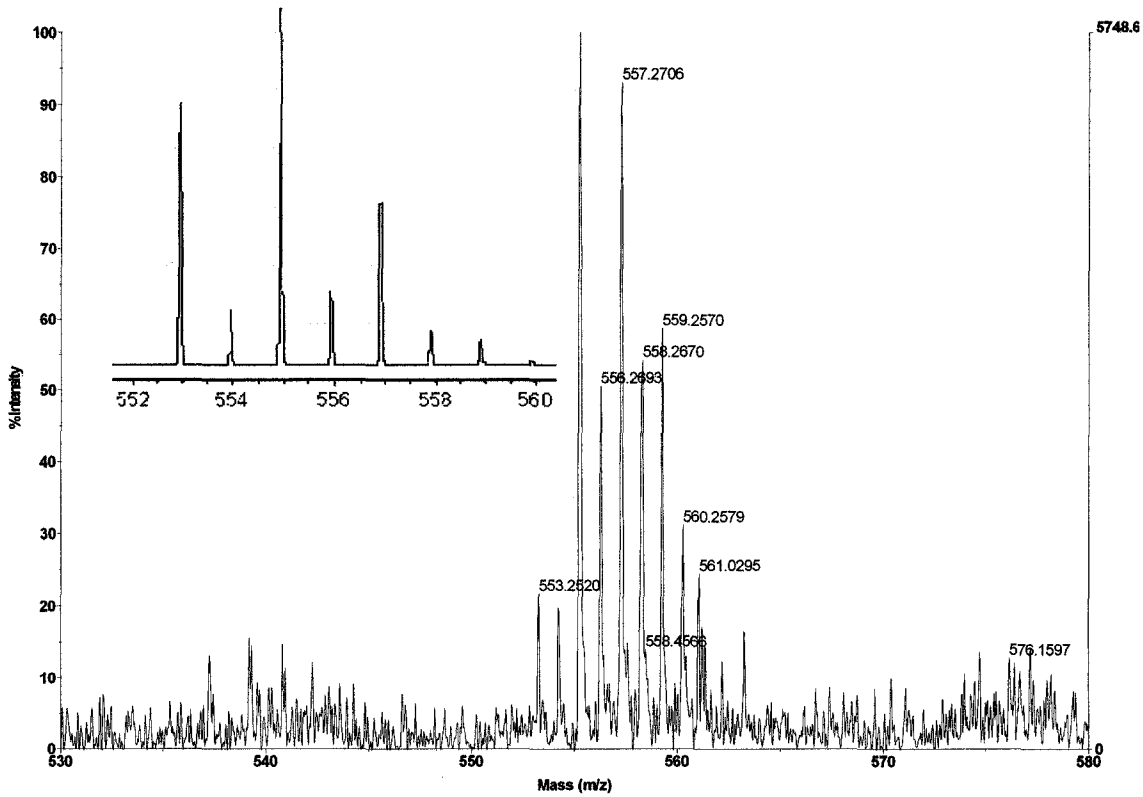

Fig. 3.4 Expansion of MALDI TOF mass spectrum of the complex **3** cation and its calculated isotopic mass distribution (inset)

3.4.2 Mass spectrometry

Mass spectrometric analysis was carried out on the complex **3** using MALDI TOF mass spectrometry. The complex **3** shows a mass peak at m/z 555 which corresponds to the molecular mass peak for $[LCu(II)_3]^+$. Fig. 3.4 shows the molecular mass peak for cation **3** and its calculated isotopic mass distribution. Based on the elemental analysis and the variable temperature magnetic profile (*Vide infra*) it is proposed that the complex in **3** is a linear trinuclear copper(II) complex with similar arrangement of Cu(II) ions as shown in Fig. 3.1

3.4.3 Magnetism

The room temperature magnetic moment for complex **1** is 11.1 μ_B per mole which is consistent with three Mn(II) centers. The moment then drops down to 5.99 μ_B at 2 K, which is indicative of antiferromagnetic coupling within the $Mn(II)_2$ unit and a residual uncoupled Mn(II) center. The variable temperature magnetic susceptibility (per mole) is shown in Fig. 3.5. The magnetic data were fitted to a $Mn(II)_2$ +1 model which can be expressed in terms of the following exchange Hamiltonian (equation 3.1), where $J = J1$ is the exchange coupling between Mn(II) centers in the oxygen coupled binuclear subunit. We considered Mn(1) (Fig. 3.2) as an isolated mononuclear center (equation 3.1) and J2 = 0 (Fig. 3.5).

$$H_{Ex} = -J(\hat{S}_1 \cdot \hat{S}_2) + \hat{S}_3 \qquad [3.1]$$

$$H_{ex} = -J(\hat{S}_1 \cdot \hat{S}_2 + \hat{S}_2 \cdot \hat{S}_3) \qquad [3.2]$$

$$\chi_M = \frac{N g^2 \beta^2}{3k(T-\theta)} \left(\frac{\sum S'(S'+1)(2S'+1)\exp(-E(S')/kT)}{\sum (2S'+1)\exp(-E(S')/kT)} \right) \qquad [3.3]$$

$$\chi_M = (1-\rho)\chi_{M'} + \left(\frac{1.094 g^2}{T} \right) \rho + TIP \qquad [3.4]$$

The spin states and their energies were calculated by the normal Kambe spin-vector coupling approach [85] and the values were substituted into the Van Vleck equation (equation. 3.3). A correction term θ (Weiss-like correction to account for intermolecular interactions; Eq. 3.3) was included. The other added terms are the temperature independent paramagnetism (TIP), and ρ, which is the fraction of paramagnetic impurity (equation 3.4). This whole task was performed within the generalized software package MAGMUN 4.1 [119]. A reasonable data fit to equation 3.4 was obtained for $g_{av} = 2.05$, $J = -5.6$ cm^{-1}, TIP = 0, cm^3 mol^{-1}, $\rho = 0.0055$, and $\theta = -0.5$ K (10^2*R = 2.2) (R = $[\Sigma(\chi_{obs} - \chi_{calcd})^2 / \Sigma\chi_{obs}^2]^{1/2}$.

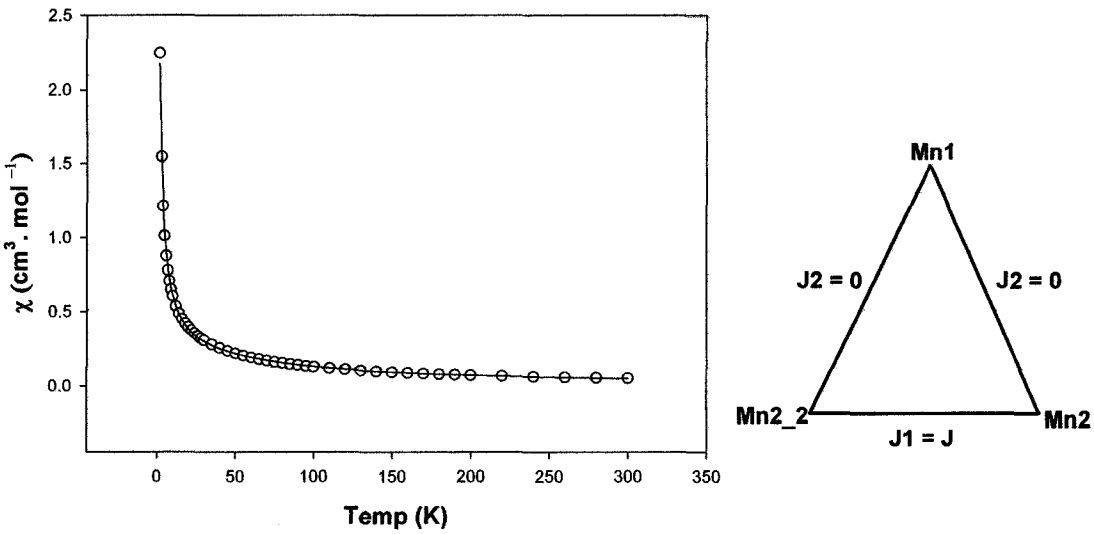

(a) (b)

Fig. 3.5 (a) Variable temperature magnetic profile for **1** (b) magnetic model for **1**

The solid line in the Fig. 3.5 was calculated using these parameters. The large Mn-O-Mn bridge angle (~116°) might be expected to lead to stronger antiferromagnetic coupling between the Mn(II) centers in the complex. Similar antiferromagnetic exchange coupling has been observed before in μ-O [120], and μ-O(R) (R = Ph) [121] bridged mixed valence Mn(II)/Mn(III) binuclear complexes with comparatively smaller bridge angles.

The smaller than expected exchange coupling might be due to the unusually long Mn-O distances (Mn(2)-O(2_2) 2.356 Å). Similarly weaker antiferromagnetic coupling due to large Mn(II)-O bond distances (2.17-2.39 Å) were observed for mixed valence

Mn(II)/Mn(III) complexes [120]. The small negative θ value indicates very weak longer range antiferromagnetic coupling.

Variable temperature magnetic susceptibility measurements were carried out on dry crystalline solid samples of all of the complexes **2-4** within the temperature range 2-300 K, at field strength of 0.1 T. All of them showed a common pattern in their μ_{mol} /T profiles. The magnetic moment of around 3 μ_B at 300 K gradually drops down to a plateau value of around 1.8 μ_B at low temperature. The overall pattern of the variable temperature magnetic data for **2-4** is very much similar to that seen before for linear trinuclear Cu(II) complexes of 2poap and analogous ligands where the copper (II) centers are bridged by single N-N diazine bond and are antiferromagnetically coupled [57, 122 (a)].

The isotropic exchange coupling for a symmetrical system with three linearly arranged S = ½ spin centers (model (below) in Fig. 3.6) can be represented by the Hamiltonian given in equation 3.2. Coupling between terminal metal ions is assumed to be insignificant due to large separation.

The variable temperature magnetic moment profile for complex **2** is shown in Fig. 3.6. The magnetic moment at 300 K is 2.86 μ_B. This value is a little low for three uncoupled Cu(II) centers. But one would assume that the magnetic moment might be reduced to some extent in cases where the copper centers are antiferromagnetically coupled. The moment then drops down to a plateau value of 1.73 μ_B at 10 K which

corresponds to a residual Cu(II) center. A further drop in the moment was observed at the low temperature range to reach a value of 1.59 μ_B which again signifies the onset of intermolecular antiferromagnetic exchange interactions between adjacent clusters. The experimental data were fitted to equation 3.3-3.4 and an excellent fitting was obtained using the following values $g_{av} = 2.02$, $J = -105\ cm^{-1}$, $TIP = 200 \times 10^{-6}\ cm^3.\ mol^{-1}$, $\rho = 0$, $\theta = -0.5$ K ($10^2 * R = 0.67$).

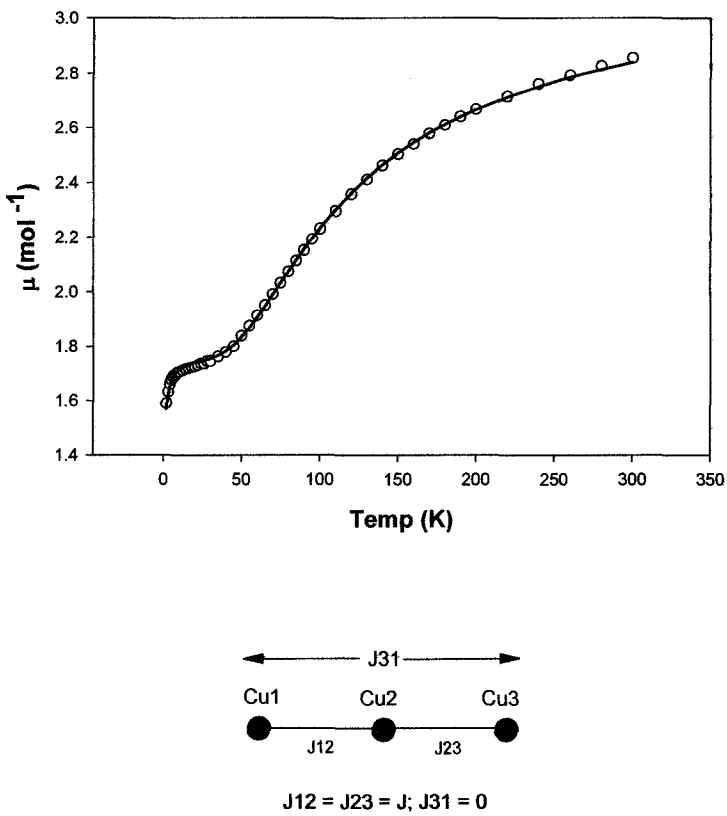

Fig. 3.6 Variable temperature magnetic profile for **2** (top); linear trinuclear copper(II) model (bottom)

The presence of the small negative θ value is an indication of the intermolecular interactions at low temperatures. The solid line in Fig. 3.6 (above) was calculated using the fitted parameters.

Complex **3** shows a magnetic moment of 3.03 μ_B at 300 K, which is equivalent to three Cu(II) centers. The moment then drops down to a value of 1.91 μ_B at 2K, which is close to a magnetic moment for one Cu(II) center. The drop signifies the presence of antiferromagnetic exchange coupling as before. The variable temperature magnetic data for **3** were fitted to equation 3.3-3.4 (S = 1/2) within the software package MAGMUN 4.1 and a good data fit was obtained with $g_{av} = 2.2$, $J = -155$ cm $^{-1}$, TIP = 173 x 10^{-6} cm^3. mol $^{-1}$, $\rho = 0.002$, $\theta = -0.2$ K (10^{2}*R = 0.84)($R = [\Sigma(\chi_{obs} - \chi_{calcd})^2 / \Sigma\chi_{obs}^2]^{1/2}$). This clearly confirms a linear trinuclear structure for the complex **3**, where the exchange integral is typical for a *trans*-N-N bridged system [57]. This is anticipated from the fact that this ligand '2noap' has a coordination 'bite' similar to other tritopic ligands e. g. 2poap [57]. The small negative θ value signifies the possible existence of weak intermolecular magnetic exchange. It might also account for very weak 1-3 coupling between the two terminal copper(II) centers as well. The overall shape of the profile is very similar to the one shown in Fig. 3.6.

Complex **4** showed a very similar magnetic profile, indicating that a similar linear trinuclear Cu(II) complex was formed in this case as well. The magnetic moment at 300 K was 3.47 μ_B which dropped down to 1.60 μ_B at low temperature. A reasonable fitting

of the magnetic data for **4** to the equation 3.3-3.4 (MAGMUN 4.1) gave g_{av} = 2.2, J = -102 cm^{-1}, TIP = 700 x 10^{-6} cm^3. mol^{-1}, ρ = 0, θ = -1.6 K (10^{2}*R = 4.3). This clearly indicates a linear trinuclear structure for the complex. The need of a substantially negative θ value in the fitted parameters is indicative of such long range interactions. The further lowering of the moment at low temperature may indicate that the complex has intermolecular magnetic exchange, which becomes significant at low temperature. The need of a substantially negative θ value in the fitted parameters might be indicative of such long range interactions. Again, the overall shape of the magnetic profile is very similar to the one shown for complex **2** in Fig. 3.6.

No structural details are available yet for the above complexes **2**, **3**, and **4**. So, it is also conceivable that the ligand might have formed isosceles triangular trinuclear Cu(II) complexes (trinuclear model in Fig. 3.5 (b)) similar to **1**, where the complex has a bis(μ-O) bridged dicopper subunit with antiferromagnetically coupled Cu(II) centers and a third isolated Cu(II) ion. Dinuclear copper(II) units where the Cu(II) centers are bridged by bis(μ-O) group with large bridge angles (~116° for the trinuclear Mn(II) complex **1**), are expected to show very strong antiferromagnetic exchange (>500 cm^{-1}). A magneto-structural study on related bis(μ-phenoxide) bridged dinuclear copper(II) complexes revealed strong antiferromagnetic coupling between Cu(II) centers with $-2J$ values in the range 689-902 cm^{-1} having bridge angles ranging from 98.8°-104.7° [122 (b)]. Such strong exchange was not observed in case of above complexes **2-4**. So, a linear trinuclear copper(II) model is more sensible.

From the preliminary structure of **5**, it is revealed that the complex contains two octahedral Ni(II) ions held at the two far ends of the molecule. Due to the large distance the metal centers are magnetically isolated and the magnetic moment shows a constant value of 4.4 μ_B throughout the entire temperature range.

3.5 Conclusion

One dinuclear and some trinuclear complexes of a new tritopic ligand are reported in this chapter. The ligand has an iminodiacetic hydrazone core, which introduced inherent ligand flexibility. Complex **1** has been structurally characterized as a trinuclear Mn(II) complex. It has an antiferromagnetically coupled $Mn(II)_2$ subunit with two neutral carbonyl oxygen bridges and one isolated Mn(II) center. The magnetic data were fitted to a $Mn(II)_2$+1 magnetic model.

Three copper complexes are reported here. All of them showed a common trend in their magnetic profile, which is typical for linear trinuclear complexes with N-N diazine bridges. None of the complexes were structurally characterized. Due to the fact that the ligand has an overall similar coordination 'bite' to other tritopic ligands (e.g. 2poap), a linear trinuclear complex is a reasonable structural prediction. This is justified by reasonable fitting of the experimental data to an appropriate linear trinuclear model. Complex **3** was also characterized by mass spectrometry using MALDI TOF, which clearly showed the molecular mass peak for the complex having $[LCu(II)_3]$ stoichiometry. Moderate exchange coupling has been observed for all of the trinuclear

copper(II) complexes starting from 105 cm^{-1} for the bromide analogue to 155 cm^{-1} for the nitrate complex. This is anticipated because the exchange coupling in such a linear trinuclear arrangement is dependent upon the relative torsional angle between the copper magnetic planes if they are bridged by diazine N-N group and some degree of rotational flexibility could be expected. However, what is noticeable for complex **4** is the presence of a relatively large negative θ value which signifies the onset of intermolecular exchange coupling at low temperature. This might have caused the magnetic moment to drop further beyond 10K. Complex **5** is not magnetically interesting in the sense that it comprises two magnetically isolated Ni(II) centers, which are so well separated that the complex shows a constant magnetic moment over the whole temperature range.

CHAPTER 4

Synthesis, structures and magnetic properties of some [2 x 2] tetranuclear square grids and pentanuclear clusters derived from a ditopic hydrazone ligand

4.1 Introduction

The picolinamide azine type ligands PAHAP and PMHAP (Scheme 4.1), made from picolinamide hydrazone, present variety of arrangement of their donor sites leading to a number of different dinucleating coordination modes. One very common coordination mode would involve a *trans*- dinucleating conformation of the ligand with respect to the $-NH_2$ groups which can be achieved in two different ways. In one, the metal center is simultaneously coordinated by the pyridine and diazine nitrogen (Scheme 4.1 (a)) while in the other, an amino nitrogen takes part in coordination instead of the diazine nitrogen (Scheme 4.1 (b)).

A series of dinuclear $Cu(II)_2$ complexes has been reported with Cl^-, Br^-, NO_3^-, and N_3^- where both antiferromagnetic and ferromagnetic exchanges were observed. It was further revealed that the magnetic exchange was determined by the relative orientation of the two copper magnetic orbitals along the N-N diazine bond and a linear relationship could be established between the exchange integral and the M–N–N–M torsional angle

[55]. In some complexes the two copper centers are 'locked' in a *trans* conformation due to the secondary coordination from the amino NH_2 group, and strong antiferromagnetic exchange was observed due to very large M-N-N-M torsional angles [55].

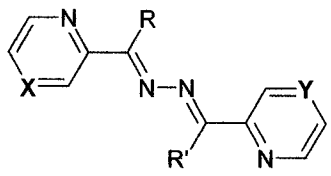

X = Y = CH, R = OH, R' = NH_2 ; PoaP
X = Y = CH, R = R' = NH_2 ; PAHAP
X = Y = CH, R = CH_3, R' = NH_2 ; PMHAP
X = CH, Y = N, R = OH, R' = NH_2 ; PoaPz
X = N, Y = CH, R = OH, R' = NH_2 ; PzOaP
X = Y = N, R = OH, R'= NH_2 ; PzoaPz

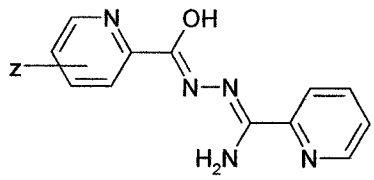

Z = 6-hydroxy ; 6PoaP
Z = 3-hydroxy ; 3PoaP
Z = 2-methyl ; mPoaP
Z = 2-COOH ; PcoaP

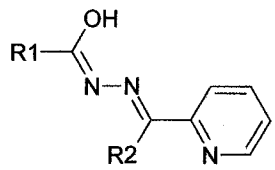

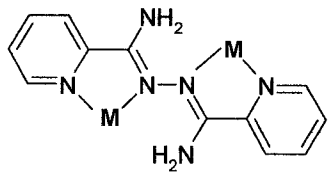

(a)

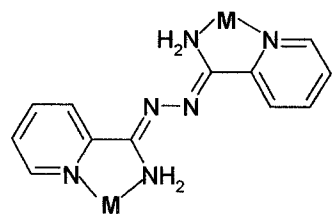

(b)

PomP (R1 = pyr; R2 = CH_3)
ioapm (R1 = 4-methyl-5-imidazole; R2 = NH_2)

Scheme 4.1 A group of tetradentate ditopic ligands.

Within the framework of the self-assembly strategy, introduction of a second dinucleating fragment into the ligand e. g. a hydrazone oxygen group, opened more options for different coordination modes and pathways for spin propagation between the metal centers throughout the resulting self-assembled cluster.

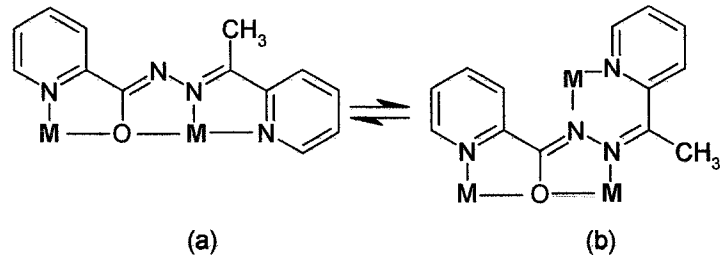

Fig. 4.1 Coordination patterns for the ligand pomp.

For example 'Poap' and its various analogues are tetradentate ditopic ligands (Scheme 4.1) with compartmental coordination pockets positioned side by side and in principle they have better suitability to form clusters with finite nuclearity by self-assembly. The diazine N-N group has already been shown to have rotational flexibility, which can lead to a variety of exchange situations. Fig. 4.1 shows the coordination patterns for the ditopic ligand 'pomp' which are similar to 'poap'. The 'partition' between the two adjacent coordination compartments, created by the hydrazone oxygen, acts as a bridge between metal centers in almost all of the self-assembled clusters with this type of ligand. So the bond flexibility in combination with the donor rich nature of the groups can lead to various structural motifs and diversity with this class of ligands.

'Poap' and its analogues such as mpoap, poapz, 6poap, pzoap, (Scheme 4.1) were found to produce tetranuclear [2 x 2] homometallic grids with Cu(II), in all cases where NO_3^-, or ClO_4^- were used as anions [58]. In a special case, a mixed metal Cu_2Fe_2 heterometallic tetranuclear square grid was formed with 'Pcoap' [123]. In all $Cu(II)_4$ cases, self-assembly produced either a square grid with a $[M_4(\mu\text{-}O)_4]$ core, where all the

Cu(II) centers are bridged by hydrazone oxygen, or a rectangle with an alternate N-N diazine and hydrazone oxygen bridge between metal centers (Fig. 4.2).

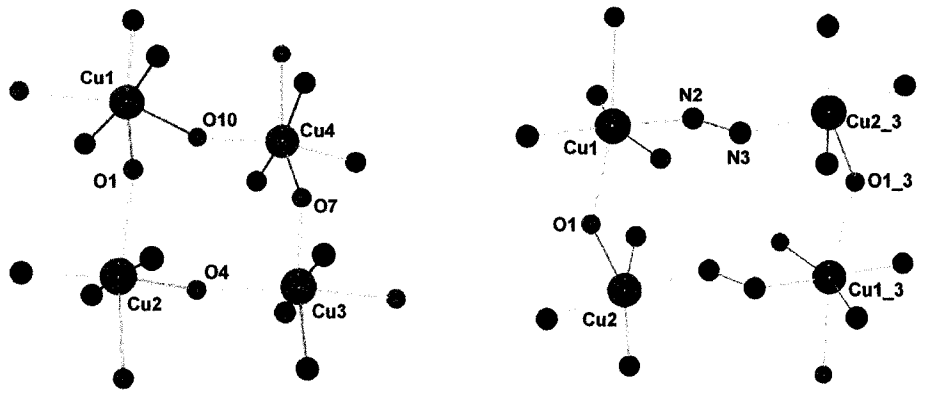

Cu_4 with all hydrazone oxygen bridge

Cu_4 with alternative hydrazone oxygen and diazine bridge

Fig. 4.2 Two different types of bridging in [2 x 2] $Cu(II)_4$ complexes.

All of the square copper clusters exhibited intramolecular ferromagnetism associated with an orthogonal hydrazone oxygen bridging arrangement of the copper magnetic orbitals, while for the rectangular systems the overall exchange was dominated by antiferromagnetic coupling via the N-N diazine bridge. However, when Cl^- or Br^- were used as anions, dinuclear species resulted, where two copper centers were 'locked' in a *trans-* position around the N-N diazine bond. Short hydrogen bonding contacts between bromide and the NH_2 groups were found to have contributed to keeping the complex in such a conformation [124].

Similar tetranuclear [2 x 2] grids were formed in the case of Ni(II) [58], Co(II) and Zn(II) [59, 62]. A spin coupled $[M(II)_4(\mu\text{-}O)_4]$ central core formed in all tetranuclear

cases where the metal centers were bridged exclusively by hydrazone oxygen. However, due to non-orthogonal connections between metal magnetic orbitals and moderate to fairly large M-O-M bridge angles, all the $Ni(II)_4$ and $Co(II)_4$ complexes exhibited intramolecular antiferromagnetic exchange. In the case of Mn(II), however, a choice of nuclearity of the outcome was observed, which was dependent upon the identity of the anion used. Perchlorate (ClO_4^-) is a weak base and a poor donor anion. The use of $Mn(ClO_4)_2.6H_2O$ resulted in the formation of homoleptic pentanuclear clusters $[L_6Mn_5]$, where the core structure of the complex had trigonal bipyramidal metal geometry. In this system, there was an exact match between the total coordination requirement of the five octahedral metal ions and the total coordination pocket donor content available from the six ligand arrangement. All pentanuclear Mn(II) clusters in this system showed intramolecular antiferromagnetic exchange due to large M-O-M bridge angles. Similar pentanuclear clusters were also obtained with other transition metals such as Co(II), and Zn(II) ions [62], where intramolecular antiferromagnetic exchange coupling was observed for cobalt.

However, nitrate (NO_3^-) and triflate ($SO_3CF_3^-$) are weak bases but are relatively better donor anions than the perchlorates. When such donor anions were used, square tetranuclear $[Mn_4(\mu\text{-}O_4)_4]$ grids were formed, where all the four Mn(II) centers were bridged by hydrazone oxygen bridges leading to intramolecular antiferromagnetic coupling.

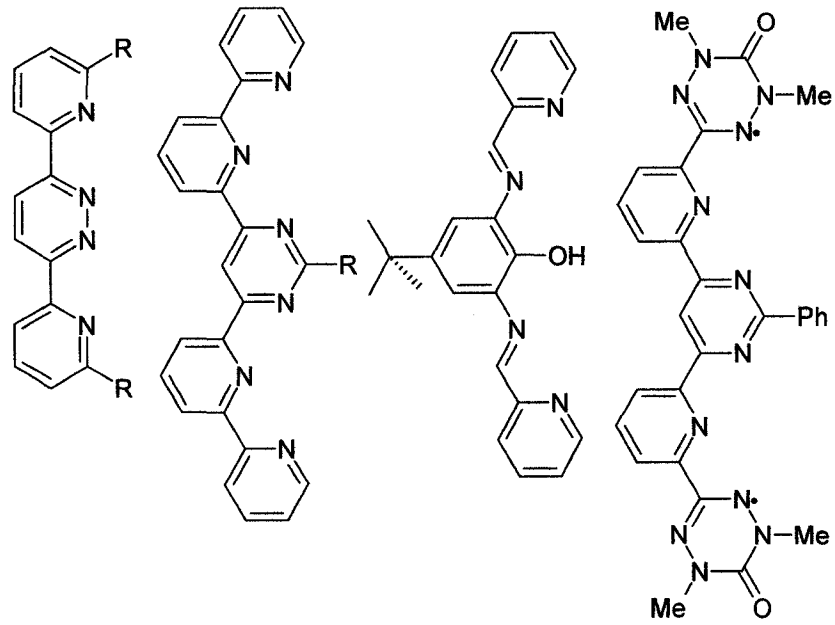

Scheme 4.2 Rigid ditopic ligands.

Tetranuclear [2 x 2] grid structures using relatively rigid bisbidentate or bistridentate ligands (Scheme 4.2), where the center of the ligand contains a bipyridine or terpyridine type moiety have been reported by several other groups. Many of these grids are formed in high yield simply from reactions of the free ligand and the metal ion source. $Cu(II)_4$ squares by Lehn [93, 125], $Co(II)_4$ and $Zn(II)_4$ grid complexes by Rojo et al. [18], and non-magnetic tetranuclear $Ag(I)_4$ [17] and $Pb(II)_4$ squares [22] are a few to mention. A unique example of a tetranuclear copper complex obtained by self-assembly from a pyrazine based diamide ligand [126] was presented in Chapter 1, Fig. 1.3 (a). The adjacent copper centers are bridged by the aromatic pyrazine group. The magnetic exchange couplings between the metal centers in the case of some of the complexes were observed to be very weak (less than 1 cm^{-1}) due to the large intermetallic distances (4.04-

5.35 Å). In all of the above grids, ligands are an integral part of the grid and play an important role in building the structure of the grid. They are rather a passive contributor toward the electronic functionality of the grids. No examples of supramolecular grids with redox active ligands are available yet. However, the synthesis of a stable pyrimidine-verdazyl radical (Scheme 4.2) has been reported, which has the structural attributes suitable for [2 x 2] grid self-assembly [127].

In the present chapter, examples of tetranuclear [2 x 2] $Mn(II)_4$ and $Cu(II)_4$ grids and a trigonal bipyramidal pentanuclear $Mn(II)_5$ cluster obtained from the ligand 'pomp' will be presented. Single crystal x-ray structures of all the complexes will be discussed and the variable temperature magnetic properties will be explained in terms of the corresponding structural features.

4.2 Experimental

4.2.1 Materials

Commercially available solvents and chemicals were used without further purification.

4.2.2 Characterization

Analysis, spectroscopic and physical measurements were done according to the procedure described in Chapter 2.

4.2.3 Synthesis of the Ligands

Synthesis of the ligand used in this chapter is given in Chapter 2 with spectroscopic details.

4.2.4 Synthesis of the complexes

$[Cu_4(pomp\text{-}H)_4(H_2O)_2]\,(NO_3)_4$ (1)

$Cu(NO_3)_2.3H_2O$ (0.2 g, 0.8 mmol) was dissolved in methanol/H_2O (20 mL/5 mL) mixture. The ligand pomp (0.1 g, 0.4 mmol) was added, with continuous stirring. The solution turned deep blue in color. A few drops of Et_3N were added to the resulting solution and was stirred overnight (for ~18h). The mother liquor was filtered before it was kept for crystallization at room temperature. Dark green crystals suitable for x-ray analysis were obtained after two weeks (Yield 66%). Anal. Cal. (%) for $[(C_{13}H_{11}N_4O)_4Cu_4(H_2O)_2]\,(NO_3)_4$; C, 41.76; H, 3.23; N, 18.73. Found (%); C, 41.41; H, 3.28; N, 18.31.

$[Mn_4(pomp\text{-}H)_4(CF_3SO_3)(H_2O)_3]\,(CF_3SO_3)_3{\cdot}(CH_3OH)_8$ (2)

Pomp (0.1 g, 0.4 mmol) was added to a methanolic solution of $Mn(CF_3SO_3)_2.xH_2O$ (0.3 mmol). 03 drops of Et_3N were added to the ligand suspension and was stirred for several hours. The resulting deep red solution was filtered and kept for crystallization at room temperature. Dark orange crystals suitable for x-ray analysis were obtained after two weeks (Yield 26%). Anal. Cal. (%) for

$[(C_{13}H_{11}N_4O)_4Mn_4(CF_3SO_3)\ (H_2O)_3]\ (CF_3SO_3)_3\ (CH_3OH)_8$; C, 37.54; H, 3.84; N, 10.94. Found (%); C, 37.63; H, 2.85; N, 10.91.

$[Mn_4(pomp\text{-}H)_4(NO_3)_2(H_2O)_2]\ (NO_3)_2(CH_3OH)_2{\cdot}2H_2O$ (3)

Pomp (0.05 g, 0.2 mmol) was added to a solution of $Mn(NO_3)_2.6H_2O$ (0.22 g, 0.75 mmol). 03 drops of Et_3N were added to the suspension and was stirred for several hours. The resulting light orange solution was filtered. Orange colored crystals suitable for x-ray analysis were obtained after the solution was stored for 1 week (Yield 51%). IR (Nujol, cm^{-1}): 3390, 1616, 1592, 1531. Anal. Cal. (%) for $[(C_{13}H_{11}N_4O)_4\ Mn_4(NO_3)_2(H_2O)_2](NO_3)_2(CH_3OH)_2(H_2O)_2$; C, 41.55; H, 3.87; N, 17.94. Found (%); C, 41.39; H, 3.61; N, 17.80.

$[Mn_5(pomp\text{-}H)_6](ClO_4)_4(CH_3OH)_2(CH_3CN){\cdot}3.5H_2O$ (4)

Pomp (0.1 g, 0.42 mmol) was added to a solution of excess $Mn(ClO_4)_2.6H_2O$ (0.50 g, 2.0 mmol) in a methanol/acetonitrile mixture (10 mL/10mL), forming initially a light yellow clear solution. 03 drops of Et_3N were added to the resulting solution and stirred for several hours. The final solution was filtered before it was kept for crystallization at RT. Dark orange rod-like crystals were isolated after the solution was stored for several days (Yield 37%). IR (Nujol, cm^{-1}): 1091 ($\nu\ ClO_4^-$). Anal. Calc. (%) for $[(C_{13}H_{11}N_4O)_6Mn_5](ClO_4)_4(CH_3OH)_2(CH_3CN)(H_2O)_{3.5}$; C, 43.27; H, 3.72; N, 15.38. Found (%); C, 43.11; H, 3.46; N, 15.10.

4.3 Crystallographic data collection and refinement of structures

A Bruker P4/CCD diffractometer with graphite monochromated Mo-Kα radiation and a sealed tube source was used in all cases for data collection, except for **3** where an AFC8 diffractometer with a Rigaku Saturn CCD area detector was used. Hydrogen atoms were introduced in calculated positions and difference map positions with isotropic thermal parameters set twenty percent greater than those of their bonding partners. They were not refined except in cases of complex **1** and **3** where they were optimized and refined by positional refinement and using a riding model respectively. Non-hydrogen atoms were refined anisotropically. Some hydrogen atoms in case of the cluster **1** were also refined isotropically. One triflate anion showed 50% disorder in complex **2** and some atoms of that anion were refined isotropically to achieve convergence. Complex **2** contained one water molecule as lattice solvent with ¾ occupancy. The corresponding hydrogen atoms were not included in the model.

There are 9.5 hydrogen atoms missing from the symmetry expanded model for complex **2**. Complex **4** contained two methanol molecules with partial occupancy. They were refined isotropically. In general, the data were collected at a temperature of 193 K except for the complex **3**, where the data collection was performed at 153 K. The full hemispheres of data were collected to a maximum 2θ value of 52.8° for complex **1** and **2**. The corresponding 2θ values were 61.9° and 53.1° for **3** and **4** respectively. Crystal mounting for data collection was done using glass fiber in all cases. A green plate crystal with dimensions 0.45 x 0.17 x 0.08 mm for complex **1** and

an orange plate crystal of dimensions 0.41 x 0.31 x 0.05 mm for complex **4** were used. The Siemens area detector absorption routine (SADABS) was used in both cases to correct the data with maximum and minimum effective transmissions of 0.8879 and 0.5474 for **1** and 0.9577 and 0.7162 for **4** respectively. For complex **2**, an orange prism crystal of dimensions 0.69 x 0.30 x 0.29 mm was used for data collection. The data was corrected for absorption using a face indexed Gaussian integration algorithm with maximum and minimum effective transmissions of 0.7831 and 0.5799 respectively. An orange prism crystal with dimensions of 0.38 x 0.37 x 0.16 mm was used for **3**.

The data were corrected using CrystalClear (from Rigaku) with transmission factors ranging from 0.7401 to 0.6096 as maximum and minimum. All the data were corrected for Lorentz and polarization effects. The structures were solved by direct methods [99] and expanded using Fourier techniques [100]. Neutral atom scattering factors were taken from the usual source of Cromer and Waber [101]. Anomalous dispersion effects were included in F_{calc} [102]. The values for $\Delta f'$ and $\Delta f''$ were those of Creagh and McAuley [103]. The values for the mass attenuation coefficients are those of Creagh and Hubbell [104]. All calculations were performed using the teXsan [105 (a)] crystallographic software package of Molecular Structure Corporation except for the complex **3**, where calculations were performed using CrystalStructure [128-129]. Crystallographic refinements were performed using SHELXL-97 [99] in all cases.

4.4 Results and Discussion

4.4.1 Structural details

$[(pomp)_4Cu_4(H_2O)_2]\ (NO_3)_4$ (1)

The crystal structure of the tetranuclear copper complex **1** is shown in Fig. 4.3. A crystallographic summary and a list of important bond distances and bond angles are given in Table 4.1. and Table 4.2 respectively. Four ligands self-assemble with four Cu(II) ions to form the tetranuclear rectangular complex. Two ligands bridge two adjacent copper(II) ions in anti-parallel fashion along the longer arms of a rectangle using N-N diazine groups. Each ligand takes up a *trans* conformation along the longer arms. Two other ligands 'clip' the two adjacent Cu(II) ions along the shorter arms perpendicular to the first pair of ligands, thereby, completing the rectangle using hydrazone oxygen bridges.

The Cu(1) ions are six coordinate, where the sixth position is filled by a water molecule with a (Cu(1)-O(9)) bond length of 2.486 Å. Cu(2) ions are five coordinate with square pyramidal geometry ($\tau = 0.09$). The access to the sixth axial copper coordination site in Cu(2) is blocked by a $-CH_3$ group (C(27)) from the adjacent ligand along the longer arm. This can be clearly seen from Fig. 4.3. The Cu-Cu separations are 4.813 Å (longer arms) and 4.102 Å (shorter arms). The Cu-O-Cu bridge angle is 141.2 ° and Cu-N-N-Cu torsional angle is 159.2 °. The basal plane of the square pyramidal Cu(2) is defined by O(1), N(3), N(5) and N(6), with a long axial contact to N(4) (Cu(2)-N(4) 2.172 Å) (Fig. 4.4), while the basal plane around pseudo octahedral

Cu(1) is made up by O(2), N(1), N(2) and N(8), with the Jahn-Teller axis along O(9)-Cu(1)-O(1) (Cu(1)-O(1) 2.331 Å and Cu(1)-O(9) 2.486 Å) (Fig. 4.4).

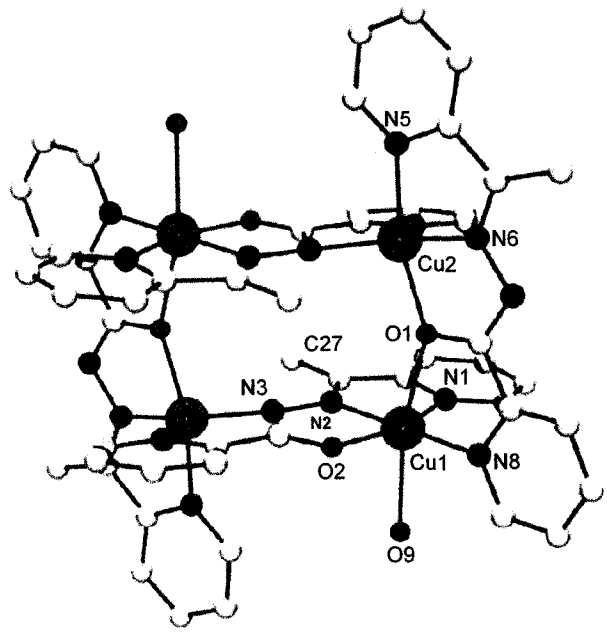

Fig. 4.3 POVRAY© representation of the x-ray crystal structure for 1

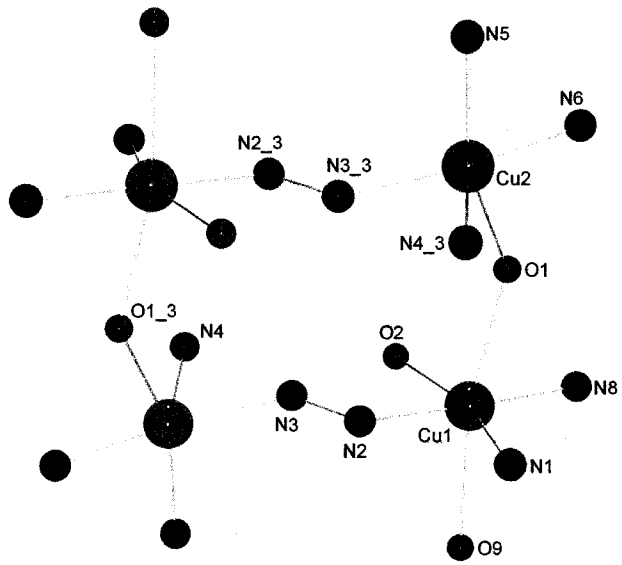

Fig. 4.4 Abbreviated structure for 1 showing only the metal bonding connectivity.

Table 4.1 Summary of crystallographic data for **$[Cu_4(pomp\text{-}H)_4(H_2O)_2](NO_3)_4$ (1)**

Empirical Formula	$C_{52}H_{48}N_{20}O_{18}Cu_4$
Formula Weight	1495.26
Crystal Color, Habit	Green, Plate
Crystal Dimensions	0.45 X 0.17 X 0.08 mm
Crystal System	Monoclinic
Lattice Type	Primitive
Lattice Parameters	a = 14.4439 (6) Å b = 12.8079 (5) Å c = 16.4240 (7) Å $\beta = 105.199\ (1)^\circ$ $V = 2932.1\ (2)\ Å^3$
Space Group	$P2_1/n$ (#14)
Z value	2
D_{calc}	1.693 g/cm^3
F_{000}	1520.00
$\mu(MoK\alpha)$	15.23 cm^{-1}
Temp (K)	193 ± 1
R1	0.036
wR2	0.093

Table 4.2 Selected Bond lengths (Å) and Bond angles (°) for **$[Cu_4(pomp\text{-}H)_4(H_2O)_2](NO_3)_4$ (1)**

Cu1	N2	1.943(2)	Cu2	O1	2.017(2)
Cu1	N8	1.994(2)	Cu2	N5	2.019(2)
Cu1	O2	1.9971(18)	Cu2	N3	2.026(2)
Cu1	N1	2.009(2)	Cu2	N4	2.172(2)
Cu1	O1	2.3305(18)	N2	N3	1.386(3)
Cu1	O9	2.486(2)	Cu2-O1- Cu1		141.23(9)
Cu2	N6	1.923(2)	Cu1- N2- N3 Cu2		159.25(14)

The bond lengths and bond angles are consistent with those in similar rectangular complexes seen before with 'poap' [58].

$[Mn_4(C_{13}H_{11}N_4O)_4(CF_3SO_3)(H_2O)_3]$ $(CF_3SO_3)_3 \cdot (CH_3OH)_8$ (2)

The structure of the heteroleptic complex **2** is shown in Fig. 4.5 and an abbreviated structure showing bonding connectivity with only the immediate donor atoms around Mn(II) ions is shown in Fig. 4.6. A summary of the crystal structure is given in Table 4.3 and a list of important bond lengths and bond angles is given in Table 4.4. The tetranuclear [2 x 2] square complex contains four ligands bound to four Mn(II) ions. The square [2 x 2] grid consists of two eclipsed, parallel ligands bound on each face of the $[Mn(II)_4(\mu\text{-}O)_4]$ core. All of the Mn(II) ions are six coordinate. However, there are four vacant sites in this arrangement.

The vacant site on Mn(1) is occupied by one triflate monodentate anion while vacant sites on Mn(3) and Mn(4) are taken up by a total of three water molecules. Mn-Mn distances fall within the range 3.94 - 4.00 Å. Mn-O-Mn bond angles are in the range of 128.8 °-129.9 °. The infrared spectrum of the ligand indicated significant ketonic character of the C=O group on the basis of the observation of a ν C=O band at 1700 cm^{-1} (Experimental section 2.6.1, Chapter 2). The fairly long C-O distances of the ligands in the crystal structure of **2** fall in the range 1.298 - 1.309 Å. This indicates a predominance of single bond character in the carbonyl bond and that some rehybridization of the ligands has occurred [130].

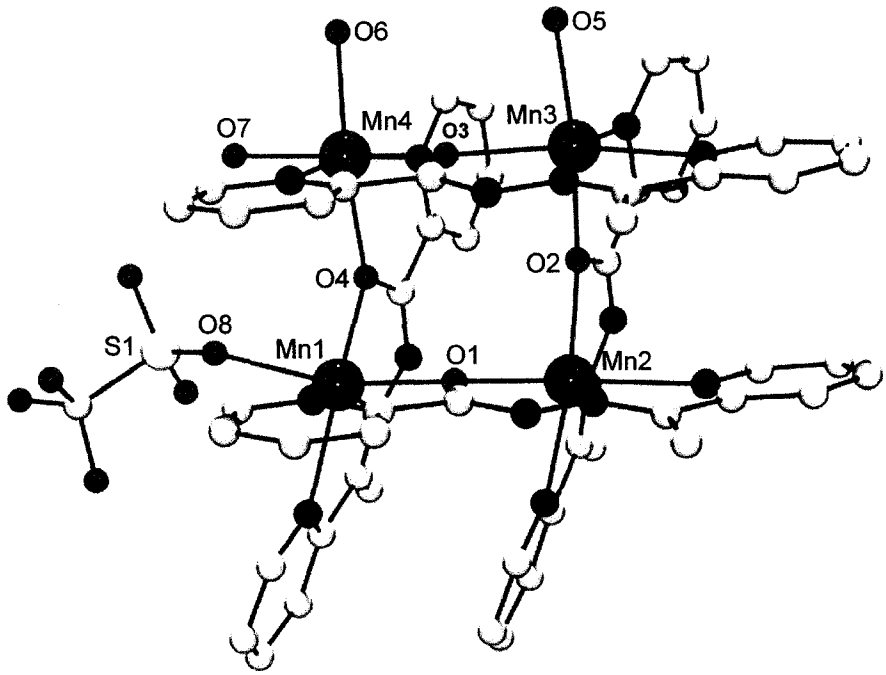

Fig. 4.5 POVRAY© representation of the x-ray structure of **2**

Table 4.3 Summary of crystallographic data for **$[Mn_4(C_{13}H_{11}N_4O)_4\ (CF_3SO_3)(H_2O)_3]$ $(CF_3SO_3)_3 \cdot (CH_3OH)_8$ (2)**

Empirical Formula	$C_{57}H_{54}N_{16}O_{20}S_4F_{12}Mn_4$
Formula Weight	1859.12
Crystal Color, Habit	Orange, Prism
Crystal Dimensions	0.69 X 0.30 X 0.29 mm
Crystal System	Triclinic
Lattice Type	Primitive
Lattice Parameters	a = 12.4058 (8) Å b = 14.462 (1) Å c = 22.110 (2) Å α = 72.629 (1)° β = 80.747 (1) ° γ = 78.257 (1)° V = 3685.3 (4) $Å^3$
Space Group	P-1 (#2)
Z value	2
D_{calc}	1.675 g/cm^3
F_{000}	1880.00
μ(MoKα)	8.94 cm^{-1}
Temp (K)	193 ± 1
R1	0.045
wR2	0.127

Table 4.4 Selected Bond lengths (Å) and Bond angles (°) for **$[Mn_4(C_{13}H_{11}N_4O)_4(CF_3SO_3)(H_2O)_3](CF_3SO_3)_3 \cdot (CH_3OH)_8$ (2)**

Mn1	O8	2.171(2)	Mn3	N9	2.328(3)
Mn1	N15	2.181(2)	Mn4	O6	2.139(2)
Mn1	O1	2.1840(19)	Mn4	O4	2.1605(18)
Mn1	O4	2.2095(18)	Mn4	O7	2.178(2)
Mn1	N1	2.230(2)	Mn4	O3	2.1857(19)
Mn1	N16	2.312(2)	Mn4	N12	2.236(2)
Mn2	N6	2.175(2)	Mn4	N13	2.249(2)
Mn2	N3	2.176(2)			
Mn2	O1	2.1938(19)	Mn1	O1	Mn2	128.80(9)
Mn2	O2	2.2250(18)	Mn3	O2	Mn2	129.28(8)
Mn2	N5	2.278(2)	Mn4	O3	Mn3	129.55(8)
Mn2	N4	2.309(2)	Mn4	O4	Mn1	129.87(9)
Mn3	O5	2.166(2)			
Mn3	O2	2.1791(18)	Mn1	Mn2	3.948(1)
Mn3	N10	2.191(2)	Mn2	Mn3	3.980(2)
Mn3	O3	2.2342(19)	Mn3	Mn4	3.999(1)
Mn3	N8	2.267(2)	Mn4	Mn1	3.959(1)

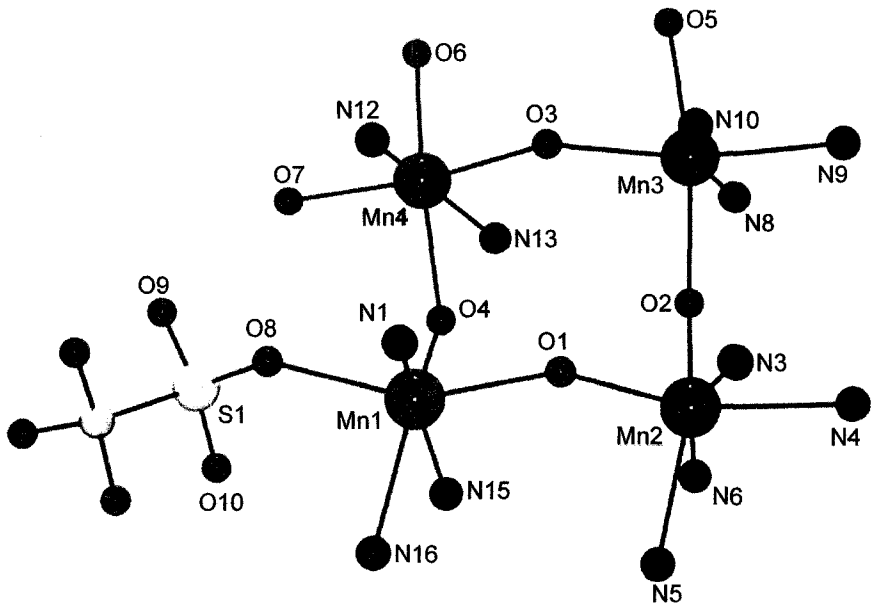

Fig. 4.6 POVRAY© representation of an abbreviated structure of **2** showing only the cationic framework.

$[Mn_4(C_{13}H_{11}N_4O)_4\ (NO_3)_2(H_2O)_2]\ (NO_3)_2(CH_3OH)_2{\cdot}2H_2O$ (3)

The x-ray crystal structure of the heteroleptic tetranuclear Mn(II) complex **3** is shown in Fig. 4.7. A simplified picture of the cationic framework showing only the immediate donor atoms around each metal center is provided in Fig. 4.8. A summary of the crystallographic data and lists of important bond distances and bond angles are given in Table 4.5 and Table 4.6 respectively. The tetranuclear [2 x 2] square complex contains a $[Mn(II)_4(\mu\text{-}O)_4]$ core at the center of the cluster similar to **2**. Again four ligands bind to four Mn(II) ions in an eclipsed fashion with pairs of two parallel ligands similar to the arrangement observed for **2**. All of the Mn(II) ions are six

coordinate with Mn(II)-L distances falling in the range 2.183-2.322 Å. However, again there are a total of four vacant sites in this arrangement. The vacant sites on Mn(1) and Mn(4) are occupied by one monodentate nitrate anion each (Mn(1)-O(13) 2.319 Å and Mn(4)-O(5) 2.169 Å). Similar vacant sites on Mn(3) are taken up by two water molecules (Mn(3)-O(20) 2.170 Å and Mn(3)-O(21) 2.177 Å). Mn-Mn distances fall within the range 3.87-3.98 Å. Mn-O-Mn bond angles are in the range 124.5 °-128.20 °. The infrared spectrum of the complex indicated significant single bond character of the C=O group on the basis of observation of a ν CO band around 1600 cm^{-1}. This is further evidenced from the fairly long C-O distances in the crystal structure that fall in the range 1.295 - 1.303 Å. The average bond distances and bond angles in complexes **2** and **3** are consistent with similar tetranuclear [2 x 2] square $Mn(II)_4$ grids seen before with 'poap' and its analogous ligands [130,131].

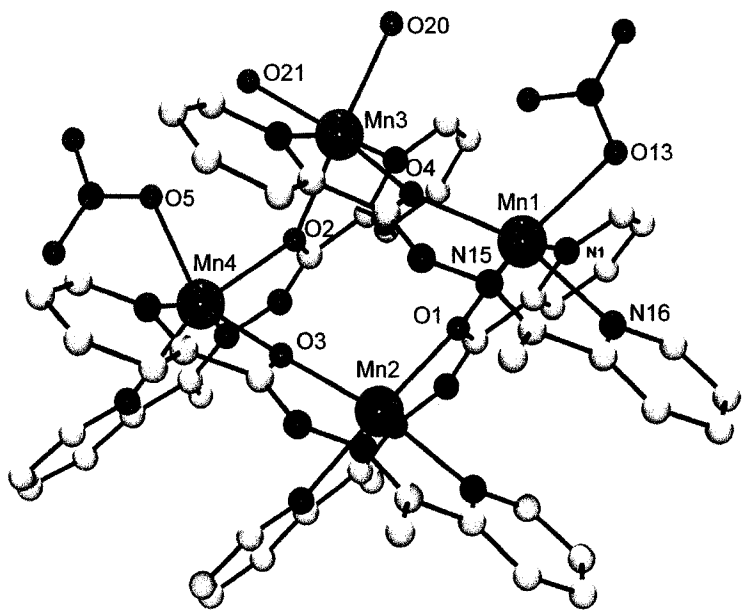

Fig. 4.7 A POVRAY© representation of the x-ray crystal structure for **3**

Table 4.5 Summary of crystallographic data for **$[Mn_4(C_{13}H_{11}N_4O)_4(NO_3)_2(H_2O)_2](NO_3)_2(CH_3OH)_2 \cdot 2H_2O$ (3)**

Empirical Formula	$C_{52}H_{53.50}Mn_4N_{20}O_{20.75}$
Formula Weight	1510.37
Crystal Color, Habit	Orange, prism
Crystal Dimensions	0.38 X 0.37 X 0.16 mm
Crystal System	Triclinic
Lattice Type	Primitive
Lattice Parameters	a = 13.859 (10) Å b = 15.001 (7) Å c = 16.381 (9) Å α = 99.584 (3)° β = 111.326 (16)° γ = 94.865 (14)° V = 3089 (3) $Å^3$
Space Group	P-1 (#2)
Z value	2
D_{calc}	1.620 g/cm^3
F_{000}	1543
μ(MoKα)	8.92 cm^{-1}
Temp (K)	153 ± 1
R1	0.0650
wR2	0.1807

Table 4.6 Selected Bond lengths (Å) and Bond angles (°) for **$[Mn_4(C_{13}H_{11}N_4O)_4(NO_3)_2(H_2O)_2](NO_3)_2(CH_3OH)_2{\cdot}2H_2O$ (3)**

Mn1	N15	2.205(3)	Mn3	N13	2.275(3)
Mn1	O1	2.213(2)	Mn4	O5	2.169(2)
Mn1	O4	2.250(2)	Mn4	O3	2.183(2)
Mn1	N1	2.267(3)	Mn4	N7	2.190(3)
Mn1	O13	2.319(3)	Mn4	O2	2.237(2)
Mn1	N16	2.323(3)	Mn4	N9	2.248(3)
Mn2	O3	2.191(2)	Mn4	N8	2.322(3)
Mn2	N3	2.193(3)			
Mn2	N11	2.209(3)	Mn1	O1	Mn2	128.20(10)
Mn2	O1	2.216(2)	Mn3	O2	Mn4	127.03(10)
Mn2	N12	2.276(2)	Mn4	O3	Mn2	124.55(9)
Mn2	N4	2.305(3)	Mn3	O4	Mn1	128.11(10)
Mn3	O4	2.161(2)			
Mn3	O20	2.170(3)	Mn1	Mn2	3.984(2)
Mn3	O2	2.171(3)	Mn2	Mn4	3.872(3)
Mn3	O21	2.177(2)	Mn4	Mn3	3.945(2)
Mn3	N5	2.267(3)	Mn3	Mn1	3.966(3)

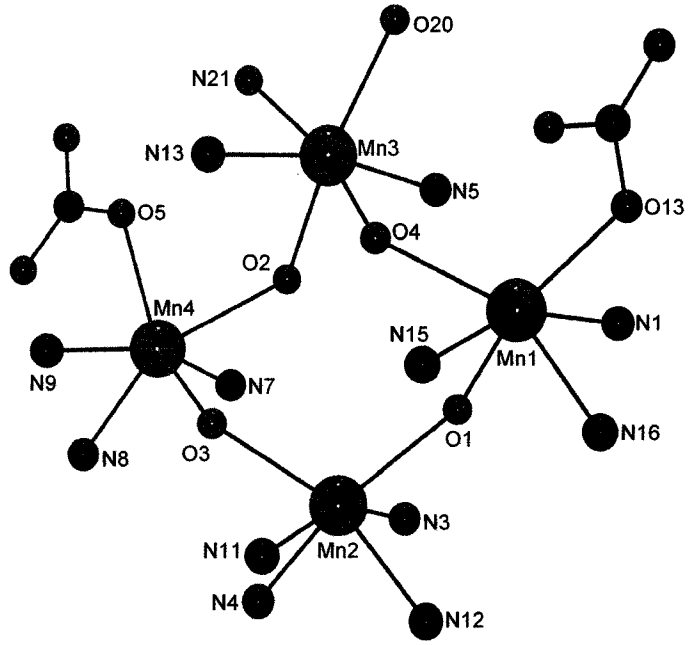

Fig. 4.8 POVRAY© representation for the cationic framework for **3** showing the NO_3^- as auxiliary ligand.

$[Mn_5(C_{13}H_{11}N_4O_6)_6](ClO_4)_4(CH_3OH)_2(CH_3CN)\cdot 3.5H_2O$ (4)

The structure of the homoleptic pentanuclear cation is depicted in Fig. 4.9. A summary of crystallographic data and a list of important bond distances and bond angles are given in Table 4.7 and Table 4.8 respectively. A much simpler picture of the core showing only the metals and the oxygen bridged network is shown in Fig. 4.10. Six tetradentate ligands self-assemble with five Mn(II) metal ions in such a way that they form the core of a trigonal bipyramid, where all the Mn(II) centers are bridged by hydrazone oxygen atoms. The presence of a weakly coordinating anion such as perchlorate in this case is thought to have favored the formation of this homoleptic cluster

over the heteroleptic tetranuclear [2 x 2] grids seen previously in the cases of **2**, and **3**. Similar self-assembled L_6M_5 homoleptic pentanuclear structures have been observed before with other transition metal ions (M = Co(II), Zn(II)) [62]. The Mn-Mn distances in **4** fall within the range 3.896-3.991 Å while the Mn(II)-L distances around each metal center are within the range of 2.165-2.330 Å. The Mn-O-Mn bond angles are in the range 126.92 °- 131.51 ° and they are consistent with similar pentanuclear Mn(II) clusters published earlier [130, 131].

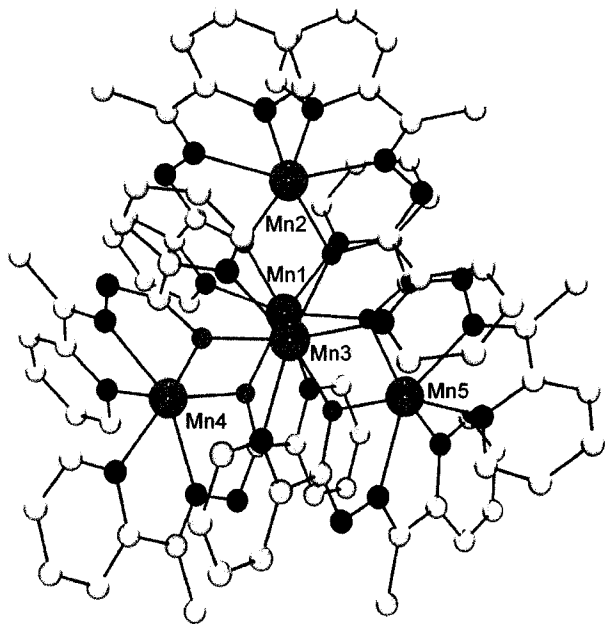

Fig. 4.9 POVRAY© representation for the solid state crystal structure for **4**

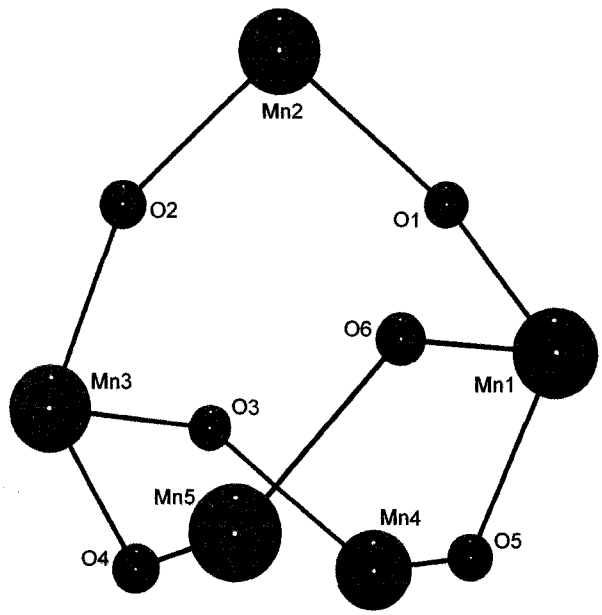

Fig. 4.10 POVRAY© representation for the cationic framework for **4** showing only the bridging connections between metal centers.

4.4.2 Tetranuclear versus pentanuclear cluster - what determines the outcome

It is very difficult to assess and predict the underlying mechanism in self-assembly which would give a rationale for the preferences of pentanuclear clusters over tetranuclear or vice versa. What is apparent from the observed results is that the outcome is mostly dependent upon the type of anion used during the self-assembly. One could envisage an initial step involving the formation of a mononuclear species, where one metal ion may occupy a coordination site of a single ligand, while the other metal sites would compete for coordination by other solvent molecules or coordinating anions.

Table 4.7 Summary of crystallographic data for $[Mn_5C_{13}H_{11}N_4O_6)_6](ClO_4)_4(CH_3OH)_2(CH_3CN)\cdot 3.5H_2O$ (4)

Empirical Formula	$C_{81.50}H_{75}O_{23.50}N_{25}Cl_4Mn_5$
Formula Weight	2197.14
Crystal Color, Habit	Orange, plate
Crystal Dimensions	0.41 X 0.31 X 0.05 mm
Crystal System	Monoclinic
Lattice Type	Primitive
Lattice Parameters	a = 13.999(1) Å b = 22.318(2) Å c = 29.476(3) Å β = 93.573(2) ° V = 9191(1) Å^3
Space Group	$P2_1/n$ (#14)
Z value	4
D_{calc}	1.588 g/cm^3
F_{000}	4480.00
μ(MoKα)	8.72 cm^{-1}
Temp (K)	193 ± 1
R1	0.075
wR2	0.244

Table 4.8 Selected Bond lengths (Å) and Bond angles (°) for $[Mn_5(C_{13}H_{11}N_4O_6)_6](ClO_4)_4(CH_3OH)_2(CH_3CN)\cdot 3.5H_2O$ (4)

Mn1	O5	2.165(4)	Mn4	N18	2.183(5)
Mn1	O1	2.168(4)	Mn4	O5	2.191(4)
Mn1	O6	2.189(4)	Mn4	O3	2.201(4)
Mn1	N20	2.221(5)	Mn4	N17	2.301(5)
Mn1	N24	2.230(5)	Mn4	N12	2.311(5)
Mn1	N1	2.247(5)	Mn5	N22	2.173(5)
Mn2	N6	2.173(5)	Mn5	N15	2.180(5)
Mn2	N3	2.183(5)	Mn5	O6	2.189(4)
Mn2	O1	2.186(4)	Mn5	O4	2.207(4)
Mn2	O2	2.187(4)	Mn5	N21	2.290(5)
Mn2	N4	2.295(5)	Mn5	N16	2.321(5)
Mn2	N5	2.330(5)			
Mn3	O4	2.151(4)	Mn1	Mn2	3.896(3)
Mn3	O2	2.170(4)	Mn2	Mn3	3.943(3)
Mn3	O3	2.177(4)	Mn3	Mn5	3.941(3)
Mn3	N9	2.226(5)	Mn5	Mn1	3.941(2)
Mn3	N8	2.236(5)	Mn1	Mn4	3.909(3)
Mn3	N13	2.249(5)	Mn3	Mn4	3.991(3)
Mn4	N11	2.171(5)			

Mn1	O1	Mn2	126.92(18)	Mn3	O4	Mn5	129.41(18)
Mn3	O2	Mn2	129.66(18)	Mn1	O5	Mn4	127.67(18)
Mn3	O3	Mn4	131.51(18)	Mn1	O6	Mn5	128.40(18)

The second step may involve the 'docking' of one subunit to another subunit which would probably take place by replacing loosely coordinated solvent molecules. This process would then continue sequentially until the last step is complete and the square tetranuclear or pentanuclear cluster is produced (Scheme 4.3).

Triflates and perchlorates are weak donor anions but are likely to compete with solvent molecules and ligand donor sites in the initial formation of a mononuclear intermediate. The approach of one pre-assembled mononuclear subunit to another leads to the formation of metal ligand bonds to additional metal ions to complete the [2 x 2] square, and vacant metal sites are then filled with solvent molecules or anions (e. g. nitrate, triflate).

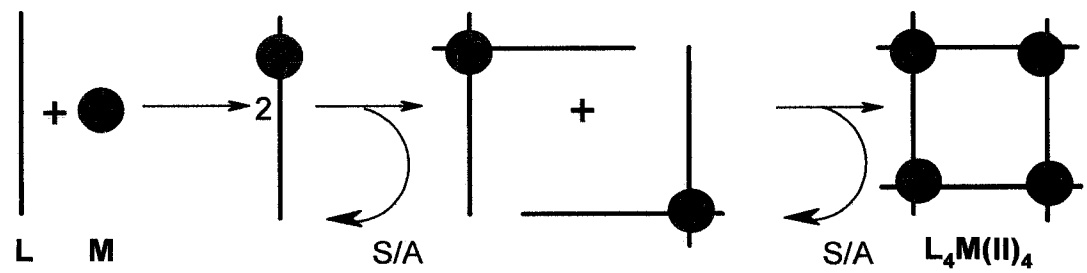

Scheme 4.3 Self-assembly by solvent/anion replacement.

In the case of the weaker perchlorate ligand, pentanuclear homoleptic clusters are generally formed in preference to [2 x 2] square grids, where all six coordination sites of the five metal ions are filled by six tetradentate ligands [58, 62].

4.4.2 Magnetism

Variable temperature magnetic measurements have been carried out on all four of the crystalline solid samples of **1-4** at field strength of 0.1 T and operating between 2-300 K. Exchange interactions in the general cases of tetranuclear square complexes with D_{4h} symmetry, distorted square complexes with D_{2d} symmetry or rectangular complexes with three different coupling integrals J1, J2 and J3 (where J1 ≠ J2 ≠ J3) can be expressed in terms of the exchange Hamiltonian shown in equation 4.1. In the case of complex **1**, J3 can be considered zero, because there is no cross-coupling connection (Scheme 4.4 (a)). So, the equation 4.1 reduces to equation 4.2.

The calculations of the different spin states for S = ½ and their corresponding energies were calculated and substituted into the Van Vleck equation (equation 4.6) to obtain molar susceptibilities at temperatures in the range 2 to 300 K as described earlier using the generalized software package MAGMUN 4.1.

$$H_{ex} = -J1\{\hat{S}_1 \cdot \hat{S}_2 + \hat{S}_3 \cdot \hat{S}_4\} - J2\{\hat{S}_1 \cdot \hat{S}_4 + \hat{S}_2 \cdot \hat{S}_3\} - J3\{\hat{S}_1 \cdot \hat{S}_3 + \hat{S}_2 \cdot \hat{S}_4\} \quad [4.1]$$

$$H_{ex} = -J1\{\hat{S}_1 \cdot \hat{S}_2 + \hat{S}_3 \cdot \hat{S}_4\} - J2\{\hat{S}_1 \cdot \hat{S}_4 + \hat{S}_2 \cdot \hat{S}_3\} \quad [4.2]$$

$$H_{ex} = -J\{\hat{S}_1 \cdot \hat{S}_2\} \quad [4.3]$$

$$H_{ex} = -J\{\hat{S}_1 \cdot \hat{S}_2 + \hat{S}_2 \cdot \hat{S}_3 + \hat{S}_3 \cdot \hat{S}_4 + \hat{S}_4 \cdot \hat{S}_1\} \quad [4.4]$$

$$H_{ex} = -J\{\hat{S}_1 \cdot \hat{S}_2 + \hat{S}_1 \cdot \hat{S}_4 + \hat{S}_1 \cdot \hat{S}_5 + \hat{S}_3 \cdot \hat{S}_2 + \hat{S}_3 \cdot \hat{S}_4 + \hat{S}_3 \cdot \hat{S}_5\} \quad [4.5]$$

$$\chi_M' = \frac{N g^2 \beta^2}{3k(T-\theta)} \left(\frac{\sum S'(S'+1)(2S'+1)\exp(-E_n^{(0)}/kT)}{\sum (2S'+1)\exp(-E_n^{(0)}/kT)} \right) + N\alpha \quad [4.6]$$

$$\chi_M = \chi_M'(1-\rho) + \left(\frac{S(S+1)N g^2 \beta^2}{3kT} \right) \rho + N\alpha \quad [4.7]$$

$$\chi_M = \frac{2N g^2 \beta^2}{3k(T-\theta)} \left[\frac{1}{3+\exp(-2J/kT)} \right] (1-\rho) + \left(\frac{N g^2 \beta^2}{4kT} \right) \rho + N\alpha \quad [4.8]$$

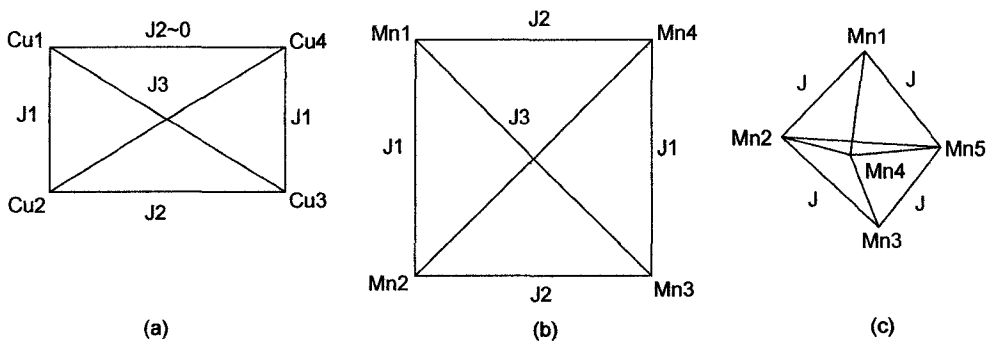

Scheme 4.4 Various magnetic models used for magnetic data fitting (a) for rectangular Cu(II) complex **1** (b) for tetranuclear Mn(II) complexes **2**, and **3** (c) for pentanuclear cluster **5**

Molecular field corrections θ (Weiss-like correction to account for long range intermolecular interactions), a paramagnetic impurity correction term ρ and a temperature independent paramagnetism term (Nα) were also included (equation 4.7). The variable temperature (between 2-300 K) magnetic profile for **1** as molar susceptibility (χ) vs. temperature is shown in Fig. 4.11. The profile shows a gradual increase in susceptibility with lowering of the temperature until it reaches a maximum at 130 K, which indicates intramolecular antiferromagnetic exchange prevailing in the complex. The susceptibility reaches a plateau value of 7.18 x 10^{-4} cm^3. mol^{-1} at around 10 K, which is followed by a steady increase to 2 K. This is a signature of the presence of a small amount of paramagnetic impurity, which becomes dominant at lower temperatures.

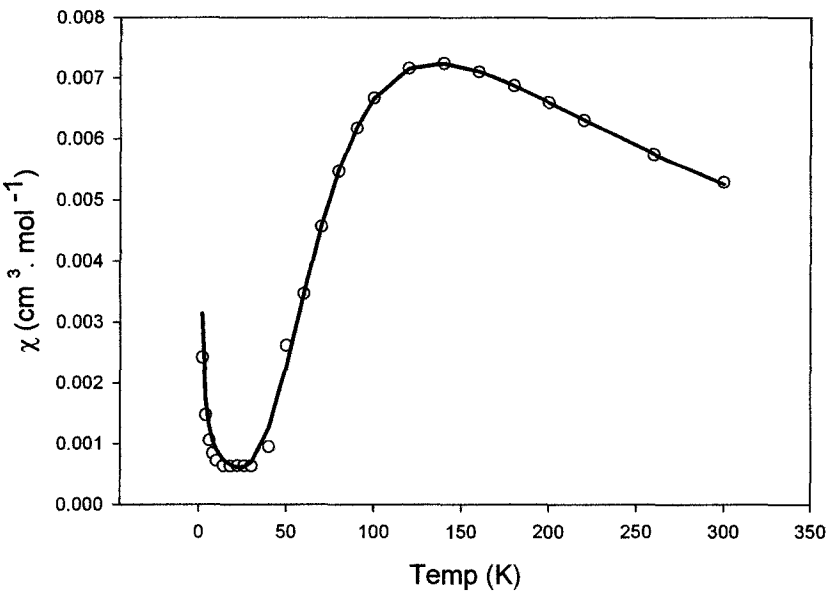

Fig. 4.11 Variable temperature susceptibility profile (χ mol^{-1} vs. T) for **1**

The experimental data were fitted to equation 4.7 based on the exchange Hamiltonian in equation 4.2 for S = ½ with two different J values appropriate for the N-N diazine and hydrazone oxygen bridges. An excellent fitting gave g_{av} = 2.23 (3), J1 = -151(5) cm^{-1}, J2 = 0 cm^{-1}, ρ = 0.003, θ = -0.4 K, TIP = 340 x 10^{-6} $cm^3.mol^{-1}$, 10^2 *R = 0.62 ($R = [\Sigma(\chi_{obs} - \chi_{calcd})^2 / \Sigma\chi_{obs}^2]^{1/2}$). The solid line in Fig. 4.11 was calculated using the fitted parameters. The fact that the fitting requires a value for J2 = 0 cm^{-1} is entirely consistent with the orthogonal nature of the hydrazone oxygen bridge along the shorter arms and hereby validates the initial assumption. The J1 value on the other hand is consistent with the large Cu-N-N-Cu torsional angle (159.2°) at the N-N diazine bridge and agrees well with the correlation between the torsional angles and exchange integral observed previously for other similar dinuclear copper complexes [55, 114].

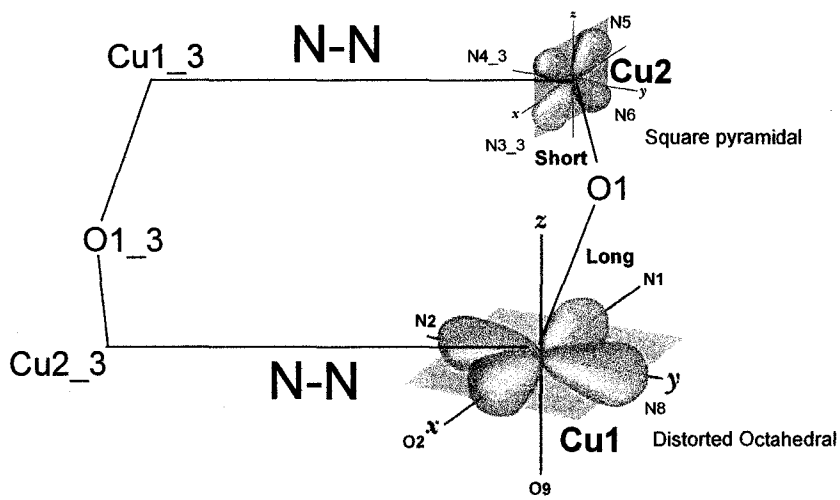

Fig. 4.12 Orthogonal connectivity through the hydrazone oxygen bridge.

Fig. 4.12 shows a pictorial representation of the orthogonal nature of the hydrazone oxygen bridges. As the antiferromagnetic exchange is mediated only through the N-N diazine bridge in **1** and there is no antiferromagnetic exchange by the hydrazone oxygen bridge, the above complex might well be considered as a pair of antiferromagnetically coupled dimers. So a second attempt was carried out to fit the experimental data to an exchange Hamiltonian appropriate for a simple dimer with S= ½ (equation 4.3). An excellent fitting of the experimental data to the modified Bleaney-Bowers equation for a dimer (S1 = S2 = ½) (equation 4.8) gave g_{av} = 2.20, J = - 155 cm^{-1}, ρ = 0.001, θ = - 0.5 K, TIP = 340 x 10^{-6} $cm^3.mol^{-1}$, 10^2*R = 0.13. These values are consistent with the previous fitting parameters, and prove that the N-N diazine is the only significant exchange pathway between the Cu(II) centers in the tetranuclear cluster. Essentially, similar results from the two fits might also signify that the 'dimer of dimers' is a better magnetic model to represent the rectangular $Cu(II)_4$ cluster in **1**.

The variable temperature magnetic profile of the complex **2** is shown in Fig. 4.13 as a plot of μ_{mol} versus temperature. The other tetranuclear complex **3** also showed a similar magnetic profile within the 2-300 K temperature range (Fig. 4.14). In complex **2**, the drop in magnetic moment from 11.6 μ_B at 300 K to a value of 1.8 μ_B at 2 K indicates significant overall intramolecular antiferromagnetic exchange.

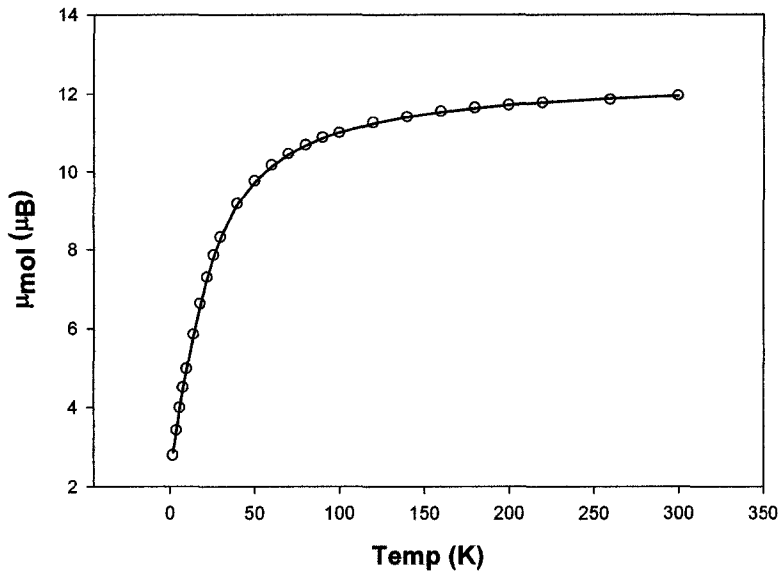

Fig. 4.13 Variable temperature susceptibility profile (μ_{mol} vs. T) for **2**

For the complexes **2** and **3**, the third diagonal exchange coupling constant J3 can again be considered to be zero because of the absence of any direct bonds (Scheme 4.4 (b)). It is also reasonable to consider that J1 = J2 = J because of the presence of very similar hydrazone oxygen bridges in both the complexes. So for both the complexes **2** and **3**, a square tetranuclear magnetic model (Scheme 4.4 (b)) was used where all the exchange integrals are considered equal. An appropriate Hamiltonian for such an exchange can be written as in equation 4.4. By using MAGMUN 4.1, an excellent fitting of the experimental data for complex **2** to equation 4.4 was obtained for g_{av} = 2.08 (2), J = -2.95 (3) cm $^{-1}$, TIP = 0, ρ = 0.04, θ = - 0.5 K, 10^2 R = 0.21. The solid line in Fig. 4.13 was calculated using these parameters.

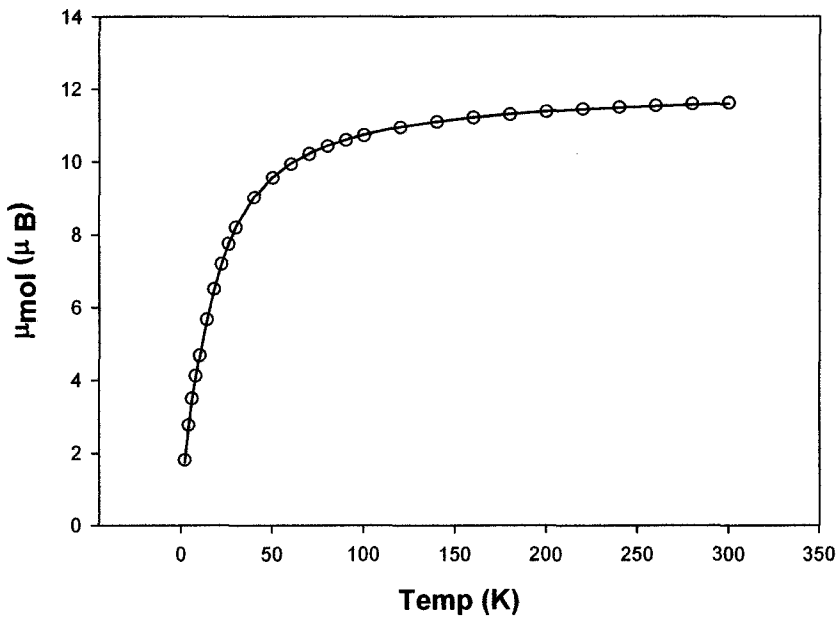

Fig. 4.14 Variable temperature molar magnetic profile for **3**

A significant but small paramagnetic impurity correction was required for a good fit of the data. It may reasonably be associated with the presence of a small amount of mononuclear Mn(II) species or a small amount of a pentanuclear cluster, which is the second major product of this class of ligands. Fitting of the experimental data for **3** to equations 4.4, for S = 5/2 again gave an excellent fit with $g_{av} = 2.03$, J = - 2.6 (7) cm^{-1}, TIP = 0, $\rho = 0.005$, θ = - 0.4 K, $10^2 R = 0.36$ ($R = [\Sigma(\chi_{obs} - \chi_{calcd})^2 / \Sigma\chi_{obs}^2]^{1/2}$). The solid line in Fig. 4.14 was calculated using these parameters. The magnitude of the exchange integral in both complexes **2** and **3** is around - 3 cm^{-1}. This can be explained by the similar hydrazone bridge angle between metal centers in both complexes.

The exchange integrals between adjacent Mn(II) ions in both cases are very similar to those with [2 x 2] $Mn(II)_4$ grid complexes observed before with other related ligands [58, 59].

Complex **4** is a pentanuclear Mn(II) cluster and the profile for its variable temperature molar magnetic moment is shown in Fig. 4.15. The complex has a magnetic moment of 12.7 μ_B at 300 K which is slightly less than the expected spin only value for a pentanuclear cluster with five Mn(II) centers.

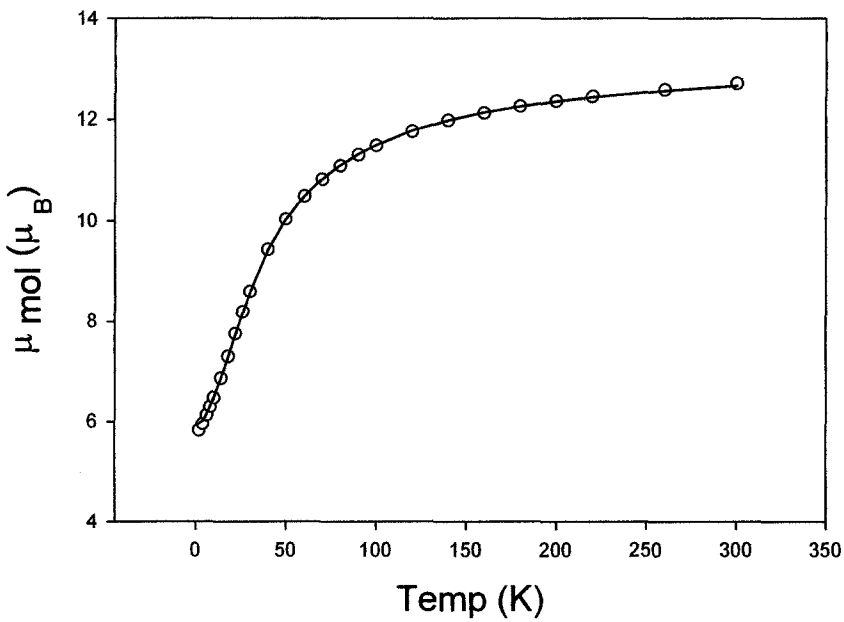

Fig. 4.15 Variable temperature molar magnetic profile for **4**

The gradual drop in moment with the lowering of temperature signifies the presence of intramolecular antiferromagnetic exchange. The low temperature moment of 5.82 μ_B at 2 K indicates the presence of one uncoupled Mn(II) center with a ground state S = 5/2, associated with the fact that an odd number of spin (S = 5/2 each) centers are antiferromagnetically coupled in the cluster.

The magnetic data were fitted to equation 4.7 using the exchange Hamiltonian in equation 4.5. A very good fitting of the data gave $g_{av} = 2.01$ (2), J = - 3.0 cm^{-1}, TIP = 0, ρ = 0, θ = 0 K, 10^2 R = 0.43 ($R = [\Sigma(\chi_{obs} - \chi_{calcd})^2 / \Sigma\chi_{obs}^2]^{1/2}$). The solid line in Fig. 4.15 was calculated using these parameters. The negative J value indicates overall antiferromagnetic exchange within the cluster. The exchange integral is very consistent with that of other similar pentanuclear clusters (-1.50 to -2.65 cm^{-1}) with this class of ditopic 'poap' like ligands and is associated with Mn-O-Mn bridge angles within the range 125-132 ° [62, 130, 131]. A comparable exchange integral (J = -2.85 cm^{-1}) was observed for a $[Mn_4(\mu\text{-}O)_4]$ square [2 x 2] grid complex of the ligand 'poapz' (Scheme 4.1) which had comparable Mn-Mn separations (3.910(1) Å, 3.962(1) Å) and Mn-O-Mn angles (127.9°,129.3°) [59].

Magnetization data as a function of field for **4** at 2 K in the range 0-5 T is shown in Fig. 4.16. The solid line represents the theoretical Brillouin function for S =5/2 system at 2 K (g = 2.01). This is consistent with the proposed ground state.

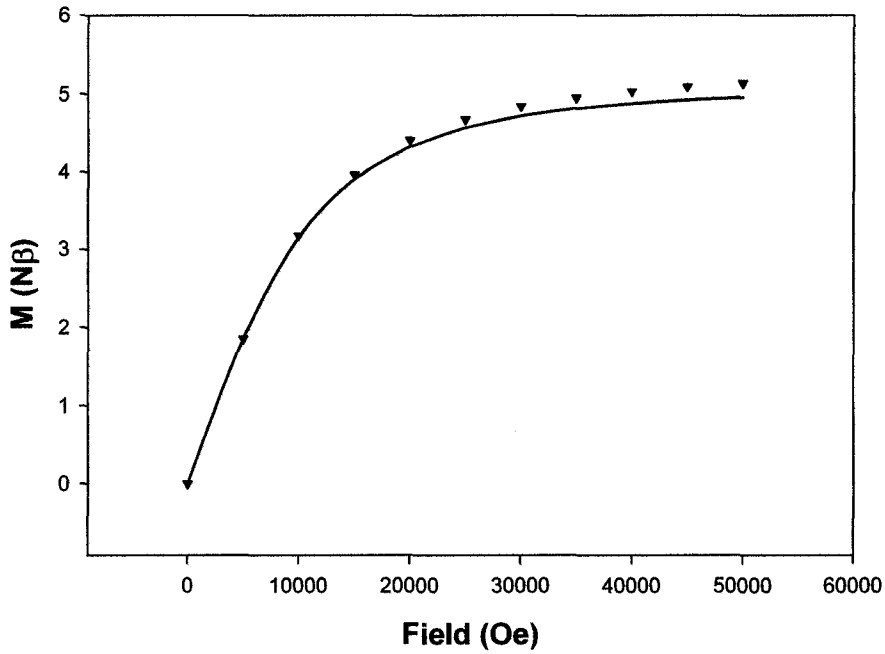

Fig. 4.16 Magnetization data (▲) as a function of field (Oe) at 2 K for **4**

4.5 Conclusion

In this chapter three tetranuclear [2 x 2] square grids and one trigonal bipyramidal pentanuclear Mn(II) cluster are reported. In the tetranuclear rectangular copper cluster, two different bridging groups were identified. The hydrazone oxygen bridges along the shorter arms of the complex led to no antiferromagnetic exchange interaction between the Cu(II) centers due to orthogonal connection (90° alternation of the Jahn-Teller axis of the Cu (II) magnetic orbitals). However, the N-N diazine bond along the longer arms of the cluster was the alternative and only pathway for significant exchange between the Cu(II) centers in the tetranuclear cluster which led to antiferromagnetic exchange.

The variable temperature magnetic data were fitted to two different models, a tetranuclear model with two different exchange integrals and also to a simple dimer with one coupling constant. Results were comparable in both the cases. Both the [2 x 2] $Mn(II)_4$ heteroleptic square grids and the pentanuclear cluster showed antiferromagnetic exchange with comparable exchange integrals. This is associated with fairly large hydrazone oxygen bridge angles present in both types of complexes. In the [2 x 2] square grids, there is partial filling of the metal coordination sites. Participant donor anions (e.g. nitrate, triflate), and solvent molecules (e.g. water) occupied the extra coordination sites. But in the pentanuclear cluster, the coordination requirements of all the metal sites were completely fulfilled by the ligand donor sites.

CHAPTER 5

'Ferromagnetic' octanuclear pinwheel clusters - structures and magnetism

5.1 Introduction

The symmetric tritopic hydrazone ligand 2poap and its various analogues (Scheme 5.1) self-assemble in high yield to form homoleptic [3 x 3] $M(II)_9$ grids [65-66, 107-111]. The preference for the nonanuclear grid from self-assembly is fairly straight- forward when transition metals such as Mn(II) or Zn(II) are used and the grid is obtainable in all conditions. The grid molecules contain six ligands to create a common $[M_9(\mu\text{-}O)_{12}]$ core with hydrazone oxygen bridging between all the metal centers. The dimensions of the central core are very similar (~4 Å) in all the [3 x 3] grids. Antiferromagnetic exchange coupling was observed for nonanuclear $Mn(II)_9$ grids. However, in the case of Cu(II), the situation is not simple.

When copper(II) reacts with 2poap and other related ligands (Scheme 5.1), trinuclear, octanuclear or [3 x 3] nonanuclear complexes can result. The variety in structural isomers becomes a function of the reaction conditions and the anion used. Strongly binding counter anions such as acetates, lead to linear trinuclear complexes as the principal products. In the trinuclear compounds, the coordination spheres of the metal cations are partially filled by donor anions or solvent molecules. The use of

comparatively less strongly binding anions leads to homoleptic [3 x 3] $Cu(II)_9$ grids as the usual outcome [68, 108]. In the $Cu(II)_9$ grids, all the Cu(II) ions are bridged by hydrazone oxygen and all $Cu(II)_9$ grids show ferromagnetism. However, under mild reaction conditions, such as in weakly polar solvents, and at ambient temperature, octanuclear Cu_8 pinwheels are the major product [67-68, 132 (a)].

In terms of the fulfillment of the coordination vacancies of the metal ions during the self-assembly, two situations prevail in these two classes of clusters. In the case of homoleptic [3 x 3] grid complexes, all the coordination vacancies of the metal ions are filled by the ligand donor atoms only. So, there is then an exact match between the coordination requirements of the metal ions and the available coordination pockets in the ligand.

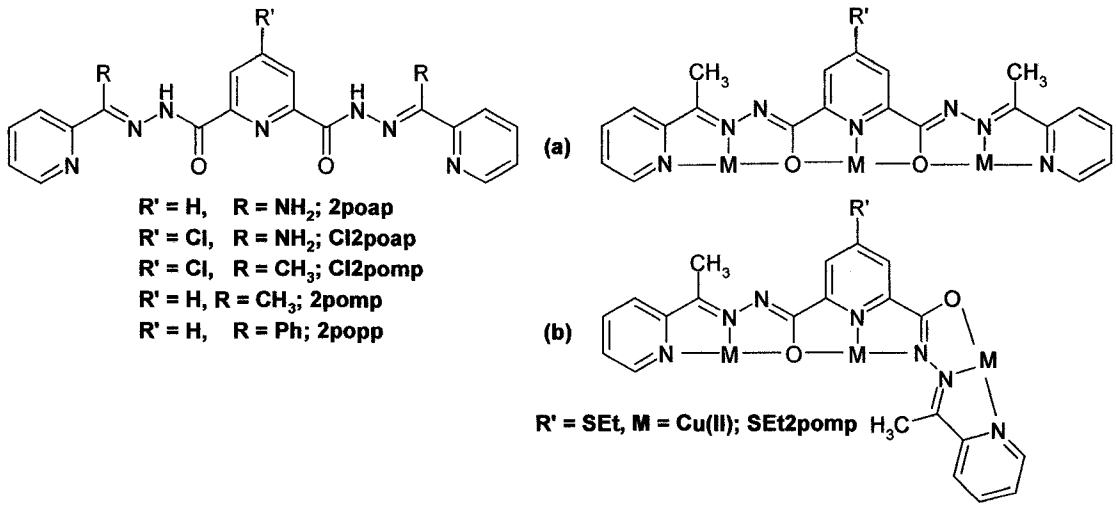

Scheme 5.1 Tritopic hydrazone ligands. (a,b) Binding modes of 2pomp (R′ = H).

In cases where there are not enough donor sites in the ligand, the extra coordination sites are filled by the coordinating anions or donor solvents. Such a scenario is observed in the case of the octanuclear pinwheel complexes. A pinwheel complex is comprised of a total of four ligands. The ligands intersect to make a tetranuclear core of the complex while the external pockets of each ligand bind a peripheral copper, creating the pinwheel (Fig. 5.1). The six coordinate Cu(II) centers within the central core are hydrazone oxygen bridged in all pinwheel complexes. The bridging connection of the peripheral coppers to the inner core depends on the binding mode of the participating ligands.

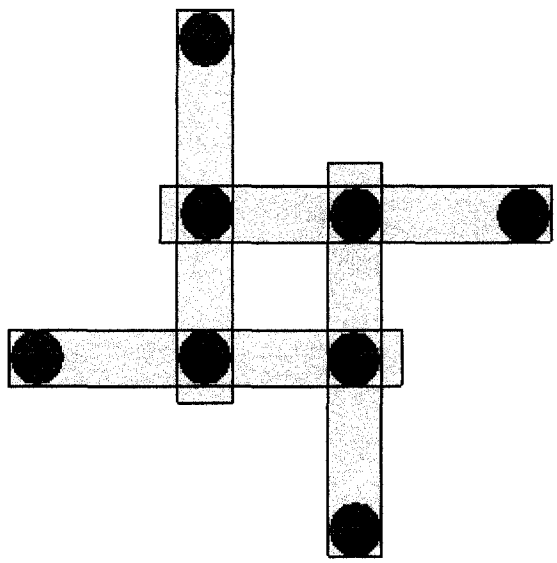

Fig. 5.1 A representation of a pinwheel

Two different binding modes adopted by the Schiff base type ligand SEt2pomp were observed and are presented in Scheme 5.1. Mode (a) in which the ligand binds one copper(II) ion in each coordination pocket in a linear fashion has been exhibited

by all the copper pinwheel clusters so far reported [67-68, 132] and the peripheral copper(II) ions are bridged by hydrazone oxygen atoms to the inner core. In mode (b), the free end of each ligand rotates around the C-C single bond adjacent to the central pyridine ring to accommodate the external copper. This rotation results in the N-N diazine bond to bridge the peripheral copper to the core [132(a)]. The central copper(II) ions are bridged by hydrazone oxygen to make the $[Cu_4(\mu\text{-}O)_4]$ core as in other pinwheel complexes, where they are six coordinate. The peripheral copper(II) ions are square pyramidal. The [3 x 3] $Cu(II)_9$ grids and octanuclear pinwheel $Cu(II)_8$ clusters show ferromagnetic exchange with S = 7/2 and S = 8/2 ground states respectively.

In several cases it was possible to convert an octanuclear $Cu(II)_8$ pinwheel complex to a nonanuclear [3 x 3] $Cu(II)_9$ grid by simply heating the pinwheel complex in strongly polar solvents. This suggests that the pinwheel complexes are the kinetic products of the reactions of 2poap type ligands with Cu(II) while the grids are the thermodynamic products. However, this conversion was only possible with pinwheel complexes made from amidrazone based ligands (e. g. Scheme 5.1 R = NH_2). In general amidrazone are monoacid bases which form salts with inorganic acids e. g. hydrochlorides [132 (b)].

The intramolecular ferromagnetism observed in both the pinwheels and [3 x 3] grids, is attributed to the strictly orthogonal (alternating long-short connections

The intramolecular ferromagnetism observed in both the pinwheels and [3 x 3] grids, is attributed to the strictly orthogonal (alternating long-short connections between copper(II) orbitals) magnetic connectivity between the Cu(II) centers both within and outside the central core. Self-assembled octanuclear copper clusters are not rare but polynuclear assemblies carrying ferromagnetic molecular subunits are not common.

An octanuclear copper(II) paddle wheel $[Cu_8(dpd\text{-}2H)_4(\mu_2\text{-}MeCOO)_4\{2\text{-}(OH)C_5H_4N\}_4](ClO_4)(H_2O)_4$ [133] was reported, synthesized from the ligand dipyridyl diol (dpd) ((a) Scheme 5.2). The cluster contains an inner core of four copper(II) centers, which have hydroxyl bridging. This central core is connected to four other external copper centers in the periphery through simultaneous hydroxyl and acetate oxygen bridges. The complex has a close structural similarity overall with the octanuclear copper pinwheels. However, it exhibited intramolecular antiferromagnetic exchange due to the non-orthogonal (equatorial-equatorial) connectivity between the copper magnetic orbitals [133]. A POVRAY© representation of the complex is provided in Fig. 5.2 (b).

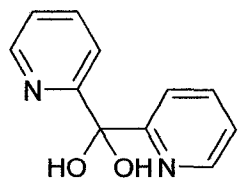

(a) dpd

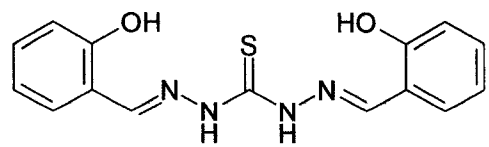

(b)

Scheme 5.2

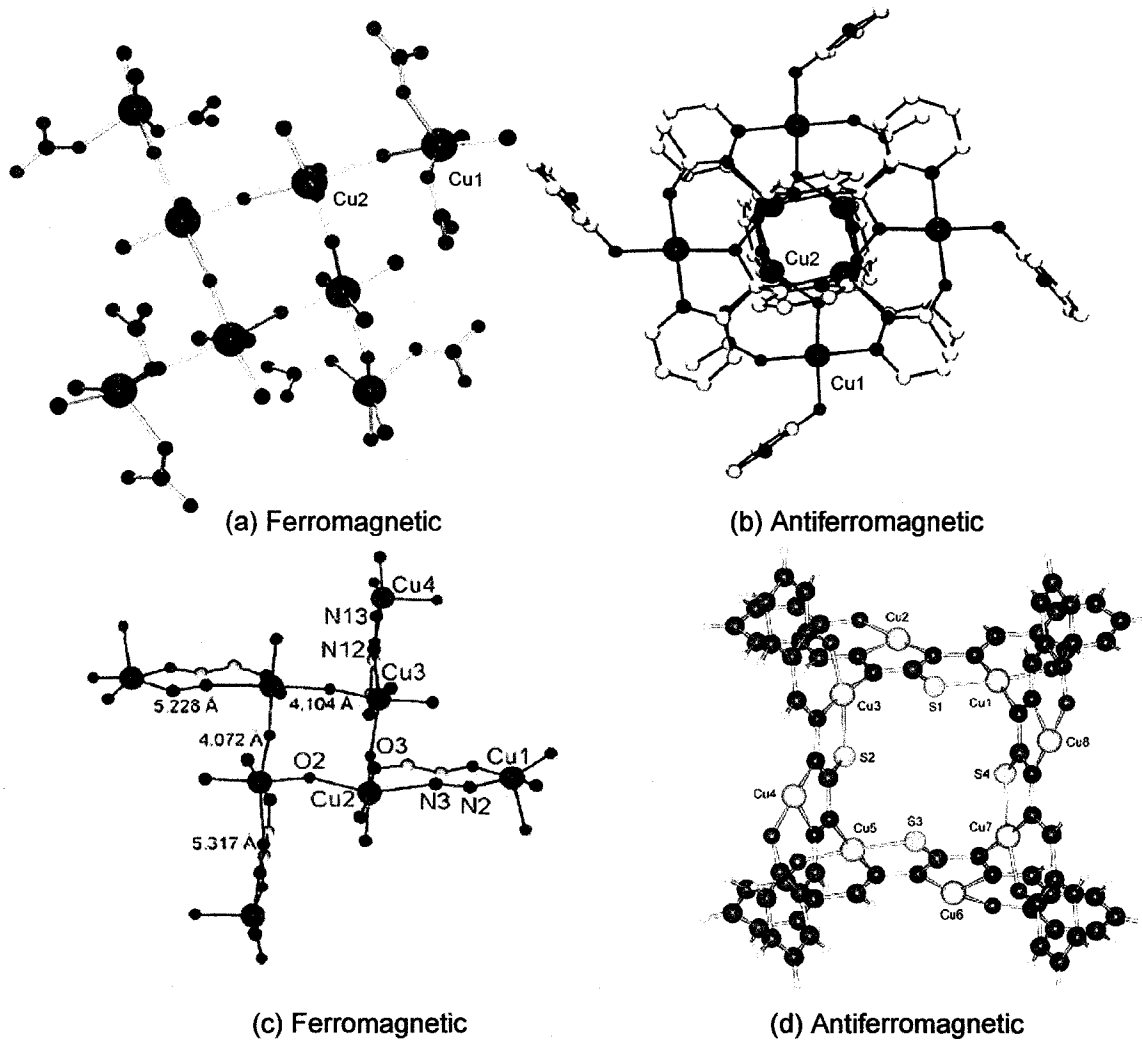

Fig. 5.2 (a) Octanuclear regular pinwheel showing all hydrazone oxygen bridging; (b) Octanuclear paddle wheel complex [133]; (c) Octanuclear pinwheel complex with N-N peripheral bonding to the core; (Magenta = Cu, Blue = N, White = C, Red = O) (d) Octanuclear cluster with N-N diazine and thiolato bridging (Cyan = Cu, Blue = N, Dark grey = C, Yellow = S, Red = O).

Another azine-bridged octanuclear complex $[Cu_8L_4(DMF)_8(H_2O)]$ $(DMF)_{3.5}$ $(H_2O)_3$ [134], which is also structurally close to octanuclear pinwheel complexes, was synthesized from the reaction of copper(II) acetate and a ditopic single-stranded thiocarbohydrazone ligand H_4L (L = 1,5-bis(2-hydroxybenzaldehyde) thiocarbohydrazone ((b) Scheme 5.2). The cluster contains four fully deprotonated ligands binding to eight Cu(II) ions to create a tetranuclear core, which is bonded to four additional copper(II) centers similar to pinwheels, except the fact the peripheral copper(II) ions are bonded directly to the inner core ((d) Fig. 5.2). The copper centers in the inner core are four coordinate square planar and bridged by NC=S functional groups while the peripheral coppers are trigonal bipyramidal or square pyramidal. Solvent molecules such as DMF take up the extra coordination sites. The peripheral copper(II) centers are bridged by N-N bonds to the inner $Cu(II)_4$ unit. Due to fairly large Cu-N-N-Cu torsional angles (176°), strong antiferromagnetic coupling (J = -128 cm^{-1}) was observed in the cluster.

Fig. 5.2 (a) and (c) shows the skeletal view of a regular pinwheel complex and a clear view of the boding between peripheral copper centers and the $Cu(II)_4$ core. The octanuclear copper pinwheel clusters are unique in the sense that they exhibit ferromagnetic exchange coupling as opposed to the antiferromagetism normally seen in polymetallic copper clusters. Additional interest in the pinwheel systems lies in the fact that they are heteroleptic clusters, with labile ligands at their external coordination sites. These can be replaced with suitable co-ligands or linker groups, which could

bridge the individual ferromagnetic subunits, and form a larger magnetic network. Earlier attempts have had some success with the octanuclear cluster $[Cu_8(Cl2pomp\text{-}2H)_4(N(CN)_2)_8](H_2O)_9(CH_3CN)_2$ [132 (a)] using dicyanamide as the linker group. The individual pinwheel clusters were not directly bonded, but the extended structure in the unit cell revealed several short contacts (3.372 Å) between the ligand functional group (Cl atom of the adjacent ligand) and the anion (dicyanamide). These short contacts were considered to be responsible for a staggered stacking of the pinwheels, and magnetic data suggested weak long range order.

This chapter will present the structures and magnetic properties of some ferromagnetic copper(II) pinwheels. All of the complexes were prepared from the Schiff based ligand 2pomp (Scheme 5.1). Structural characterization of one pinwheel complex revealed a different bridging motif than expected. The copper(II) centers in the tetranuclear core had hydrazone oxygen bridging, while four peripheral copper(II) centers were N-N diazine bridged to the central core. This difference in bridging leads to interesting magnetic consequences. One of the pinwheel clusters also shows long range structural ordering by direct covalent bonding between pinwheel subunits. The ordering originates from the covalent interactions between peripheral copper centers through a single bromide atom bridge.

5.2 Experimental

5.2.1 Materials

Commercially available solvents and chemicals were used without further purification.

5.2.2 Characterization

Analysis, spectroscopic and physical measurements were carried out according to the procedure described in Chapter 2.

5.2.3 Synthesis of the ligand

The synthesis of the ligand was done according to the procedure describe in Chapter 2.

5.2.4 Synthesis of complexes

$[Cu_8(C_{21}H_{17}N_7O_2)_4(H_2O)_8](ClO_4)_8$ (1)

2pomp (0.24 g, 0.50 mmol) was added to a solution of $Cu(ClO_4)_2.6H_2O$ (0.60 g, 1.6 mmol) dissolved in a methanol/water mixture (10 mL/5 mL) with stirring. A deep blue green solution was formed, which was filtered after several hours of stirring and the final solution was allowed to stand at RT. Dark green crystals suitable for structural determination were obtained after two weeks (Yield 70%). IR (Nujol, cm^{-1}): 3600, 3450, (ν OH), 1620 (ν C=O), 1602, 1571 (ν C=N), 1077 (ν ClO_4^-). UV/vis (λ_{max}, nm, water): 683. Anal. Calc. (%) for $[(C_{21}H_{17}N_7O_2)_4Cu_8\ (H_2O)_8]\ (ClO_4)_8$; C, 33.11; H, 3.02; N, 12.88. Found (%); C, 33.23; H, 2.70; N, 13.03.

$[Cu_8(C_{21}H_{17}N_7O_2)_4](NO_3)_8 \cdot 12H_2O$ (2)

2pomp (0.200 g, 0.5 mmol) was added to a solution of $Cu(NO_3)_2.3H_2O$ (0.500 g, 2.0 mmol) dissolved in methanol/water (2:1 v/v) mixture with stirring. A deep green solution was formed which was filtered after several hours and the final solution was allowed to stand at room temperature. A dark green precipitate formed, which was collected and recrystallized from a methanol/water/acetonitrile (1:1:1 v/v) solvent mixture. Dark green crystals were isolated via slow evaporation of the solvent. (Yield 76%). IR (Nujol, cm^{-1}): 3390 (ν OH), 1627 (ν C=O), 1600, 1515 (ν C=N), 1280, 1025 (ν NO_3^-). Anal. Calc. (%) for $[(C_{21}H_{17}N_7O_2)_4Cu_8](NO_3)_8\ (H_2O)_{12}$; C, 35.79; H, 3.29; N, 17.89. Found (%); C, 35.75; H, 3.10; N, 17.73.

$[Cu_8(C_{21}H_{17}N_7O_2)_4](CH_3COO)_8 \cdot 30H_2O$ (3)

2pomp (0.24 g, 0.50 mmol) was added to a solution of $Cu(CH_3COO)_2.H_2O$ (0.33 g, 1.65 mmol) dissolved in methanol/water mixture (10 mL/5 mL) with stirring. A deep green brown solution was formed which was filtered after several hours of stirring and the final solution was allowed to stand at room temperature. Dark green brown crystals were collected after a couple of weeks. (Yield 66%). IR (Nujol, cm^{-1}): 3378, 1623, (ν C=O), 1596 (ν C=N). Anal. Calc. (%) for $[(C_{21}H_{17}N_7O_2)_4\ Cu_8]$ $(CH_3COO)_8(H_2O)_{30}$; C, 38.51; H, 4.91; N, 12.57. Found (%); C, 38.77; H, 3.40; N, 12.22.

$[Cu_8(C_{21}H_{17}N_7O_2)_4Br_6](CuBr_4)\cdot 11H_2O$ (4)

2pomp (0.10 g, 0.25 mmol) was added to a methanol/water (10 mL/10 mL) solution of $CuBr_2$ (0.20 g, 0.9 mmol) with stirring to form a bluish green solution. The solution was warmed slightly with addition of 5 mL of acetonitrile before it was kept for crystallization. Dark greenish brown crystals suitable for structural analysis were obtained after several weeks (Yield 30%). IR (Powder, cm^{-1}): 1623 (ν C=O). Anal. Calc. (%) for $[(C_{21}H_{17}N_7O_2)_4Cu_8Br_6](CuBr_4)(H_2O)_{11}$; C, 31.85; H, 2.86; N, 12.38. Found (%); C, 31.91; H, 2.81; N, 12.32.

5.3 Crystallographic data collection and refinement of structures

Dark green prismatic crystals of **1** and **4** with approximate dimensions 0.53 x 0.45 x 0.40 mm and 0.38 x 0.34 x 0.29 mm respectively were mounted on a glass fiber. All measurements were done on a Bruker P4/CCD system with graphite monochromated Mo-Kα radiation and a rotating anode generator. Hydrogen atoms were introduced in calculated or difference map positions with isotropic thermal parameters set twenty percent greater than those of their bonding partners at the time of their inclusion. They were not refined. Both the data sets were collected at a temperature of 193 K. The full hemisphere of data was collected to a maximum 2θ value of 52.8°. The Siemens area detector absorption routine (SADABS) was used with maximum and minimum effective transmissions of 0.5967 and 0.5158 for **1** and 0.2715 and 0.2059 for **4**.

The data were corrected for Lorentz and polarization effects. Both the structures were solved by direct methods [99] and expanded using Fourier techniques [100]. Some non-hydrogen atoms (O(13), O(14), O(15), O(16), O(17), O(18) and O(19)) were refined anisotropically in the case of **1** while the rest were refined isotropically. Non-hydrogen atoms for **4** were refined anisotropically. The maximum and minimum peaks on the final difference Fourier map corresponded to 1.20 and -1.08 e $^-$/Å^3 for **1** and 1.12 and -1.57 e$^-$/Å^3 for **4** respectively. Neutral atom scattering factors were taken from the usual source of Cromer and Waber [101]. Anomalous dispersion effects were included in F_{calc} [102]. The values for Δf' and Δf" were those of Creagh and McAuley [103]. The values for the mass attenuation coefficients are those of Creagh and Hubbell [104]. All calculations were performed using the teXsan [105 (a)] crystallographic software package of Molecular Structure Corporation except for refinement, which was performed using SHELXL-97 [99].

5.4 Result and Discussion

5.4.1 Structural details

$[Cu_8(C_{21}H_{17}N_7O_2)_4(H_2O)_8](ClO_4)_8$ (1)

The structure of the octanuclear cation **1** is shown in Fig. 5.3. A summary of the crystallographic data is provided in Table 5.1 and important bond distances and bond angles are given in Table 5.2. The eight Cu(II) centers arrange themselves in a pinwheel fashion. The overall cationic structure in **1** is very similar to the pinwheel framework found in $[Cu_8(Set2pomp\text{-}2H)_8(H_2O)_8](PF_6)_8(CH_3OH)_7(H_2O)_2(CH_3CN)_2$

[132 (a)]. The cluster contains a tetranuclear $[Cu(II)_4(\mu\text{-}O)_4]$ core with four other Cu(II) ions arranged in the outer coordination pockets of each ligand of the pinwheel. Each ligand coordinates to two Cu(II) atoms by using two consecutive pockets and these meet in the core. This allows the remaining ligand pocket to act as an external coordination site and radiate outwards and hence create the pinwheel.

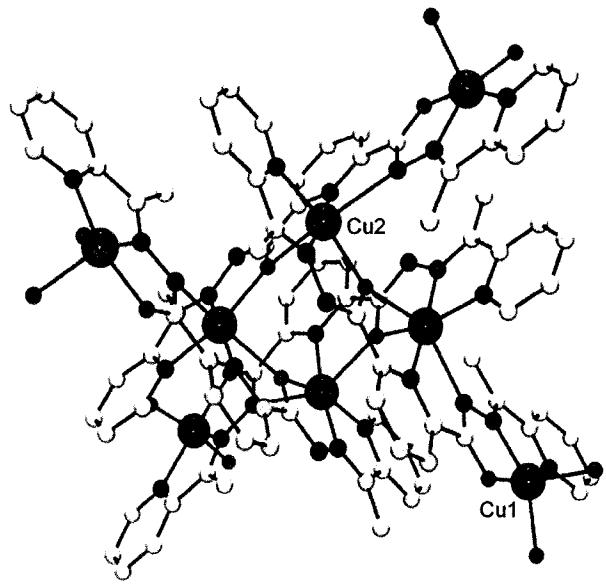

Fig. 5.3 POVRAY© image representation of **1** showing the cationic framework (Green = Cu, Blue = N, Red = O, and Grey = C).

The external coordination sites at the outer ends of each ligand are twisted by 180° and bend to hold the peripheral Cu(II) ions through μ_2-N_2 (diazine) bridges, rather than hydrazone oxygen bridges as observed in the core. Two water molecules are bound to each of the peripheral copper(II) ions. In other analogous pinwheels obtained from ligands Cl2pomp and Set2pomp (Scheme 5.1), nitrate anions and water

molecules respectively occupied similar coordination positions on the external Cu(II) sites [68, 132]. Overall the cluster has a 4-fold symmetry. The copper ions in the inner core are six coordinate, while those in the outer pockets are five coordinate and square pyramidal ($\tau = 0.1$). The connectivity within the inner core involves alternating short (2.034(3) Å, equatorial) and long (2.347(3) Å, axial) Cu-O bonds which leads to completely orthogonal connections between all four of the six coordinate metal ions in the core. The presence of eight perchlorate anions signifies that all the ligands are doubly deprotonated. The long C-O distances both in the core and in the arms (1.289(6) Å in core and 1.270(6) Å in arms) indicate single C-O bond character and a formal charge on the bridging oxygen atom. The average bond distances around each of the copper centers in the core range from 1.928(3)-2.443(4) Å. This is consistent with distances 1.933-2.340 Å seen for other pinwheel clusters with similar ligands (e.g. Cl2pompH_2) [68]. The Cu-Cu distance within the square core is 4.146(2) Å which is much shorter than the core-peripheral copper distance of 5.230(2) Å. This is again comparable with similar ranges of distances 4.072-4.104 Å within the core and 5.288-5.317 Å outside the core in the pinwheel cluster obtained from Set2pomp [132 (a)] and longer than the corresponding distances in the pinwheel cluster $[Cu_8(Cl2pomp\text{-}2H)(NO_3)_8](H_2O)_{15}$ (4.014 Å inside the core and 4.075 Å outside the core respectively) [68].

The inner core is connected to the peripheral copper(II) ions by Cu(2) through a N-N diazine bond. So far, all the pinwheel complexes have had hydrazone oxygen

bridging both in the inner core and between the core and the peripheral copper centers [67-68]. This structural motif has been seen before in a pinwheel complex with ligand Set2pomp [132 (a)]. A simplified picture of the cation in **1** showing only the immediate donor atoms around each copper(II) center is given in Fig. 5.4. Each copper ion in the core has a distorted, axially elongated octahedral geometry, typical for six coordinate Cu(II) ions. Four Cu(2) short contacts to N(4_7), N(6), N(7) and O(2) define the d_{x2-y2} orbital plane, with long axial contacts to O(2_7) and N(3_7) (Jahn-Teller axes). Cu(2_8) has long axial contacts to O(2) and N(3) with short contacts to N(4), N(6_8), N(7_8) and O(2_8) defining the location of the d_{x2-y2} orbital. The peripheral Cu(1) is square pyramidal ($\tau = 0.09$) with a long axial contact to O(3) which is the Jahn-Teller axis. Short contacts to N(1), N(2), O(1) and O(4) define the d_{x2-y2} orbital plane for Cu(1).

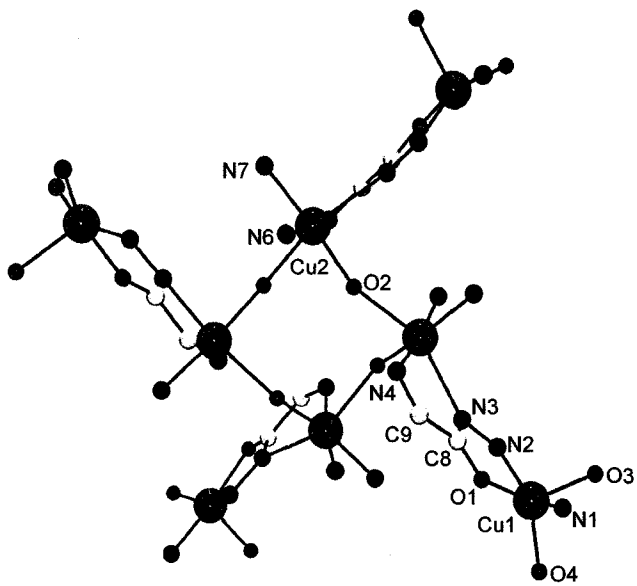

Fig. 5.4 Core structure in **1** (POVRAY© image; Green = Cu, Blue = N, Red = O, and Grey = C).

Table 5.1 Summary of crystallographic data for $[Cu_8(C_{21}H_{17}N_7O_2)_4(H_2O)_8](ClO_4)_8$ **(1)**

Empirical Formula	$C_{84}H_{120}N_{28}O_{66}Cl_8Cu_8$
Formula Weight	3370.01
Crystal Color, Habit	Green, prism
Crystal Dimensions	0.53 x 0.45 x 0.40 mm
Crystal System	Tetragonal
Lattice Type	I-centered
Lattice Parameters	a = 20.7790(4) Å c = 32.561(1) Å V = 14058.8(6)Å^3
Space Group	$I4_1/a$ (#88)
Z value	4
D_{calc}	1.592 g/cm^3
F_{000}	6864.00
μ (MoKα)	14.39 cm^{-1}
Temp (K)	193 ± 1
R1	0.061
wR2	0.203

Table 5.2 Selected Bond distances (Å) and Angles (°) for **$[Cu_8(C_{21}H_{17}N_7O_2)_4(H_2O)_8](ClO_4)_8$ (1)**

Cu1	N2	1.927(4)	Cu2	O2	2.034(3)
Cu1	O1	1.971(3)	Cu2	N7	2.045(4)
Cu1	O4	1.985(4)	Cu2	O2_7	2.347(3)
Cu1	N1	2.004(4)	Cu2	N3	2.443(4)
Cu1	O3	2.135(5)	Cu2-O2-Cu_2		142.17(14)
Cu2	N6	1.928(3)	Cu1-N2-N3-Cu2		154.6(3)
Cu2	N4	2.002(3)	Cu1	Cu2_8	5.230
			Cu2	Cu2_7	4.146

The alternating long (Cu(2_8)-N(3) 2.443(4) Å) and short (Cu(1)-N(2) 1.927(4) Å) bonding indicates that the contacts from each corner copper of the square core and the external coppers to the immediate diazine N are axial-equatorial. This again leads to a 'd' orbital orthogonality between the core and the peripheral copper centers. The Cu-N-N-Cu torsional angle is 154.6°.

The structure of **4** consists of a 2D network of octanuclear pinwheel clusters, where $Cu(II)_8$ subunits are linked together by bromide bridges between the peripheral Cu(2) centers. A crystallographic summary of the cluster is provided in Table 5.3 and bond distances and bond angles are listed in Table 5.4.

The individual pinwheel contains a similar $[Cu_4(\mu\text{-}O)_4]$ core as in **1** and in other pinwheel clusters [65-68, 110-111, 132]. A POVRAY© representation of an individual pinwheel in **4** is provided in Fig. 5.5. The copper(II) ions within the core are six coordinate and have distorted octahedral geometry. The adjacent copper centers are bridged by hydrazone oxygen as before with Cu-O bond distances ranging from 2.059(6) Å to 2.297(6) Å. Cu-Cu distances within the core are around 4.126 Å and they are comparable to those in **1**. A similar tetranuclear core can also be found in other tetranuclear $Cu(II)_4$ square complexes derived from the ditopic hydrazone ligand 'poap' and its various analogues (Scheme 4.1; Chapter 4) [58].

Four Cu(1) short contacts to N(1), N(2), N(4_5) and O(1) define the d_{x2-y2} orbital plane, with long axial contacts to Cu(1)-O(1_5) and Cu(1)-N(5_5) (Jahn-Teller axes). The Cu-O-Cu bond angles within the core are quite large (142.5(3)°) and comparable to the angles in **1**. But much like in **1**, and in all other oxygen bridged copper pinwheel complexes, the oxygen bridging connections alternate short and long (2.059(6) Å and 2.297(6) Å), and thus they are strictly orbitally orthogonal.

The peripheral Cu(II) centers have square pyramidal geometries ($\tau = 0.06$) and again they are bonded to the projected arms of each ligand of the pinwheel as in **1**. Short bonds from the external Cu(2) to N(6), N(7), O(2) and Br(2) defines the d_{x2-y2} magnetic orbital plane for Cu(2). However, two of the coordination sites in each external copper are occupied by two bromide ions instead of water molecules as in **1**.

The very long contact Cu(2)-Br(1) (2.6637(12) Å) represents the Jahn-Teller axis for Cu(2). The peripheral copper(II) ions are separated by 5.354 Å from the inner copper ions, similar to peripheral copper distances in the pinwheel cluster with Set2pomp [132 (a)].

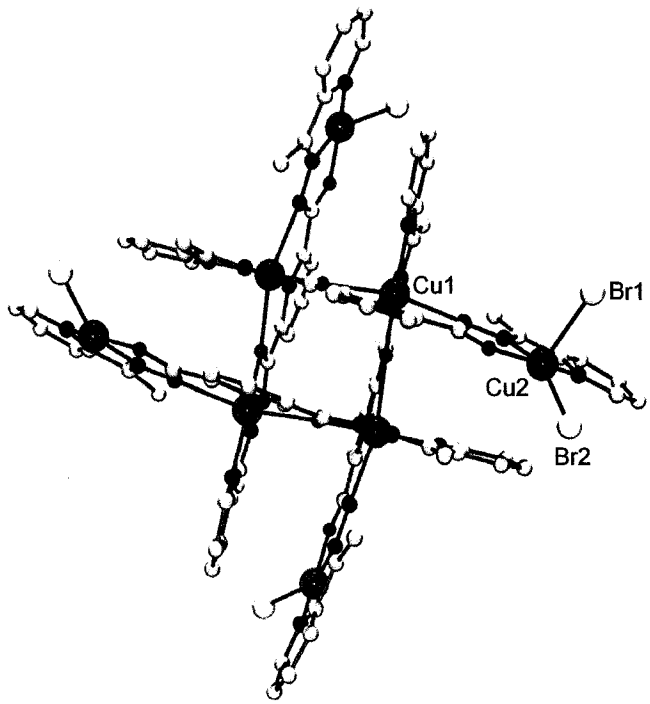

Fig. 5.5 POVRAY© image of a pinwheel subunit in **4**; $CuBr_4^{2-}$ anions are removed for clarity (Magenta = Cu, Blue = N, Red = O, and Grey = C, Yellow = Br)

The peripheral copper ions are connected to the core via *trans*-N-N diazine bridges similar to **1**. The corresponding bond distances of the core copper ion and the peripheral copper ions to the adjacent diazine moiety are Cu(1_7)-N(5) 2.493(6) Å and Cu(2)-N(6) 1.971(7) Å respectively. An abbreviated cationic framework showing only the immediate donor atoms is shown in Fig. 5.6. Once again the connectivity between

the core copper and the peripheral copper ion is long and short and orbitally orthogonal. However, a second non-orthogonal bridging O-C-C-N connection was also identified linking the peripheral copper(II) ions to the tetranuclear core, which is similar to the situation in **1**. The Cu-N-N-Cu torsional angles are larger (172.5°) compared to those in **1**. The $Cu(II)_8$ pinwheel subunits are linked through a bridging bromide ion Br(1) between two peripheral copper(II) centers of two different pinwheel clusters with each pinwheel connected to four others, one at each corner. A fragment of the lattice showing four pinwheel subunits is given in Fig. 5.7 (a).

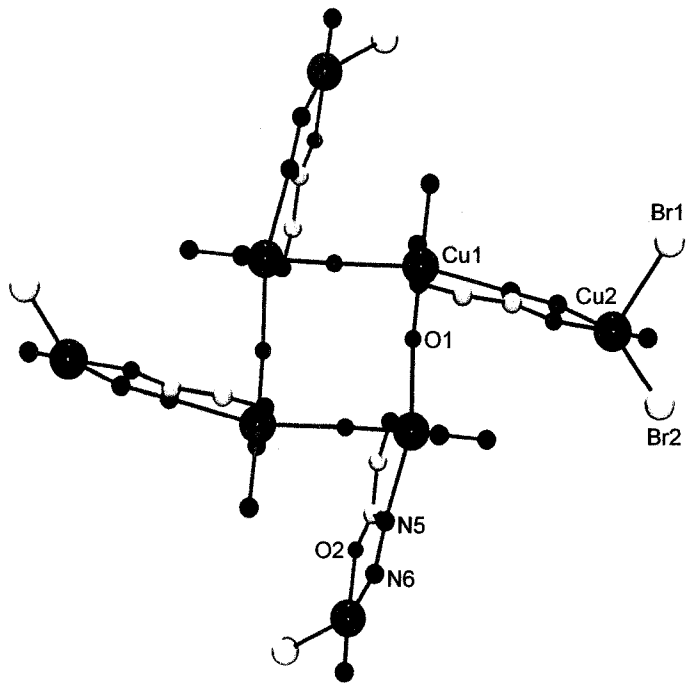

Fig. 5.6 POVRAY© image of core structure in **4** showing only the immediate donor atoms; $CuBr_4^{2-}$ ions are removed for clarity. (Magenta = Cu, Blue = N, Red = O, and Grey = C, Yellow = Br).

Table 5.3 Summary of crystallographic data for **$[(C_{21}H_{17}N_7O_2)_4Cu_8Br_6](CuBr_4)\cdot 11H_2O$ (4)**

Empirical Formula	$C_{84}H_{80}N_{28}O_{14}Cu_9Br_{10}$
Formula Weight	3076.69
Crystal Color, Habit	Green, prism
Crystal Dimensions	0.38 X 0.34 X 0.29 mm
Crystal System	Tetragonal
Lattice Type	Primitive
Lattice Parameters	a = 17.1609(5) Å c = 16.601(1) Å V = 4888.8(3) Å^3
Space Group	P-42$_1$c (#114)
Z value	2
D_{calc}	2.090 g/cm^3
F_{000}	3006.00
μ (MoKα)	60.93 cm^{-1}
Temp (K)	193 ± 1
R1	0.053
wR2	0.164

Table 5.4 Selected Bond distances (Å) and Angles (°) for **$[(C_{21}H_{17}N_7O_2)_4Cu_8Br_6](CuBr_4)\cdot 11H_2O$ (4)**

Cu1	N2	1.925(7)	Cu-Cu (arms)		5.354
Cu1	N4	1.981(6)	Cu-Cu (interwheel)		4.973
Cu1	N1	2.050(7)			
Cu1	O1	2.059(6)	Br3...H20	OH	1.544
Cu1	N5	2.493(6)	Br2...H21	OH	2.590
Cu1	O1	2.297(6)	H2O4...H17	C21	2.431
Cu2	O2	1.968(6)	Br3...H8	C10	3.028
Cu2	N6	1.971(7)			
Cu2	N7	2.017(7)	Br3...H20	OH	150.08
Cu2	Br2	2.3902(14)	Br2...H21	OH	133.05
Cu2	Br1	2.6637(12)	H2O...H17	C21	160.75
Cu2	Br1	2.6637(12)	Br3...H8	C10	130.94
Cu3	Br3	2.3527(16)			
Cu3	Br3	2.3528(16)			
Cu3	Br3	2.3528(16)			
Cu3	Br3	2.3528(15)			

Cu1-O1-Cu1	142.5(3)
Cu2-Br1-Cu2	137.99(7)
Cu1-N5-N6-Cu2	172.5
Cu – Cu (core)	4.126

The bridging Br(1) links the two peripheral Cu(2) ions from two adjacent pinwheels axially with very long bond distances of 2.6637(12) Å and with a Cu(2)-Br(1)-Cu(2) bond angle of 137.99°. This results in a Cu-Cu distance of 4.973 Å between the arms of adjacent pinwheels. Given the axial-axial connection between the bridging bromide and the peripheral copper(II) ions, any antiferromagnetic exchange interaction would be insignificant through this Cu(2)-Br(1)-Cu(2) bond due to orbital orthogonality.

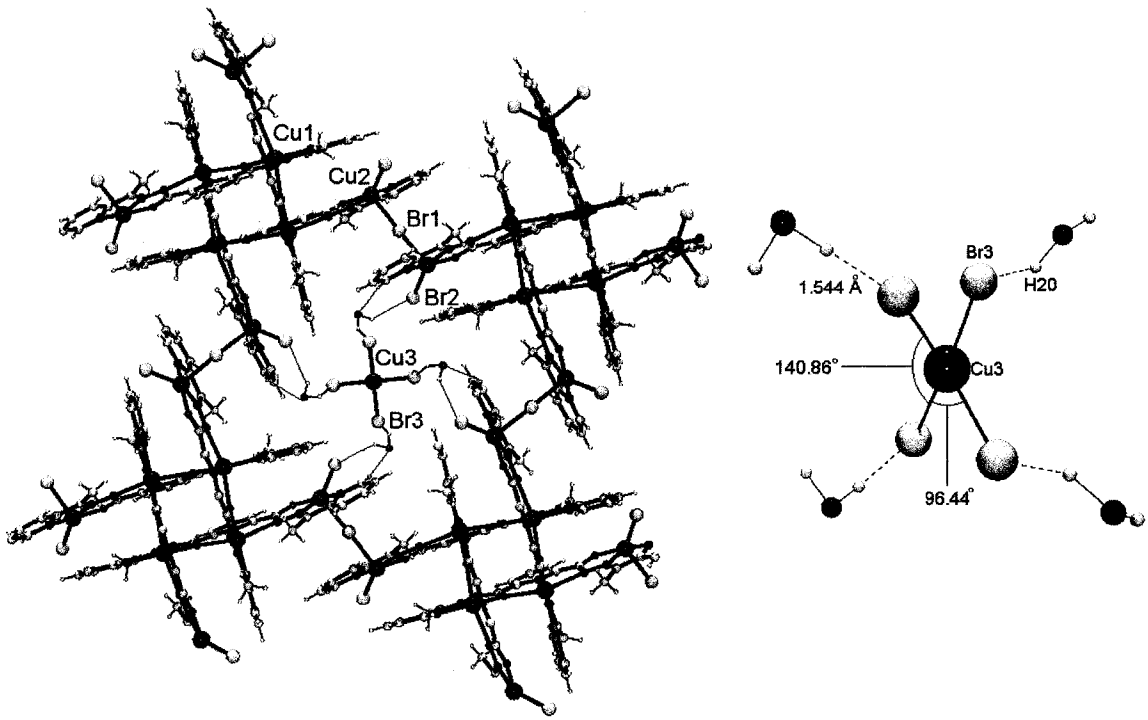

(a) **(b)**

Fig. 5.7 (a) POVRAY© representation of a portion of the extended structure in **4** (b) distorted tetrahedral $CuBr_4^{2-}$ with extremely short hydrogen bonding to water molecules; fine lines represent H-bonds.

Even though the bridging bromide ions do not contribute to the long range magnetic ordering, they nonetheless play a pivotal role in making the intricate arrangement of the pinwheel subunits which leads to a cavity in the 2D lattice with square dimensions (10.1 Å x 10.1 Å, Br-Br). Each of these cavities hosts a highly distorted tetrahedral $CuBr_4^{2-}$ guest anion (Br(3)-Cu(3)-Br(3) 96.44°, 140.86°).

A highlighted picture of the anion is depicted in Fig. 5.7(b), with hydrogen bonding contacts to four surrounding water molecules. An estimate of the Br(3)...H(20)-O(4)H hydrogen bond would be 1.544 Å with a Br-H-OH angle of 150.08°. These weak hydrogen bonds are thought to be responsible for the pronounced distortion of the anion in the cavity, and help to stabilize the 2D network of pinwheels. A similar distortion of a $CuBr_4^{2-}$ anion has been reported, but without the presence of such strong intermolecular interactions [135]. The water molecules are in turn hydrogen bonded to the terminal bromide atoms bonded to the peripheral Cu(2) ions of the pinwheels, with slightly longer bond lengths of 2.590 Å and 133.05 ° Br-H-OH bond angles. Additional H-bonding interactions were also found to exist between the water oxygen atoms and the pyridine hydrogen atoms (H(17)) of each ligand. These H-bonds are fairly long, with O(4)...H(17)-C(21) 2.431 Å bond distances and O-H-C angles of 160.75 °.

The overall arrangement of the pinwheels in the 2D network is such that the $CuBr_4^{2-}$ anion sitting in the cavity of one layer lies directly below the tetranuclear core of a pinwheel in the next layer.

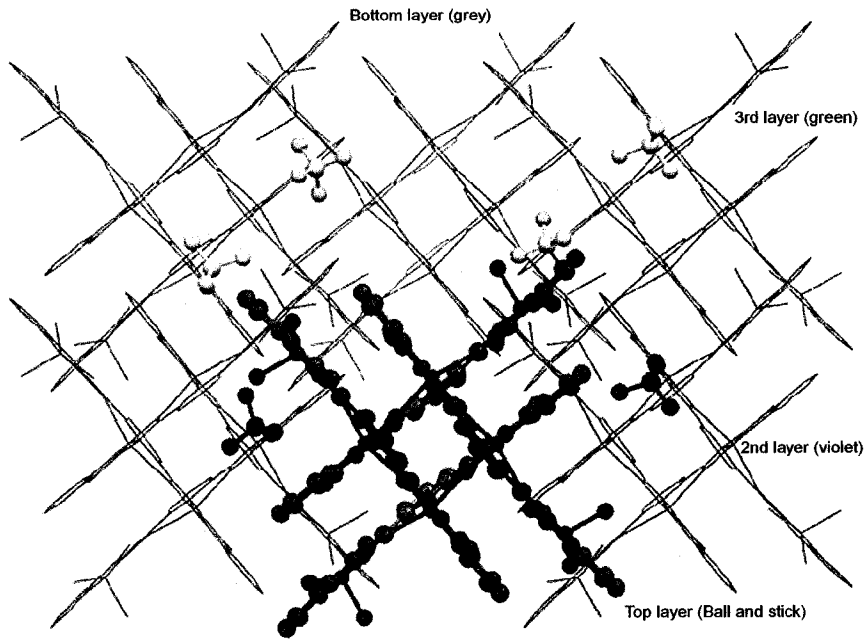

Fig. 5.8 A simplified picture of the extended structure in **4** showing bottom layer (grey), third layer (green), second layer (violet) and top layer in ball-stick style. $CuBr_4^{2-}$ anions between two different layers are shown in pink (between top and second layer), in green and red (between second and third layer).

A simplified pictorial representation of the cluster in **4** is given in Fig. 5.8. Four very weak H-bonds were found to exist between the bromide atom Br(3) and the central pyridine hydrogen of 2pomp (Br(3)...H(8)-C(10) 3.028 Å) with Br-H-CH angle of 130.94 °. This bond length is shorter than the sum of Van der Waals radii of Br and H which is 3.05 Å. The atoms are close enough and are reasonable for a very weak interaction which may or may not contribute to the extended structure. Similar types of

weak interactions have also been observed before in structures of other 2pomp derived clusters, especially where halogen or sulfur atoms were present in the ligand [136].

5.4.2 Magnetism

Single crystal x-ray structures show that the eight Cu(II) centers within the pinwheel arrangement of the complexes of **1** and **4** are coupled by two different types of bridges. The four copper(II) centers in the core are bridged solely by orthogonal arrangements of hydrazone oxygen bridges, while the four peripheral coppers are connected to the inner core primarily by N-N diazine bridges. These are again orthogonal in nature due to short and long bonds of the diazine moiety between core and peripheral copper centers. However, a second comparatively longer non-orthogonal O-C-C-N bridging was also identified between the peripheral copper and the central copper (II) ions of both complexes. A magnetic model appropriate for the pinwheel arrangement of the eight Cu(II) centers with two different J values in the complexes **1** and **4** is shown in Fig. 5.9. The expression for an isotropic exchange Hamiltonian for a pinwheel arrangement with two different J values is given in Equation 5.1. S = ½ for each copper(II) center and S′ = total spin states. J1 is the exchange integral within the core, J2 is the exchange integral outside the core, θ is a temperature correction and Nα is the temperature independent paramagnetism (TIP).

$$H_{ex} = -J_1(\hat{S}_1\cdot\hat{S}_2 + \hat{S}_2\cdot\hat{S}_3 + \hat{S}_3\cdot\hat{S}_4 + \hat{S}_4\cdot\hat{S}_1) - J_2(\hat{S}_1\cdot\hat{S}_5 + \hat{S}_2\cdot\hat{S}_6 + \hat{S}_3\cdot\hat{S}_7 + \hat{S}_4\cdot\hat{S}_8) \qquad [5.1]$$

$$\chi_M' = \frac{N g^2 \beta^2}{3k(T-\theta)} \left(\frac{\sum S'(S'+1)(2S'+1)\exp(-E_n^{(0)}/kT)}{\sum (2S'+1)\exp(-E_n^{(0)}/kT)} \right) \qquad [5.2]$$

$$\chi_M = \chi_M'(1-\rho) + \left(\frac{4S(S+1)N g^2 \beta^2}{3kT} \right) \rho + N\alpha \qquad [5.3]$$

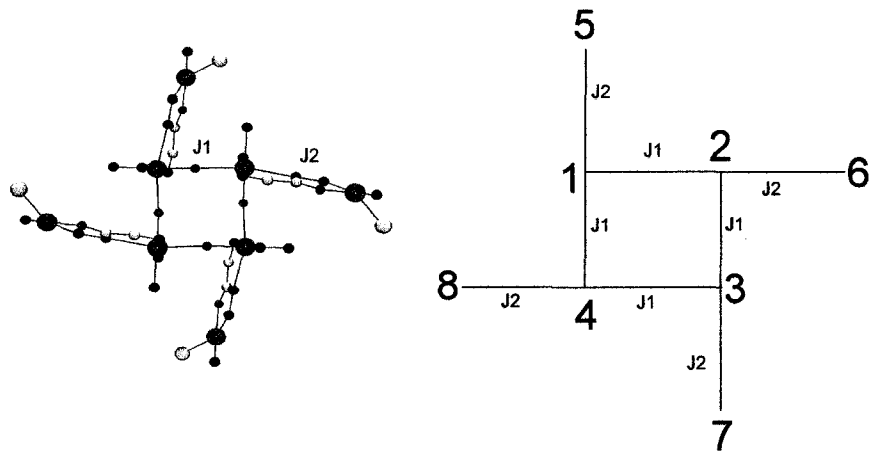

Fig. 5.9 Models for pinwheel complexes with two different J values

To derive an exchange expression for such a complex system with two 'J' values from first principles is a complicated task. The easiest way to deal with this is to calculate the different spin state combinations and their corresponding energies by vector coupling principles originating with Kambe [85] and substitute them directly into the general form of the Van Vleck equation (5.2) to calculate the molar susceptibility at a particular

temperature. This is carried out within the framework of the software package MAGMUN 4.1 [119].

The software MAGMUN 4.1 is limited in that, non-linear regression fits cannot be carried out with two or more J values where the J values are independent variables. However, in cases where the two exchange integral values J1 and J2 are dissimilar, J2 can be expressed as a fraction of J1. For example, if the input values are expressed as J1 = -1, and J2 = -0.25, then J1/J2 = 4. The non-linear regression within the MAGMUN 4.1 software will then give a best fitted value for J which will be a factor of both J1 and J2. A comprehensive description of how the software is used, including an example of an octanuclear pinwheel model, is provided in Chapter 1. Spin models including *spk files are also included in appendix A. The approach discussed above has been used to treat the magnetic exchange problem in **1** and **4**, which have dissimilar bridges (μ-O in the core and μ-NN outside the core).

Complex **1** shows a molar magnetic moment of 5.85 μ_B at 300 K which is significantly higher than the spin only value for eight copper(II) centers (4.9 μ_B per mole). The moment then drops slightly to 5.52 μ_B at around 65 K which is followed by a sharp and steady rise to 8.02 μ_B at 2 K. The overall magnetic profile is typical of a regular octanuclear ferromagnetic pinwheel cluster [67], but the slight downward trend at the beginning until 65 K might indicate that a very weak antiferromagnetic exchange effect is also active between the metal centers. The gradual drop in moment might also be

due to temperature independent paramagnetism (TIP) which is small in magnitude but also causes a slight drop in μ_B/T profile as temperature is lowered. The magnetic data were initially fitted to equations 5.1-5.3 with simplified assumption J1 = J2 = J. The best fit of the data returned $g_{av} = 2.23$, J = 3.99 cm^{-1}, TIP = 540 x 10^{-6} cm^3 mol^{-1}, $\rho = 0.003$, θ = - 0.1 K, 10^2 *R = 3.65 ($R = [\Sigma(\chi_{obs} - \chi_{calcd})^2 / \Sigma\chi_{obs}^2]^{1/2}$). The small negative θ value may account for the initial slight downward slope of the data which is associated with weak intermolecular exchange interactions. These values are consistent with the published results for other pinwheel complexes [67-68, 132]. In order to obtain a best-fit value for a two 'J' model (equation 5.1), a two step procedure was followed.

The magnetic data were fitted to equations 5.1-5.3 considering different ratios 0.8, 1.11, 1.25, 1.43, 1.66, 2.0, 2.5, 3.33, 4.0 for J1/J2 with the aid of MAGMUN 4.1. The temperature independent paramagnetism (TIP) was kept constant at 500 x 10^{-6} cm^3. mol^{-1} in all cases while the other parameters such as J, g, θ and ρ were allowed to vary independently. In the second step, the goodness-of-fit (GOF) parameters R^2 were plotted as a function of the J1/J2 ratio. This way, the best values for J1 and J2 could be obtained independently [137]. The GOF parameter R^2 as a function of J1/J2 is shown in Fig. 5.10.

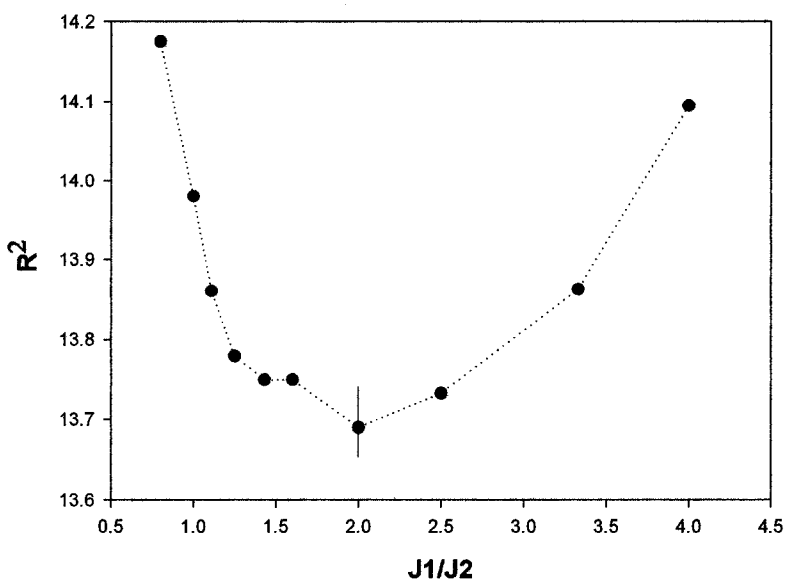

Fig. 5.10 GOF parameter R^2 as a function of the ratio J1/J2 for **1**

The plot of GOF parameter R^2 against the J1/J2 ratio gave a trough like graph with the minimum occurring at J1/J2 ~ 2.0. So, a J1/J2 value of 2.0 was estimated to be the best average ratio. In the second step the data were least-squares-fitted for the ratio of J1/J2 = 2 to equations 5.1-5.3. For R^2 values outside the minimum, the calculated susceptibility data clearly deviated from the experimental data. But for J1/J2 values within the minimum, the curves were statistically indistinguishable. A reasonable fitting gave g = 2.24, TIP = 540 x 10^{-6} cm^3 mol^{-1}, ρ = 0.007, θ = 0.1 K, 10^2 * R = 3.66 (R = $[\Sigma(\chi_{obs} - \chi_{calcd})^2 / \Sigma\chi_{obs}^2]^{1/2}$). The exchange integral J = 4.6 cm^{-1} obtained from the best fitted values, was translated into J1 (center) = 4.6 cm^{-1} and J2 (peripheral) = 2.3 cm^{-1}. The

variable temperature susceptibility and molar magnetic moment curves are shown in Fig. 5.11. The solid line was calculated using the fitted values.

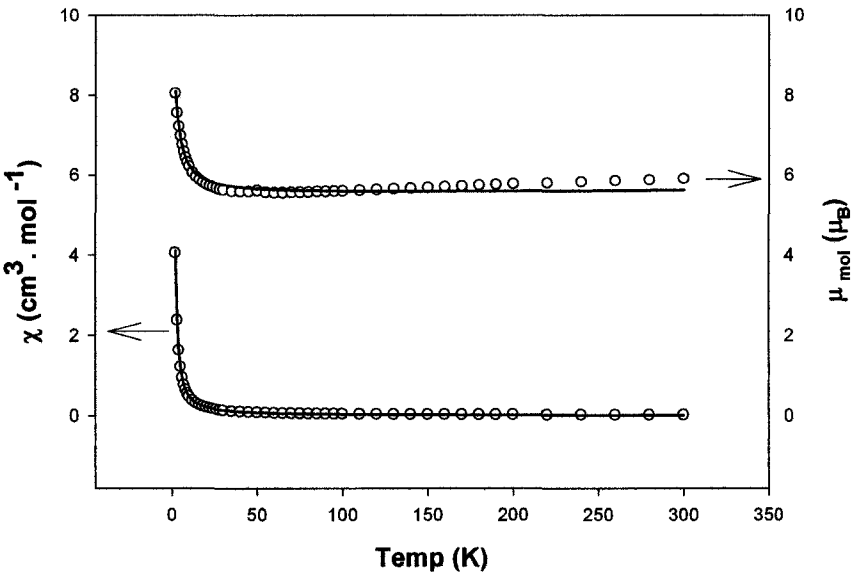

Fig. 5.11 Variable temperature magnetic data for 1

The positive coupling constant for J1 is consistent with the orthogonal nature of the hydrazone oxygen bridging within the inner core. So, any exchange interaction between the metal centers in the core would be ferromagnetic. J2 confirms the ferromagnetic term which was primarily associated with the N-N diazine connection. Large Cu-N-N-Cu torsional angles were shown previously to lead from moderate to strong antiferromagnetic exchange when copper magnetic orbitals are directly connected at the two ends of the diazine bond in dinuclear copper complexes [55, 114]. Close inspection of the structure in **1** revealed short and long connections to the diazine moiety

(Cu(1)-N(2) 1.927 Å, Cu(2)-N(3) 2.443 Å). Therefore, no antiferromagnetic exchange interaction would be expected along this bond. This is consistent with the small ferromagnetic exchange J2 found between the central core and the peripheral copper(II) centers. Fitting of the magnetic data to an alternative model where a $[Cu_4(\mu\text{-}O)_4]$ core was considered as the dominant exchange component with appropriate corrections for four Curie centers, gave an overall inferior fit with g = 2.26, J = 6.20 cm^{-1}, ρ = 0.02, θ = 0.5 K, TIP = 525 x 10^{-6} cm^3. mol^{-1}, 10^2 * R = 4.85 ($R = [\Sigma(\chi_{obs} - \chi_{calcd})^2 / \Sigma\chi_{obs}^2]^{1/2}$).

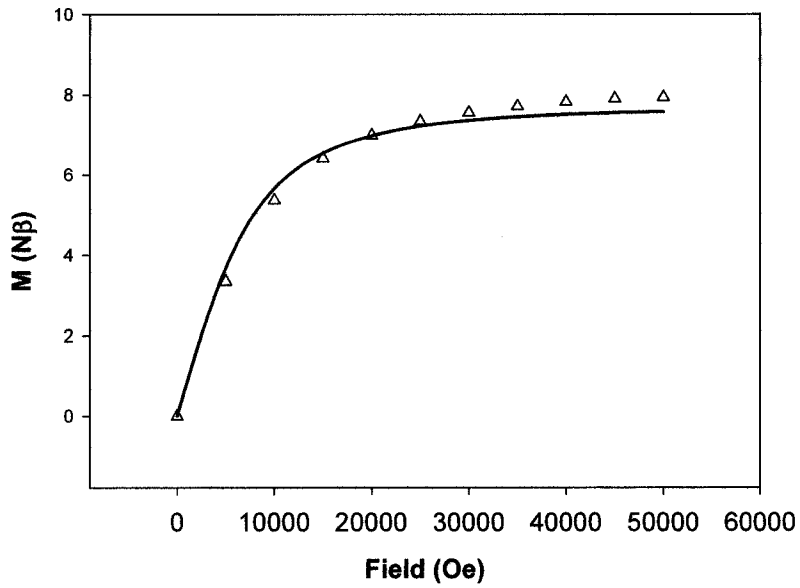

Fig. 5.12 Field dependent magnetization curve for **1**

Field dependent magnetization data were obtained for **1** to ascertain the spin ground state of the complex and the corresponding profile at 2 K is shown in Fig. 5.12. It shows that the complex **1** approaches saturation at 5 T (M = 7.9 Nβ). The calculated values are very close to a species with S = 7/2 rather than 8/2 ground state. This is in

agreement with the presence of a weak antiferromagnetic component. The solid line in Fig. 5.12 was calculated for g = 2.24, S = 3.5 at 2 K.

The variable temperature molar susceptibility and molar magnetic profile for complex **2** are given in Fig. 5.13. This shows a very similar profile to **1**. The structure of **2** is unknown but it is reasonable to assume that it will be somewhat similar to **1** since the ligand is the same. The molar magnetic moment of 5.52 μ_B at 300 K is consistent with eight copper centers. The overall profile again suggests dominant ferromagnetic exchange within the cluster.

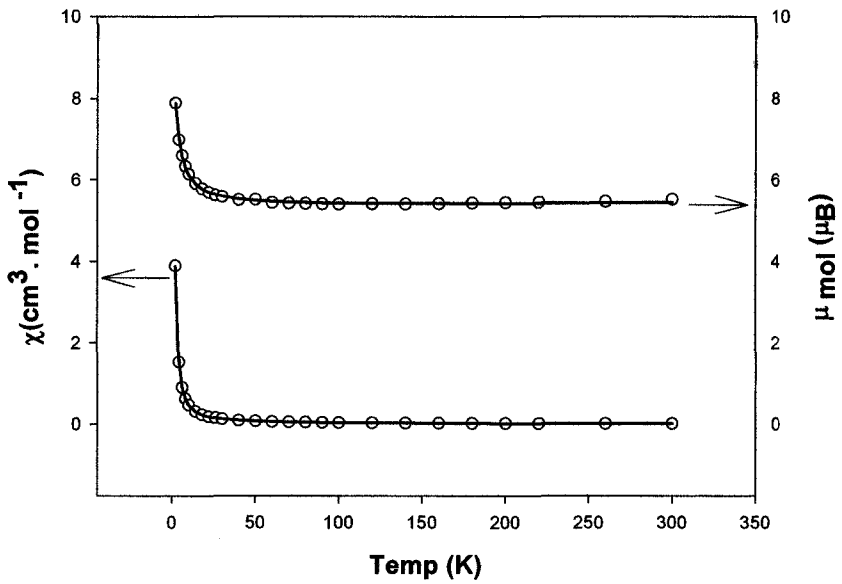

Fig. 5.13 Variable temperature magnetic data for **2**

The magnetic data were again fitted to equations 5.1-5.3 with simplified consideration of J1 = J2 = J. A good data fitting returned g = 2.16, J = 4.67 cm $^{-1}$, TIP =

500 x 10^{-6} cm^3. mol^{-1}, $\rho = 0$, $\theta = -0.2$ K, $10^2 * R = 0.91$ ($R = [\Sigma(\chi_{obs} - \chi_{calcd})^2 / \Sigma\chi_{obs}^2]^{1/2}$). The solid line drawn in Fig. 5.13 was calculated using these parameters. A systematic error analysis in order to distinguish internal and external exchange interactions was not carried out for **2**. However, field dependent magnetization data for **2** at 2 K are shown in Fig. 5.14. It shows that the complex **2** approaches saturation at 5 T (M = 8.4 Nβ). The calculated values are very close to a species with S = 8/2 ground state. The solid line in Fig. 5.14 was calculated for g = 2.16, S = 4 at 2 K.

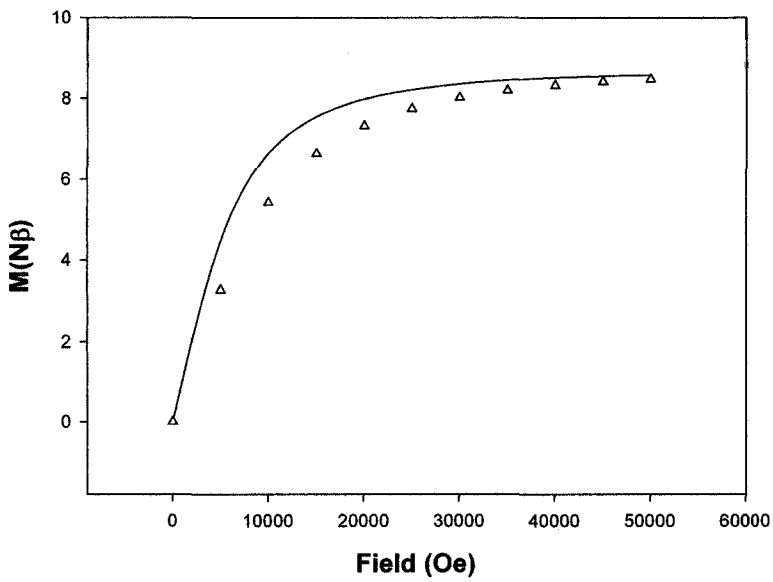

Fig. 5.14 Field dependent magnetization for **2**

The magnetic data were also fitted to the different model which included the $[Cu_4\text{-}(\mu\text{-}O)_4]$ as the dominant exchange component with corrections for the peripheral copper centers by treating them as four additional Curie centers. The best fit gave an

inferior fitting with g = 2.20, J = 7.66 cm^{-1}, ρ = 0.003, θ = 0.5 K, TIP = 515 x 10^{-6} cm^3. mol^{-1}, 10^2*R = 3.94 (R = $[\Sigma(\chi_{obs} - \chi_{calcd})^2 / \Sigma\chi_{obs}^2]^{1/2}$).

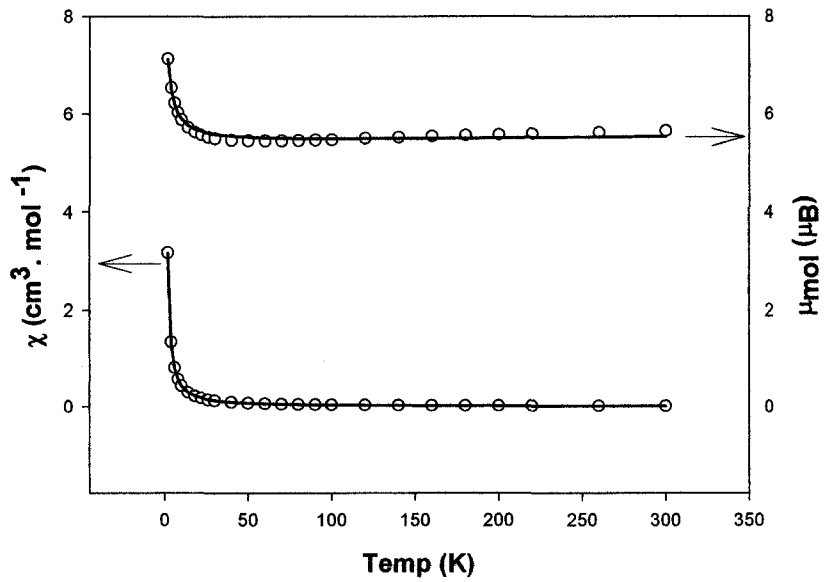

Fig. 5.15 Variable temperature magnetic profile for **3**

The variable temperature molar susceptibility and molar magnetic moment profile for complex **3** are given in Fig. 5.15. The overall magnetic profile is again typical of dominant ferromagnetic exchange similar to **1** and **2**, which might indicate a similar octanuclear pinwheel arrangement is present in the cluster. The magnetic data were fitted to equations 5.1-5.3 again considering a single J value for simplicity. The best fit gave g_{av} = 2.21, J = 2.6 cm^{-1}, TIP = 500 x 10^{-6} cm^3 mol^{-1}, ρ = 0, θ = - 0.2 K, 10^2 * R = 2.12 (R = $[\Sigma(\chi_{obs} - \chi_{calcd})^2 / \Sigma\chi_{obs}^2]^{1/2}$). The solid lines in Fig. 5.15 were calculated using the fitted parameters. A systematic error analysis to determine the individual contributions of internal and external exchange interaction was not carried out for **3** in the absence of a

structure. However, field dependent magnetization data were acquired for **3** to ascertain the spin ground state of the complex and the corresponding profile at 2 K is shown in Fig. 5.16. The calculated values are very close to a species with S = 7/2 rather than 8/2 ground state similar to **1**. This is again in agreement with the presence of a weak antiferromagnetic component in the cluster. The solid line in Fig. 5.16 was calculated for g = 2.21, S = 3.5 at 2 K.

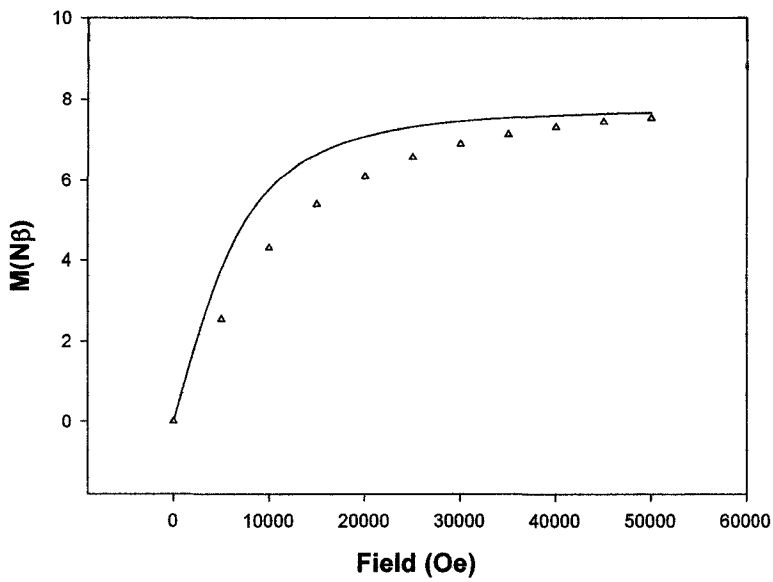

Fig. 5.16 Field dependent magnetization of **3**

The variable temperature molar magnetic moment data for **4** are shown in Fig. 5.17. The cluster has a magnetic moment of 5.9 μ_B at room temperature, which is well above the spin only value for nine Cu(II) centers (eight Cu(II) ions within the cluster plus

one Cu(II) in $CuBr_4^{2-}$). The spin only value for nine isolated Cu(II) ions would be 5.2 μ_B. The moment drops slightly to a value of 5.6 μ_B at around 65 K and then rises sharply to 7.3 μ_B as the temperature goes down to 2 K. Even though the cluster contains peripherally joined pinwheel subunits bridged by bromide, the variable temperature profile for the cluster does not reflect any unusual sign of cooperativity and the profile is typical of a regular ferromagnetic pinwheel. The data were fitted initially to a simplified magnetic model with J1 = J2 = J, including a correction for an additional isolated Cu(II) center for the $CuBr_4^{2-}$ anion. The values for the best fitted parameters were returned as g_{av} = 2.22, J = 5.4 cm $^{-1}$, TIP = 545 x 10^{-6} cm^3 mol^{-1}, ρ = 0.002, θ = - 0.9 K, 10^2 * R = 1.8. These values are consistent and similar to the previously published ferromagnetic pinwheel clusters [67-68, 132] with intermolecular ferromagnetic associations.

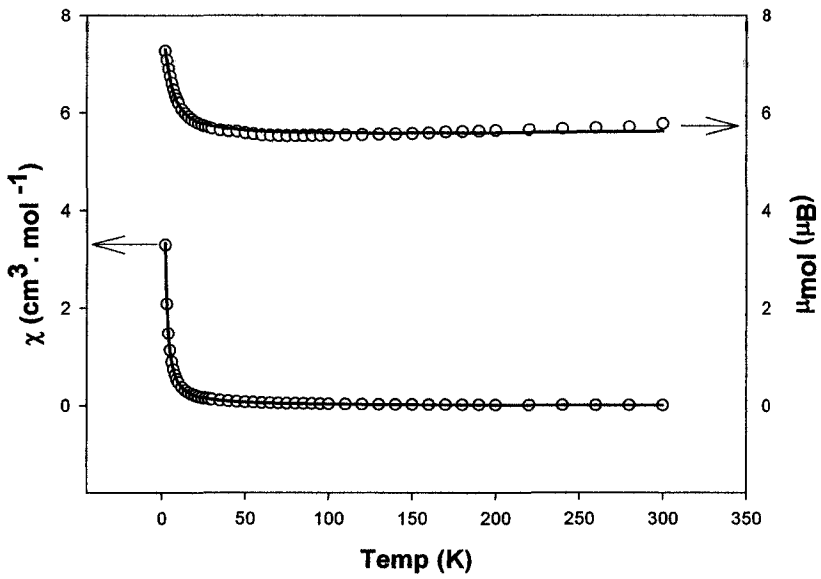

Fig. 5.17 Variable temperature magnetic profile for **4**

There are four very long and nominally orthogonal bromide bridging connections in **4** linking $Cu(II)_8$ subunits at the corners. Despite the Cu-Br-Cu bridges it can be assumed that such bridging connections would not be responsible for antiferromagnetic exchange between participating metal ions, but small ferromagnetic contributions from such bonds could be possible. However, such a contribution would be hard to detect in the presence of relatively large and dominant intramolecular ferromagnetic exchange within the cluster. Therefore, it would be difficult to predict and determine precisely how these bridges would influence the overall exchange. However, the inclusion of a small negative Weiss correction for a good fitting might account for the initial downward trend in the magnetic profile.

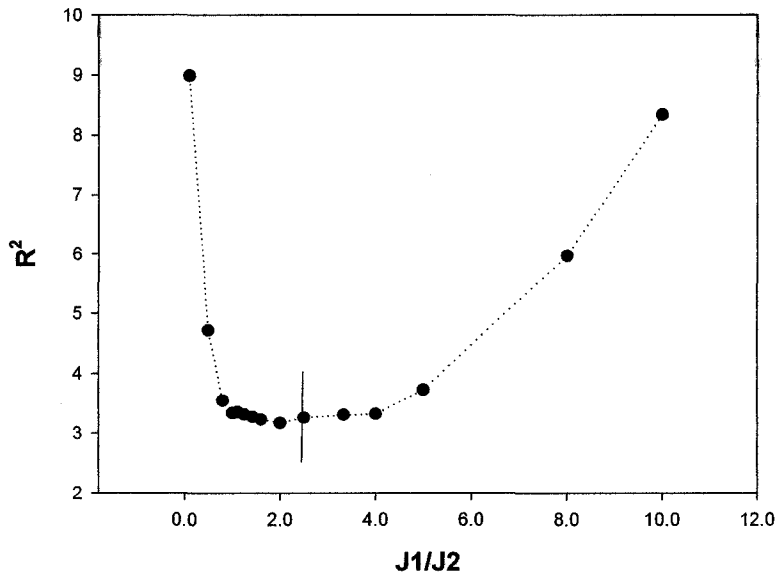

Fig. 5.18 GOF parameter R^2 as a function of J1/J2 for **4**

It may also point to a weak antiferromagnetic exchange within the cluster which may be long range intercluster in nature or a weak antiferromagnetic coupling of the inner core with the peripheral coppers via the very long O-C-C-N secondary bridge identified in the structure along the ligand backbone itself. However, the magnetic behavior that is seen is the net effect of the two competing pathways. This is similar and consistent to that in **1** and also to other pinwheel clusters obtained from Set2pomp (Scheme 5.1) [132 (a)].

In order to have a rough estimate of the possible ferromagnetic contributions from the internal hydrazone oxygen and the external orthogonal diazine N-N bridging connections, again a systematic error analysis was carried out. The procedure involved two steps as before. The susceptibility data were least-squares fitted to equations 5.1-5.3 for a range of J1/J2 values of 0.1, 0.5, 0.8, 1.0, 1.11, 1.25, 1.43, 1.6, 2.0, 2.5, 3.33, 4.0, 5.0, 8.0 and 10.0. The GOF parameter R^2 as function of J1/J2 is shown in Fig. 5.18. The goodness of fit parameter R^2 shows a troughlike dependence reaching a minimum from J1/J2 < 2.0 to about 4.0. For R^2 values outside the trough, the curves clearly deviated from the experimental data, whereas for values within the trough, the curves were statistically indistinguishable. Accordingly a J1/J2 value of 2.5 was estimated to be the best average, which gave the best fitted value g = 2.23, TIP = 545 x 10^{-6} cm^3 mol^{-1}, ρ = 0.002, θ = - 0.5 K, 10^2 * R = 1.87 ($R = [\Sigma(\chi_{obs} - \chi_{calcd})^2 / \Sigma\chi_{obs}^2]^{1/2}$). The best fitted value J = 6.3 cm^{-1} for the ratio J1/J2 = 2.5 was finally translated into J1 = 6.3 cm^{-1} within the central core and J2 = 2.5 cm^{-1} for the peripheral copper centers. The solid lines in Fig. 5.17 were calculated with these parameters.

5.5 Conclusion

A series of four octanuclear pinwheel clusters has been reported in this chapter with the tritopic ligand 2pomp. Complexes **1** and **4** have been characterized by single crystal x-ray crystallography. The structural investigation revealed two different kinds of bridging connection within the clusters **1** and **4**; a tetranuclear inner $[Cu_4(\mu\text{-}O)_4]$ component which has hydrazone oxygen bridges between four copper centers and four other peripheral copper(II) centers, which are connected to the inner core by a N-N diazine bridge. Due to orthogonal bridging connections between the copper centers both within the core and outside the core in cases of **1** and **4** (long-short Cu-O, and Cu-N bond distances within the core and along the peripheral Cu-N-N-Cu bond), the complexes showed ferromagnetic coupling. The complexes **2** and **3** could not be characterized structurally but since they were made from the same ligand and exhibited overall ferromagnetism, it is assumed that they formed analogous octanuclear pinwheel clusters.

For a special case in **4** where $CuBr_2$ was used as the metal salt, a 2D network of peripherally joined pinwheels resulted. Each of the pinwheels in the network was connected to four other pinwheels by one of its peripheral copper(II) atoms. A bromide atom acted as networking bridge or linker between adjacent pinwheels. However, again due to intercluster orthogonal connectivity (long-long Cu-Br bonds), no magnetic cooperativity was observed and the 2D cluster behaved as a collection of individual pinwheel clusters.

The general difficulty with the fitting of the magnetic data with such a system was to distinguish the individual contributions from different bridged components. It should be realized that it may not be possible to distinguish the subtleties associated with minor differences in exchange contributions, particularly in the presence of an overall dominant ferromagnetic component. However, an error analysis using a J_{core} (J1), J_{per} (J2) model suggests that ferromagnetic coupling within the $[Cu_4(\mu\text{-}O)_4]$ core is stronger than that between the core atoms and the peripheral copper centers. This is reasonable based on the longer distances to the peripheral copper sites. All of the octanuclear clusters showed ferromagnetic interactions with a range of coupling 4-8 cm^{-1}.

CHAPTER 6

Nonanuclear [3 x 3] square $Mn(II)_9$ grids - structures and magnetism

6.1 Introduction

The tritopic ligand 2poap, based on a pyridine-2,6-dihydrazone central core, and its variants (Scheme 6.1) react with transition metal salts (e.g. Mn(II), Zn(II), Fe(III), Cu(II)) to form nonanuclear [3 x 3] homoleptic $Mn(II)_9$, $Zn(II)_9$, $Fe(III)_9$, and $Cu(II)_9$ grid complexes in high yield. Complete [3 x 3] $Ni(II)_9$ and $Co(II)_9$ grid complexes could not be structurally characterized due to several complications such as aerial oxidation in cases of cobalt(II) complexes and formation of discrete grid fragments, which were seen in both the cases. However, based on other evidences such as mass spectra, variable temperature magnetic response and elemental analysis, Thompson and his group have reported the formation of such grids [65, 136]. All these grid molecules are synthesized by designed self-assembly.

Designed self-assembly has distinct advantages over other methods. In a designed self-assembly process one has the choice of putting the coordination pockets in a predesigned position in the ligand backbone. Thus the properties of the metal aggregate will be a direct consequence of the nature and position of the coordination site. Grid complexes are of special interest in the design of nanoscale materials, because of their precise two dimensional grid-like configurations. Nonanuclear $Mn(II)_9$ grids are

interesting in this class of complexes, because they are antiferromagnets with an S = 5/2 ground state resulting from intramolecular antiferromagnetic exchange throughout the entire grid. Any entity with flat geometry and a precise arrangement of spins is a potential candidate for application in information storage and processing technology [25, 138-139]. Moreover, depending on their packing pattern, grid molecules can be excellent candidates for long range ordering or single molecule magnets (SMMS).

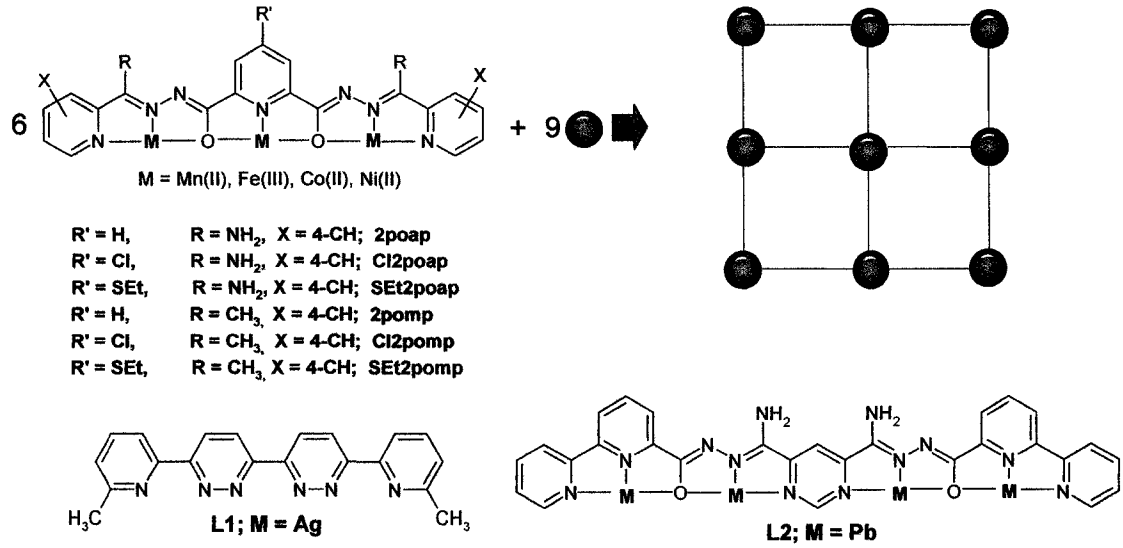

Scheme 6.1

Examples of non-magnetic [3 x 3] and higher order grids have been produced as well. A [3 x 3] $Ag(I)_9$ grid by Lehn from the reaction of a pyridazine based ligand L1 (Scheme 6.1) [24], two non-magnetic [4 x 4] [140] and [4 x (2 x 2)] $Pb(II)_{16}$ grids with the pyrimidine based ligand L2 (Scheme 6.1) [141] and a [4 x 5] Ag $(I)_{20}$ grid [24], are a few to mention, which were reported recently. The structural characterization of partial grids is also well documented. A pentanuclear Fe(III) complex from the ligand Cl2poap

(Scheme 6.1) with four missing metal centers along the edges of a regular L_6M_9 grid arrangement [111], a hexanuclear Ni(II) complex and a heptanuclear Co(II) complex [142] with more than one vacant coordination pockets are a few examples.

The core of a Mn_9 grid contains nine Mn(II) centers arranged in a [3 x 3] square arrangement, with six ligands arranged in two parallel rows, three above, and three below the core of the grid. There are three types of the coordination compartments formed from the assembly of the six tritopic ligands. The corner sites have *cis*-N_4O_2 structure, the sides *mer*-N_3O_3, and the central metal *trans*-N_2O_4. This difference in coordination sites is very important and might lead to different behavior of the metal ions at these sites depending on the metal ion identity. This may also lead to different site dependent redox potentials, different spin-ground states, or preferential site occupancy in case of mixed metal systems [143]. A ball and stick representation of a regular L_6M_9 grid arrangement is shown in Scheme 6.1.

The nonanuclear Mn_9 grids exhibit novel and important electrochemical properties. It is possible to oxidize reversibly eight of the nine Mn(II) centers to Mn(III) within the voltage range 0.6-1.8 V (vs. Ag/AgCl) [107, 143-144]. A stable mixed oxidation grid $[Mn(II)_5Mn(III)_4]$ can be synthesized by both chemical and electrochemical means. Due to an entirely isotropic interaction of all the electrons, the mixed oxidation state $[Mn(II)_5Mn)III)_4]$ grid has a ground state of S = ½ which is the result of incomplete compensation of the electron spins. Such species are considered to

be 'spin cluster qubits' which are possible building blocks for quantum computers [137]. Four new nonanuclear $Mn(II)_9$ grid complexes with the ligand 2pomp are reported in this chapter. Two of the complexes have been characterized by structural studies. Magnetic properties of all the grids will be discussed.

6.2 Experimental

6.2.1 Materials

Commercially available solvents and chemicals were used without further purification.

6.2.2 Characterization

Analysis, spectroscopic and physical measurements were done according to the procedure described in Chapter 2.

6.2.3 Synthesis of the Ligands

The synthesis of the ligand 2pomp was carried out according to the procedure described in Chapter 2.

6.2.4 Synthesis of the complexes

$[Mn_9(2pomp\text{-}2H)_6](ClO_4)_6(CH_3OH)_{1.5}\cdot 10H_2O$ (1)

2pomp (0.1 g, 0.25 mmol) was added to a CH_3OH/CH_3CN (10 mL/10 mL) solution of $Mn(ClO_4)_2.6H_2O$ (0.35 g, 1.4 mmol) and stirred for a few hours during which time the solution turned deep red yellow in color. The mixture was filtered and the resulting solution was used to grow crystals by slow evaporation of the solvent. Deep red

crystals were isolated after several days (Yield 74%). IR (cm^{-1}): 1734, 1700 (ν C=O), 1684, 1593, 1569, 1067 (ν ClO_4^-), 992 (ν pyr). MALDI TOF (CHCA matrix, MeOH/H_2O): 2887 $[L_6Mn_9]^{1+}$. Anal. Calc. (%) for $[(C_{21}H_{17}N_7O_2)_6 Mn_9](ClO_4)_6(CH_3OH)_{1.5}(H_2O)_{10}$; C, 41.21; H, 3.47; N, 15.83. Found (%); C, 41.21; H, 2.81; N, 15.64.

$[Mn_9(2pomp\text{-}2H)_6](NO_3)_6 \cdot 19H_2O$ (2)

$Mn(NO_3)_2.6H_2O$ (0.25 g, 0.87 mmol) was dissolved in a $CH_3OH/H_2O/CH_3CN$ (1:1:1 v/v, 15 mL) mixture. 2pomp (0.1 g, 0.25 mmol) was added initially forming a cloudy yellow emulsion. A few drops of Et_3N were added and the resulting emulsion was stirred for several hours. The final orange mixture was filtered and the resulting solution was kept for crystallization. Deep red crystals were isolated after several days (Yield 39%). IR (Nujol, cm^{-1}): 1616, 1592, 1569, 991 (ν pyr). MALDI TOF (CHCA matrix, MeOH/H_2O): 2888 $[L_6Mn_9]^{1+}$. Anal. Calc. (%) for $[(C_{21}H_{17}N_7O_2)_6Mn_9](NO_3)_6(H_2O)_{18}$; C, 41.97; H, 3.91; N, 18.64. Found (%); C, 42.07; H, 3.54; N, 18.49.

$[Mn_9(2pomp\text{-}2H)_6](MnCl_4)_2Cl_2(CH_3OH)_2 \cdot 7H_2O$ (3)

2pomp (0.20 g, 0.50 mmol) was added to a solution of $MnCl_2.6H_2O$ (0.40 g, 2.0 mmol) in methanol (10 mL) and the mixture was stirred with warming. The ligand quickly dissolved to give a pale yellow colored solution, and subsequently, a bright yellow precipitate formed. $Mn(CH_3COO)_3.3H_2O$ (0.2 g, 0.75 mmol) was added to the mixture, and resulted in the formation of a deep red solution. Stirring and heating were

continued for 1 h, and then the mixture was filtered and the solution was allowed to evaporate slowly at room temperature. Deep red prismatic crystals suitable for structural analysis were collected after several weeks. The structural sample was kept under mother liquor prior to structural analysis, due to crystal instability on exposure to air (Yield 35%). IR (Nujol, cm^{-1}): 1617, 1592, 1568, 992 (ν pyr). Anal. Calc. (%) for $[(C_{21}H_{17}N_7O_2)_6Mn_9](MnCl_4)_2\ Cl_2\ (CH_3OH)_2(H_2O)_7$; C, 43.36; H, 3.52; N, 16.59. Found (%); C, 43.40; H, 2.99; N, 16.78.

$[Mn_9(2pomp\text{-}2H)_6](PF_6)_6(CH_3OH)_4(CH_3CN)_2{\cdot}3H_2O$ (4)

2pomp (0.25 g, 0.62mmol) was added to a solution of $Mn(CH_3COO)_2.4H_2O$ (0.50 g, 2.0 mmol) in methanol and H_2O (~10 mL:10 mL). 4 drops of Et_3N were added and the resulting solution was stirred for 6 hours. The resulting mixture was filtered and the solution was kept for crystallization by slow evaporation of the solvent. As no crystallization started even after several days, a few of drops of NH_4PF_6 (6.0 M) were added to the solution to facilitate crystallization. Deep red, thin crystals were collected after several days (Yield 17%). Recrystallization from acetonitrile gave x-ray quality crystals. Elemental analysis Calc. (%) for $[(C_{21}H_{17}N_7O_2)_6\ Mn_9](PF_6)_6\ (CH_3OH)_4\ (CH_3CN)_2(H_2O)_3$; C, 39.98 ; H, 3.25; N, 15.31. Found (%); C, 40.17; H, 2.97; N, 14.95.

6.3 Crystallographic data collection and refinement of structures

Red orange prismatic crystals of **3** and **4** with approximate dimensions 0.39 x 0.37 x 0.16 mm and 0.52 x 0.30 x 0.26 mm respectively were mounted on glass fibers. All measurements were done on a Bruker P4/CCD system with graphite monochromated Mo-Kα radiation from a sealed tube generator. Hydrogen atoms were introduced in calculated or difference map positions with isotropic thermal parameters set twenty percent greater than those of their bonding partners at the time of their inclusion. They were not refined in either case. Data were collected at a temperature of 193 K. The full hemispheres of data for both cases were collected with 30 second frame exposure, to a maximum 2θ value of 52.9°. The Siemens area detector absorption routine (SADABS) was used in both cases to collect the data with maximum and minimum effective transmissions of 0.8612 and 0.7052 for **3** and 0.8231 and 0.6874 for **4** respectively. The data were corrected for Lorentz and polarization effects. Both the structures were solved by direct methods [99] and expanded using Fourier techniques [100].

All non-hydrogen atoms in **3** and some non-hydrogen atoms in **4** were refined anisotropically while the rest were refined isotropically. Some lattice acetonitrile molecules and some PF_6^- anions were refined isotropically and some of the PF_6^- anions were fixed for the final round of refinement to achieve convergence. The maximum and minimum peaks on the final difference Fourier map corresponded to 1.08 and -1.26 $e^-/Å^3$ in case for **3** and 1.23 and -0.61 $e^-/Å^3$ for **4** respectively. Neutral atom scattering factors were taken form the usual source of Cromer and Waber [101]. Anomalous dispersion

effects were included in F_{calc} [102]. The values for Δf' and Δf" were those of Creagh and McAuley [103]. The values for the mass attenuation coefficients are those of Creagh and Hubbell [104]. All calculations were performed using the teXsan [105 (a)] crystallographic software package of Molecular Structure Corporation except for refinement, which was performed using SHELXL-97 [99].

6.4 Results and Discussion

6.4.1 Structural details

A crystallographic summary is provided in Table 6.1 and important bond distances and bond angles are given in Table 6.2. From the tetragonal space group of the complex, it is evident that the cation has four- fold symmetry. The cation comprises a total of six ligands and nine Mn(II) ions. Two sets of three roughly parallel heptadentate ligands bind nine Mn(II) ions from opposite faces of the $[Mn(II)_9(\mu\text{-}O)_{12}]$ core. The structure of the cation in **3** is shown in Fig. 6.1.

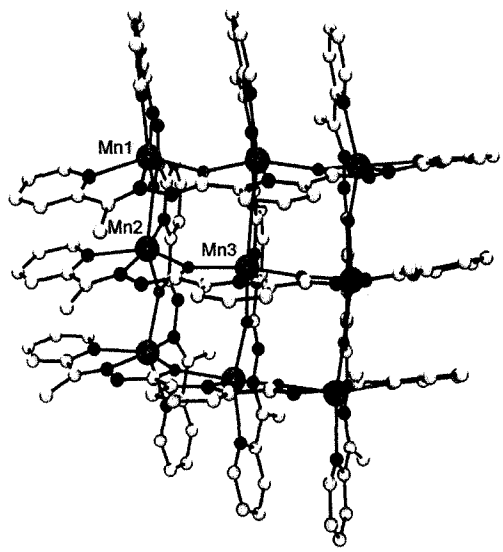

Fig. 6.1 POVRAY© representation of the grid structure in **3**

Table 6.1 Summary of the crystallographic data for $[Mn_9(C_{21}H_{17}N_7O_2)_6](MnCl_4)_2Cl_2(CH_3OH)_2 \cdot 7H_2O$ **(3)**

Empirical Formula	$C_{126}H_{118}N_{42}O_{20}Cl_{10}Mn_{11}$
Formula Weight	3499.44
Crystal Color, Habit	Red orange, prism
Crystal Dimensions	0.16 x 0.37 x 0.16 mm
Crystal System	Tetragonal
Lattice Type	I-centered
Lattice Parameters	a = 18.2700(5) c = 26.753(2) Å V = 8929.8(5)Å^3
Space Group	I-4 (# 82)
Z value	2
D_{calc}	1.301 g/cm^3
F_{000}	3546.00
μ(MoKα)	9.63 cm^{-1}
Temp (K)	193 ± 1
R1	0.061
wR2	0.195

All the Mn(II) centers in the cluster are hydrazone oxygen bridged. Mn-Mn distances fall in the range 3.905-3.966 Å. Mn-O-Mn angles fall in the range 127.62-128.55 °. The central atom Mn(3) is equidistant from the four connecting side Mn(II) ions (3.905 Å). For Mn(3), all Mn-N and Mn-O bond distances (2.181 Å and 2.200 Å respectively) are equal. A simplified presentation of the core with immediate coordinated connectivity between metal centers is given in Fig. 6.2. The lateral corner to corner Mn-Mn distance in the grid is 7.824 Å. The average Mn-N distances from corner Mn atom and side Mn atoms to external pyridine rings are 2.257-2.286 Å and 2.180-2.285 Å respectively, which are comparatively longer than average Mn-N distances from central Mn which is 2.181 Å. This might be a consequence of the way in which the ligands are stretched over the nonanuclear core [143]. The pyridine rings in each set of three ligands on each side are positioned approximately parallel to each other with fairly short inter-ring separations of 3.847 Å between the central ring and 3.730-4.589 Å between the outer projected pyridine rings.

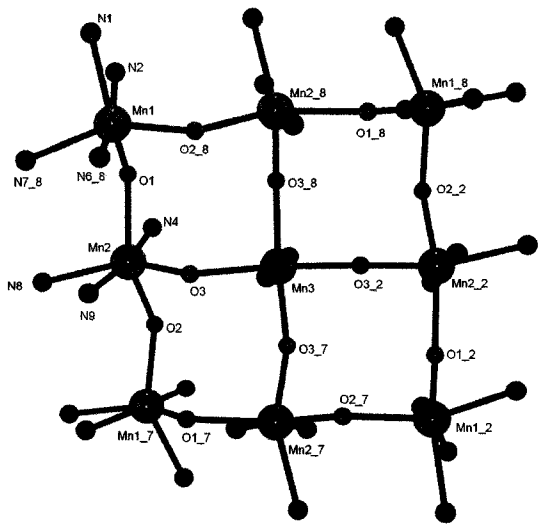

Fig. 6.2 POVRAY© representation of the grid core in **3**

Table 6.2 Bond distances (Å) and Angles (°) for $[Mn_9(C_{21}H_{17}N_7O_2)_6](MnCl_4)_2Cl_2(CH_3OH)_2 \cdot 7H_2O$ (3)

Mn1	O1	2.172(4)	Mn3	O3	2.199(3)
Mn1	N6	2.172(5)	Mn4	Cl1	2.3674(14)
Mn1	O2	2.181(3)	Mn4	Cl1	2.3674(14)
Mn1	N2	2.196(5)	Mn4	Cl1	2.3675(14)
Mn1	N7	2.256(4)	Mn4	Cl1	2.3675(14)
Mn1	N1	2.286(4)	Mn5	Cl2	2.3647(19)
Mn2	O3	2.153(3)	Mn5	Cl2	2.3647(19)
Mn2	N9	2.176(5)	Mn5	Cl2	2.3648(19)
Mn2	N4	2.180(5)	Mn5	Cl2	2.3648(19)
Mn2	O2	2.200(3)	Mn1	Mn2	3.966
Mn2	O1	2.230(3)	Mn2	Mn3	3.905
Mn2	N8	2.286(5)	Mn1	Mn2_8	3.943
Mn3	N11	2.180(6)			
Mn1	O1	Mn2	128.52(18)		
Mn1	O2	Mn2	128.38(18)		
Mn2	O3	Mn3	127.64(16)		

This close arrangement presumably leads to a significant π-π interactions between the rings and contributes to the stabilization of the grid during self-assembly.

The lattice in **3** contains several solvent molecules, Cl^-, and also $MnCl_4^{2-}$ anions. The average C-O distances of 1.282-1.311 Å in the ligands reveal that all the ligands are doubly deprotonated, which requires two $MnCl_4^{2-}$ anions per unit cation for the charge balance. Fig. 6.3 shows three such $MnCl_4^{2-}$ units. The figure also shows the close overlapping of the terminal pyridine rings from two adjacent nonanuclear grids with ring-ring distances of 3.703-4.579 Å. These aromatic π interactions between grids might contribute to the overall grid association in the lattice.

An extended structural view revealed more interesting long range associations within the lattice. There are four stacks of nonanuclear grids in two pairs positioned 90 ° with respect to each other. The two grids within a pair dock close to each other through possible π-π interactions between the terminally projected pyridine rings, one next to the other. Such an arrangement creates a channel between the four grid subunits which is occupied by a $MnCl_4^{2-}$ anion sitting right along the channel above each layer. A depiction with different color coding to show the perpendicular arrangement of the four grids is given in Fig. 6.4. The figure also shows that the chlorine atoms of the $MnCl_4^{2-}$ unit have long hydrogen bonding contacts to four water molecules surrounding the anion at distances of 3.217 Å. This is very long hydrogen bonding compared to similar hydrogen bonding seen in the polymeric ribbon-like cluster [4,4′-H_2bipy][MCl_4] (Where M = Zn) with distances 2.30-2.63 Å [145].

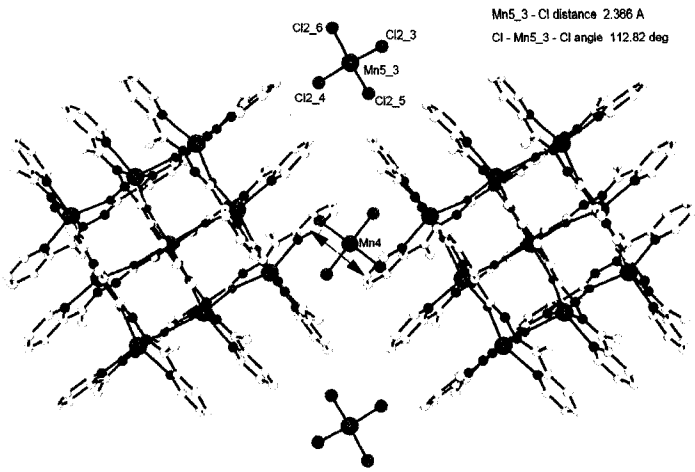

Fig. 6.3 Docking of two nonanuclear grid molecules in the extended structure of **3** and an interstitial $MnCl_4^{2-}$ unit occupying the channels between grids (Color Code: Magenta = Mn, Grey = C, Blue = N, Red = O)

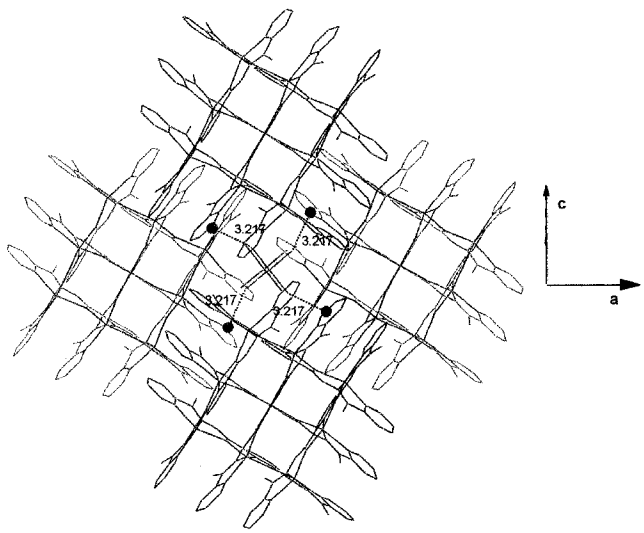

Fig. 6.4 Different color used to show different layers of the extended structure; (Hydrogen atoms and other $MnCl_4^{2-}$ anions removed for clarity). Color code: Green = Lower layer, Multi color = Upper layer (Magenta = Mn, Red = O, Grey = C, Blue = N); ---- line = hydrogen bonding; Red ball = O atom of water molecule.

The structural representation of the grid cation in **4** is given in Fig. 6.5. The overall cationic framework and the dimensions of the grid in **4** are very similar to **3**. A simplified pictorial presentation showing only the immediate donor atoms is given in Fig. 6.6. The overall grid dimensions in **4** are very similar to those of **3** and also with the parent grid complex $[Mn_9(2poap)_6](ClO_4)_6(H_2O)_{18}$ (2poap; Scheme 6.1) [107]. The Mn-Mn distances fall in the range 3.92-3.98 Å, while the Mn-O-Mn bond angles are in the range 126.8-129.8 °.

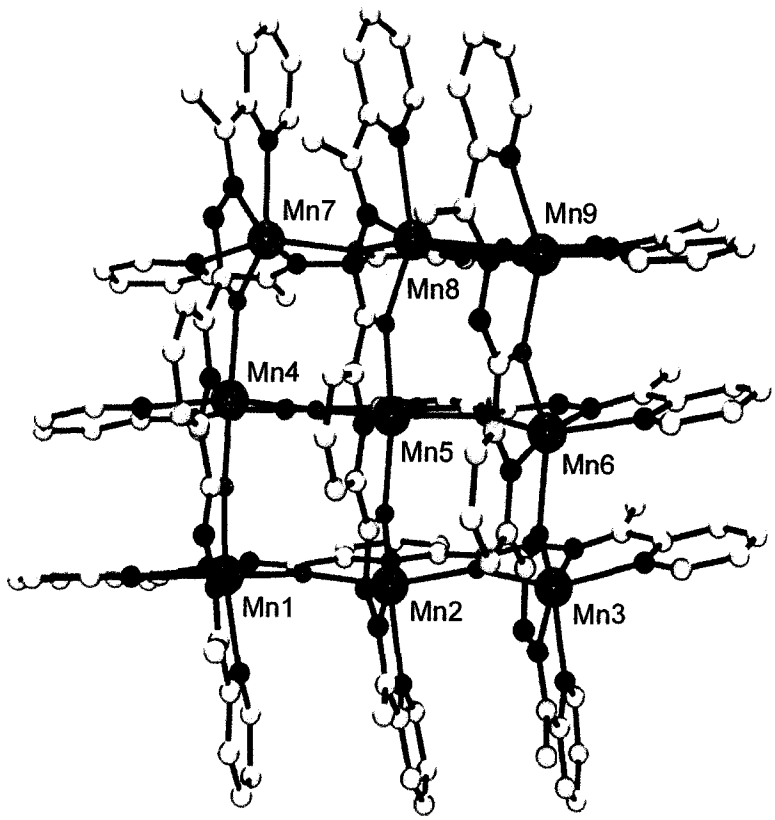

Fig. 6.5 POVRAY© representation of [3x3] grid structure in **4**

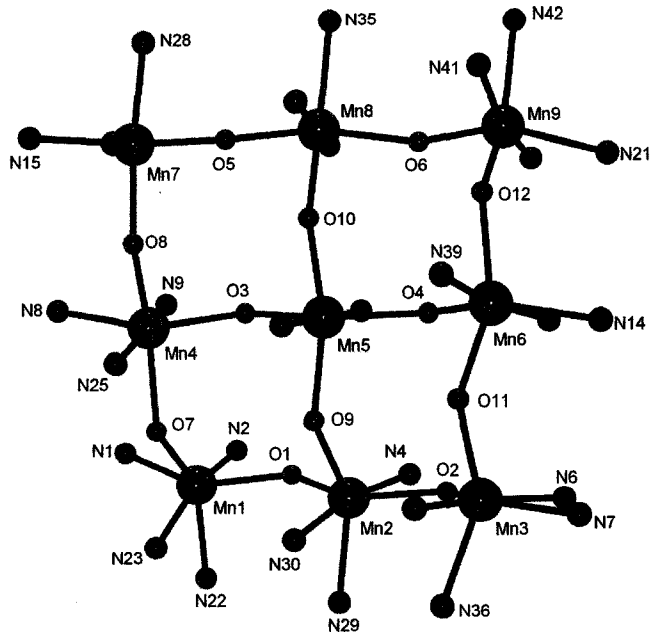

Fig. 6.6 POVRAY© structural representation of the grid core in **4**

The Mn-L distances fall in the range 2.199-2.224 Å [113]. The packing (Fig. 6.7) shows a group of four nonanuclear grids similar to **3** with close π contacts between aromatic pyridine rings from adjacent grids. The pyridine rings are arranged in roughly parallel fashion with short ring separations of 3.73-3.84 Å for the central ring and 3.74-4.69 Å for the external rings. The inter-ring distance between two adjacent grids is 3.458 Å. The short interligand contacts might again suggest that π contacts may be the driving force behind the parallel alignment of the two groups of ligands above and below the metallic plane and also for the associations of grids in the lattice.

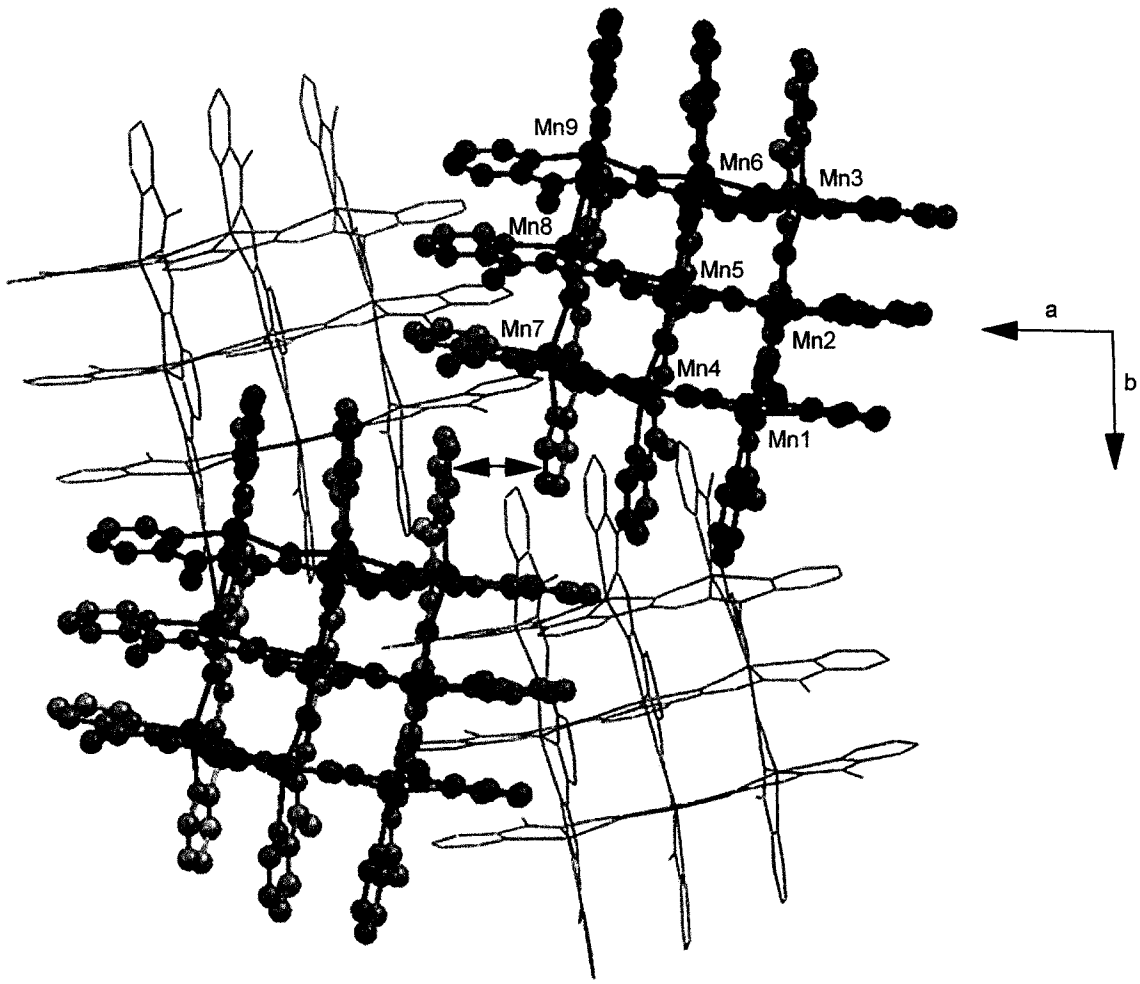

Fig. 6.7 Arrangement of grids in the unit cell of **4**; Different color used to show different layers; (Hydrogen atoms and other PF_6^- anions and solvents removed for clarity). Color code: Green = Lower layer, Ball and stick (Multi color) = Upper layer (Magenta = Mn, Red = O, Grey = C, Blue = N).

Table 6.3 Summary of crystallographic data for $[Mn_9(C_{21}H_{17}N_7O_2)_6](CH_3COO)_2(PF_6)_6 \cdot H_2O$ (4)

Empirical Formula	$C_{138}H_{120}O_{12}F_{36}N_{48}P_6Mn_9$
Formula Weight	4007.01
Crystal Color, Habit	Red-orange, prism
Crystal Dimensions	0.52 X 0.30 X 0.26 mm
Crystal System	Monoclinic
Lattice Type	C-centered
Lattice Parameters	a = 26.071(2) Å b = 26.150(2) Å c = 26.592(2) Å β = 102.467(2) ° V = 17702(2) Å^3
Space Group	Cc (#9)
Z value	4
D_{calc}	1.503 g/cm^3
F_{000}	8076.00
μ(MoKα)	7.79 cm^{-1}
Temp (K)	193 ± 1
R1	0.088
wR2	0.259

Table 6.4 Selected Bond distances (Å) and Angles (°) for **$[Mn_9(C_{21}H_{17}N_7O_2)_6](CH_3COO)_2(PF_6)_6 \cdot H_2O$ (4)**

Mn1	O7	2.153(6)	Mn4	N25	2.164(7)
Mn1	N23	2.169(8)	Mn4	N9	2.178(7)
Mn1	O1	2.182(6)	Mn4	O7	2.208(6)
Mn1	N2	2.189(7)	Mn4	O8	2.241(6)
Mn1	N22	2.261(8)	Mn4	N8	2.293(7)
Mn1	N1	2.268(7)	Mn5	N11	2.162(7)
Mn2	O9	2.138(6)	Mn5	N32	2.170(6)
Mn2	N4	2.159(8)	Mn5	O4	2.209(6)
Mn2	N30	2.204(7)	Mn5	O3	2.211(5)
Mn2	O2	2.211(6)	Mn5	O9	2.217(6)
Mn2	O1	2.224(6)	Mn5	O10	2.222(6)
Mn2	N29	2.279(8)	Mn6	O4	2.188(6)
Mn3	N37	2.177(7)	Mn6	N39	2.197(7)
Mn3	O11	2.177(6)	Mn6	O12	2.199(6)
Mn3	O2	2.182(6)	Mn6	N13	2.200(7)
Mn3	N6	2.182(8)	Mn6	O11	2.239(6)
Mn3	N7	2.229(7)	Mn6	N14	2.307(8)
Mn3	N36	2.283(9)	Mn7	O8	2.175(6)
Mn4	O3	2.164(5)	Mn7	N16	2.182(8)

Mn7	O5	2.200(6)		Mn7	O5	Mn8	128.0(3)
Mn7	N27	2.203(8)		Mn9	O6	Mn8	128.1(3)
Mn7	N15	2.283(8)		Mn1	O7	Mn4	128.6(2)
Mn7	N28	2.300(8)		Mn7	O8	Mn4	126.8(3)
Mn8	N18	2.173(8)		Mn2	O9	Mn5	128.5(3)
Mn8	O10	2.180(6)		Mn8	O10	Mn5	127.8(3)
Mn8	N34	2.187(8)		Mn3	O11	Mn6	127.7(3)
Mn8	O5	2.224(6)		Mn9	O12	Mn6	129.8(3)
Mn8	O6	2.247(6)					
Mn8	N35	2.299(8)		Mn1	Mn2	3.971	
Mn9	O6	2.138(6)		Mn2	Mn3	3.958	
Mn9	N41	2.153(9)		Mn3	Mn6	3.965	
Mn9	O12	2.178(6)		Mn6	Mn9	3.963	
Mn9	N20	2.186(9)		Mn9	Mn8	3.942	
Mn9	N42	2.240(9)		Mn8	Mn7	3.976	
Mn9	N21	2.301(7)		Mn7	Mn4	3.949	
				Mn4	Mn1	3.929	
Mn1	O1	Mn2	128.7(3)	Mn5	Mn2	3.923	
Mn3	O2	Mn2	128.6(3)	Mn5	Mn4	3.944	
Mn4	O3	Mn5	128.7(3)	Mn5	Mn8	3.953	
Mn6	O4	Mn5	128.4(3)	Mn5	Mn6	3.959	

6.4.2 Magnetism

The full isotropic exchange Hamiltonian considering spin only exchange for a $Mn(II)_9$ square grid would be given by the equation 6.1.

$$\boldsymbol{H}_{ex} = -J_R(\hat{S}_1\cdot\hat{S}_2 + \hat{S}_2\cdot\hat{S}_3 + \hat{S}_3\cdot\hat{S}_4 + \hat{S}_4\cdot\hat{S}_5 + \hat{S}_5\cdot\hat{S}_6 + \hat{S}_6\cdot\hat{S}_7 + \hat{S}_7\cdot\hat{S}_8 + \hat{S}_8\cdot\hat{S}_1)$$

$$-Jc(\hat{S}_2\cdot\hat{S}_9 + \hat{S}_4\cdot\hat{S}_9 + \hat{S}_6\cdot\hat{S}_9 + \hat{S}_8\cdot\hat{S}_9) \quad \text{[6.1]}$$

This equation assumes only nearest neighbor exchange terms within an isotropic magnetic environment. Other terms such as dipole-dipole interactions, second order ligand field, and Zeeman effects are ignored. J_R is the exchange coupling constant between the Mn centers along the eight membered outer ring and J_C is the exchange integral between the central Mn(II) ion and the ring (See Fig. 6.8). The full analysis of the data to determine the parameters in equation 6.1 is hampered simply because of the enormity of the calculations involved.

The dimension of the Hilbert space for calculation of an isotropic exchange interaction for a $Mn(II)_9$ grid with 45 electrons is 10,077,696. To handle this huge amount of data is far beyond the capability of any PC computer, and even beyond most mainframe computers [110]. Exploiting symmetry elements such as spin rotational symmetry and idealized D_4 spin permutational symmetry reduces the amount of data to be handled substantially, reducing the largest dimension to 22,210. Unfortunately, this is

still too large for matrix diagonalization and subsequent spin state and energy calculations with the average computer.

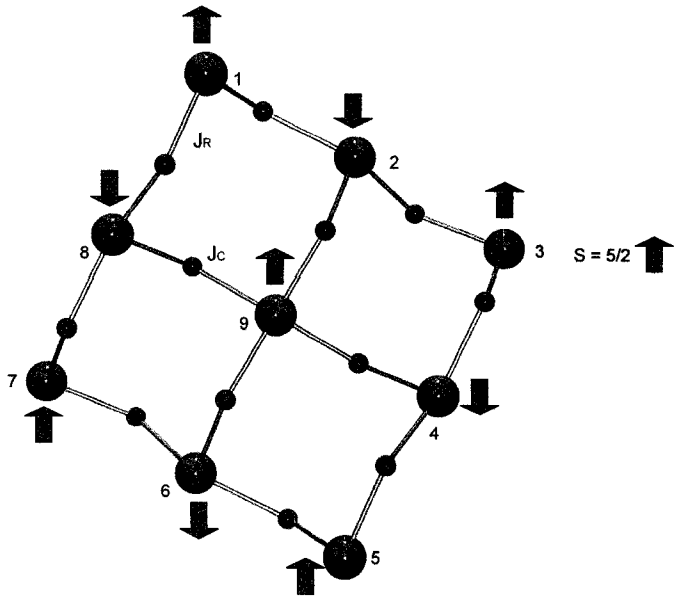

Fig. 6.8 Spin dipole model for an antiferromagnetically coupled $Mn(II)_9$ grid system.

Data analysis for the partially oxidized manganese grid $[Mn(III)_4Mn(II)_5(2poap\text{-}2H)_6](ClO_4)_{10}(H_2O)_{10}$, where there is a smaller number of electrons (41 electrons; four corner atoms of Mn(III) d^4) is comparatively less time consuming and less complicated. With the appropriate imposition of D_4 spin rotational symmetry and spin permutational symmetry, one can reduce the dimension of the largest matrix to a size of 12,486. This is still a large computation but can be handled with a PC computer with 2 GB memory storage (RAM) [137]. Thus, a full least-square fitting of the susceptibility data for a mixed oxidation $[Mn(II)_5Mn(III)_4]$ grid with two integrals J_R and J_C is then possible. However, a single calculation for one set of parameters with two different exchange integrals (J_R and J_C), requires about 2 days on such a PC [110].

The full analysis of an isotropic exchange situation in a $Mn(II)_9$ grid is then virtually unrealistic. However, we have simplified the analysis of the magnetic properties of a $Mn(II)_9$ grid by using a different model which treats the grid as a linear combination of a chain of S = 5/2 centers, representing the outer ring, plus an isolated Mn(II) at the center. The model further assumes that the intramolecular exchange within the grid is dominated by the exchange within the outer ring of eight Mn(II) centers (J_R), and that the exchange between the ring and the central Mn(II) (J_C) can effectively be ignored because the ground state is S = 5/2. This assumption is not rigorously correct from a theoretical point of view, although it is reasonable at low temperatures. In reality it cannot be assumed that $J_C = 0$ but the approach allows us to have an estimate of J_R. The large local spin S = 5/2 in each of the Mn(II) ions is treated as a classical vector. The assumption that the outer ring can be modeled as a chain is a valid consideration for a chain length of eight spin centers. This treatment is accomplished by using the following two equations 6.2-6.3 from the Fischer model [146] and correcting the calculated susceptibility by including the extra Curie like Mn(II) center (Equation 6.4).

$$\chi_{Mn} = \frac{N g^2 \beta^2 S(S+1)}{3kT} \frac{(1+u)}{(1-u)} \qquad [6.2]$$

$$u = \coth\left[\frac{JS(S+1)}{kT}\right] - \left[\frac{kT}{JS(S+1)}\right] \qquad [6.3]$$

$$\chi_{mol} = \left[\left(8\chi_{Mn} + 1.094 g^2\right)/(T-\Theta)\right](1-\alpha) + \left(1.094 g^2/T\right)\alpha + TIP \qquad [6.4]$$

$$\chi_{mol} = \left[\left(8\chi_{Mn} + 1.094g^2\right)/(T-\Theta)\right]\left[(1-\alpha) + 3*\left(1.094g^2/T\right)\alpha\right] + TIP \qquad [6.5]$$

Complexes **1** and **2** showed nearly identical magnetic profiles within the variable temperature range 2-300 K. The profiles are shown in Fig. 6.9 and Fig. 6.10 respectively. They are typical for regular $Mn(II)_9$ grids. The room temperature magnetic moments for **1** and **2** are 16.9 and 16.8 μ_B respectively, dropping down to 6.3 and 6.6 μ_B respectively at 2 K, which are signatures of antiferromagnetic exchange within the grids. The magnetic moments at 2 K indicate S = 5/2 ground states. Fitting the magnetic data with equations 6.1-6.4 gave the following results $g_{av} = 2.01$, $J_R = -4.3$ cm^{-1}, $J_C = 0$, TIP = 0, $\rho = 0.002$, $\theta = -2$ K, $10^2 * R = 1.5$ for **1** and $g_{av} = 2.0$, $J_R = -4.5$ cm^{-1}, $J_C = 0$, TIP = 0, $\rho = 0.0005$, $\theta = -2$ K, $10^2 * R = 1.9$ for **2** ($R = [\Sigma(\chi_{obs} - \chi_{calcd})^2 / \Sigma\chi_{obs}^2]^{1/2}$).

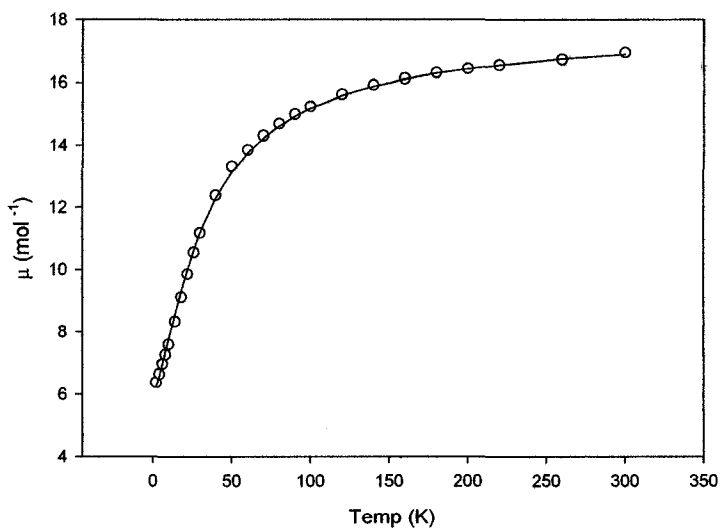

Fig. 6.9 Variable temperature magnetic moment for **1**

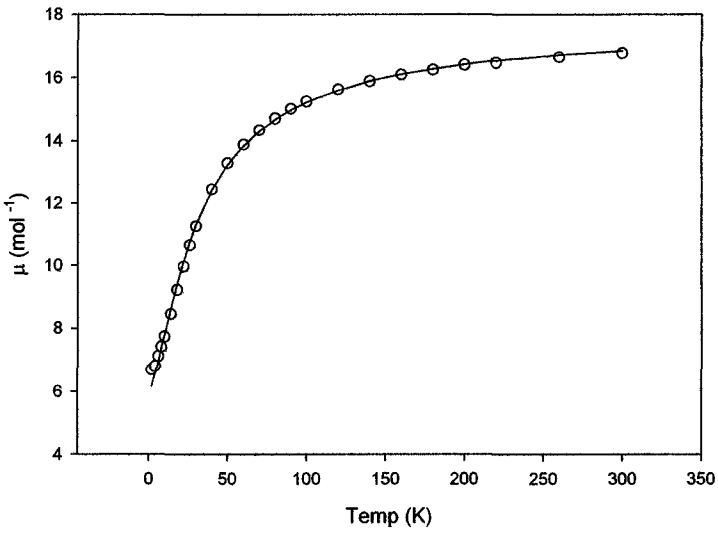

Fig. 6.10 Variable temperature magnetic moment for **2**

These results are consistent with previous results obtained for similar $Mn(II)_9$ grids. The solid lines in Figures 6.9 and 6.10 were calculated with these fitted parameters.

Fig. 6.11 shows the magnetic moment of **3** per mole as a function of temperature. The magnetic moment per mole is 19.4 μ_B at 300 K, which drops down to a value of 10.5 μ_B at 2 K consistent with a $Mn(II)_9$ grid and two Curie like mononuclear Mn(II) species. The χ expression in equation 6.4 is scaled for the eight Mn(II) centers in the spin coupled eight membered chain, and corrected for temperature-independent paramagnetism (TIP), the paramagnetic impurity fraction (α), intermolecular exchange effects (Θ = Weiss like temperature correction), and the "isolated" Mn(II) center. In order to fit the magnetic data for **3**, the molar susceptibility was further adapted for two additional mononuclear Mn(II) centers (equation 6.5). A good data fit to the equations 6.2-6.5 gave g_{av} = 2.05,

J_R = - 4.3 cm^{-1}, J_C = 0, TIP = 0, ρ = 0, θ = -1.5 K, 10^2 * R = 0.87 (R = $[\Sigma(\chi_{obs} - \chi_{calcd})^2 / \Sigma\chi_{obs}^2]^{1/2}$). The solid line in Fig. 6.11 was drawn according to the fitted parameters.

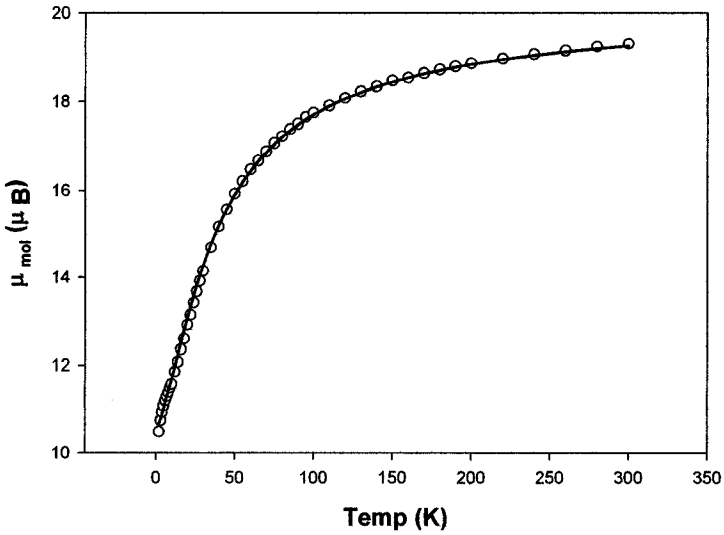

Fig. 6.11 Variable temperature magnetic moment for **3**

The presence of two mononuclear $MnCl_4^{2-}$ units in the lattice is responsible for the high magnetic moment at room temperature, but does not complicate the magnetic exchange situation. The total magnetic moment at room temperature corresponded to a $Mn(II)_9$ grid plus two mononuclear units.

Complex **4** shows a similar magnetic profile within the temperature range 2-300 K (Fig. 6.12). The magnetic moment at room temperature is 17.1 μ_B, which corresponds to nine Mn(II) centers. The data were fitted again to equations 6.1-6.4. An excellent data fitting gave g_{av} = 2.02, J_R = - 4.6 cm^{-1}, J_C = 0, TIP = 0, ρ = 0.001, θ = - 3 K, 10^2 * R = 2.2

($R = [\Sigma(\chi_{obs} - \chi_{calcd})^2 / \Sigma\chi_{obs}^2]^{1/2}$). J_R is consistent with the other related $Mn(II)_9$ grids. The relatively large negative θ value is normally associated with intermolecular magnetic exchange, but it might suggest that another significant intramolecular antiferromagnetic effect is present, which can reasonably be assigned to J_C.

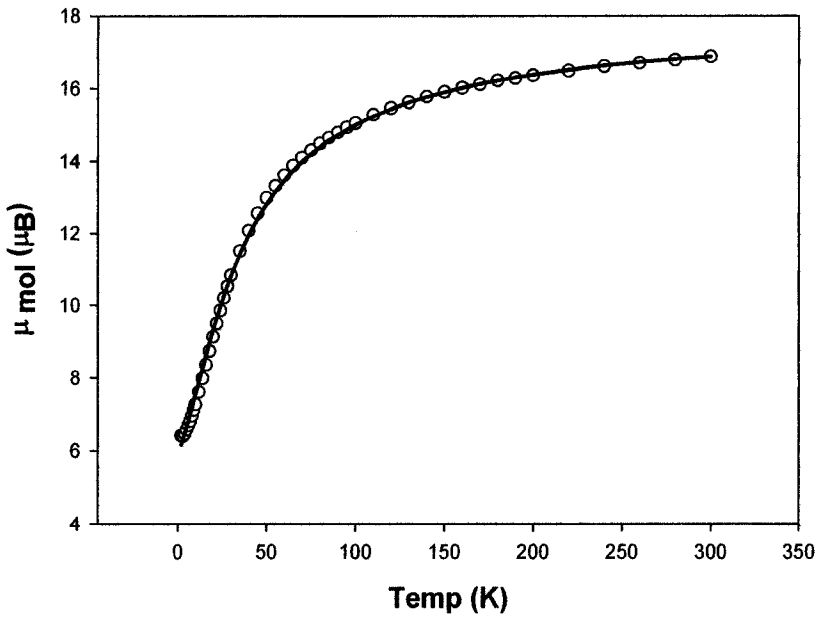

Fig. 6.12 Variable temperature magnetic moment for **4**

The coupling of S = 5/2 spins in the eight membered ring due to the antiferromagnetic exchange in the low temperature limit results in an S = 0 state leaving an overall S = 5/2 ground state, in agreement with the odd number of Mn(II) ions. The solid line in Fig. 6.12 was calculated with the fitted parameters. Magnetization data as a function of field were also acquired for **4,** which showed an increase in M with field, and a slight inflection at around 3 T (Fig. 6.13).

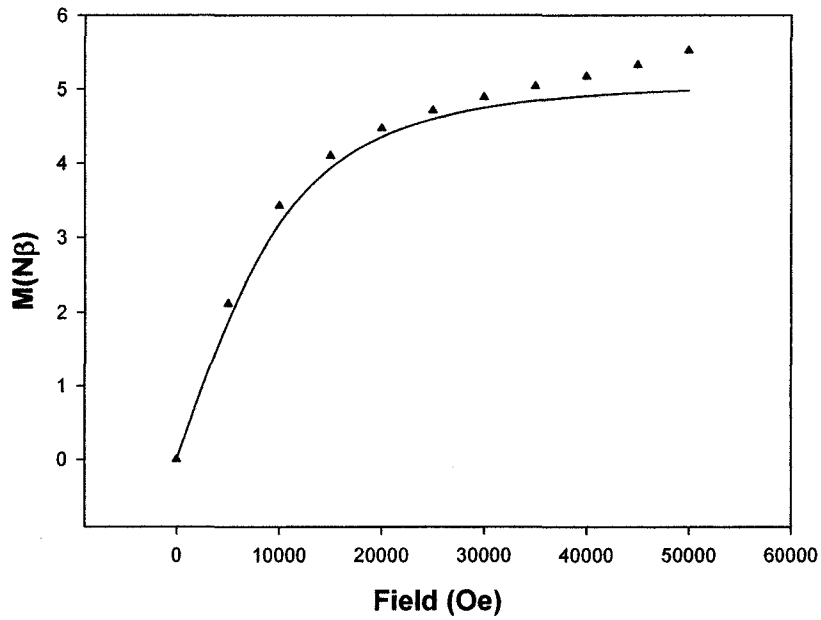

Fig. 6.13 Magnetization data as a function of field at 2K for **4**; The solid line is drawn to show a comparison and was calculated using the standard Brillouin function for S = 5/2 at g = 2.02.

The solid line is calculated for g = 2.02 and S = 5/2 at 2 K. This kind of behavior is typical for $Mn(II)_9$ grids, and it is associated with population of low lying excited states at higher magnetic fields [110].

The intramolecular coupling constants are consistent with the large Mn-O-Mn bridge angles. The fact that the data in each case were reproduced accurately over the whole temperature range indicates that the chain model is reasonable down to 2K, and the results are consistent with similar grids e.g. $[Mn_9(2poap\text{-}2H)_6](ClO_4)_6(H_2O)_{18}$ and $[Mn_9(Cl2poap\text{-}2H)_6](ClO_4)_6(H_2O)_{10}$ [111]. The terminal $-CH_3$ group on the ligand

(Scheme 6.1) apparently does not have any significant effect on the structure and magnetic properties within the grid. In addition it has been shown with a more in-depth analysis of the mixed oxidation state grid $[Mn(III)_4Mn(II)_5(2poap\text{-}2H)_6](ClO_4)_{10}(H_2O)_{10}$ that the exchange integral between the ring and the central Mn(II) ion (J_C) is not zero, rather the two exchange integrals are comparable in magnitude [87]. This would be reasonable also for complexes **1-4**.

6.5 Conclusion

Four nonanuclear $Mn(II)_9$ grids are reported in this chapter. **3** and **4** have been structurally characterized. All of the complexes behaved magnetically like previously characterized nonanuclear $Mn(II)_9$ grids. Complex **3** contained two mononuclear $MnCl_4^{2-}$ anionic units in addition to the nonanuclear grid in the unit cell. The presence of the extra magnetic centers did not complicate the magnetic situation other than increasing both the room temperature and low temperature magnetic moments to higher values than usual (17 μ_B at room temperature dropping to 6 μ_B corresponding to an S = 5/2 ground state). The magnetic data for all the complexes could be fitted well to a Fisher chain model which treats the $Mn(II)_9$ grid as composite of an octanuclear chain plus an isolated Mn(II) center. The Mn(II) centers in the outer eight membered rings in the grid are antiferromagnetically coupled with an average $-J_R$ of 4.0-4.6 cm^{-1}.

CHAPTER 7

Complexes of semi flexible polydentate ligands - example of an octanuclear inorganic [2] catenane

7.1 Introduction

Singly or doubly intertwined macrocyclic catenanes have intrigued synthetic chemists since their first successful synthesis by Wasserman following a statistical method [147]. Catenanes are interesting not only because of their topological beauty but also for the fact that they form by an intricate molecular self-assembly, which had been a challenge for synthetic chemists for decades by classical synthetic routes [148-149]. Unlike other self-assembled molecules, the catenanes contain covalent bonds which are robust. The use of labile metal-ligand coordination bonds allows the synthesis and isolation of this type of complexes with high yield under thermodynamic control. Figure 7.1 conveys the structural specificities of catenanes and gives a comparison with some other members of interlocking ring systems.

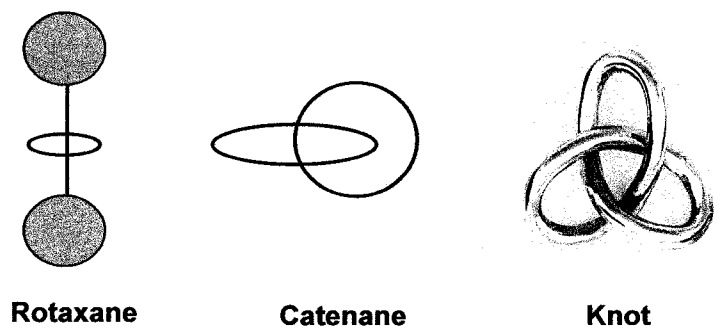

Fig. 7.1 Structural features of rotaxanes, catenanes, and molecular knots.

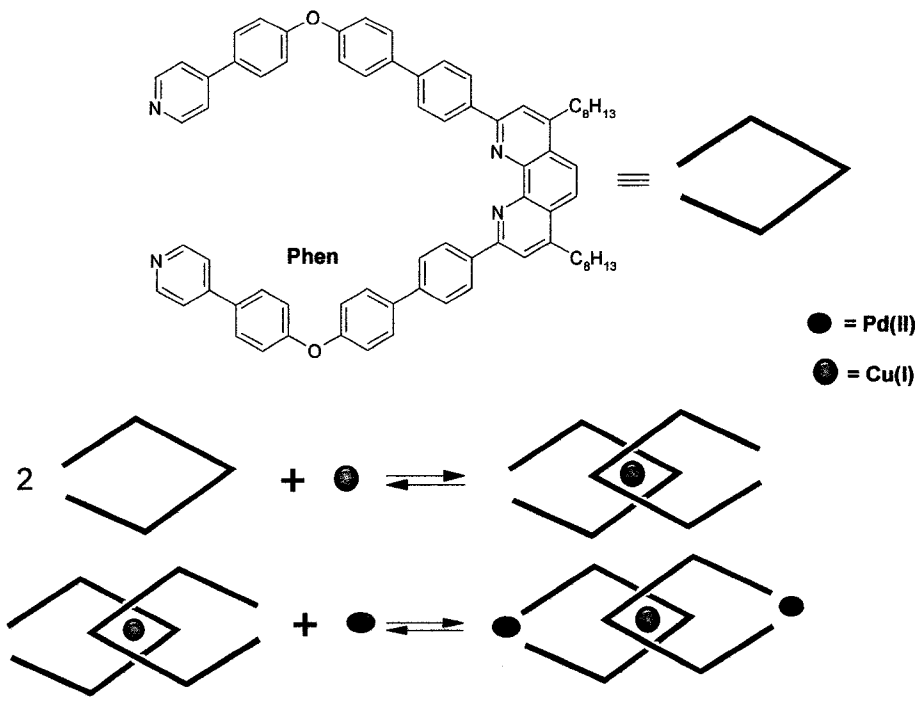

Scheme 7.1 Cyclisation and clipping off of catenane ring.

Several new synthetic strategies have led to the synthesis of molecular clusters with increasingly intricate topology. Sauvage et al. developed the first synthetic route to catenanes taking advantage of pre-organization by a metal template [150]. Metal atoms such as Li [151], Ru(II) [152], Rh(III) [153], Zn(II) [154], Cu(I) and Pd(II) [155], and Ni(I) [156] have been reported as metal templates in catenane synthesis. More organic-like catenanes have been synthesized by Stoddart et al. exploiting the charge transfer interactions between electron deficient and electron rich species [157]. Scheme 7.1 shows an example of a chelating ligand 'phen' (1,10-phenanthroline) affording a cyclisation between two rings with Cu(I) as the templating ion [155].

The first example of an organometallic catenane was an organo-magnesium complex [158]. Organo-gold catenanes have also been reported by Puddephatt and co-workers [159]. The basis for the formation of most of the organo-gold catenanes is the Au...Au aurophilic attraction between diacetylide digold rings, leading to two intertwined rings clipped by diphosphine ligands. The degree of catenation, ring size and the ultimate outcome of the catenated product depended solely on the size of the oligomeric di-gold (I) diacetylide and the spacer group in the diphosphine ligand [160]. Acetylide based macrocycles have shown promise in constructing optical devices [161], and luminescent chemical sensors [162]. Other techniques, which were successfully exploited for catenane formation, are the use of π-π interactions [163], anion templated self-assembly [164], affinity between electron rich and electron deficient homo or heteropolymetallic moieties [165] and hydrogen bonding [166]. Transition metal containing catenanes were found to be well suited to build molecular machines, which can be driven electrochemically or by light [167].

Oxalic dihydrazide based polydentate ligands, with flexible linker groups joining the terminal donor units, can exist in *cis* or *trans* conformations, and have the potential to bind metals in a variety of different ways (Fig. 7.2). Depending on the relative orientation of the terminal donor sets, self-assembly can lead to di- or polymetallic clusters or square and rectangular [2x2] grid complexes [70]. Tetranuclear square complexes were obtained due to the compartmental nature of the oxalic hydrazide group in reactions with transition metal salts like $CoBr_2$ and $Fe(ClO_4)_2$. Self-assembly led to a tetranuclear ring with four

metal centers at each corner of the tetragon having an N_4O_2 donor environment. This left a large void within the center of the complex.

Another kind of tetranuclear complex has also been observed with Ni(II) salts. Four octahedral Ni(II) centers are arranged in a tetrahedron without involving the oxalic hydrazide fragment. The ligand binds the metal centers using only the N-N terminal components. Large intermetallic separations in the cluster lead to a situation where there is no magnetic connectivity between metal centers. A remarkable exception is the synthesis of an octanuclear $Ni(II)_8$ complex which was synthesized from the ligand 'ppttp' (Fig. 7.2) on reaction with $Ni(BF_4)_2$ [71]. This cluster contained eight Ni(II) centers in a ring held by four ligands with only N-N bridging between metal centers leading to intramolecular anti-ferromagnetic exchange. A POVRAY© representation of the cluster was shown in Chapter 1 (Fig. 1.4).

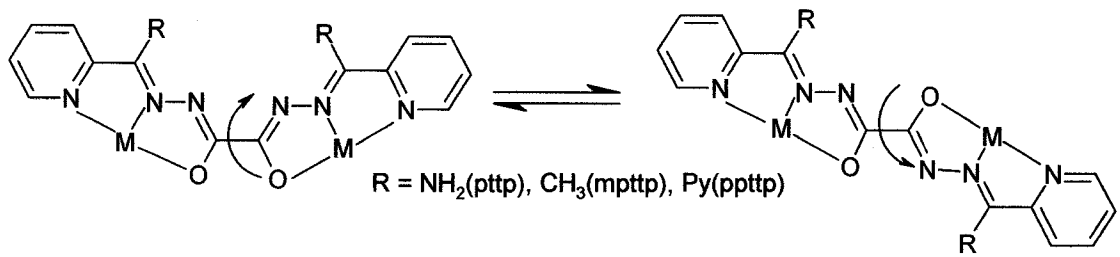

Fig. 7.2 Flexibility around C-C bond leading to different coordination mode.

This chapter presents the synthesis and characterization of a series of polymetallic complexes of a semiflexible polydentate ligand 'pttp' including a cobalt(II) [2] catenane.

7.2 Experimental

7.2.1 Materials

Commercially available solvents and chemicals were used without further purification.

7.2.2 Characterization

Analysis, spectroscopic and physical measurements were done according to the procedures described in Chapter 2.

7.2.3 Synthesis of the Ligands

pttp

The ligand pttp was prepared according to the published procedure [70]. Reaction of pttp with $Co(II)Br_2 \cdot 6H_2O$ and $Fe(II)(ClO_4)_2 \cdot 6H_2O$ salts in air gave the tetranuclear L_4M_4 [2x2] square complexes $[Co_4(pttp)_4]Br_6 \cdot 9H_2O$ (**1**) and $[Fe_4(pttp)_4](ClO_4)_6 \cdot 7.5H_2O$ (**2**) respectively. Details of those complexes have been published earlier [70].

7.2.4 Synthesis of complexes

$[Co_4(pttp\text{-}H)_4](NO_3)_6(CH_3OH)_4(CH_3CN) \cdot 9H_2O$ (3)

pttp (0.10 g, 0.31 mmol) was added to a warm solution of $Co(NO_3)_2.6H_2O$ (0.16 g, 0.55 mmol) in CH_3OH/CH_3CN (10 mL/10 mL). The resulting solution was stirred for several hours. The resulting dark red-brown mixture was filtered and the solution was kept for crystallization by slow evaporation of the solvent. Deep red crystals were isolated in good yield after several weeks (Yield 70%). Anal. Calc. (%) for

$[Co_4(C_{14}H_{13}N_8O_2)_2\ (C_{14}H_{13}N_8O_2)_2](NO_3)_6(CH_3OH)_4(CH_3CN)(H_2O)_9$; C, 33.23; H, 4.00; N, 24.38. Found (%); C, 33.23; H, 3.13; N, 24.49.

$[Co_8(pttp\text{-}2H)_4\ (pttp\text{-}H)_4]\ [Co(SCN)_4]_2(SCN)_4 \cdot 13H_2O$ (4)

3 (0.035 g, 0.15 mmol) was dissolved in CH_3OH (~ 20 mL). A dark brown solution resulted. A methanolic solution of $NH_4(SCN)$ (0.100 g, 1.31 mmol in ~ 10 mL) was added to it and the mixture was stirred for several hours with warming. The colour of the mixture turned to a darker green brown. The final mixture was filtered and the solution was kept for crystallization. Dark black crystals suitable for x-ray diffraction were obtained (Yield 64%) by slow ether diffusion into the solution. IR (Nujol, cm^{-1}): 2059 (ν SCN^-), 1680,1658. Anal. Calc. (%) for $[(C_{14}H_{12}N_8O_2)_4(C_{14}H_{13}N_8O_2)_4Co_8]$ $[Co(SCN)_4]_2(SCN)_4(H_2O)_{13}$; C, 36.15; H, 3.09; N, 25.86. Found (%); C, 36.02; H, 2.58; N, 25.73.

$[Co(II)_3Co(III)(pttp)_2(pttp\text{-}H)_2]\ (BF_4)_7 \cdot 2H_2O$ (5)

pttp (0.15g, 0.5 mmol) was added to a solution of $Co(BF_4)_2.6H_2O$ (0.20 g, 0.5 mmol) in a mixture of solvents CH_3CN:CH_3OH:H_2O (~ 2:1:1 mL/mL). The resulting solution was stirred for 2 hours. Initially it formed a brown solution. The solution was kept for crystallization after filtration. Dark brown crystals were collected after two days. (Yield 18%). IR (Nujol, cm^{-1}): 1067 (ν BF_4^-). Anal. Calc. (%) for $[Co_4\ (C_{14}H_{13}N_8O_2)_2$ $(C_{14}H_{14}N_8O_2)_2]\ (BF_4)_7\ (H_2O)_2$; C, 30.81; H, 2.67; N, 20.53. Found (%); C, 30.68; H, 2.99; N, 20.57.

7.3 Crystallographic data collection and refinement of the structure

$[Co_8(pttp\text{-}2H)_4(pttp\text{-}H)_4][Co(SCN)_4]_2(SCN)_4 \cdot 13H_2O$ (4)

A dark black block crystal of approximate dimensions 0.45 x 0.21 x 0.16 mm was mounted on a glass fibre. All measurements were made on a Bruker P4/CCD system with monochromated Mo-Kα radiation and a sealed tube generator. The data were collected at 193 (1) K. The full hemisphere of data was collected to a maximum 2θ value of 53°. A total of 67989 reflections were taken and 37713 of them were considered unique. The data were corrected for absorption using a face indexed Gaussian integration algorithm with maximun and minimum effective transmissions of 0.8459 and 0.6416 respectively. The data were also corrected for Lorentz and polarization effects. The structure was solved by direct methods [99] and expanded using Fourier techniques [100]. Some non-hydrogen atoms were refined anisotropically, while the rest were refined isotropically. Hydrogen atoms were included in calculated positions but not refined. There are two hydrogen atoms missing from the two *trans* oriented ligands, which cary a one minus charge each. The *cis* oriented ligands carry a two minus charge each. A total of 27 hydrogen atoms missing from the model including 25 hydrogen atoms from the hydroxyls of the latice methanol and lattice water molecules. The maximum and minimum peaks on the final difference Fourier map corresponded to 2.63 and -1.25 $e^-/Å^3$ respectively. Neutral atom scattering factors [101] and anomalous-dispersion terms [102-103] were taken from the usual sources. All calculations were performed using the teXsan crystallographic software package [105 (a)] of Molecular Structure Corporation except for the refinement, which was performed using SHELXL-97 [99].

7.4 Results and Discussion

7.4.1 Structures

$[(C_{14}H_{12}N_8O_2)_4(C_{14}H_{13}N_8O_2)_4Co_8][Co(SCN)_4]_2(SCN)_4 \cdot 13H_2O$ (4)

A crystallographic summary for the complex **4** is provided in Table 7.1 and important bond distances and bond angles are listed in Table 7.2. Two tetracobalt [2 x 2] square grid subunits, derived from four metal centers and four ligands, intersect each other in a self-assembled manner to give a mono-braided catenane complex. A close inspection of the Co-Co distances within each ring reveals that the 'squares' are slightly distorted with unequal Co-Co distances (Co(1)-Co(4) 6.723 Å, Co(6)-Co(7) 6.721 Å, Co(2)-Co(3) 7.164 Å, Co(5)-Co(8) 7.220 Å), consistent with the side by side arrangement of Co(II) and Co(III) pairs in each ring respectively. The structure of each component tetragon is similar to that observed in **1**.

Closer inspection of the metal-ligand bonds reveals that Co(1) (Av. 1.905 Å), Co(4) (Av. 1.893 Å), Co(6) (Av. 1.898 Å) and Co(7) (Av. 1.892 Å) have very short contacts typical of Co(III), while Co(2) (Av. 2.107 Å), Co(3) (Av. 2.104 Å), Co(5) (Av. 2.110 Å), and Co(8) (Av. 2.114 Å) have comparatively much longer contacts typical of Co(II). A full structural representation of the complex is shown in Fig. 7.3 while the core structure of the catenane is depicted in Fig. 7.4 with the aromatic rings abbreviated to just the immediate donor atoms. To support the oxidation state assignment, Bond Valence Sums (BVS) were calculated for each of the metal centers [168]. Details of the values are given in Table 7.4.

Table 7.1 Summary of crystallographic data for complex **4**

Empirical Formula	$C_{132}H_{149}O_{32}N_{76}S_{12}Co_{10}$
Formula Weight	4286.17
Crystal Color, Habit	Black, block
Crystal Dimensions	0.45 X 0.21 X 0.16 mm
Crystal System	Triclinic
Lattice Type	Primitive
Lattice Parameters	a = 17.359(2) Å b = 20.870(2) Å c = 27.545(2) Å α = 81.671(1) ° β = 84.037(2) ° V = 9282(1) Å^3
Space Group	P-1 (#2)
Z value	2
D_{calc}	1.534 g/cm^3
F_{000}	4382.00
μ(MoKα)	10.91 cm^{-1}
Temp (K)	193 ± 1
R1	0.087
wR2	0.302

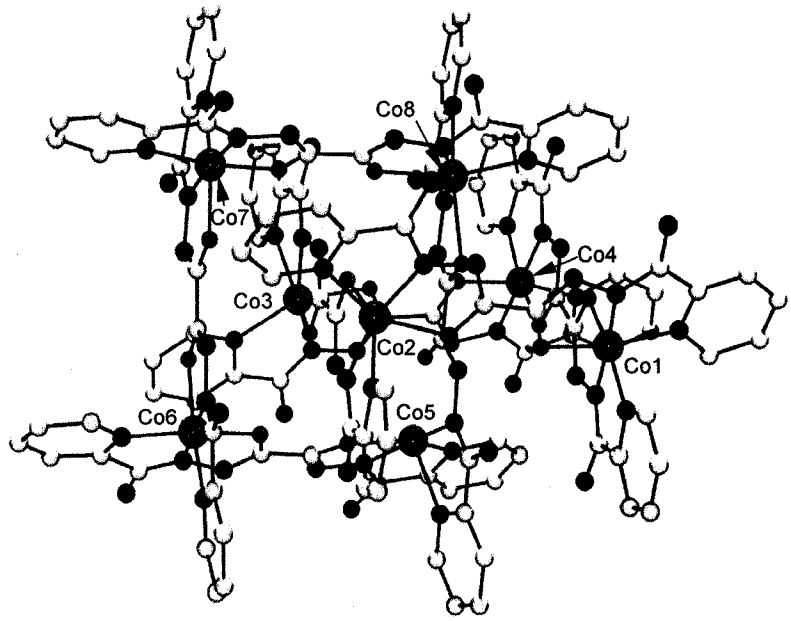

Fig. 7.3 POVRAY© representation of the catenane **4**

The bond valance sum offers a relatively simple method for determining the oxidation state of a particular metal center in a complex. The basics include the concept that the valence of an atom or ion can be defined in terms of the sum of the individual bond valences around that atom. The BVS result shows that all four metal ions along the catenated intersection correspond to Co(II) (Av. BVS 2.35-2.39), while the other four Co centers on the periphery of the two intersecting rings have much higher values (Av. BVS 4.05-4.18) and clearly correspond to the Co(III) state. At this point it is not clear why the +III oxidation state for Co in this system has such a high BVS value, but there is no evidence to suggest Co(IV). Complex **1** has average BVS values of 2.3 and 3.9 for Co(II) and Co(III) sites respectively, and a comparison with other $[Co(II)_4]$ and $[Co(II)_2Co(III)_2]$ systems with similar ligands reveals comparable values [58-59].

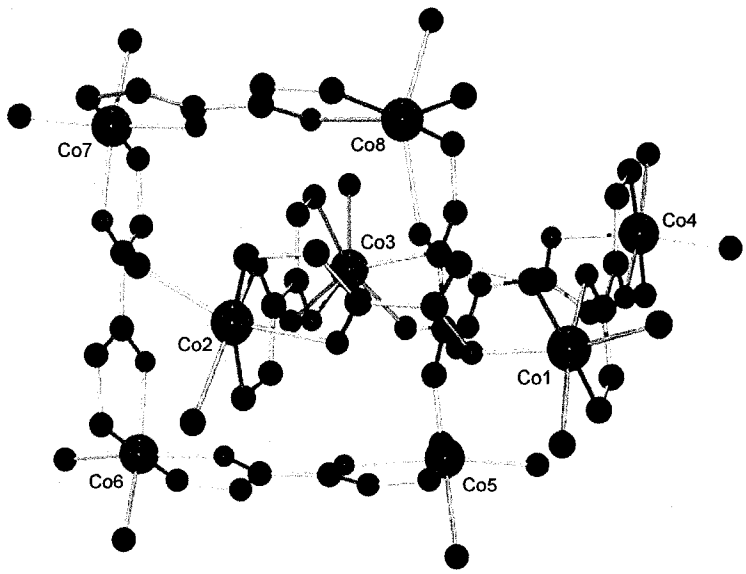

Fig. 7.4 Solid state core structure of the [2] catenane **4** (color code: magenta = cobalt, blue = nitrogen, red = oxygen, black = carbon). Terminal pyridine rings are abbreviated as single nitrogen (blue) atoms.

Each ligand has two readily ionizable protons associated with the oxalic hydrazone fragment. So, a charge balance in **4** would require a total of 12 negative charges distributed over the eight ligands. The external NH_2 groups are unlikely to deprotonate. Two hydrazone NH protons appear in difference maps in the central portion of the catenane structure in the region where the four Co(II) centres are situated. A number of significant hydrogen bonds have been located in this region also (Fig. 7.5, dotted lines), and the figure highlights this important element in the stabilization of the catenane structure. Figure 7.6 shows a segment of the crystal packing diagram for the complex. The overall structure also reveals four SCN^- anions, and two $[Co(SCN)_4]^{2-}$ units in the lattice in addition to solvent.

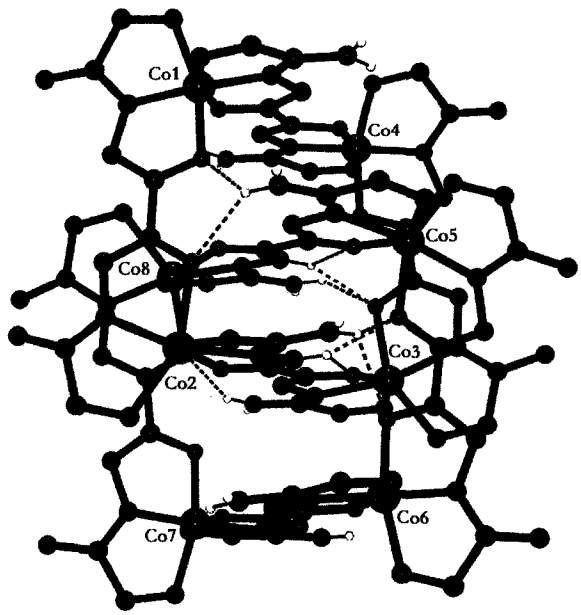

Fig. 7.5 Hydrogen bonding network between the two building blocks of the catenane.

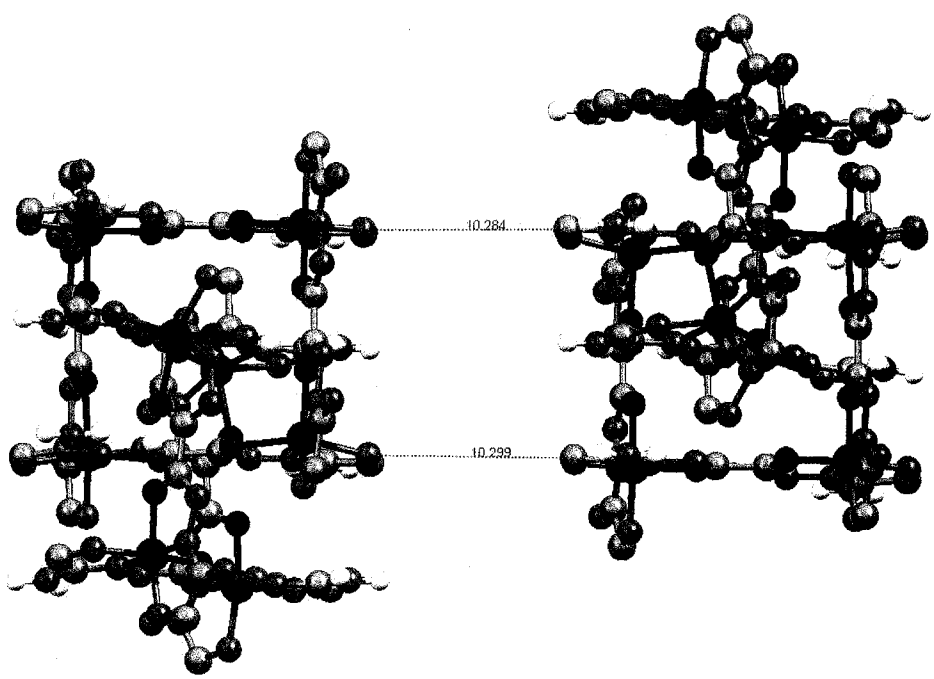

Fig. 7.6 A segment of crystal packing in catenane **4**

Table 7.2 Important Bond distances (Å) for **4**

Co1	N30	1.845(7)	Co4	O6	1.900(5)
Co1	N3	1.853(7)	Co4	O7	1.907(5)
Co1	O1	1.913(5)	Co4	N25	1.923(7)
Co1	O8	1.926(5)	Co4	N24	1.923(7)
Co1	N1	1.945(7)	Co5	N35	2.002(6)
Co1	N32	1.949(6)	Co5	N62	2.064(6)
Co2	N11	2.042(6)	Co5	O9	2.105(5)
Co2	N6	2.042(6)	Co5	N33	2.112(6)
Co2	N8	2.109(6)	Co5	N64	2.161(7)
Co2	O2	2.146(5)	Co5	O16	2.218(5)
Co2	O3	2.152(5)	Co6	N43	1.853(6)
Co2	N9	2.153(6)	Co6	N38	1.857(6)
Co3	N19	2.032(6)	Co6	O10	1.887(4)
Co3	N14	2.050(6)	Co6	N40	1.921(6)
Co3	N17	2.106(6)	Co6	O11	1.925(5)
Co3	O5	2.119(5)	Co6	N41	1.951(6)
Co3	N16	2.149(7)	Co7	N51	1.842(6)
Co3	O4	2.167(5)	Co7	N46	1.848(6)
Co4	N27	1.850(7)	Co7	O13	1.884(4)
Co4	N22	1.854(8)	Co7	O12	1.907(5)

Co7	N48	1.929(6)	Co9	N67	1.914(9)
Co7	N49	1.942(6)	Co9	N65	1.928(12)
Co8	N54	2.001(7)	Co9	N68	1.961(8)
Co8	N59	2.048(6)	Co9	N66	1.969(11)
Co8	O14	2.122(5)	Co10	N70	1.940(8)
Co8	N56	2.155(7)	Co10	N69	1.952(10)
Co8	N57	2.157(7)	Co10	N72	1.954(10)
Co8	O15	2.202(5)	Co10	N71	1.985(12)

Co1	Co2	6.673 Å	Co5	Co6	6.551 Å
Co1	Co4	6.723 Å	Co5	Co8	7.220 Å
Co2	Co3	7.164 Å	Co6	Co7	6.721 Å
Co3	Co4	6.577 Å	Co7	Co8	6.592 Å

Table 7.3 List of Hydrogen bonding contacts (N – O) for **4**

N10… H6…O9	1.98	N58…H29…O6	2.26
N10…H6…O10	2.44	N58…H30…O30	2.32
N15…H7…O13	2.40	N63…H32…O1	2.17
N15…H7…O14	2.14	N63…H32…O2	2.40

Table 7.4 Bond Valence Sum (BVS) calculations for **4** and **1**

Atom	**BVS values**		**Ligand environment**
	4	**1**	
Co1	4.058 (+III)	2.30	N_4O_2
Co2	2.37	2.29	
Co3	2.39	3.806 (+III)	
Co4	4.175 (+III)	4.085 (+III)	
Co5	2.37		
Co6	4.113 (+III)		
Co7	4.18 (+III)		
Co8	2.35		

7.4.2 Mechanistic suggestions for catenane formation

Reaction of pttp with Co(II)$Br_2 \cdot 6H_2O$ and Fe(II)$(ClO_4)_2 \cdot 6H_2O$ salts in air gave the tetranuclear L_4M_4 [2 x 2] square complexes $[Co_4(pttp)_4]Br_6 \cdot 9H_2O$ (**1**) and $[Fe_4(pttp)_4](ClO_4)_6 \cdot 7.5H_2O$ (**2**) respectively [70]. Partial oxidation occurred in both cases with the formation of $[M(II)_2M(III)_2]$ (M = Co, Fe) derivatives. Reaction of pttp with $Co(NO_3)_2.6H_2O$ in CH_3OH/CH_3CN solvent mixture in air gave the dark red crystalline [2 x 2] grid complex $[(pttp)_4\text{-}4H)Co(III)_2Co(II)_2](NO_3)_6(CH_3OH)_4(CH_3CN)(H_2O)_9$ (**3**), confirmed by elemental analysis and magnetic measurements. Exposure of the reaction mixture to air led again to oxidation of two of the Co(II) centers, similar to the situation found for **1**.

Since the catenane was formed from a [2 x 2] self-assembled square grid precursor on reaction with SCN^-, the mechanism for catenane formation must involve a dynamic ligand dissociation/association process and a grid-ring opening. Transition metal-ligand bonds are fairly labile in nature, and do remain intact under ordinary conditions, but can become 'reversible' in highly polar media, and at elevated temperatures [169]. In the present case, where methanol was used as solvent, the presence of the strong donor SCN^- ligand, even at room temperature it is likely to lead to some dissociation of the pttp coordination bonds in **3**. Such dissociation is more likely to occur at the Co(II) sites, which are more labile than Co(III) sites, because of relatively weaker M-L bond strength compared to Co(III), and could lead to the opening of a [2 x 2] ring (unlocking). Insertion of an open ring through a complete ring would then occur, and lead to catenane formation by subsequent ring closure (locking).

A cartoon picture of the above mechanism is depicted in Scheme 7.2. Implicit in this suggestion would be the fact that one ligand dissociates at one end only prior to ring insertion, and that ring closing is accompanied by re-coordination of the ligand. The polar nature of the solvent medium may have favoured ring opening, but it is much more likely that the SCN^- ion is responsible for pttp dissociation, and coordination to a Co(II) centre in some oligomeric intermediate.

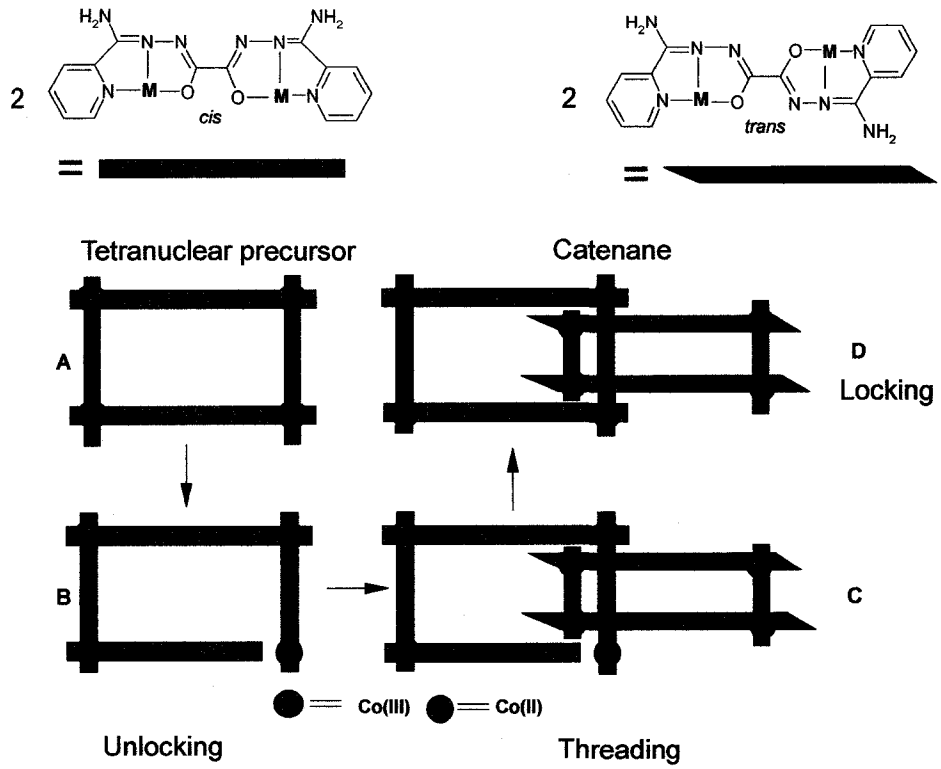

Scheme 7.2 Cartoon picture for formation mechanism of molecular lock.

The presence of the $[Co(SCN)_4]^{2-}$ ion in the lattice is good evidence for such a mechanism taking place, and indicates that thiocyanate actually scavenges Co(II). However, a 'Mobius strip' type mechanism, where intramolecular ligand exchange occurs between the intermediate structures, is not totally ruled out [170].

Another driving factor which may have influenced the catenane formation is 'space filling'. The tetranuclear complex 1 has a roughly square central void with dimensions of 6.7-7.0 Å between the oxygen atoms on the ligand [70]. Molecular boxes can undergo catenane formation if they posses a large enough cavity to allow resulting van der Waals'

separations between closely spaced atoms of ca. 3.5 Å [171-172]. The cavity size in the precursor **3** must therefore be close to this limit, and so the catenane framework might be stabilized by filling the cavity of one ring with another copy of itself [173] (Fig. 7.7).

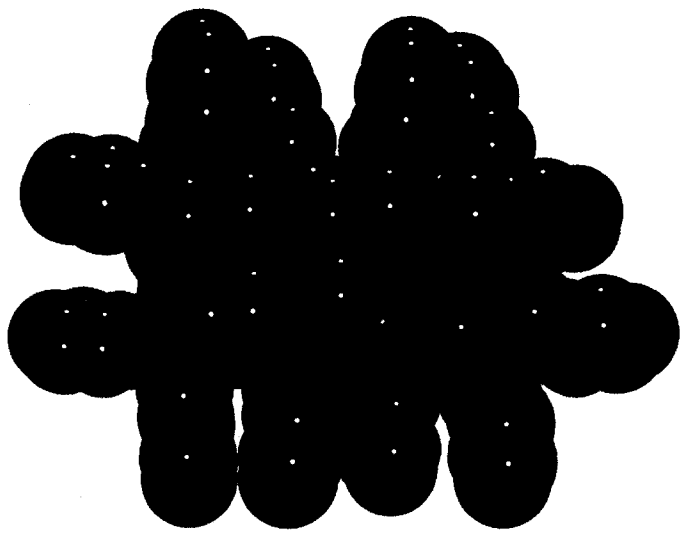

Fig. 7.7 Complete space filling structural representation of [2] catenane in **4** (Black = C, Blue = N and Red = O)

However the significant hydrogen bonding interactions in the region where the rings interpenetrate (N-H---O contacts with N-O distances from 1.98 Å to 2.44 Å (Fig. 7.5)), suggest that a significant driving force for stabilization of the catenane structure must come from these hydrogen bonds. A list of possible hydrogen bonds is provided in Table 7.3.

7.4.3 Magnetism

The reaction between the ligand 'pttp' and $Co(NO_3)_2.6H_2O$ to form **3** was repeated several times under similar reaction conditions in an effort to get x-ray quality crystals. Variable temperature magnetic studies were carried out on bulk samples from each batch. The magnetic moment per mole of a bulk sample of **3** indicates (Fig. 7.8) a room temperature magnetic moment of 7.49 μ_B with a steady rise in moment when the temperature is lowered, until it reaches a maximum of 7.83 μ_B at 80 K . Finally the moment drops to 6.14 μ_B at 2 K. The room temperature magnetic moment is not consistent with the presence of four high spin octahedral Co(II) centers.

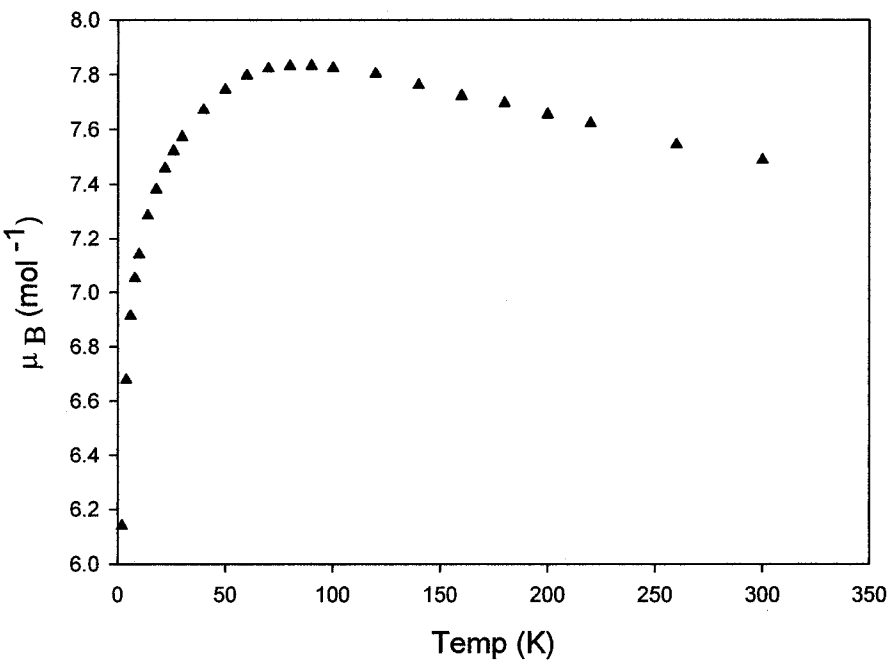

Fig. 7.8 Variable temperature magnetic profile for **3**

The magnetic moment per metal ion, assuming four paramagnetic centers would be 3.74 μ_B which seems very low for octahedral Co(II). Typical values range from 4.7 μ_B to 5.2

μ_B [82]. Recalculation of the data assuming two Co(II) centers and two Co(III) gives a moment of 5.3 μ_B per metal which is much more sensible. So it is apparent that partial oxidation has occurred in **3**. This is not unlikely for cobalt complexes formed and isolated in air.

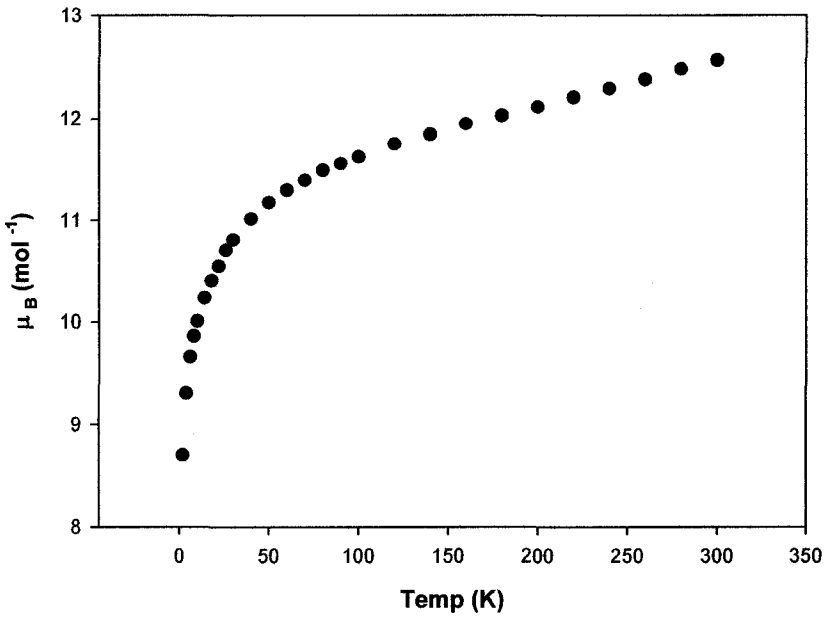

Fig. 7.9 μ_B (per mol) vs temperature profile for **4**

The complex **4** contains four Co(III) centers (Co(1), Co(4), Co(6) and Co(7), Fig. 7.4) which are diamagnetic. A clear picture of the catenane structural framework is shown in Fig. 7.4. The Co(III) centers lie along the two opposite edges of two rings. Four Co(II) centers lie along the other two sides of each ring where they intersect. So magnetically the structure resembles two [$Co(II)_2$] dinuclear subunits (Co(2)-Co(3) and Co(5)-Co(8)) which are fairly close to each other. The distances between the two Co(II)

centers in the same ring are 7.164 Å (Co2-Co3) and 7.220 Å (Co5-Co8) respectively. No magnetic interaction is expected over such a long bond distance. Within the central hydrogen bonded framework, Co(2) and Co(3) are quite close to Co(8) and Co(5) (Co(2)-Co(8) 5.165 Å and Co(3)-Co(5) 5.116 Å) which might give rise to very weak magnetic interactions. Besides that, the structure also contains two $[Co(SCN)_4]^{2-}$ anionic units which will act as paramagnetic centers and contribute to the overall magnetic moment.

The variable temperature magnetic profile shows (Fig. 7.9) a moment of 12.6 μ_B at 300 K, which corresponds reasonably to a total of six Co(II) centers [2Co(II)-Co(II) + 2Co(II)]. The overall profile shows a small drop to 11 μ_B at ~ 50 K followed by a more precipitous drop down to 8.7 μ_B at 2 K. Such behavior could be consistent with very weak anti-ferromagnetic coupling between the Co(II) centers. However, the drop in moment could also be associated with zero field splitting (D). No attempts were made to fit the magnetic data in terms of any superexchange model.

The complex **5** shows a similar magnetic profile to **3**. The room temperature moment is 7.81 μ_B which slowly rises to a plateau of 8.0 μ_B around 50 K and then finally drops more profoundly to 6.48 μ_B. It is apparent from the room temperature magnetic moment that less aerial oxidation has occurred in this complex. The room temperature moment gives 3.9 μ_B per metal if we consider four octahedral Co(II) centers. But recalculation of the moment with the assumption that at least one cobalt center has oxidized, gives 4.5 μ_B per metal which is not unreasonable. As no precautions were taken

to avoid oxygen from air during the synthesis of these complexes, it is perhaps no surprise that aerial oxidation has occurred in all of the cobalt complexes, but to a variable extent.

7.4.4 Other complexes with pttp type ligand

Several other reactions of the ligand pttp were carried out with different transition metals such as Mn(II) and Ni(II). In most cases, solid powdery precipitates were collected. However, the variable temperature measurements done on the bulk samples do indicate that the ligand produced polynuclear complexes. Mass spectra and elemental analyses were inconclusive for a full characterization of these complexes.

7. 5 Conclusion

Three complexes are reported with the oxalic dihydrazide based ligand 'pttp'. Two of them are regular tetranuclear complexes while one is an octanuclear Co_8 catenane in which two tetranuclear rings are joined together. Even though organic and organometallic catenanes are common, inorganic catenanes with transition metals acting as backbones are scarce. This is in fact the first example of an inorganic cobalt catenane. The catenane was formed from a preformed tetranuclear cobalt complex. One of the rings in the tetranuclear precursor appeared to have opened in the presence of SCN^-, threaded through another ring and then closed. Extensive hydrogen bonding has been revealed in the structure which suggests that these hydrogen bonds have helped to stabilize the 'ring-in-a-ring' structure by locking the two rings along their intersection.

Air oxidation has been observed in almost all of the cobalt complexes. Aerial oxidation is normal for cobalt complexes synthesized in air. Very weak or insignificant magnetic coupling was observed in all of the cobalt complexes, which is attributed to very long inter-metal distances. The metal centers are coordinated by two end pockets of each ligand, which results in a five bond distance between coupled metal centers.

CHAPTER 8

Structure and magnetic properties of a self-assembled high nuclearity complex - a spheroidal triakontahexanuclear Cu_{36} cluster

8.1 Introduction

The self-assembly approach to nano-scale poly-metallic clusters has led to the syntheses of many high nuclearity species. Complexes containing 24 metal centers *e.g.* Ni_{24} [174] and Co_{24} [175] were reported by Winpenny *et al.* using simple ligand mixtures such as Hmpo (3-methyl-3-pyrazolin-5-one) and Hmhp (2-methyl-6-hydroxypyridine) (Scheme 8.1) with nickel acetate and cobalt chloride respectively. In synthesizing the above two complexes, the authors took advantage of a process called 'serendipitous assembly' where the element of strict design is absent [176]. Fe_{17} and Fe_{19} clusters by Powell [177-178], using imino poly-carboxylic acids (e.g. H_3heidi; Hydroxyethyliminodiacetic acid) as the primary ligand are other relevant examples. The Ni_{24} cluster is the result of a set of complicated interactions between the Hmpo and acetate ligands, which led to very weak antiferromagnetism within the metal array. Other auxiliary ligands, *e.g.* OH^-, O^{2-}, H_2O, solvent, were also incorporated into the non-homoleptic clusters, as they form from anionic components and solvent fragments.

The chelating nature of the imino poly-carboxylic acid based ligands (e.g. H_3heidi, H_3metheidi, H_3etheidi) (Scheme 8.1) has been well exploited to encourage the formation of large metal arrays. Ways of manipulating the supramolecular exchange interactions have been demonstrated by making small changes to the auxiliary groups of the parent ligand, and by changing the choice of anion (e.g. NO_3^-, Cl^-) leading to well engineered arrays of ordered magnetic particles [177]. Using nitrilodipropionic acid (H_3ndpa) and nitrilotripropionic acid (H_3ntpa) (Scheme 8.1) has enabled Powell and her group to synthesize two large Cu(II) aggregates; a $Cu(II)_{36}$ [75] and a $Cu(II)_{44}$ [76] respectively. Both clusters showed Curie-Weiss type behavior above temperatures around 60 K. Adopting a similar strategy, Murrie *et al.* synthesized a $Ni(II)_{21}$ cage using citrate as the ligand, which is a very recent addition to this class of clusters [179].

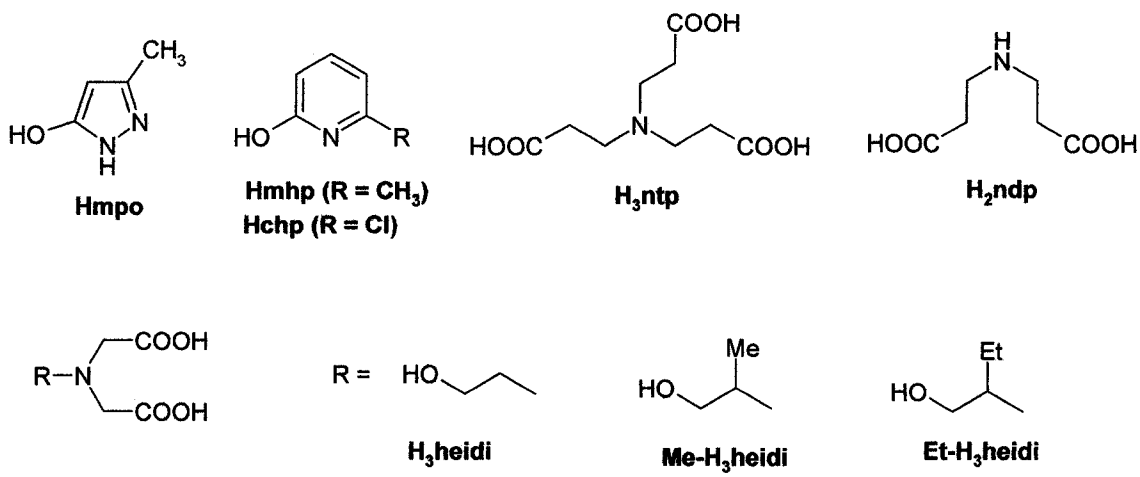

Scheme 8.1

Relying on the 'serendipitous assembly' approach has allowed the synthesis of a new class of polynuclear metal 'cages' as shown by Winpenny and his co-workers. In this approach, ligands are allowed to use several different coordination modes, unlike in designed self-assembly. Many of these approaches take advantage of the creation of a mismatch between the number or type of coordination sites available on the single metal site and the donor set rendered by the ligand. In these attempts, the rich coordination chemistry of the very simple ligand 'chp' (6-chloro-2-pyridonate) and its derivative 'mhp' (6-methyl-2-pyridonate) (Scheme 8.1) has been revealed. The ligand itself or as a mixture with a variety of carboxylates resulted in a number of polynuclear metal cages when combined with transition metal ions such as Ni(II), Co(II). Two isostructural dodecanuclear $\{Ni_{12}\}$[73] and $\{Co_{12}\}$[180] cyclic polynuclear wheels have been reported to result from the ligand 'Hchp' (Scheme 8.1). Both complexes contain intersecting M_2O_2 rings similar to the 'decanuclear' ferric $\{Fe_{10}\}$wheel [181] in which fundamental structural subunits are additionally bridged by carboxylate bridges (e.g. acetate). Both the wheels showed ferromagnetic exchange interactions with ground states $S_T = 12$ for nickel and $S_T = 6$ for cobalt.

In comparison to the heteroleptic clusters obtained from serendipitous assembly, homoleptic systems are much more difficult to create, and require the preprogramming of essential coordinating elements into the ligands. However, a pool of square, self-assembled tetranuclear [2 x 2] $[M_4(\mu\text{-}O)_4]$ grid-like structures (M_4, M = Mn, Co, Ni, Cu) has been obtained with ditopic ligands like 'poap' (Scheme 8.2), in

which the close proximity of the metal ions led to magnetic exchange within the grids [58-59, 123]. Ditopic ligands were extended to tritopic ligands by including an extra pocket, (*e.g.* R2poap; Scheme 8.2). This created a suitable framework for the formation of [3 x 3] $[M_9(\mu\text{-}O)_{12}]$ homoleptic, square nonanuclear grids (M_9, M = Mn, Fe, Co, Ni, Cu, Zn) in high yield by self-assembly reactions [65, 107-108]. These systems exhibited intramolecular antiferromagnetic (for Mn, Co, Ni), and ferromagnetic (for Cu) exchange resulting from the close proximity of the metal centers with an alkoxide bridge. Several related non-magnetic, homoleptic grids such as a Ag_9 and a Pb_{16} have been produced with polytopic extended pyridazine and pyrimidine based ligands [17, 22].

Tritopic ligands of this type contain a contiguous linear arrangement of coordination pockets, which form five-membered chelate rings upon coordination with transition metals. This makes them ideal templates for programmed self-assembly. As the geometrical features of the donor groupings are preprogrammed into the coordination pockets of the ligand's backbone, the complexes become a logical and predictable outcome. Following a similar strategy, extension of ligands to form larger grids, *e.g.* M_{16}, M_{25} *etc.*, is possible, but this has turned out to be quite a synthetic challenge. A 4 x [2 x 2] $Mn(II)_{16}$ square grid with a pyridazine based tetratopic ligand has been reported very recently [182]. However, putting terminal substituents, with the potential for additional bridging interactions, on the end of a basic ligand framework, *e.g.* an oxime group in dpocco, is comparatively straightforward (Scheme 8.2), and

presents the possibility of extending the nuclearity of a grid assembly or perhaps linking grid subunits together. This chapter will present two polynuclear metal complexes of a tritopic ligand 'dpocco' and its analogue 'Cl-dpocco'. The structural details of the $Cu(II)_{36}$ complex will be presented in detail and variable temperature magnetic properties will also be discussed. The complex contains an assembly of Cu_3-(μ_3-O) triangular subunits (Scheme 8.2).

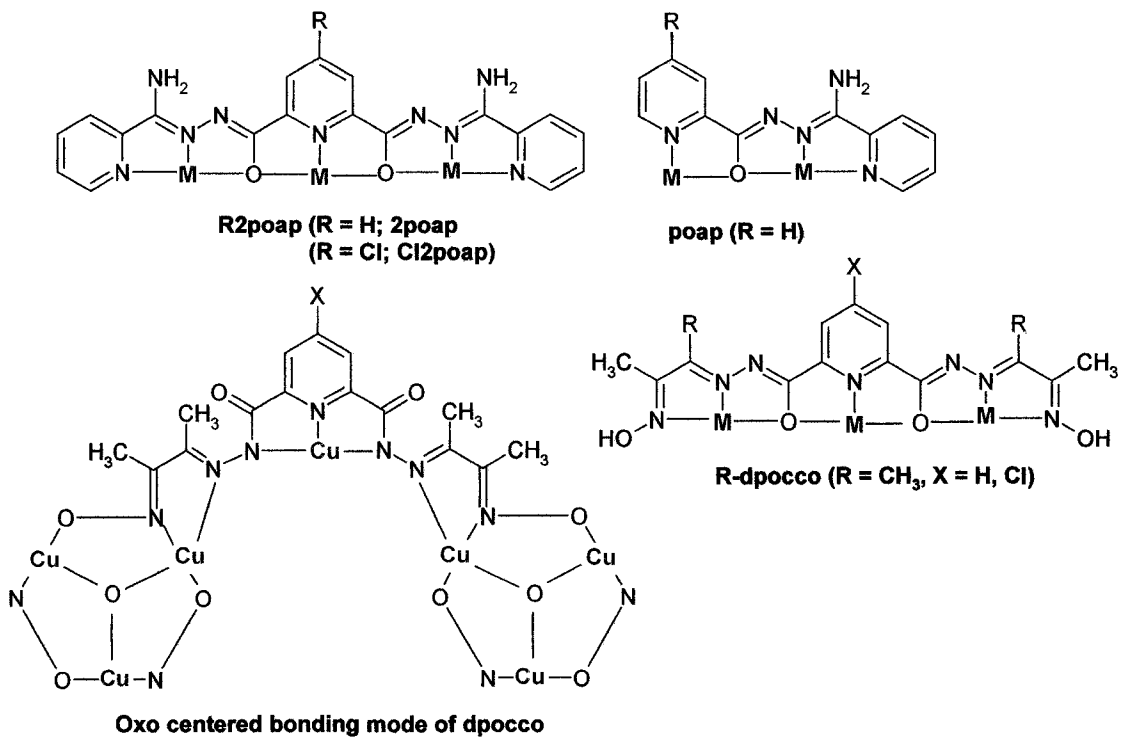

Scheme 8.2 Tritopic ligands and their functionalized derivatives adopting different conformations.

Oxo-centered trinuclear subunits where an OH group or O^{2-} takes the central position of a triangular metal array have been of great interest from a magnetic, structural and theoretical point of view. Several such trinuclear oxo-centered [M_3O] complexes have been reported in the literature, with different transition metals (M = Mn(II) [183], mixed valence Fe(III)/Fe(II) [183-184], Cu(II) [185-186]). A variety of different simple ligands with oxime functional group ends such as pyridine-2-carbaldehyde oxime [185], 3-(phenylimino)-butanone-1-oxime ((b) Fig. 8.1), and 1,2-diphenyl-2-(methylimino) ethanone-1-oxime ((c) Fig. 8.1) [186], even simple tri-substituted carboxylates R_3CCOO (R = CH_3, Ph) ((a) Fig. 8.1) [184] or a mixture of carboxylates and neutral donor groups (e.g. pyridine) [183] self-assemble in a concerted fashion to form the arms of a polymetallic triangular network.

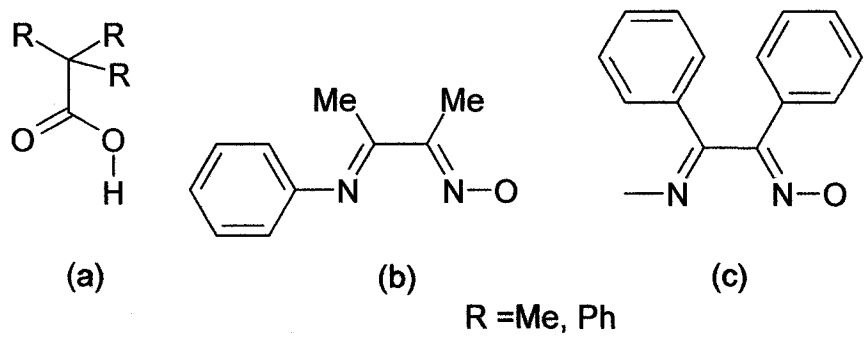

Fig. 8.1 Single ligands bearing carboxylic acid and oxime ends.

Fig. 8.1 shows some examples of ligands bearing oxime ends and carboxylic acid ends, which acted as the building blocks in the formation of oxo-centered trinuclear complexes. Certain structural features were found to influence the overall magnetic coupling within the complex. These include M-O-M bridge angles, planar-

tetrahedral distortions [187-192], coplanarity of the principal ligand planes [193] and strength of the bridging bonds [194]. However, high planarity in oxime bridged units had been shown to provide the strongest coupling [195]. Fig. 8.2 shows the basic framework of the triangular subunit built by oxime ends of the ligand pyridine-2-carbaldehyde oxime in an oxo-centered trinuclear complex [196].

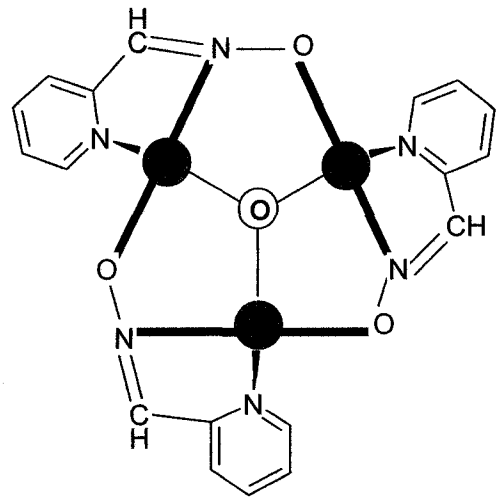

Fig. 8.2 A pictorial representation of the basic framework of the triangular subunit built by oxime ends of the ligand pyridine-2-aldehyde oxime in a oxo-centered trinuclear complexes.

8.2 Experimental

8.2.1 Materials

Commercially available solvents and chemicals were used without further purification.

8.2.2 Characterization

Analysis, spectroscopic and physical measurements were carried out according to the procedure described in Chapter 2.

8.2.3 Synthesis of the Ligands

The synthesis of the ligands dpocco and Cl-dpocco were prepared according to the procedure given in Chapter 2.

8.2.4 Synthesis of the complexes

$[Cu_{36}(dpocco\text{-}4H)_{12}(\mu_3\text{-}OH)_8](CH_3COO)_{16}]\cdot 96H_2O$ (1)

dpocco (0.18 g, 0.50 mmol) was added to a solution of copper(II) acetate (0.40 g, 2.0 mmol) in MeOH/H_2O (20 mL/5 mL) with stirring at room temperature. After stirring for 12 h the solution was filtered and kept for crystallization. Dark greenish black crystals suitable for x-ray analysis were obtained after a week (Yield 12.5%). Anal. Calc. (%) for $[(C_{15}H_{15}N_7O_4)_{12}Cu_{36}](OH)_8$ $(CH_3COO)_{16}(H_2O)_{96}$; C, 27.13; H, 4.59; N, 12.54. Found (%); C, 26.83; H, 3.84; N, 12.42.

$[Cu_{36}(Cldpocco\text{-}4H)_{12}](OH)_{21}(CH_3COO)_3\cdot 95H_2O$ (2)

Cl-dpocco (0.100 g, 0.25 mmol) was added to a solution of copper(II) acetate (0.22 g, 1.0 mmol) in MeOH/H_2O (2:1 v/v) with stirring at room temperature. After stirring for few hours the solution was filtered. Greenish black crystals were obtained after a week (Yield 10%). Anal. Calc. (%) for $[(C_{15}H_{14}N_7O_4Cl)_{12}$ $Cu_{36}](OH)_{21}$ $(CH_3COO)_3(H_2O)_{95}$; C, 24.19; H, 4.23; N, 12.74. Found (%); C, 24.18; H, 2.54; N, 12.80.

8.2.5 Other reactions carried out with dpocco

Several other reactions of the ligand dpocco and Cl-dpocco were carried out with different transition metal salts other than copper such as Mn(II), Mn(III), Co(II), and Ni(II). In most cases, solid powdery precipitates were collected. Single crystals could not be grown due to solubility issues and due to the fact the ligand is unstable in the presence of aqueous solvents and starts to decompose if kept for extended periods of time for crystallization. However, variable temperature magnetic measurements done on the bulk samples do indicate that the ligand produced polynuclear complexes. Mass spectra and elemental analyses were inconclusive for the full characterization of these complexes.

8.3 Crystallographic data collection and refinement of structures

$[(dpocco\text{-}4H)_{12}Cu_{36}(\mu_3\text{-}OH)_8](CH_3COO)_{16}]\cdot 96H_2O$ (1)

A dark black-green prismatic crystal of approximate dimensions 0.53 x 0.28 x 0.20 mm was mounted on a glass fibre. All measurements were made on a Bruker P4/CCD system with monochromated Mo-Kα radiation and a sealed tube generator. The data were collected at 193 (1) K. The full hemisphere of data was collected with 30s per 0.3 deg frames to a maximum 2θ value of 52.9 °. A total of 101,668 reflections were taken and 82,136 of them were considered unique. The data were corrected for absorption using a face indexed Gaussian integration algorithm with maximum and minimum effective transmissions of 0.75847 and 0.39617 respectively. The data were also corrected for Lorentz and polarization effects. The structure was

solved by direct methods [197] and expanded using Fourier techniques [100]. Some non-hydrogen atoms (O(17)-O(35)) were refined anisotropically, while the rest were refined isotropically. Hydrogen atoms were included in their calculated positions but not refined. Isotropic thermal parameters were set twenty percent greater than those of their bonding partners at the time of their inclusion. The maximum and minimum peaks on the final difference Fourier map corresponded to 2.25 and -1.04 $e^-/Å^3$, respectively. Neutral atom scattering factors were taken from Cromer and Weber [101] and anomalous-dispersion terms [102-103] were taken from the usual source.

All calculations were performed using the teXsan crystallographic software package [105 (a)] of Molecular Structure Corporation except for the refinement, which was performed using SHELXL-97 [99]. Abbreviated crystal data are given in Table 8.1. The data set does not support full anisotropic refinement of the model primarily due to weak diffraction and a subsequent low percentage of observed data. A sensible charge balance can be obtained from the elemental analysis, which assumes that each copper triad is bridged by hydroxide. Based on the ligand charge of four minus, the charge balance indicates that there are ten acetate anions missing from the model and the oxygen and carbon values were corrected to reflect this in the formula. There are also 170 hydrogen atoms missing, 30 from the acetates, 132 from lattice water and 8 from the hydroxide anions.

8.4 Results and Discussion

8.4.1 Structural details

The molecular structure of **1** shows that it is a spheroidal shaped cluster consisting of thirty six copper(II) atoms. Fig. 8.3 illustrates one of the two essentially identical spheroidal clusters in the complex, which are related by an inversion centre, with four [Cu_3(OH)] subunits at the top and four at the bottom of the molecule. Each corner of each triangle is linked by a single dpocco ligand, bonded to its central copper ion. All the central coppers joining adjacent trinuclear subunits are five coordinate, except for two which are six coordinate. Lists of important bond distances and inter-metallic contacts are given in Table 8.2 and Table 8.3 respectively. Dpocco, like its R2poap counterparts, can adopt several different conformations, and in **1** the diazine nitrogen atoms bridge a central copper within each ligand to two terminal copper ions (Scheme 8.2), which then form part of a nearly equilateral triangle of copper ions. Bridging oxime N-O linkages from three interconnecting ligands form the three edges of the triangle. In order to understand the connections between the metal centers, the cluster in **1** can simply be compared with a cube where each corner of the cube represents one Cu_3 subunit while the apex of the corner represents the μ_3-OH. Each of the trinuclear units at the corner of the cube is connected to three others along the edge of the cube through another Cu(II) center in the middle. A pictorial representation of the model is shown in Fig. 8.4.

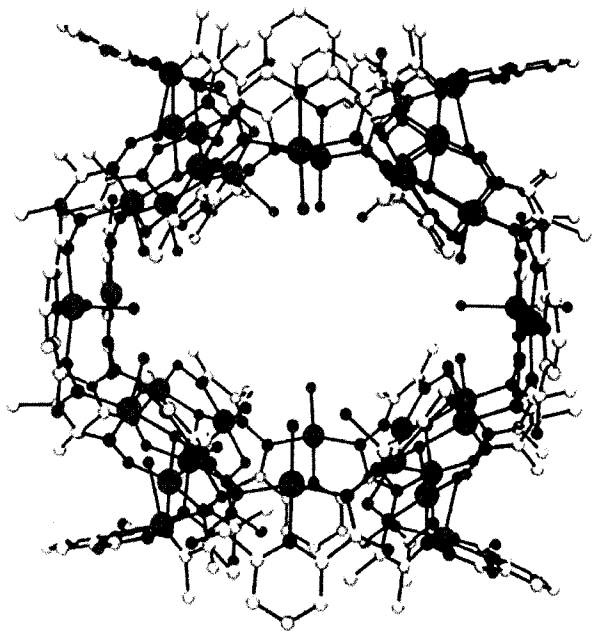

Fig. 8.3 Spheroidal subunit of the cluster in **1**

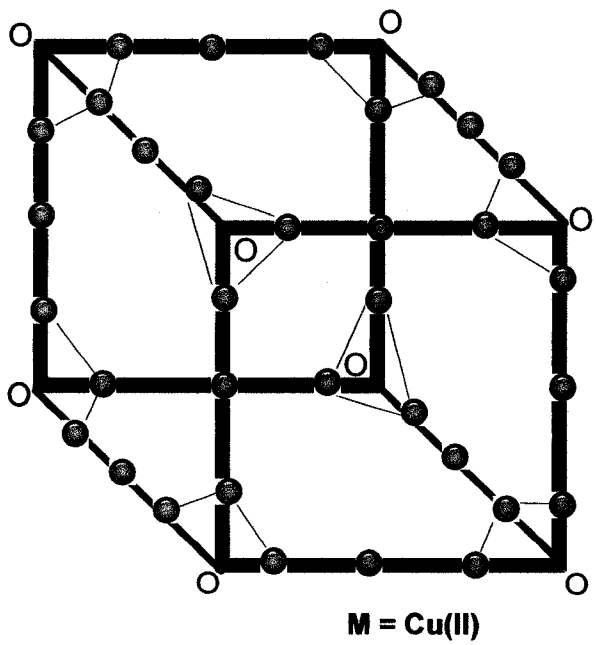

Fig. 8.4 A cube model to highlight the copper centers and their connectivity.

A μ_3-OH group lies at the center of each triangle in a capped fashion. The sum of the solid angles around each μ_3-O is 329.9° revealing that the hydroxo group does not sit in the trimetallic plane, but rather it is raised out of the Cu_3 plane slightly toward the center of the cluster. The distances of a μ_3-O group from its triangular Cu_3 plane are in the range 0.5876 Å-0.6606 Å. The diagram given in Fig. 8.5 clearly illustrates two trinuclear copper subunits and the connectivity between two subunits through a N-N-Cu-N-N chain.

The overall structure in each cluster shows a large cavity in the center, which contains several coordinated acetate ions, and water molecules. A simplified view of a segment is shown in Fig. 8.6, which highlights the immediate bonding connections between the copper ions. The cavity is surrounded by a sheath of coordinated water molecules, butanedione monoxime methyl groups, and acetate groups. All copper centers within each trimetallic unit have six coordination environments. Cu-Cu separations within each triangle fall in the range 3.15-3.30 Å with Cu-OH-Cu angles in the range 107–112°. Within each ligand the copper ions are more widely separated (Cu-Cu 4.25-4.50 Å), with Cu-N-N-Cu torsional angles in the range 77-92°. The μ_3-OH and μ_2-N_2 diazine groups define the magnetic connectivity in the cluster. It is anticipated that the μ_3-OH will mediate intramolecular antiferromagnetic exchange within the tri-metallic copper planes based on examples with other similar bridging situations [114, 198].

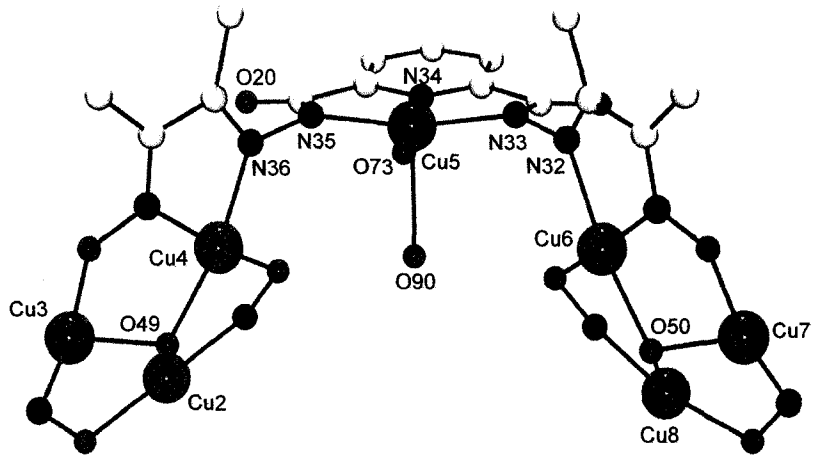

Fig. 8.5 POVRAY© representation of two triangular subunits (color code: Grey = C, Blue = N, Red = O, and Magenta = Cu(II).

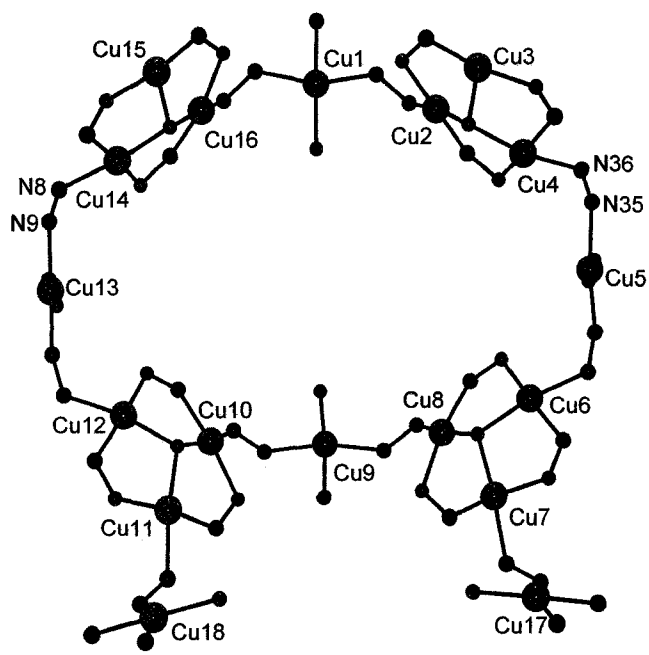

Fig. 8.6 Core structure for the asymmetric unit in **1** with just immediate donors and metals. (POVRAY© Color code; Magenta = Cu, Blue = nitrogen, Red = oxygen).

Table 8.1 Crystallographic summary for **1**

Empirical Formula	$C_{212}H_{368}O_{154}N_{84}Cu_{36}$
Formula Weight	8845.37
Crystal Color, Habit	Deep green-black, prism
Crystal Dimensions	0.53 X 0.28 X 0.20 mm
Crystal System	Triclinic
Lattice Type	Primitive
Lattice Parameters	a = 26.022 (3) Å b = 26.291 (3) Å c = 42.147 (5) Å α = 80.586 (3) ° β = 84.344 (2) ° γ = 61.558 (2) ° V = 25006 (5) $Å^3$
Space Group	P-1 (#2)
Z value	2
D_{calc}	1.175 g/cm^3
F_{000}	9008.00
μ(MoKα)	15.66 cm^{-1}
Temp (K)	193 ± 1
R1	0.149
wR2	0.460

Table 8.2 Important bond distances (Å) in **1**

Cu1	N1	1.954(14)	Cu5	O73	1.932(16)
Cu1	O86	1.967(13)	Cu5	N33	1.989(15)
Cu1	N42	2.006(14)	Cu5	N35	2.003(14)
Cu1	N2	2.005(14)	Cu5	O90	2.360(14)
Cu1	O85	2.318(15)	Cu6	O14	1.941(11)
Cu2	N41	1.942(13)	Cu6	N31	1.952(14)
Cu2	O22	1.946(13)	Cu6	O50	1.998(11)
Cu2	N40	1.946(16)	Cu6	N32	2.019(13)
Cu2	O49	1.969(10)	Cu6	O91	2.385(17)
Cu3	O21	1.929(12)	Cu7	O18	1.944(11)
Cu3	O49	1.930(11)	Cu7	O50	1.954(12)
Cu3	N38	1.964(14)	Cu7	N26	1.957(16)
Cu3	N39	1.964(14)	Cu7	N27	2.004(16)
Cu3	O62	2.316(17)	Cu7	O77	2.357(16)
Cu4	N37	1.920(14)	Cu8	O15	1.893(14)
Cu4	O23	1.924(12)	Cu8	N25	1.960(14)
Cu4	N36	1.946(14)	Cu8	O50	1.959(11)
Cu4	O49	1.974(12)	Cu8	N24	1.983(13)
Cu4	O110	2.383(19)	Cu8	O59	2.236(18)
Cu5	N34	1.918(13)	Cu9	O57	1.899(13)

Cu9	N22	1.906(15)	Cu14	O52	1.948(11)
Cu9	N23	2.002(15)	Cu14	N7	1.954(15)
Cu9	N21	2.039(14)	Cu14	N8	1.979(15)
Cu9	O84	2.349(13)	Cu15	O4	1.923(13)
Cu10	N19	1.971(14)	Cu15	O52	1.931(12)
Cu10	O10	1.980(13)	Cu15	N6	1.962(16)
Cu10	O51	1.982(11)	Cu15	N5	1.993(17)
Cu10	N20	2.017(13)	Cu15	O63	2.328(15)
Cu10	O72	2.364(12)	Cu16	O3	1.924(14)
Cu11	O7	1.901(13)	Cu16	N4	1.937(15)
Cu11	O51	1.939(10)	Cu16	O52	1.990(11)
Cu11	N18	1.986(15)	Cu16	N3	1.985(14)
Cu11	N17	1.996(15)	Cu16	O61	2.34(2)
Cu12	O51	1.921(11)	Cu17	N29	1.880(15)
Cu12	O11	1.938(12)	Cu17	O74	1.890(14)
Cu12	N13	1.948(14)	Cu17	N28	2.044(15)
Cu12	N12	1.972(15)	Cu17	N30	2.047(14)
Cu13	N10	1.915(13)	Cu17	O60	2.281(13)
Cu13	O71	1.946(14)	Cu18	N14	1.889(13)
Cu13	N11	2.014(14)	Cu18	N15	1.980(12)
Cu13	N9	2.022(14)	Cu18	N16	2.001(13)
Cu14	O2	1.942(13)	Cu18	O75	2.002(19)

Table 8.3 Important metal-metal distances (Å) and Cu-N-N-Cu torsional angles (°) in complex **1**

Cu-Cu separation within the trinuclear subunit (Å)

Cu2	Cu3	3.183	Cu10	Cu11	3.23
Cu3	Cu4	3.249	Cu11	Cu12	3.183
Cu4	Cu2	3.192	Cu12	Cu10	3.195
Cu6	Cu7	3.207	Cu14	Cu15	3.198
Cu7	Cu8	3.244	Cu15	Cu16	3.25
Cu8	Cu6	3.234	Cu16	Cu14	3.233

Cu (central)-Cu (corner metal of each triangle) separations (Å)

Cu1	Cu2	4.269	Cu9	Cu8	4.255
Cu1	Cu16	4.258	Cu9	Cu10	4.284
Cu5	Cu4	4.242	Cu17	Cu7	4.222
Cu5	Cu6	4.258	Cu18	Cu11	4.294

Torsional angle Cu (central)-N-N-Cu (corner) (°)

Within the range from 77.9 (Cu(5)-N(35)-N(36)-Cu(4)) to 92.9 (Cu(14)-N(8)-N(9)-Cu(13)).

Table 8.4 Important bond angles (°) in **1**

Cu3	O49	Cu2	109.4(5)	Cu20	O53	Cu22	109.5(6)
Cu3	O49	Cu4	112.6(5)	Cu20	O53	Cu21	109.6(6)
Cu2	O49	Cu4	108.1(5)	Cu22	O53	Cu21	107.7(6)
Cu7	O50	Cu8	112.0(6)	Cu25	O54	Cu26	107.1(6)
Cu7	O50	Cu6	108.5(6)	Cu25	O54	Cu24	110.3(5)
Cu8	O50	Cu6	109.6(5)	Cu26	O54	Cu24	109.5(5)
Cu12	O51	Cu11	111.1(5)	Cu30	O55	Cu29	111.5(7)
Cu12	O51	Cu10	109.9(5)	Cu30	O55	Cu28	109.0(6)
Cu11	O51	Cu10	110.9(5)	Cu29	O55	Cu28	110.9(6)
Cu15	O52	Cu14	111.0(6)	Cu32	O56	Cu34	111.1(6)
Cu15	O52	Cu16	112.0(5)	Cu32	O56	Cu33	112.7(6)
Cu14	O52	Cu16	110.3(5)	Cu34	O56	Cu33	111.9(6)

8.4.2 Magnetism

Variable temperature magnetic data for two complexes were collected in the range 2-300 K, in a 0.1 T external field (Quantum Design MPMS5S SQUID magnetometer). The magnetic moment for the complex **1** is 10.1 μ_B at 300 K, which is consistent with the Cu_{36} cluster. The moment gradually drops to 4.76 μ_B as temperature is lowered to ~ 30 K. This is a signature of overall intramolecular antiferromagnetic exchange. Within each hydroxo (μ_3-OH) centered triangular

subunit, the oxygen atom exhibits sp^3 hybridization, which forces the oxygen above the tri copper plane, which in turn disrupts the orbital overlap with the copper d_{x2-y2} orbitals suggesting weak magnetic exchange. The non-planar bonding configuration is achieved at the expense of magnetic exchange reduction. Hydroxo bridges have been well documented to mediate intramolecular antiferromagnetic exchange for copper dimers with a dependence on the bridge angle for planar or nearly planar hydroxo bridges [199], and on dihedral angle (δ) in case of non-planar roof shaped hydroxo bridges [200]. So, in the low temperature limit, each triangular subunit is expected to result in a spin doublet ($S' = ½$) ground state, which would then be expected to couple antiferromagnetically to the other central copper atoms *via* the N-N bridges.

Diazine N-N bridges are known to mediate antiferromagnetic coupling between connected copper(II) dimers. The spin exchange depends on the degree of overlap of the d_{x2-y2} copper magnetic orbitals via the *p* orbitals on the nitrogen atoms of the N-N bridges [114]. The degree of overlap between copper magnetic orbitals is a direct consequence of the rotation of the copper magnetic orbitals around the N-N bond. In several previous magnetostructural studies with dicopper(II) complexes, where the copper centers have d_{x2-y2} magnetic ground states, magnetic properties were directly related to the angle of rotation about the N-N single bond. Rotational angles < 80° led to ferromagnetic exchange, while for larger angles, antiferromagnetic behavior was observed [55, 114]. In the present case, torsional angles range from 77.9°-92.9°. These values are consistent with the literature values and are expected to lead to

relatively weak overall antiferromagnetic exchange in the cluster. Any inherent ferromagnetic component might be overcome by the larger antiferromagnetic terms acting within the cluster. From the observed magnetic properties of the cluster, it is apparent that the overall magnetic behavior is controlled by the antiferromagnetic components in the cluster. This combined effect would reasonably lead towards a zero magnetic moment at low temperature.

The complexity of the exchange problem presented by this novel polyhedral array of spin centers has thus far prevented a full evaluation of the exchange integrals within the fundamental subunits. The matrix sizes for the calculation of the full exchange situation for this 36 electron cluster are too large to be attempted by the average computer. However, to approach the problem, we have currently done two things. We have tried to model the complex as multiples of a capped nonanuclear trigonal bipyramidal shaped subunit (Fig. 8.7), which has the appropriate features and magnetic connections to account for the magnetic exchange pathways present in the complex. Each apex of the model contains a trinuclear subunit and each corner of the trigonal plane has a single Cu(II) ion. So, three Cu(II) ions in the plane join the three corners of a trinuclear subunit to the similar three corners of the other subunit. We also treated the total exchange situation on the simplified basis of just two J values. One being within each triangle mediated by the hydroxo centered bridge, and another through N–N bridges connecting corners of two adjacent trimetallic subunits via a common metal center in the middle.

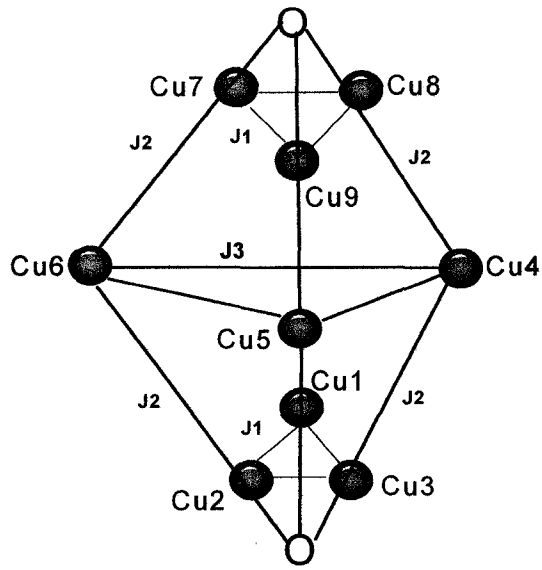

Fig. 8.7 Capped trigonal bipyramidal magnetic model used for **1**

The trigonal bipyramidal model used is depicted in Fig. 8.7. The appropriate exchange Hamiltonian for this model is given in Equation 8.1. The exchange model was treated using MAGMUN 4.1 and the total spin state (S′) values, and their energies for all spin vector combinations were calculated using normal vector addition principles [85]. The values were substituted into the Van-Vleck equation (equation 8.2) within the internal structure of the software package [119] to calculate the susceptibility (χ_M) data as a function of temperature.

$$H_{ex} = -J_1(\hat{S}_1\cdot\hat{S}_2 + \hat{S}_2\cdot\hat{S}_3 + \hat{S}_3\cdot\hat{S}_1 + \hat{S}_7\cdot\hat{S}_8 + \hat{S}_8\cdot\hat{S}_9 + \hat{S}_9\cdot\hat{S}_7)$$
$$-J_2(\hat{S}_1\cdot\hat{S}_5 + \hat{S}_5\cdot\hat{S}_9 + \hat{S}_2\cdot\hat{S}_6 + \hat{S}_6\cdot\hat{S}_7 + \hat{S}_3\cdot\hat{S}_4 + \hat{S}_4\cdot\hat{S}_8 \qquad [8.1]$$

$$\chi_M' = \frac{N g^2 \beta^2}{3k(T-\theta)} \left(\frac{\sum S'(S'+1)(2S'+1)\exp(-E_n^{(0)}/kT)}{\sum (2S'+1)\exp(-E_n^{(0)}/kT)} \right) \quad [8.2]$$

$$\chi_M = \chi_M'(1-\rho) + \left(\frac{4S(S+1)N g^2 \beta^2}{3kT} \right) \rho + N\alpha \quad [8.3]$$

MAGMUN 4.1 allows the input of any exchange energy term for any bridging connection, but as already discussed in Chapter 1 in detail and in Chapter 5, it is limited in the sense that non-linear regression fits cannot be used where two or more J values are direct variables. The variable temperature magnetic response (χ) for the whole complex was calculated for the nine Cu(II) centers in the trigonal bipyramidal model (Cluster Cu_{36} x ¼ = trigonal bipyramidal model Cu_9) and the data fitted to equations 8.1-8.3 within the software MAGMUN 4.1, with a simplified assumption that *J2* is *J1*/100, so that *J1*/*J2* = 100. The ratio between J1 and J2 was not chosen arbitrarily but on the basis of literature values of exchange integrals for complexes with similar bridging systems having comparable Cu-OH-Cu bridge angles and Cu-N-N-Cu torsional angles. And it was also assumed due to the large intermetallic separation that *J3* = 0. A Weiss-like temperature correction (θ) to account for the intermolecular exchange effects and a correction for temperature-independent-paramagnetism (TIP) were applied. The best data fit gave g = 2.04, J = - 109 cm^{-1}, TIP = 500 x 10^{-6}, emu. mol^{-1}, ρ = 0.005 θ = - 6 K (10^2 *R* = 3.89; *R* = $[\Sigma(\chi_{obsd} - \chi_{calcd})^2/\Sigma\chi_{obs}^2]^{1/2}$). The circles in Fig. 8.8 are experimental values and the solid line was

calculated with these parameters.

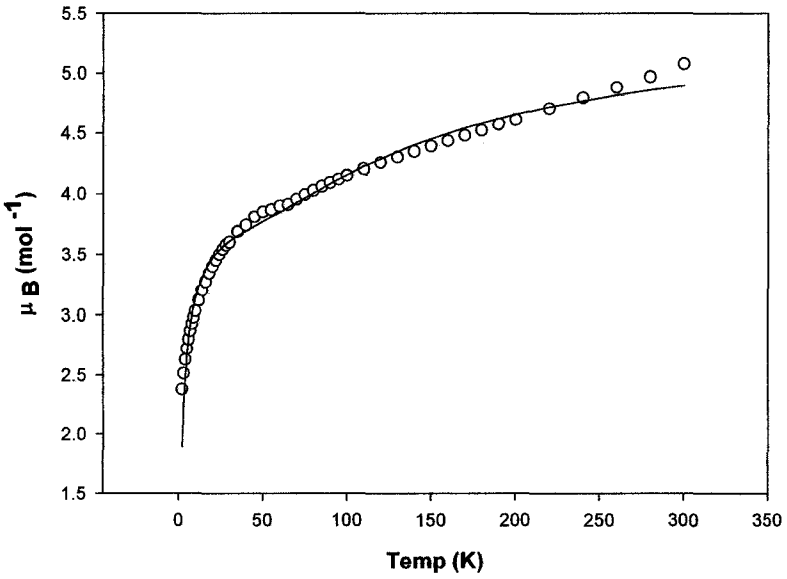

Fig. 8.8 Plot of variable temperature magnetic moment for **1** (per mole) scaled up for a $Cu(II)_9$ model.

From the fitted value of the exchange parameter J = - 109 cm^{-1}, the individual coupling constants *J1* and *J2* were evaluated. It is evident that *J1* which is the exchange coupling within the trinuclear subunit is about -109 cm^{-1} and *J2* which will account for the intertrimer interactions through the N-N bridges turned out to be -1.1 cm^{-1}. The value for *J1* is consistent with literature values for other complexes having similar kinds of bridging pathways. In an analogous μ_3-hydroxo centered trinuclear copper(II) complex, the exchange coupling within the trinuclear subunit was reported to be -122 cm^{-1}, where Cu-OH-Cu angles were ~108° [186]. The value of *J2* obtained from the fitting of the magnetic data is also reasonable. At the low temperature limit,

there will be one unpaired electron per Cu_3 unit (S = ½ ground state). *J2* reflects the exchange coupling of this trinuclear unit (S = ½) with the single copper(II) atom (central) with rotational angles ranging from 77-92°. Simple dinuclear Cu(II) complexes with rotational angles within the range of 85-90° are predicted to have very small (-2 cm^{-1} to 0 cm^{-1}) exchange integrals, which can be obtained from the magnetic plane rotational angle-exchange integral relationship [114].

The requirement of a relatively large θ value is informative and confirms the presence of antiferromagnetic exchange interactions other than those existing within the trinuclear subunit. *J2* accounts for the inter-subunit interaction to some extent given the simple model but it is not enough to account for a further drop in moment in the low temperature range. The combination of *J2* and θ would reasonably account for interactions between the trinuclear subunits and the single copper(II) atoms, connected through the N-N bridges. However, we should keep in mind that it is not a rigorous model, and only represents a simplified picture of the overall exchange situation prevailing within the cluster.

Complex **2** also shows a similar variable temperature magnetic profile within the 2-300 K range as shown in Fig. 8.9. The room temperature magnetic moment is 11.4 μ_B, which gradually drops down to 4.86 μ_B, which is a signature of overall antiferromagnetic exchange prevailing within the cluster. Cl-dpocco is analogous to dpocco. So it is conceivable that with $Cu(OAc)_2$ it would have produced a similar kind

of cluster since all the necessary features which were present in the previous ligand such as the oxime end, which had a pivotal role in building the trinuclear subunits are present in Cl-dpocco as well.

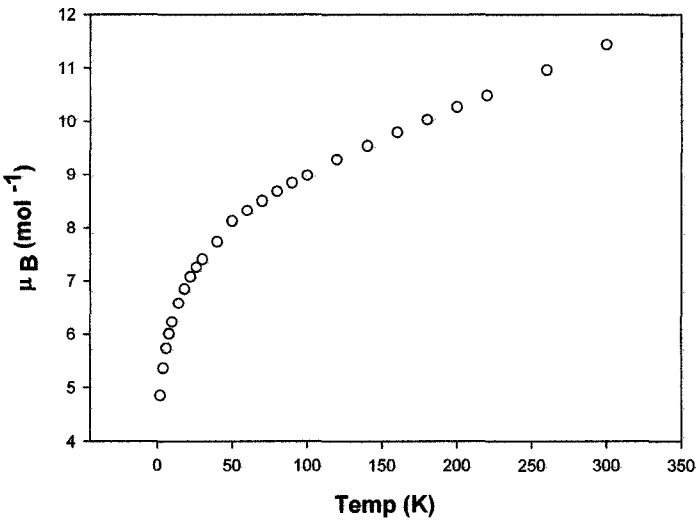

Fig. 8.9 Variable temperature magnetic profile for **2** (moment per mole)

Chlorine, being an electronegative atom might have an electron withdrawing inductive effect which will weaken the overall magnetic exchange within the cluster. However, no attempts were made to fit the data.

8.5 Conclusion

The reactivity of the tritopic ligand dpocco and its analogue Cl-dpocco with transition metal ions has been investigated in this chapter. Being a linear tritopic ligand, dpocco has coordination pockets aligned properly in a linear fashion. It was shown that by placing terminal coordinating substituents such as an oxime group at the

ligand end, one can introduce additional bonding interactions by creating satellite metallic Cu_3 assemblies which are bridged by a μ_3-hydroxo group. The magnetic exchange coupling within the trinuclear assemblies is mediated by Cu-O-Cu bridging interactions, which depend on the degree of co-planarity of the μ_3-O group with the trimetallic plane. Each of these subunits is connected by N-N bridges through another single copper(II) center leading to an extended magnetic network. The magnetic exchange between adjacent trinuclear subunits is mediated by N-N bridges. A simplified magnetic model was used to estimate the magnitude of the magnetic exchange in the cluster. The exchange integral within the trimetallic unit (*J1*) was found to be ~ -109 cm^{-1}, which is close and well within the error limit of literature values for similar μ_3-OH bridged trinuclear copper(II) complexes. The exchange integral *J2*, which accounts for the coupling between Cu_3 subunits by N-N bridges through another single copper(II) atom, was found to be even smaller (~ -1.1 cm^{-1}), but is again consistent with literature values. Dinuclear copper(II) complexes with rotational angles of the magnetic planes of ~85-90° around a N-N single bond were found to have negative exchange integrals of similar magnitude.

CHAPTER 9

Synthesis of a large $Mn(II)_{25}$ [5 x 5] grid-characterization through CITS imagery and magnetism

9.1 Introduction

The purpose of the ligand extension described in Chapter 2 was to create larger transition metal grids with effective magnetic exchange coupling between the metal centers. The use of predesigned picolinic hydrazone ligands with suitable coordination pockets within the ligand skeleton allows fundamental control over the nuclearity of the resulting complexes (see Chapters 4, 6 for examples of [2 x 2] and [3 x 3] grids). It also allows tuning of the molecular grid properties by manipulating the choice of donor atom groupings within the ligand. Moreover, grids can be made to form self-assembled monolayers (SAMS) by functionalizing the organic ligand by adding an appropriate 'tether' (e. g. S, Cl), which would adhere to a suitable surface (e. g. Au, graphite).

The integration of molecules into electronic circuits is a relatively new idea, which started with hopes of reducing the size of electronic chips and their production cost per functional unit as well. For this novel goal to be achieved, adsorption of the functional molecules onto a solid substrate became very

important. [n x n] grid type architectures are very good candidates for this purpose. Within these polymetallic grids, a finite number of metal ions are arranged in an orderly fashion within a two dimensional framework with molecular 'wiring' completed by organic ligand functional groups (e. g. hydrazone oxygen).

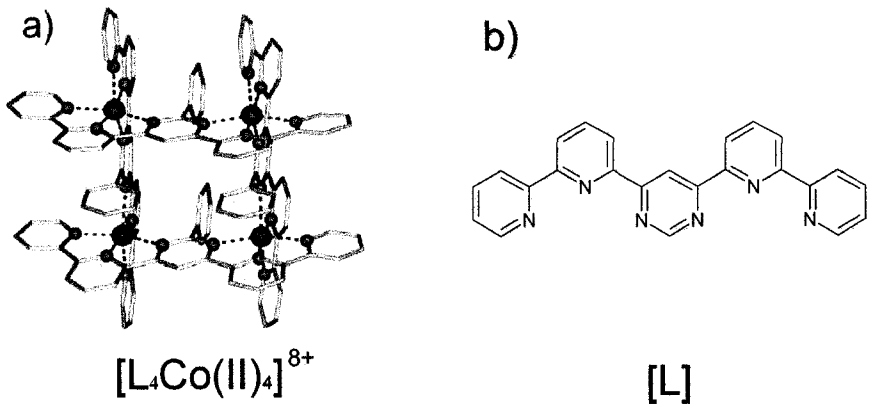

Fig. 9.1 (a) Tetracobalt complex $[L_4Co(II)_4]^{8+}$ (color code: green = N, ink blue = Co(II)) and (b) polypyridine ligand **L**.

A polypyridine derived square [2 x 2] tetranuclear $Co(II)_4$ grid (Fig. 9.1(a)) appeared to be of particular interest because of its structural, optical, magnetic, and electronic properties [24, 91, 201-204]. The complex formed a self- assembled monolayer (SAM) on graphite surfaces. STM studies on densely packed monolayers of this cluster on graphite surface have been conducted [205-206]. In order to understand the dynamics behind the

organization of this class of molecules over the solid surface, STM and STS (Scanning Tunneling Spectroscopic) studies were carried out on 1D and 2D ensembles and also on single crystals of this molecule deposited on a HOPG (Highly Oriented Pyrolytic Graphite) surface [207]. A topographical STM image of the Van der Waals' surface of the Co_4 grid molecule appeared as a featureless 'blob'. However, the molecular cross sections obtained from such images are still informative because they are consistent with molecular dimensions which can be obtained from x-ray crystallography.

In order to obtain more definitive information, especially to investigate the electronic properties of the molecule, the CITS (Current imaging tunneling spectroscopy) technique was applied to the grid-substrate system. CITS is based on STS (Scanning Tunneling Spectroscopy) spectroscopic techniques. It basically maps out the molecular energy levels of a molecule, especially those close to the Fermi level, which are dominated by metal 3d HOMOs (Highest Occupied Molecular Orbitals) [207]. Different functional subunits present in a molecule constitute different energy states on the molecular level. STS spectroscopy can provide direct information about a particular molecular energy level if the levels are energetically well separated. The CITS mapping revealed a quadratic array of four bright spots associated just with metal 3d HOMO levels. The distance between two adjacent spots is about 0.7 nm which

is fully consistent with the distance between two neighboring Co atoms in the tetranuclear grid [207].

The nonanuclear grid $[Mn_9(S2poap)_6](ClO_4)_{10}\cdot 12H_2O$ obtained from the sulfur appended ligand S2poap (H_2L^1) (Fig. 9.2, (a)) formed SAMS on a Au(III) surface and STM imagery was performed on the grid-substrate system (Fig. 9.3) [143, 208] showing the 2D surface arrangement. STM and CITS imagery were obtained on the grid $[Mn_9(Cl2poap)_6](ClO_4)_6$ derived from the Cl-substituted ligand Cl2poap (H_2L^2; Fig. 9.2 (a)) [113], on HOPG, where individual Mn(II) ions in the grid were addressed.

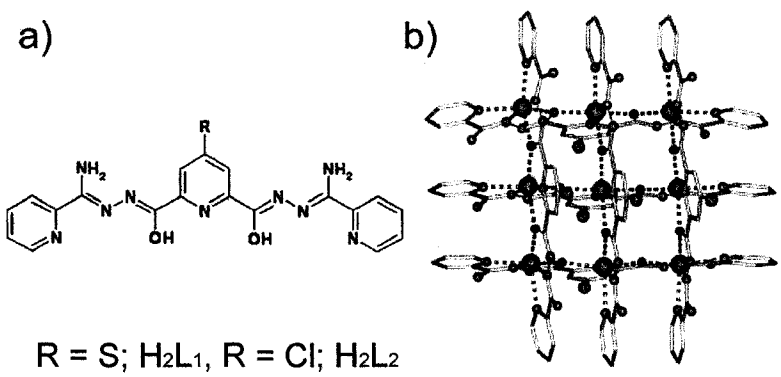

Fig. 9.2 a) 2poap type functionalized tritopic ligand R = S when S2poap and R = Cl when Cl2poap; b) Nonanuclear grid $[Mn_9(Cl2poap)_6]^{6+}$ (color code: pink = Mn(II), green = Cl, blue = N).

STM studies showed several molecular motifs on HOPG. Figures 9.3 a) and b) show single, double and triple strand like arrangements. The grid

molecules aggregate along the step edges of the HOPG surface. Fig. 9.3 c) is a representation of crystal-like molecular arrays, where several grid strands stack together. The interactions between the grid molecules and the surface appear to be dominated by π contacts between the ligand aromatic rings and the graphite, resulting in a sideways attachment of the grid cations [113].

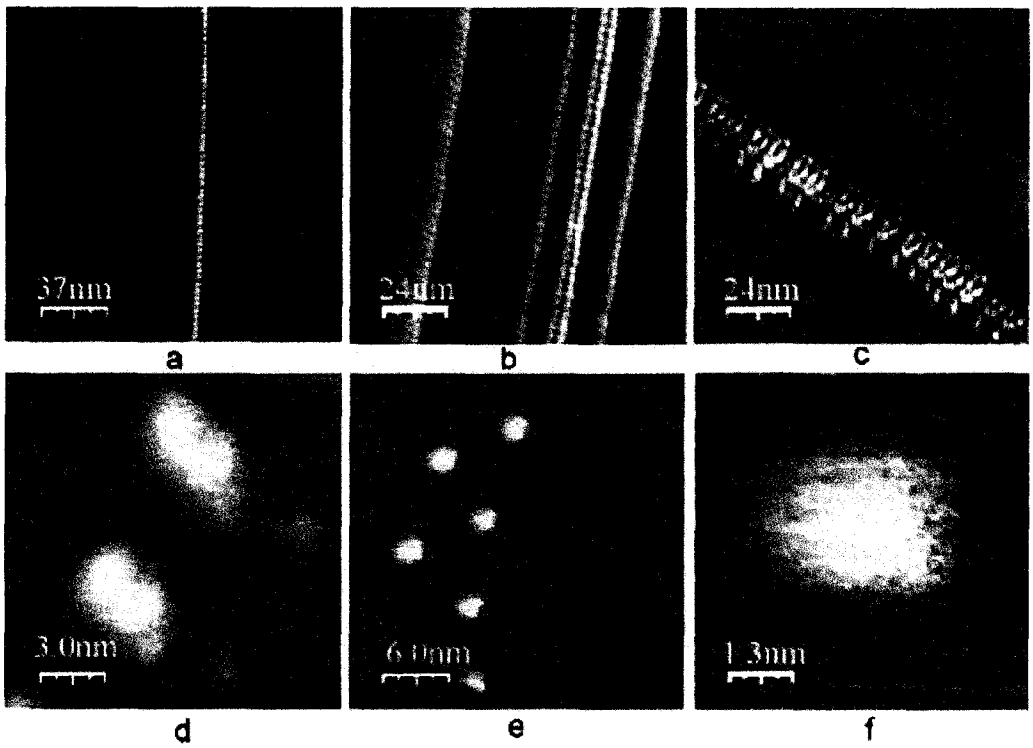

Fig. 9.3 STM imagery of grid complex $[Mn_9(Cl2poap)_6](ClO_4)_{10}.10H_2O$; different molecular arrangement a) Single molecular line b) single, double and triple stranded ribbon c) extended crystal arrays d) dimer e) random distribution of grid molecules f) an individual grid molecule.

Relatively blurred and apparently featureless individual blobs were imaged when single grid molecules were addressed (Fig. 9.3 (d) and (e)). But the rough dimensions of the bright spot obtained from the STM topographical image (Fig. 9.3 (f)) mirrored the approximate dimensions of a single [3 x 3] $Mn(II)_9$ grid obtained from an x-ray study.

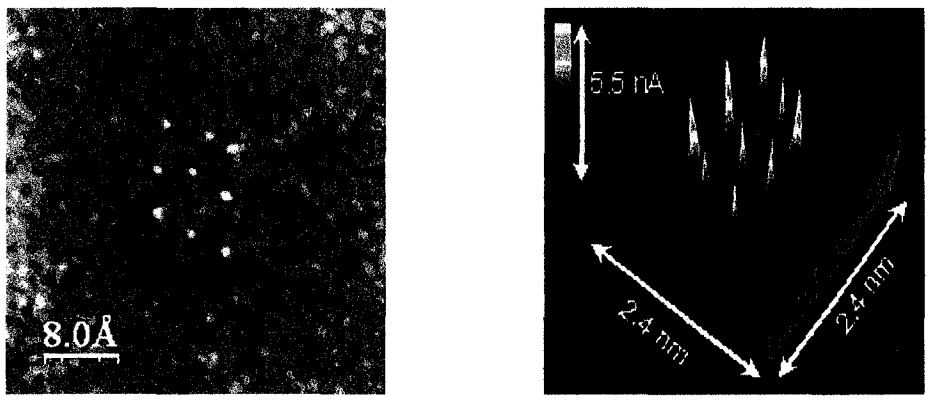

(a) **(b)**

Fig. 9.4 a) Simultaneously recorded STM and CITS images of the $[Mn_9(Cl2poap)_6]^{6+}$; the bright spots correspond to the Mn(II) centers b) A plot of current isopols drawn as function of voltage. 3D peaks are an augmented representation of the position of Mn(II) ions within the grid with maximum contrast.

CITS measurements, which consist of actually recording the *I-V* characteristics of each of the pixel positions of the STM topographic map, were very informative. The spatially resolved current image taken at a bias

voltage -0.73 V below the Fermi level revealed a regular array of nine bright spots aligned in a grid-like arrangement. The distances between two adjacent spots are around 0.4 nm, which exactly corresponds to the Mn-Mn distances in nonanuclear grids obtained from x-ray crystallography [113]. The puckered peak arrangement in Fig. 9.4 (a) is also reflected in the x-ray structure. However, no features from the ligands were revealed from these images.

This is anticipated from the principles of the CITS technique, because the organic ligand based energy levels lie far from the Fermi level. So mapping the local maxima of electron density over the Fermi level is actually mapping the electronic properties of the highest occupied molecular orbital (HOMO) of the molecule, which is mainly associated with Mn(II) 'd' orbitals. DFT calculations in the case of the $Co(II)_4$ [2 x 2] grid show that HOMO levels of the $Co(II)_4$ complex are dominated by contributions from the cobalt(II) 'd' orbitals [207].

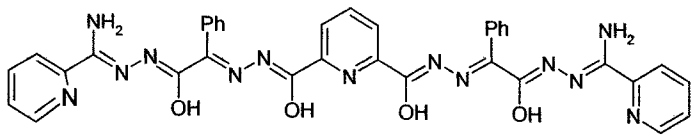

L7 (4popap)

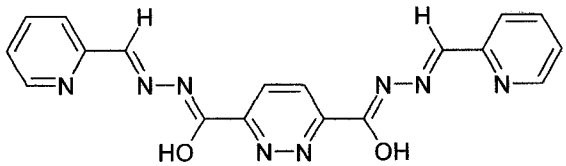

Pd2poHp

Scheme 9.1 Pentatopic and a tetratopic ligand.

Thus CITS has successfully mapped the real 'positions' of the Mn(II) centers in the [3 x 3] grid as bright spots according to the molecular contribution of the metals alone. Similar imagery techniques were also employed successfully to map the metal positions in a [4 x 4] $Mn(II)_{16}$ grid molecule obtained from the tetratopic ligand 2PdoHp (Scheme 9.1) [182, 209].

9.2 Experimental

9.2.1 Materials

Commercially available solvents and chemicals were used without further purification.

9.2.2 Characterization

Analysis, spectroscopic and physical measurements were done according to the procedure described in Chapter 2.

9.2.3 STM / CITS images

Dr. M. S. Alam, and Prof. Dr. P. Müller, Physikalisches Institut III, Universität Erlangen-Nürnberg, Erwin-Rommel-Strasse 1, 91058 Erlangen, Germany, are acknowledged for the STM/CITS measurements. The measurements were carried out with a home built low drift STM head equipped with commercially available low current control electronics (RHK technology) under ambient conditions. For higher resolution STM studies, the Highly Oriented Pyrolytic Graphite (HOPG) was freshly cleaved with adhesive

tape. The graphite surface was then imaged by STM to confirm the high resolution of the tip. Mechanically cut Pt-Ir (90/10) tips of diameter 0.25 mm were used. Distances were calibrated in the STM images by observing atomic spacing on the HOPG surface. After imaging the graphite surface successfully, a droplet of a solution of the complex being examined with concentration approx. 10^{-9} mol/L was deposited and allowed to run down the surface. Typically, tunneling currents between 5 and 200 pA were employed. The bias voltage was ±100 mV to ± 200 mV. The scan frequency was varied between 2 to 5 Hz. The resolution was 256 x 256 points for STM topography and 128 x 128 points for CITS measurements. In CITS mode, current-voltage (*I-V*) curves were taken simultaneously with a constant-current STM image using the interrupted-feedback loop technique.

9.2.4 Synthesis of the complexes

$[\{(4popap)_{10}\text{-}30H\}Mn_{25}](ClO_4)_{20}(H_2O)_{65}]$ (1) and complexes 2 and 3

L7 (0.1g, 0.14 mmol) was added to a solution of $Mn(ClO_4)_2.6H_2O$ (0.12 g, 0.33 mmol) in ethanol (25 mL). The mixture was stirred for 5 hours which resulted in a dark yellow fine polycrystalline powder. (Yield 62.5%). IR (Nujol, cm^{-1}): 3548, 3455, 3355, 1646, 1099 (ν ClO_4^-). Anal. Calc. (%) for $[\{(C_{35}H_{29}N_{13}O_4)_{10}\text{-}30H\}Mn_{25}](ClO_4)_{20}(H_2O)_{65}]$; C, 36.68; H, 3.43; N, 15.88, Cl, 6.18. Found; C, 36.52; H, 2.68; N, 15.45; Cl, 6.29. A similar reaction in a different solvent mixture MeOH/CH_3CN (2:1 v/v) gave a dark orange

crystalline solid $[\{(C_{35}H_{29}N_{13}O_4)_{10}\text{-}25H\}Mn_{25}](ClO_4)_{25}(H_2O)_{50}$ **(2)** with incomplete ligand deprotonation. In a separate reaction, a nitrate analogue of the cluster was prepared. 0.050 g (0.072 mmol) of the ligand **L7** was added to a $Mn(NO_3)_2.6H_2O$ (0.095 g, 0.33 mmol) solution in a mixture of solvents $MeOH:CH_3CN:H_2O$ (1:2:1 v/v). The mixture was stirred for several hours which resulted in a dark red solution. To help crystallization, $NaOOCCH_3$ (0.1 g, 1.2 mmol) was added to the solution with stirring. A red crystalline solid was obtained by slow diffusion of ether into the solution. Anal. Calc. (%) for $[(C_{35}H_{25}N_{13}O_4)_{10}\ Mn_{25}](CH_3COO)_{10}\ (CH_3OH)\ (H_2O)_{40}$ **(3)**; C, 46.00; H, 4.10; N, 18.35. Found; C, 45.90; H, 3.43; N, 18.35.

[Mn(4popap-2H)] (4)

0.1g (0.14 mmol) of the ligand **L7** was added to a $MeOH/CH_3Cl$ (3:1 v/v) solvent mixture which formed a cloudy suspension. The resulting suspension was added dropwise to an aqueous solution of $Mn(CF_3SO_3).xH_2O$ ($MeOH/H_2O$ 4:1) (~10 mL, 0.03 g/mL, 0.85 mmol), with addition of a further 10 mL of MeOH. The final solution was stirred for 5 hours. A deep orange colored clear solution formed which was filtered and kept for crystallization by slow evaporation. A red-yellow fine polycrystalline solid precipitated out after two weeks. (Yield 11%). X-ray quality crystals were obtained by slow diffusion of diethyl ether into a solution of the complex in $MeOH:CH_3CN:CHCl_3$ (1:1:1 v/v).

9.3 Crystallographic data collection and refinement of structures

An orange prismatic crystal of **4** with approximate dimensions 0.40 x 0.20 x 0.10 mm was mounted on a glass fiber. All measurements were done on a Rigaku AFC8 Goniometer with a Rigaku Saturn area detector using graphite monochromated Mo-Kα radiation. Hydrogen atoms were included in calculated or difference map positions with isotropic thermal parameters set twenty percent greater than those of their bonding partners at the time of inclusion. They were refined using the riding model. The data were collected at 153 ± 1 K to a maximum 2θ value of 61.5°. The data were corrected for Lorentz and polarization effects. The structure was solved by direct methods [210] and expanded using Fourier techniques [211].

All non-hydrogen atoms were refined anisotropically. The maximum and minimum peaks on the final difference Fourier map corresponded to 0.39 and -0.54 $e^-/Å^3$. Neutral atom scattering factors were taken from the usual source of Cromer and Waber [101]. Anomalous dispersion effects were included in F_{calc} [102]. The values for Δf' and Δf" were those of Creagh and McAuley [103]. The values for the mass attenuation coefficients are those of Creagh and Hubbell [104]. All calculations were performed using the CrystalStructure [128-129] crystallographic software package except for refinement, which was performed using SHELXL-97 [99].

9.4 Results and Discussion

9.4.1 Structural details

The x-ray structure in **4** shows a neutral mononuclear complex with [(L-2H)Mn] stoichiometry (Fig. 9.5). Metal ligand and other important distances are given in Table 9.2. The ligand is doubly deprotonated. Protons are lost from O(3) and O(4). The short C=O bond distances of 1.218 Å and 1.213 Å, bonding to O(2) and O(1) respectively, indicate double bond character for these two carbonyl groups. The L-Mn-L angles around the Mn(II) atom fall in the range 70.30(19) ° to 96.8(2) °. Even though this kind of coordination mode is not appropriate for grid formation, the structural determination of the complex established the formation of the ligand, and also points out that other oligomeric product are possible from this ligand depending on the reaction conditions.

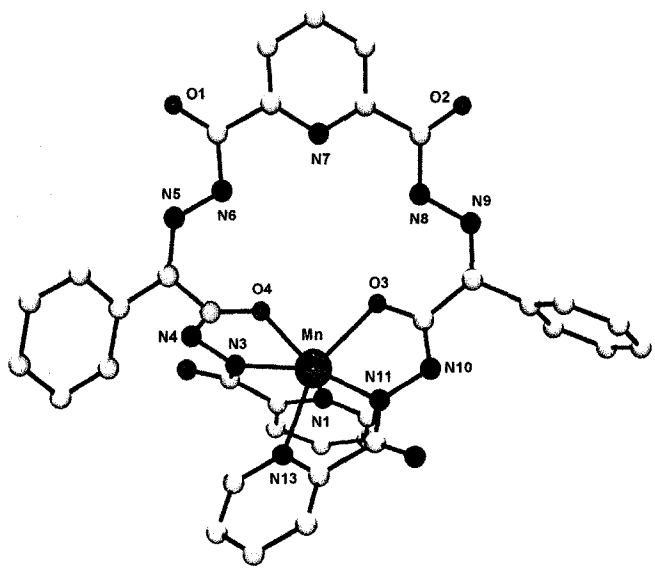

Fig. 9.5 POVRAY© representation of the mononuclear cluster in **4**

Table 9.1 Crystallographic summary for **4**

Empirical Formula	$C_{35}H_{27}N_{13}O_4Mn$
Formula Weight	748.62
Crystal Color, Habit	Orange, prism
Crystal Dimensions	0.40 x 0.20 x 0.10 mm
Crystal System	Monoclinic
Lattice Type	C-centered
Lattice Parameters	a = 15.140(10) Å b = 10.791(7) Å c = 21.138(13) Å β = 97.04(2) ° V = 3427(4) Å^3
Space Group	Cc (#9)
Z value	4
D_{calc}	1.451 g/cm^3
F_{000}	1540.00
μ(MoKα)	4.462 cm^{-1}
T (K)	153 ± 1
R1	0.0883
wR2	0.2174

Table 9.2 Important bond distances (Å) in **4**

Mn-O3	2.158(4)	Mn-O4	2.144(6)
Mn-N11	2.129(6)	N5-N6	1.402(7)
Mn-N1	2.298(6)	N8-N9	1.377(8)
Mn-N13	2.385(6)	C15-O1	1.213(9)
Mn-N3	2.146(6)	C21-O2	1.218(7)

The complex contains a vacant cavity in the middle with approximate dimensions of 4.1 x 4.8 Å. A summary of the crystal data is given in Table 9.1 and important bond distances are given in Table 9.2.

9.4.2 CITS imagery on 2

The successful application of the CITS imaging technique in cases of the [2 x 2] $Co(II)_4$ square and [3 x 3] $Mn(II)_9$ grid complexes prompted us to use the same technique for the $Mn(II)_{25}$ cluster (**2**) deposited on HOPG as an exploratory tool to locate the Mn(II) metal centers and thereby substantiate the evidence for the formation of a [5 x 5] square grid. The STM and CITS images of the complex provided clear evidence of the existence of the grid on the graphite surface, with exact location of the metal Mn(II) centers at the expected grid separations.

Fig. 9.6 a) shows a topographic STM image of a portion of the HOPG surface containing a molecular chain arrangement of grid molecules. This arises because of the tendency of the grid molecules to aggregate along the step edges of the graphite surface. The second STM image is an image of a single molecule featuring basically a blob of contrasting electron density.

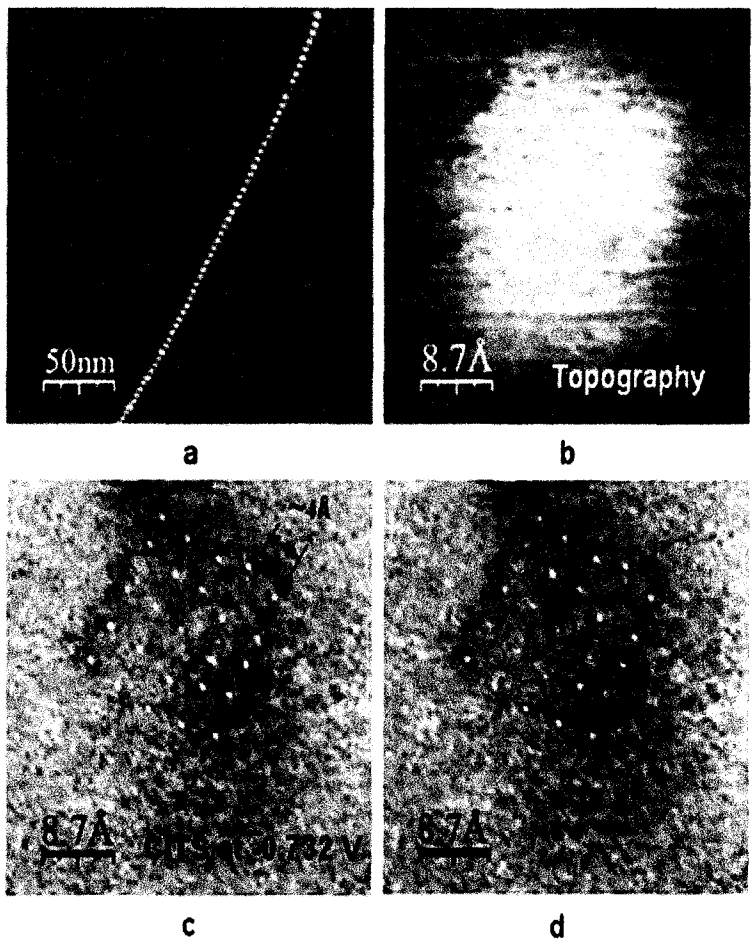

Fig. 9.6 a) STM image showing a molecular chain motif b) An asymmetric featureless 'blob' of a single molecule c) An array of [5 x 5] square grid; bright spots indicate the location of Mn(II) ions d) Highlighted metal positions within the grid.

The estimated rough size of the feature is ~ 2.8 x 3.2 Å. The estimated size of a single [5 x 5] grid molecule in the STM image is 3 x 3 nm, based on simple extension of the dimensions of a related nonanuclear $Mn(II)_9$ grid. The size of the blob in Fig. 9.6 b) is therefore reasonable for a [5 x 5] grid.

To obtain an even more precise picture of the grid, CITS measurements were carried out for each point on the surface that was mapped in the STM experiment. The tunneling voltage was kept comparable with those used for $Mn(II)_9$ and $Co(II)_4$ grids. Fig. 9.6 c) shows a [5 x 5] square array having an estimated edge length of 17 Å. The well defined bright spots represent the precise atomic positions of the Mn(II) ions with inter-metallic separations of ~ 4 Å, which is in good agreement with similar atomic separations seen in numerous $Mn(II)_4$ and $Mn(II)_9$ grid molecules [113], with μ-O (hydrazone) bridging connections.

Fig. 9.6 d) shows the metal ion positions highlighted with green circles. What is remarkable in this picture is that it even shows the expected puckered arrangement of the metal ions within the grid. This kind of metal arrangement is typical for a regular $Mn(II)_9$ grid, and confirms the CITS technique as a very powerful secondary investigative tool, especially in cases where more definitive structural evidence from x-ray structural data is not available. However, even though this remarkable result confirms the presence of twenty five metal centers in the square grid array, it does not tell us anything about the ten organic ligands necessary to form the grid. But, it is reasonable to presume that the

precise arrangement of 25 metal centers in such an orderly fashion would not be possible if there were no ligands present.

9.4.3 Magnetism

Variable temperature magnetic measurements were carried out on **1** and **2**. The plot of μ_{mol} against T profile for **2** is given in Fig. 9.7. The two complexes **1** and **2** gave identical profiles within the 2-300 K temperature range. The magnetic moment of 30.1 μ_B at room temperature is consistent with the presence of 25 Mn(II) centers. The moment gradually drops down to a value of 18.8 μ_B at 2 K. This indicates an intramolecular antiferromagnetic exchange within the cluster. From the point of the well understood magnetism of numerous [3 x 3] $Mn(II)_9$ grids, a ground state of S = 5/2 might be expected for a [5 x 5] $Mn(II)_{25}$ grid, because of the odd number of spin centers. This presumption supposes that the intra-grid connections between metal centers are similar to those which exist in regular [3 x 3] grid systems, with all hydrazone μ-O linkages. However, the magnetic moment at 2 K is much higher than what would be expected for an S = 5/2 ground state.

This would suggest two things. Firstly, the exchange coupling between the metal centers within the grid may not be uniform and secondly that the exchange coupling is probably weaker than in the $Mn(II)_9$ grids. The ligand '4popap' has four ionizable protons which would dissociate during the course of the reaction in order to make the fully deprotonated L_{10}^{40-} ligand framework within the [5 x 5] grid. In most cases

involving the synthesis of regular [3 x 3] $Mn(II)_9$ grids, addition of base is not necessary for proton loses, which occurs spontaneously. However, in the present case, where a large number of protons is involved, it might require fairly basic conditions for the full deprotonation of all the ligands.

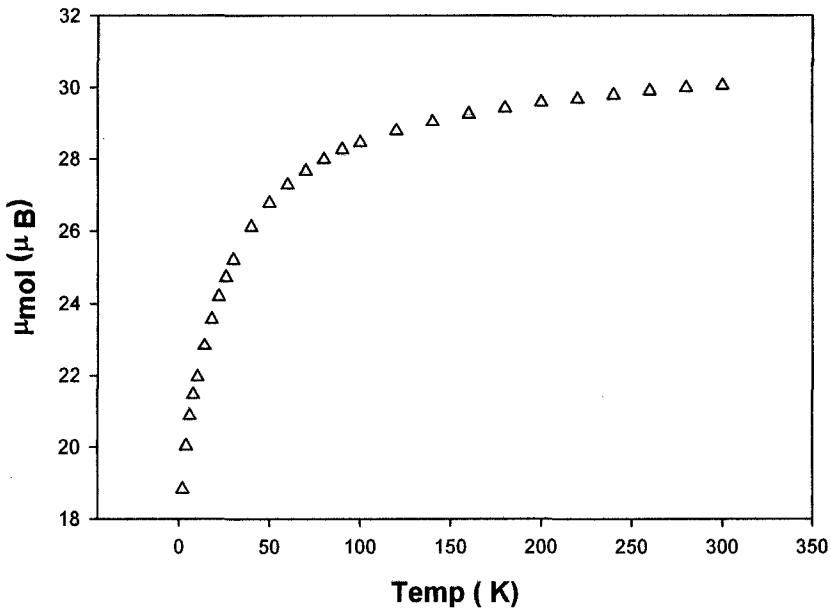

Fig. 9.7 μ_{mol} (μ_B) vs. Temperature profile for **2**

Any less basic reaction condition would lead to a mixture of ligands with partial deprotonation. Partial deprotonation has been observed before with the tritopic ligand 2pmoap in the nonanuclear $[Cu_9(2pmoap\text{-}2H)_2(2pmoap\text{-}H)_4](ClO_4)_{10}$ grid, which contains a mixture of singly and doubly deprotonated ligands [130]. So, in the present case of the $Mn(II)_{25}$ grid, some neutral C=O groups could be acting as bridges between the Mn(II)

ions, which would lead to longer Mn-O bonds and in turn result in weaker magnetic exchange.

Magnetization data as a function of field at 2K were also obtained for **2**. The M/H profile is shown in Fig. 9.8. The profile shows a gradual rise to a very large Nβ value and at high field the profile is not typical of a system approaching saturation. The overall profile is however similar to a typical $Mn(II)_9$, having a change in slope at around 3T. This is due to a field dependent anisotropy effect in $Mn(II)_9$ systems [110]. In an attempt to model the magnetization profile, an interesting aspect of the profile was revealed.

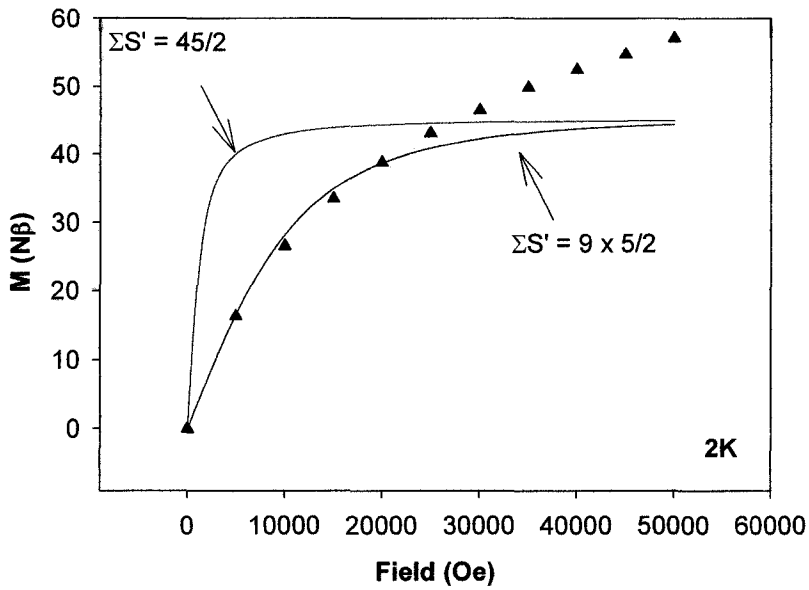

Fig. 9.8 Magnetization vs. field data for **2**. Blue line drawn with S = 9 x 5/2 at 2K; Red line with S = 45/2 at 2 K. ▲Experimental data.

It seemed that the large Nβ value is not associated with one large ordered collection of spins with S = 45/2 (Red line; Fig. 9.8). Rather it is much closer to a profile with nine 'satellite' clusters of spins, each having S = 5/2. In fact, the lower portion of the profile could be modeled with this suggested arrangement of spins with g = 2.0 at 2 K (Blue line Fig. 9.8). The variable temperature magnetic data as a function of temperature from 2-300 K for **4** were collected. A magnetic moment of 5.74 μ_B was observed over the whole temperature range. This is consistent with a mononuclear species in **4**.

9.5 Conclusion

Polymetallic ordered arrangements of metal ions with [n x n] square structures can be synthesized by using tritopic (n = 3) 2,6-picolinic dihydrazone and tetratopic 3,6-pyridazine dihydrazone (n = 4) based linear ligands [113, 182], where the metal ions within the cluster framework are bridged by single hydrazone oxygen atoms (M_9) and a combination of hydrazone, hydroxide and pyridazine (M_{16}) . The key element that most of these linear ligands have is the compartmental and linear positioning of the coordination pockets. Such an arrangement encourages the linear alignment of octahedral metal ions. The *mer*-arrangement of the donor atoms in each of the coordination pockets also directs the incoming ligand to have a perpendicular twist around each metal ion in order to coordinate. These two effects result in [n x n] square grids through self-assembly.

A logical extension of a hydrazone based ligand by introducing similar tridentate donor pockets on either side of a 2,6-picolinic dihydrazone core resulted in the pentatopic ligand 4popap, which enabled creation of a large [5 x 5] square $Mn(II)_{25}$ grid. The difficulty regarding the complete characterization of the grid was associated mostly with solubility issues, and difficulties in obtaining good x-ray quality crystals. However, this limitation has been overcome by using surface imagery techniques (STM and CITS), which showed that the $Mn(II)_{25}$ grid does exist. The images showed a well defined [5 x 5] square array of $Mn(II)_{25}$ ions as bright spots with expected distances of separation between adjacent metal centers. This approach has opened up new possibilities of using this structural probe as an exploratory tool for metal ion assemblies in general.

General Conclusions

A number of mono and dihydrazide based ligands have been synthesized and characterized. Starting from simple ditopic picolinic hydrazone based ligands, longer and relatively linear ligands with higher coordination ability such as a pentatopic ligand were developed and synthesized, with preplanned and symmetric extensions. The resulting polynuclear clusters were characterized structurally and their magnetic behavior with variable temperature was examined.

The ditopic ligand 'pomp' yielded tetranuclear [2 x 2] $Cu(II)_4$ and $Mn(II)_4$ grid complexes, and also pentanuclear (homoleptic) $Mn(II)_5$ clusters with Mn(II) ions. In all of these complexes, the metal ions are hydrazone oxygen bridged except in the case of the $Cu(II)_4$ complex where the rectangular grid contains a mixture of hydrazone and N-N diazine bridges. All of the complexes exhibited intramolecular antiferromagnetic exchange. An overall higher exchange coupling (~ - 3 cm^{-1}) between the Mn(II) centers was observed in the pentanuclear cluster compared to other homologous $[L_6Mn(II)_5]$ complexes with ligands having -NH_2 groups (e.g. poap). The delocalization of the overall electron density caused by the 'mesomeric' effect of the -NH_2 lone pair, causes comparatively weaker (~ - 1.8 cm^{-1}) exchange coupling. This type of effect is not possible with the Schiff base type linkage in 'pomp' with -CH_3 groups.

Two different categories of tritopic ligands were synthesized and characterized. The ones with secondary -*NH* groups in the middle mostly yielded linear trinuclear

complexes with Cu(II) ions and a triangular trinuclear complex when reacted with Mn(II). In one special case, the ligand formed a dinuclear complex with Ni(II) with $[L_3Ni_2]$ stoichiometry, with well separated Ni(II) centers. Structural elucidation of the trinuclear $Mn(II)_3$ complex revealed the flexible nature of this class of ligands in general, which is not suitable for the formation of [3 x 3] grids. All of the complexes except the dinuclear Ni(II) complex showed intramolecular antiferromagnetic coupling. Tritopic ligands with a relatively rigid central pyridine group e.g. 2pomp, yielded several nonanuclear $[L_6Mn(II)_9]$ [3 x 3] grids when reacted with Mn(II) ions. The hydrazone oxygen bridging network within the square grid resulted in antiferromagnetic exchange coupling, with comparable magnitude to that seen before in similar nonanuclear grids.

Octanuclear 'pinwheel' clusters formed when '2pomp' was reacted with Cu(II) ions. Each ligand binds to two metals to make a $[Cu_4(\mu\text{-}O)_4]$ central core, while the other end of the ligand adopts a 180° twisted conformation which projects out from the central core and coordinates to a second Cu(II) ion making the pinwheel arms. Due to orthogonal connections between the copper(II) magnetic orbitals the pinwheel clusters exhibited intramolecular ferromagnetism, which is relatively rare in this polynuclear class of metal complexes.

Ligands with more coordination compartments are necessary to create larger grids. Extension of a tritopic 2,6-disubstituted pyridine carboxylic acid dihydrazide fragment with methyl benzoyl formate gave the pentatopic ligand '4popap'. The

pentatopic ligand 4popap yielded a [5 x 5] $Mn(II)_{25}$ cluster when reacted with Mn(II) ions to form orange crystalline products, but no satisfactory structural result was obtained using x-ray crystallography. STM and CITS surface imagery techniques on HOPG however clearly showed that the $Mn(II)_{25}$ [5 x 5] grid does exist. The image showed a clear array of 25 Mn(II) centers in a [5 x 5] square grid arrangement with expected distances of separation between adjacent metal centers.

Changing the basic ligand structure to include a central oxalic dihydrazide group with pyridine end groups, led to [2 x 2] square tetranuclear complexes with Co(II) ions. Reaction of $[L_4Co(II)_2Co(III)_2]$ tetranuclear complex with NH_4SCN gave a unique octanuclear mixed oxidation state $[L_8Co(II)_4/Co(III)_4]$ [2] catenane complex. Inorganic catenanes with transition metal backbone are rare.

Another dramatic consequence of changing the terminal ligand functional group was realized when the two end groups of a nominally tritopic ligand were replaced with oxime substituents. The oxime groups introduced extra coordination capability, and when reacted with $Cu(OAc)_2$ the ligand produced a unique polynuclear $Cu(II)_{36}$ cluster, involving an intricate assembly of eight triangular tri-copper subunits bridged along the edges of a cubic structural arrangement to single copper ions.

References

[1] P. D. Beer, P. A. Gale, D. K. Smith, *Supramolecular Chemistry*, Oxford University Press, 1999.

[2] F. Wöhler, *Poggendorfs Ann. Physik.*, 1828, **12**, 253.

[3] K. B. Mullis was awarded Nobel Prize in Chemistry in 1993 for his work in surmounting the barrier to synthesize oligonucleotides by the Polymerase Chain Reaction (PCR).

[4] M. Simard, D. Su, J. D. Wuest, *J. Am. Chem. Soc.*, 1991, **113**, 4696.

[5] J.-M. Lehn, *Supramolecular Chemistry- Concepts and perspectives*, VCH, 1995.

[6] H. W. Kroto, *Angew. Chem.*, 1992, **104**, 113; *Angew. Chem. Int. Ed. Engl.*, 1992, **31**, 111.

[7] T. W. Ebbesen, *Annu. Rev. Mater. Sci.*, 1994, **24**, 235.

[8] M. M. Harding, U. Koert, J.-M. Lehn, A. M. -Rigault, C. Piguet, J. Siegel, *Helv. Chim. Acta.*, 1991, **74**, 594.

[9] D. Wester, G. J. Palenik, *J. Chem. Soc., Chem. Commun.*, 1975, 74.

[10] J.-M. Lehn, A. Rigault, *Angew. Chem.*, 1988, **100**, 1121; *Angew. Chem. Int. Ed. Engl.*, 1988, **27**, 1095.

[11] J.-P. Sauvage, *Transition Metals in Supramolecular Chemistry*, John Wiley and Sons, 1999.

[12] P. N. W. Baxter, *Comprehensive Supramolecular Chemistry* (Eds.: J. L. Atwood, J. E. D. Davies, D. D. MacNicol, F. Vögtle, J.-M. Lehn), *Metal ion directed assembly of*

complex molecular Architecture and nanostructures, Vol.-9, (Eds.: J.-P. Sauvage, M. W. Hosseini), 1st ed., Pergamon, Oxford, 1996.

[13] E. C. Constable, *Comprehensive Supramolecular Chemistry* (Eds.: J. L. Atwood, J. E. D. Davies, D. D. MacNicol, F. Vögtle, J.-M. Lehn), *Polynuclear Transition metal Helicates*, Vol.-9, (Eds.: J.-P. Sauvage, M. W. Hosseini), 1st ed., Pergamon, Oxford, 1996.

[14] M. Fujita, *Comprehensive Supramolecular Chemistry* (Eds.: J. L. Atwood, J. E. D. Davies, D. D. MacNicol, F. Vögtle, J.-M. Lehn), *Self assembled Macrocycles, cages, and Catenanes containing Transition Metals in their backbones*, Vol.-9, (Eds.: J.-P. Sauvage, M. W. Hosseini), 1st ed., Pergamon, Oxford, 1996.

[15] J.-C. Chambron, C. Dietrich-Buchecker, J.-P. Sauvage, *Comprehensive Supramolecular Chemistry* (Eds.: J. L. Atwood, J. E. D. Davies, D. D. MacNicol, F. Vögtle, J.-M. Lehn), *Transition metals as Assembling and Templating species: Synthesis of Catenanes, and Molecular Knots*, Vol.-9, (Eds.: J.-P. Sauvage, M. W. Hosseini), 1st ed., Pergamon, Oxford, 1996.

[16] A. Klug, *Angew. Chem. Int. Ed. Engl.*, 1983, **22**, 565.

[17] P. N. W. Baxter, J.-M. Lehn, B. O. Kneisel, D. Fenske, *Angew. Chem. Int. Ed. Engl.*, 1997, **36**, 1978.

[18] J. Rojo, F. J. Romero-Salguero, J.-M. Lehn, G. Baum, D. Fenske, *Eur. J. Inorg. Chem.*, 1999, 1421.

[19] M. Ruben, E. Breuning, J.-P. Gisselbrecht, J.-M. Lehn, *Angew. Chem. Int. Ed.*, 2000, **39**, 4139.

[20] A. Petitjean, N. Kyritsakas, J.-M. Lehn, *J. Chem. Soc., Chem. Commun.*, 2004, 1168.

[21] E. Breuning, G. S. Hanan, F. J. Romero-Salguero, A. M. Garcia, P. N. W. Baxter, J.-M. Lehn, E. Wegelius, K. Rissanen, H. Nierengarten, A. V. Dorsselaer, *Chem. Eur. J.*, 2002, **8**, 3458.

[22] A. M. Garcia, F. J. Romero-Salguero, D. M. Bassini, J.-M. Lehn, G. Baum, D. Fenske, *Chem. Eur. J.*, 1999, **5**, 1803.

[23] D. J. Cram, *Preorganization from solvents to Spherands, Angew. Chem. Int. Ed. Engl.*, 1986, **25**, 1039.

[24] P. N. W. Baxter, J.-M. Lehn, J. Fischer, M.-T. Youinou, *Angew. Chem. Int. Ed. Engl.*, 1994, **33**, 2284.

[25] P. N. W. Baxter, J.-M. Lehn, J. Fischer, M.-T. Youinou, *Angew. Chem.*, 1994, **106**, 2432.

[26] J.-M. Lehn, *Supramolecular Science: Where it Is and Where it Is going* (Eds.: R. Ungaro, E. Dalcanale), Kluwer publication, Dordrecht, 1999, 287.

[27] V. Smith, J.-M. Lehn, *J. Chem. Soc., Chem. Commun.*, 1996, 2733.

[28] L. K. Thompson, V. T. Chacko, J. A. Elvidge, A. B. P. Lever, R. V. Parish, *Can. J. Chem.*, 1969, **47**, 4141.

[29] A. B. P. Lever, L. K. Thompson, W. M. Reiff, *Inorg. Chem.*, 1972, **11**, 104.

[30] L. K. Thompson, *Can. J. Chem.*, 1983, **61**, 579.

[31] L. K. Thompson, A. W. Hanson, B. S. Ramaswami, *Inorg. Chem.*, 1984, **23**, 2459.

[32] L. K. Thompson, F. W. Hartstock, P. Robicahud, A. W. Hanson, *Can. J. Chem.*, 1984, **62**, 2755.

[33] S. K. Mandal, L. K. Thompson, A. W. Hanson, *J. Chem. Soc., Chem. Commun.*, 1985, 1709.

[34] L. K. Thompson, T. C. Woon, D. B. Murphy, E. J. Gabe, F. L. Lee, Y. Le Page, *Inorg. Chem.*, 1985, **24**, 4719.

[35] L. K. Thompson, S. K. Mandal, E. J. Gabe, J.-P. Charland, *J. Chem. Soc., Chem. Commun.*, 1986, 1537.

[36] L. Rosenberg, L. K. Thompson, E. J. Gabe, F. L. Lee, *J. Chem. Soc., Dalton Trans.*, 1986, 625.

[37] S. K. Mandal, L. K. Thompson, M. J. Newlands, F. L. Lee, Y. Lepage, J.-P. Charland, E. J. Gabe, *Inorg. Chim. Acta.*, 1986, **122**, 199.

[38] S. K. Mandal, T. C. Woon, L. K. Thompson, M. J. Newlands, E. J. Gabe, *Aust. J. Chem.*, 1986, **39**, 1007.

[39] L. K. Thompson, S. K. Mandal, E. J. Gabe, F. L. Lee, A. W. Addison, *Inorg. Chem.*, 1987, **26**, 657.

[40] L. K. Thompson, S. K. Mandal, L. Rosenberg, F. L. Lee, E. J. Gabe, *Inorg. Chim. Acta.*, 1987, **133**, 81.

[41] L. K. Thompson, F. L. Lee, E. J. Gabe, *Inorg. Chem.*, 1988, **27**, 39.

[42] L. K. Thompson, S. K. Mandal, J.-P. Charland, E. J. Gabe, *Can. J. Chem.*, 1988, **66**, 348.

[43] T. Wen, L. K. Thompson, F. L. Lee, E. J. Gabe, *Inorg. Chem.*, 1988, **27**, 4190.

[44] S. K. Mandal, L. K. Thompson, M. J. Newlands, J.-P. Charland, E. J. Gabe, *Inorg. Chim. Acta.*, 1990, **178**, 169.

[45] S. S. Tandon, L. K. Thompson, R. C. Hynes, *Inorg. Chem.*, 1992, **31**, 2210.

[46] L. Chen, L. K. Thompson, J. N. Bridson, *Inorg. Chem.*, 1993, **32**, 2938.

[47] L. Chen, L. K. Thompson, J. N. Bridson, *Inorg. Chim. Acta.*, 1993, **214**, 67.

[48] S. S. Tandon, L. Chen, L. K. Thompson, J. N. Bridson, *Inorg. Chem.*, 1994, **33**, 490.

[49] S. S. Tandon, L. K. Thompson, J. N. Bridson, *J. Chem. Soc., Chem. Commun.*, 1993, 804.

[50] S. S. Tandon, L. K. Thompson, M. E. Manuel, J. N. Bridson, *Inorg. Chem.*, 1994, **33**, 5555.

[51] L. K. Thompson, S. S, Tandon, M. E. Manuel, *Inorg. Chem.*, 1995, **34**, 2356.

[52] S. S. Tandon, L. K. Thompson, D. O. Miller, *J. Chem. Soc., Chem. Commun.*, 1995, 1907.

[53] L. K. Thompson, S. S. Tandon, *Comments Inorg. Chem.*, 1996, **18**, 125.

[54] C. L. Sheppard, S. S. Tandon, L. K. Thompson, J. N. Bridson, D. O. Miller, M. Handa, F. Lloret, *Inorg. Chim. Acta.*, 1996, **250**, 227.

[55] Z. Xu, L. K. Thompson, D. O. Miller, *Inorg. Chem.*, 1997, **36**, 3985.

[56] Z. Xu, L. K. Thompson, D. O. Miller, H. J. Clase, J. A. K. Howard, A. E. Goeta, *Inorg. Chem.*, 1998, **37**, 3620.

[57] L. Zhao, L. K. Thompson, Z. Xu, D. O. Miller, D. R. Stirling, *J. Chem. Soc., Dalton Trans.*, 2001, 1706.

[58] C. J. Matthews, K. Avery, Z. Xu, L. K. Thompson, L. Zhao, D. O. Miller, K. Biradha, K. Poirier, M. J. Zoworotko, C. Wilson, A. E. Goeta, J. A. K. Howard, *Inorg. Chem.*, 1999, **38**, 5266.

[59] L. K. Thompson, C. J. Matthews, L. Zhao, Z. Xu, D. O. Miller, C. Wilson, M. A. Leech, J. A. K. Howard, S. L. Heath, A. G. Whitaker, R. E. P. Winpenny, *J. Solid State Chem.*, 2001, **159**, 308.

[60] Z. Xu, L. K. Thompson, C. J. Matthews, D. O. Miller, A. E. Goeta, J. A. K. Howard, *Inorg. Chem.*, 2001, **40**, 2446.

[61] C. J. Matthews, Z. Xu, S. K. Mandal, L. K. Thompson, K. Biradha, K. Poirier, M. J. Zaworotko, *J. Chem. Soc., Chem. Commun.*, 1999, 347.

[62] C. J. Matthews, L. K. Thompson, S. R. Parsons, Z. Xu, D. O. Miller, S. L. Heath, *Inorg. Chem.*, 2001, **40**, 4448.

[63] J. Hausmann, G. B. Jameson, S. Brooker, *J. Chem. Soc., Chem. Commun.*, 2003, 2992.

[64] C. S. Campos-Fernández, B. L. Schottel, H. T. Chifotides, J. K. Bera, J. Bacsa, J. M. Koomen, D. H. Russell, K. R. Dunbar, *J. Am. Chem. Soc.*, 2005, **127**, 12909.

[65] L. Zhao, Z. Xu, L. K. Thompson, D. O. Miller, *Polyhedron*, 2001, **20**, 1359.

[66] Z. Xu, L. K. Thompson, D. O. Miller, *Polyhedron*, 2002, **21**, 1715.

[67] Z. Xu, L. K. Thompson, D. O. Miller, *J. Chem. Soc., Chem. Commun.*, 2001, 1170.

[68] V. A. Milway, V. Niel, T. S. M. Abedin, Z. Xu, L. K. Thompson, H. Grove, D. O. Miller, S. R. Parsons, *Inorg. Chem.*, 2004, **43**, 1874.

[69] R. E. Winpenny, *Transition metals in Supramolecular Chemistry*, Ed., J.-P. Sauvage, 1999, John Wiley & Sons Ltd.

[70] L. Zhao, V. Niel, L. K. Thompson, Z. Xu, V. A. Milway, R. G. Harvey, D. O. Miller, C. Wilson, M. Leech, J. A. K. Howard, S. L. Heath, *J. Chem. Soc., Dalton Trans.*, 2004, 1446.

[71] Z. Xu, L. K. Thompson, V. A. Milway, L. Zhao, T. L. Kelly, D. O. Miller, *Inorg. Chem.*, 2003, **42**, 2950.

[72] R. Bhula, D. C. Weatherburn, *Angew. Chem. Int. Ed. Engl.*, 1991, **30**, 688.

[73] A. J. Blake, C. M. Grant, S. Parsons, J. M. Rawson, R. E. P. Winpenny, *J. Chem. Soc., Chem. Commun.*, 1994, 2363.

[74] A. J. Blake, C. M. Grant, S. Parsons, J. M. Rawson, G. A. Solan, R. E. P. Winpenny, *J. Chem. Soc., Dalton Trans.*, 1995, 2311.

[75] M. Murugesu, R. Clérac, C. E. Anson, A. K. Powell, *J. Chem. Soc., Chem. Commun.*, 2004, 1598.

[76] M. Murugesu, R. Clérac, C. E. Anson, A. K. Powell, *Inorg. Chem.*, 2004, **43**, 7269.

[77] (a) S. P. Watton, P. Fuhrmann, L. E. Pence, A. Caneschi, A. Cornia, G. L. Abbati, S. J. Lippard, *Angew. Chem.*, 1997, **109**, 2917. (b) S. P. Watton, P. Fuhrmann, L. E. Pence, A. Caneschi, A. Cornia, G. L. Abbati, S. J. Lippard, *Angew. Chem. Int. Ed. Engl.*, 1997, **36**, 2774.

[78] A. L. Dearden, S. Parsons, R. E. Winpenny, *Angew. Chem.*, 2001, **113**. 156.

[79] A. J. Tasiopoulos, A. Vinslava, W. Wernsdorfer, K. A. Abboud, G. Christou, *Angew. Chim. Int. Ed. Engl.*, 2004, **43**, 2117.

[80] O. Kahn, *Molecular Magnetism*, VCH publishers, 1993.

[81] I. Morgenstern-Badarau, D. Cocco, A. Desideri, G. Rotilio, J. Jordanov, N. Dupré, *J. Am. Chem. Soc.*, 1986, **108**, 300.

[82] R. L. Carlin, *Magnetochemistry*, Springer-Verlag, New York, 1986, 65.

[83] J. H. Van Vleck, *The Theory of Electrical and Magnetic Susceptibilities*, Oxford university press, 1952.

[84] B. Bleaney, K. D. Bowers, *Proc., R. Soc., London Ser., A.*, 1952, **214**, 451

[85] K. Kambe, *J. Phys. Soc. Jpn.*, 1950, **5**, 48.

[86] R. W. Jotham, S. F. A. Kettle, *Inorg. Chim. Acta.*, 1970, **4**, 145.

[87] L. K. Thompson, O. Waldmann, Z. Xu, *Coord. Chem.*, 2005, **249**, 2677.

[88] V. A. Milway, *PhD Thesis*, July 2006, Memorial University of Newfoundland, St. John's, Canada.

[89] W. Steed, J. L. Atwood, *Supramolecular Chemistry*, sec 7.4.1, p. 479, John Wiley and Sons, Ltd., 2000.

[90] B. Hasenknopf, J.-M. Lehn, N. Boumediene, A. D.-Gervais, A. V. Dorsselaer, B. Kneisel, D. Fenske, *J. Am Chem. Soc.*, 1997, **119**, 10956.

[91] O. Waldmann, J. Hassmann, P. Müller, G. S. Hanan, D. Volkmer, U. S. Schubert, J. -M. Lehn, *Phys. Rev. Lett.*, 1997, **78**, 3390.

[92] O. Waldmann, J. Hassmann, P. Müller, G. S. Hanan, D. Volkmer, U. S. Schubert, J. -M. Lehn, *Phys. Rev., B* 1998, **58**, 3277.

[93] P. N. W. Baxter, J. -M. Lehn, B. O. Kneisel, D. Fenske, *J. Chem. Soc., Chem. Commun.*, 1997, 2231.

[94] J. Zabicky (Ed.), *The Chemistry of Amides,* Interscience, London, 1970, 515.

[95] F. H. Case, *J. Org. Chem.*, 1965, **30**, 931.

[96] S. R. Parsons, L. K. Thompson, unpublished results.

[97] M. B. Ferrari, A. Bonardi, G. G. Fava, C. Pelizzi, P. Tarasconi, *Inorg. Chim. Acta.*, 1994, **223**, 77.

[98] T. L. Kelly, V. A. Milway, H. Grove, V. Niel, T. S. M. Abedin, L. K. Thompson, L. Zhao, R. G. Harvey, D. O. Miller, M. Leech, A. E. Goeta, J. A. K. Howard, *Polyhedron*, 2005, **24**, 807.

[99] SHELXL97: G. M. Sheldrick, 1997.

[100] DIRDIF94: P. T. Beurskens, G. Admiraal, G. Beurskens, W. P. Bosman, R. de Gelder, R. Israel, and J. M. M. Smith, 1994. The DIRDIF program system, Technical Report of the Crystallography Laboratory, University of Nijmigen, The Netherlands.

[101] D. T. Cromer, J. T. Waber, International Tables for X-ray crystallography., Vol. IV, The Kynoch Press, Birmingham, England, Table 2.2 A (1974).

[102] J. A. Ibers & W. C. Hamilton, *Acta. Crystallogr.*, 1964, **17**, 781.

[103] D. C. Creagh & W. J. McAuley, "International Tables for Crystallography", Vol C, (A. J. C. Wilson Ed.), Kluwer Academic Publishers, Boston, Table 4.2.6.8, 1992, 219.

[104] D. C. Creagh & J. H. Hubbell, "International Tables for Crystallography", Vol C, (A. J. C. Wilson Ed.), Kluwer Academic Publishers, Boston, Table 4.2.4.3, 1992, 200.

[105] (a) teXsan for Windows version 1.06: Crystal Structure Analysis Package, Molecular Structure Corporation (1997-1999). (b) For a systematic determination of structural geometries between square pyramidal and tetragonal bipyramidal five

coordinate copper centers using structural index parameter (τ) see A. W. Addison, T. N. Rao, *J. Chem. Soc., Dalton Trans.*, 1984, 1349.

[106] Z. Xu, L. K. Thompson, C. J. Matthews, D. O. Miller, A. E. Goeta, C. Wilson, J. A. K. Howard, M. Ohba, H. Okawa, *J. Chem. Soc., Dalton Trans.*, 2000, 69.

[107] L. Zhao, C. J. Matthews, L. K. Thompson, S. L. Heath, *J. Chem. Soc., Chem. Commun.*, 2000, 265.

[108] L. Zhao, Z. Xu, L. K. Thompson, S. L. Heath, D. O. Miller, M. Ohba, *Angew. Chem. Int. Ed.*, 2000, 39, 3114.

[109] O. Waldmann, R. Koch, S. Schromm, P. Müller, L. Zhao, L. K. Thompson, *Chem. Phys. Lett.*, 2000, **332**, 73.

[110] O. Waldmann, L. Zhao, L. K. Thompson, *Phys, Rev. Lett.*, 2002, **88**, 066401.

[111] L. K. Thompson, L. Zhao, Z. Xu, D. O. Miller, W. M. Reiff, *Inorg. Chem.*, 2003, **42**, 128.

[112] L. K. Thompson, O. Waldmann, Z. Xu, *Magnetic Properties of Self-Assembled [2 × 2] and [3 × 3] Grids, Magnetism: Molecules to Materials IV,* 2003, 173, *Copyright © 2002 Wiley-VCH Verlag GmbH & Co. KGaA.*

[113] V. A. Milway, S. M. T. Abedin, V. Niel, T. L. Kelly, L. N. Dawe, S. K. Dey, D. W. Thompson, D. O. Miller, M. S. Alam, P. Müller, L. K. Thompson, *J. Chem. Soc., Dalton Trans.*, 2006, 2835.

[114] L. K. Thompson, Z. Xu, A. E. Goeta, J. A. K. Howard, H. J. Clase, D. O. Miller, *Inorg. Chem.*, 1998, **37**, 3217.

[115] L. K. Thompson, C. J. Matthews, L. Zhao, C. Wilson, M. A. Leech, J. A. K. Howard, *J. Chem. Soc., Dalton Trans.*, 2001, 2258.

[116] (a) S. K. Mandal, V. G. Young, Jr., L. Que, Jr., *Inorg. Chem.*, 2000, **39**, 1831. (b) C. Boskovic, E. Rusanov, H. Stoeckli-Evans, H. U. Güdel, *Inorg. Chem. Commun.*, 2002, **5**, 881.

[117] J. Estienne, R. Weiss, *J. Chem. Soc., Chem. Commun.*, 1972, 862.

[118] P. Christian, G. Rajaraman, A. Harrison, M. Helliwell, J. J. W. McDouall, J. Raftery, R. E. P. Winpenny, *J. Chem. Soc., Dalton Trans.*, 2004, 2550.

[119] MAGMUN 4.1 is available free of charge. It has been developed by Dr. Zhiqiang Xu (Memorial University) in collaboration with Prof. L. K. Thompson (lthomp@mun.ca) and Dr. O. Waldmann (oliver.waldmann@iac.unibe.ch). All the magnetic data fitting in this thesis were done using this software. The source code of this software is not distributed. The program may be used for scientific purposes only, and economic utilization is not allowed.

[120] H. R. Chang, S. K. Larsen, P. D. W. Boyd, C. G. Pierpont, D. N. Hendrickson, *J. Am. Chem. Soc.*, 1988, **110**, 4565.

[121] S.-B. Yu, C.-P. Wang, E. P. Dey, R. H. Holm, *Inorg. Chem.*, 1991, **30**, 4067.

[122] (a) V. A. Milway, L. Zhao, T. S. M. Abedin, L. K. Thompson, Z. Xu, *Polyhedron*, 2003, **22**, 1271. (b) L. K. Thompson, S. K. Mandal, S. S. Tandon, J. N. Bridson, M. K. Park, *Inorg. Chem.*, 1996, **35**, 3117.

[123] Z. Xu, L. K. Thompson, D. O. Miller, *J. Chem. Soc., Dalton Trans.*, 2002, 2462.

[124] H. Grove, T. L. Kelly, L. K. Thompson, L. Zhao, Z. Xu, T. S. M. Abedin, D. O. Miller, A. E. Goeta, C. Wilson, J. A. K. Howard, *Inorg. Chem.*, 2004, **43**, 4278.

[125] J. Rojo, J.-M. Lehn, G. Baum, D. Fenske, O. Waldmann, P. Müller, *Eur. J. Chem.*, 1999, 517.

[126] J. Klingele (née Hausmann), J. F. Boas, J. R. Pilbrow, B. Moubaraki, K. S. Murrey, K. J. Berry, K. A. Hunter, G. B. Jameson, P. D. W. Boyd, S. Brooker, *J. Chem. Soc., Dalton Trans., Advance Articles, DOI:* 1039/b614796h.

[127] R. G. Hicks, B. D. Koivisto, M. T. Lemaire, *Org. Lett.*, 2004, **6**, 1887.

[128] CrystalStructure 3.7.0: Crystal structure Analysis package, Rigaku and Rigaku / MSC (2000-2005). 9009 New Trails Dr. The Woodlands TX 77381 USA.

[129] CRYSTALS Issue 10: D. J. Watkin, C. K. Prout, J. R. Carruthers, P. W. Betteridge, Chemical Crystallography Laboratory, Oxford, UK, 1996.

[130] L. N. Dawe, T. S. M. Abedin, T. L. Kelly, L. K. Thompson, D. O. Miller, L. Zhao, C. Wilson, M. A. Leech, J. A. K. Howard, *J. Mater. Chem.*, 2006, **16**, 2645.

[131] L. K. Thompson, *Coord. Chem. Rev.*, 2002, **233-234**, 193.

[132] (a) V. A. Milway, S. M. T. Abedin, L. K. Thompson, D. O. Miller, *Inorg. Chim. Acta.*, 2006, **359**, 2700. (b) D. G. Neilson, R. Roger, J. W. M. Heatlie, L. R. Newlands, *Chem. Rev.*, 1970, **70**, 151.

[133] M.-L. Tong, H. K. Lee, Y.-X. Tong, X.-M. Chen, T. C. W. Mak, *Inorg. Chem.*, 2000, 39, 4666.

[134] D. Dragancea, V. B. Arion, S. Shova, E. Rentschler, N. V. Gerbeleu, *Angew. Chem. Int. Ed.*, 2005, **44**, 7938.

[135] F. M. Woodward, A. S. Albrecht, C. M. Wynn, C. P. Landee, M. M. Turnbull, *Phys. Rev.*, 2002, **B 65**, 144412.

[136] V. A. Milway, L. K. Thompson, unpublished results.

[137] O. Waldmann, H. U. Güdel, T. L. Kelly, L. K. Thompson, *Inorg. Chem.*, 2006, **45**, 3295.

[138] G. S. Hanan, D. Volkmer, U. S. Schubert, J.-M. Lehn, G. Baum, D. Fenske, *Angew. Chem.*, 1997, **109**, 1929.

[139] E. Breuning, M. Ruben, J.-M. Lehn, F. Renz, Y. Garcia, V. Ksenofontov, P. Gütlich, E. Wegelius, K. Rissanen, *Angew. Chem.*, 2000, **112**, 2563.

[140] M. Barboiu, G. Vauhan, R. Graff, J.-M. Lehn, *J. Am. Chem. Soc.*, 2003, **125**, 10257.

[141] S. T. Onions, A. M. Frankin, P. N. Horton, M. B. Hursthouse, C. J. Matthews, *J. Chem. Soc., Chem. Commun.*, 2003, 2864.

[142] V. A. Milway, L. Zhao, T. L. Kelly, L. K. Thompson, unpublished results.

[143] L. Zhao, Z. Xu, H. Grove, V. A. Milway, L. N. Dawe, T. S. M. Abedin, L. K. Thompson, T. L. Kelly, R. G. Harvey, D. O. Miller, L. Weeks, J. G. Shapter, K. J. Pope, *Inorg. Chem.*, 2004, **43**, 3812.

[144] L. K. Thompson, T. L. Kelly, L. N. Dawe, H. Grove, M. T. Lemaire, J. A. K. Howard, E. C. Spencer, C. J. Matthews, S. T. Onions, S. J. Coles, P. N. Horton, M. B. Hursthouse, M. E. Light, *Inorg. Chem.*, 2004, **43**, 7605.

[145] A. L. Gillon, A. G. Orpen, J. Starbuck, X. -Meng Wang, Y. Rodríguez-Martín, C. Ruiz-Pérez, *J. Chem. Soc., Chem. Commun.*, 1999, 2287.

[146] M. E. Fisher, *Am. J. Phy.*, 1964, **32**, 343.

[147] E. Wasserman, *J. Am. Chem. Soc.*, 1960, **82**, 4433.

[148] G. Schill, *Catenanes, Rotaxanes, and Knots*, Academic Press, NY, 1971.

[149] D. M. Walba, *Tetrahedron*, 1985, **41**, 3161.

[150] C. O. Dietrich-Buchecker, J.-P. Sauvage, *Chem. Rev.*,1987, **87**, 795.

[151] C. Dietrich-Buchecker, J. -P. Sauvage, *J. Chem. Soc., Chem. Commun.*, 1999, 615.

[152] B. X. Colasson, J.-P. Sauvage, *Inorg. Chem.*, 2004, **43**, 1895.

[153] P. Mobian , J. -M. Kern, J. -P. Sauvage, *Inorg. Chem.*, 2003, **42**, 8633.

[154] C. Hamann, J. -M. Kern , J.-P. Sauvage, *Inorg. Chem.*, 2003, **42**, 1877.

[155] C. Dietrich-Buchecker, N. Geum, A. Hori, M. Fujita, S. Sakamoto, K. Yamaguchi, J. -P. Sauvage, *J. Chem. Soc., Chem. Commun.*, 2001, 1182.

[156] C. O. Dietrich-Buchecker, J. –M. Kern, J. -P. Sauvage, *J. Chem. Soc., Chem. Commn.*, 1985, 760.

[157] For examples see (a) D. W. Steuerman, H. -R. Tseng, A. J. Peters, A. H. Flood, J. O. Jeppesen, K. A. Nielsen, J. F. Stoddart, J. R. Heath, *Angew. Chem.*, 2004, **116**, 6648. (b) S.-H. Chiu, A. R. Pease, J. F. Stoddart, A. J. P. White, D. J. Williams, *Angew. Chem.*, 2002, **114**, 280. (c) V. Balzani, A. Credi, F. M. Raymo, J. F. Stoddart, *Angew. Chem. Int. Ed.*, 2000, **39**, 3348.

[158] G.-J. M. Gruter, F. J. J. de Kanter, P. R. Markies, T. Nomoto, O. S. Akkerman, F. Bickelhaupt, *J. Am. Chem. Soc.*, 1993, **115**, 12179.

[159] W. J. Hunks, J. Lapierre, H. A. Jenkins, R. J. Puddephatt, *J. Chem. Soc., Dalton Trans.*, 2002, 2885.

[160] See for examples (a) C. P. McArdle, S. Van, M. C. Jennings, R. J. Puddephatt, *J. Am. Chem. Soc.*, 2002, **124**, 3959. (b) C. P. McArdle, M. C. Jennings, J. J. Vittal, R. J. Puddephatt, *Chem. Eur. J.*, 2001, **7**, 3572. (c) C. P. McArdle, M. J. Irwin, M. C. Jennings, J. J. Vittal, R. J. Puddephatt, *Chem. Eur. J.*, 2002, **8**, 723.

[161] *Comprehensive Supramolecular Chemistry*, J. L. Atwood, J. E. D. Davies, D. D. MacNicol, F. Vögtle, K. S. Suslick, eds., Pergamon Press, Oxford, 1996.

[162] M. H. Keefe, K. D. Benkstein, J. T. Hupp, *Coord. Chem. Rev.*, 2000, **205**, 201.

[163] S. J. Loeb, J. A. Wisner, *J. Chem. Soc., Chem. Commun.*, 2000, 845.

[164] M. R. Sambrook, P. D. Beer, J. A. Wisner, R. L. Paul, A. R. Cowley, *J. Am. Chem. Soc.*, 2004, **126**, 15364.

[165] (a) M. E. Padilla-Tosta, O. D. Fox, M. G. B. Drew, P. D. Beer, *Angew.Chem. Int. Ed.*, 2001, **40**, 4235. (b) W. W. H. Wong, J. Cookson, E. A. L. Evans, E. J. L. McInnes, J. Wolowska, J. P. Maher, P. Bishop, P. D. Beer, *J. Chem. Soc., Chem. Commun.*, 2005, 2214.

[166] C. A. Hunter, *J. Am. Chem. Soc.*, 1992, **114 (13)**, 5303.

[167] J. -P. Sauvage, *J. Chem. Soc., Chem. Commun.*, 2005, 1507.

[168] (a) G. J. Palenik, *Inorg. Chem.*, 1997, **36**, 122. (b) M. O'Keeffe, N. E. Brese, *J. Am. Chem. Soc.*, 1991, **113**, 3226.

[169] M. Fujita, F. Ibukuro, K. Yamaguchi, K. Ogura, *J. Am. Chem. Soc.*, 1995, **117**, 4175.

[170] M. Fujita, F. Ibukuro, H. Seki, O. Kamo, M. Imanari, K. Ogura, *J. Am. Chem. Soc.*, 1996, **118**, 899.

[171] B. Odell, M. V. Reddington, A. M. Z. Slawin, N. Spencer, J. F. Stoddart, D. J. Williams, *Angew. Chem. Int. Ed. Eng.*, 1988, **27**, 1547.

[172] The term "van der Waals interplane separation" is defined as a surface-to-surface distance in the cavity of the box. Though the interplanar seperation (atom-to-atom distance) measured with X- ray is actually about ~7 Å. The surface-to-surface distance is shorter by double the van der Waals radius of an aromatic carbon (ca. 3.5 Å).

[173] M. Fujita, M. Aoyagi, F. Ibukuro, K. Ogura, K. Yamaguchi, *J. Am. Chem. Soc.*, 1998, **120**, 611.

[174] A. L. Dearden, S. Parsons, R. E. P. Winpenny, *Angew. Chem. Int. Ed.*, 2001, **40**, 152.

[175] E. K. Brechin, S. G. Harris, A. Harrison, S. Parsons, A. G. Whittaker, R. E. P. Winpenny, *J. Chem. Soc., Chem. Commun.*, 1997, 653.

[176] R. E. P. Winpenny, *J. Chem. Soc., Dalton Trans.*, 2002, 1 and references therein.

[177] W. Schmitt, M. Murugesu, J. C. Goodwin, J. P. Hill, A. Mandel, R. Bhalla, C. E. Anson, S. L. Heath, A. K. Powell, *Polyhedron*, 2001, **20**, 1687.

[178] J. C. Goodwin, R. Sessoli, D. Gatteschi, W. Wernsdorfer, A. K. Powell S. L. Heath, *J. Chem. Soc., Dalton Trans.*, 2000, 1835.

[179] M. Murrie, H. S.-Evans, H. U. Güdel, *Angew. Chem., Int. Ed.*, 2001, **40**, 1957.

[180] E. K. Brechin, O. Cador, A. Caneschi, C. Cadiou, S. G. Harris, S. Parsons, M. Vonci, R. E. P. Winpenny, *J. Chem. Soc., Chem. Commun.*, 2002, 1860.

[181] K. L. Taft, C. D. Delfs, G. C. Papaefthymiou, S. Foner, D. Gatteshi, S. J. Lippard, *J. Am. Chem. Soc.*, 1994, **116**, 823.

[182] S. K. Dey, L. K. Thompson, L. N. Dawe, *J. Chem. Soc., Chem. Commun.*, 2006, 4967.

[183] J. B. Vincent, H. –R. Chang, K. Folting, J. C. Huffman, G. Christou, D. N. Hendrickson, *J. Am. Chem. Soc.*, 1987, **109**, 5703.

[184] R. Wu, M. Poyraz, F. E. Sowrey, C. E. Anson, S. Wocadlo, A. K. Powell, U. A. Jayasooriya, R. D. Cannon, T. Nakamoto, M. Katada, H. Sano, *Inorg. Chem.*, 1998, **37**, 1913.

[185] R. Beckett, B. F. Hoskins, *J. Chem. Soc., Dalton Trans.*, 1972, 291.

[186] R. J. Butcher, C. J. O'Connor, E. Sinn, *Inorg. Chem.*, 1981, **20**, 537.

[187] W. T. Robinson, E. Sinn, *J. Chem. Soc., Chem. Commun.*, 1972, 359.

[188] P. Gluvchinsky, G. M. Mockler, P. C. Healy, E. Sinn, *J. Chem. Soc., Dalton Trans.*, 1974, 1156.

[189] R. M. Countryman, W. T. Robinson, E. Sinn, *Inorg. Chem.*, 1974, **13**, 2013.

[190] (a) E. Sinn, *J. Chem. Soc., Chem. Commun.*, 1975, 665. (b) E. Sinn, *Inorg. Chem.*, 1976, **15**, 358.

[191] J. A. Davis, E. Sinn, *J. Chem. Soc., Dalton Trans.*, 1976, 165.

[192] R. J. Butcher, E. Sinn, *Inorg. Chem.*, 1976, **15**, 1604.

[193] E. Sinn, *Inorg. Chem.*, 1976, **15**, 2698.

[194] C. J. O'Connor, D. P. Freyberg, E. Sinn, *Inorg. Chem.*, 1979, **18**, 1077.

[195] R. J. Butcher, C. J. O'Connor, E. Sinn, *Inorg. Chem.*, 1979, **18**, 1913.

[196] R. Beckett, R. Cotton, B. F. Hoskins, R. L. Martin, D. G. Vince, *Aust. J. Chem.*, 1969, **22**, 2527.

[197] SAPI91: Fan Hai-Fu (1991), *Structure Analysis Programs with Intelligent Control*, Rigaku Corporation, Tokyo, Japan.

[198] D. Datta, A. Chakravorty, *Inorg. Chem.*, 1983, **22**, 1611.

[199] V. H. Crawford, H. W. Richardson, J. R. Wasson, D. J. Hodgson, W. E. Hatfield, *Inorg. Chem.*, 1976, **15**, 2107.

[200] (a) M. F. Charlot, S. Jeannin, O. Kahn, J. L.-Abul, J. M.-Frere, *Inorg. Chem.*, 1979, **18**, 1675. (b) M. F. Charlot, O. Kahn, S. Jeannin, Y. Jeannin, *Inorg. Chem.*, 1980, **19**, 1410.

[201] (a) M. Ruben, J. Rojo, F. J. Romero-Salguero, L. H. Uppadine, J.-M. Lehn, *Angew. Chem. Int. Ed.*, 2004, **43**, 3644. (b) M. Ruben, *Angew. Chem. Int. Ed.*, 2005, **44**, 1594.

[202] P. N. W. Baxter, J.-M. Lehn, G. Baum, D. Fenske, *Angew. Chem. Int. Ed. Engl.*, 1997, **36**, 1987.

[203] M. Ruben, J.-M. Lehn, G. Vaughan, *J. Chem. Soc., Chem. Commun.*, 2003, 1338.

[204] (a) E. Breuning, M. Ruben, J.-M. Lehn, F. Renz, Y. Garcia, V. Ksenofontov, P. Gültich, E. Wegelius, K. Rissanen, *Angew. Chem. Int. Ed.*, 2000, **39**, 2504. (b) M. Ruben, E. Breuning, J.-M. Lehn, V. Ksenofontov, F. Renz, P. Gültich, G. Vaughan, *Chem. Eur. J.*, 2003, 9, 4422. (c) M. Ruben, U. Ziener, J.-M. Lehn, V. Ksenofontov, P. Gültich, G. B. M. Vaughan, *Chem. Eur. J.*, 2005, **11**, 94.

[205] (a) A. Semenov, J. P. Spatz, J.-M. Lehn, C. H. Weidl, U. S. Schubert, M. Möller, *Appl. Surf. Sci.*, 1999, 456, 144. (b) A. Semenov, J. P. Spatz, M. Möller, J.-M. Lehn, B. Sell, D. Schubert, C. H. Weidl, U. S. Schubert, *Angew. Chem. Int. Ed.*, 1999, **38**, 2547.

[206] U. Ziener, J.-M. Lehn, A. Mourran, M. Möller, *Chem. Eur. J.*, 2002, **8**, 951.

[207] M. S. Alam, S. Strömsdörfer, V. Dremov, P. Müller, J. Kortus, M. Ruben, J.-M. Lehn, *Angew. Chem. Int. Ed.*, 2005, **44**, 7896.

[208] (a) J. G. Shapter, L. Weeks, L. K. Thompson, K. J. Pope, Z. Xu, M. R. Johnston, *Smart Mater. Struct.*, 2006, **15**, S171 (b) L. Weeks, L. K. Thompson, J. G. Shapter, K. J. Pope, Z. Xu, *J. Microsc.*, 2003, **212**, 102 (c) J. G. Shapter, L. Weeks, L. K. Thompson, K. J. Pope, Z. Xu, M. Johnston, *Proc. SPIE-Int. Soc. Eng.*, 2004, **5275**, 59.

[209] S. K. Dey, T. S. M. Abedin, L. N. Dawe, S. S. Tandon, L. K. Thompson, A. V. Postnikov, M. S. Alam, P. Müller, *Accepted, Inorg. Chem.*

[210] SIR92: A. Altomare, G. Cascarano, C. Giacovazzo, A. Guagliardi, M. Burla, G. Polidori, M. Camalli, *J. Appl. Cryst.*, 1994, 27, 435.

[211] DIRDIF99: P. T. Beurskens, G. Admiraal, G. Beurskens, W. P. Bosman, R. de Gelder, R. Israel, and J. M. M. Smith, 1999. The DIRDIF-99 program system, Technical Report of the Crystallography Laboratory, University of Nijmegen, The Netherlands.

Appendix A: Magnetic models, vector coupling schemes

A1: Trinuclear complexes

A trinuclear complex with three metal centers can be arranged in several different ways; an equilateral triangle with single *J*, an isosceles triangle with two different *J* values, a scalene triangle with three different *J*, or a linear trinuclear compound with again two different J values. Technically the magnetic exchange situation in a linear trinuclear complex and an isosceles triangle are similar. So, they can be treated in the same manner.

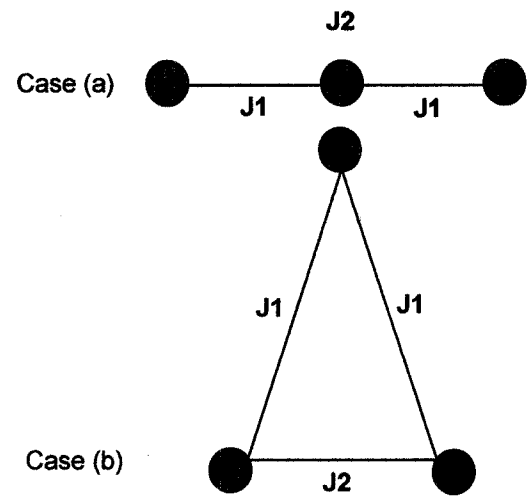

Fig. A1-1 Two magnetic models for trinuclear complexes.

Figure A1-1 gives two models for a trinuclear case. *J2* can be the exchange integral along the short arms of the isosceles triangle and generally stronger than *J1* (case (b); Fig A1-1) or it can be the exchange coupling between the two ends of a linear

trinuclear compound. In which case, it will be weaker than *J1* (case (a); Fig A1-1). If *J1* = *J2*, then the diagram would represent an equilateral triangle. In cases where *J2* >> *J1*, the complex can be treated as a dinuclear complex plus an additional curie center such that *J1*= 0. One such trinuclear complex has been reported in this thesis (Chapter 3). Scalene triangular complexes are rare and will not be discussed. Linear trinuclear and isosceles triangular complexes have been reported in this thesis. Derivation of the exchange equations using normal vector additions for these types will be presented and discussed. The exchange Hamiltonian for a trinuclear case as shown above with two different J values (J1 and J2) would be given by

$$H_{ex} = -2J1\,[\hat{S}_1.\hat{S}_2 + \hat{S}_2.\hat{S}_3] - 2J2\,[\hat{S}_3.\hat{S}_1] \qquad [1]$$

Let three spins be defined as S1, S2 and S3. If S* is defined as $S^* = S_1+S_3$, the quantum number S* will have values (S_1+S_3).....(S_1-S_3). Again if $S' = S_1 + S_2 + S_3$ (= $S^* + S_2$), then S′ will have values $(S^* + S_2)$.....$(S^* - S_2)$.

Using $S^*S^* = 2S\,(S+1) + 2S_1S_3$ [2]

So, $S_1S_3 = \frac{1}{2}\,[S^*(S^*+1)-2S(S+1)]$ [3]

Similarly, $S'S' = 3S\,(S+1) + 2S_1S_2 + 2S_2S_3 + 2S_1S_3$ [4]

Rearranging for $S_1S_2 + S_2S_3$ and substituting in equation [1], we get

$$H_{ex} = - J1[S'(S'+1) + S^*(S^* + 1) - S(S+1)] - J2[S^*(S^* + 1) - 2S(S+1)] \quad [5]$$

And the energy becomes

$$E(S, S') = - J1[S'(S'+1) + S^*(S^* + 1) - S(S+1)] - J2[S^*(S^* + 1) - 2S(S+1)] \quad [6]$$

For an equilateral triangle where $J1 = J2 = J$, the above equations further simplify to

$$H_{ex} = - J [S'(S'+1) - 3S(S+1)] \quad [7]$$

$$E(S, S') = - J [S'(S'+1) - 3S(S+1)] \quad [8]$$

The last term in the energy expression are usually omitted during energy term calculation.

The best way to understand this vector addition is to take a specific example. Let us take $S_1 = S_2 = S_3 = ½$ (e. g. trinuclear Cu^{2+} complex)

S* will have values from

$S_1 + S_3 = 1$ $\qquad$ S' (S* + S_2) = ½, 3/2

$S_1 + S_3 = 0$ $\qquad$ S' (S* + S_2) = ½

The particular value of S'= ½ appeared twice from two different combinations of spins. So, the multiplicity of the corresponding energy level (S = ½) is 2, and we have to consider that.

Table A1-1 summarizes the total S′ values, energy levels with their total multiplicities.

$S_1 + S_3$	$S^* + S_2$	S′	Total multiplicity [2S′+1]	Energy J[S′(S′+1)]
1	½, 3/2	3/2	1	15/4 J
0	½	½	2	¾ J

At this stage different spin states from S′ values, the energies and degeneracies need to be substituted into the Van-Vleck equation (equation [9]) in order to find out the molar susceptibility as a function of temperature.

$$\chi_M = \frac{N g^2 \beta^2}{3kT}\left(\frac{\sum S'(S'+1)(2S'+1)\Omega \exp(-E(S')/kT)}{\sum (2S'+1)\Omega \exp(-E(S')/kT)}\right) \qquad [9]$$

The term Ω in the above form of the Van-Vleck equation is the degeneracy term. By putting the appropriate values of S′ and energies we get

$$\chi_M = \frac{N g^2 \beta^2}{3kT}\left[\frac{(\frac{3}{2}).(\frac{5}{2}).4.\exp(-\frac{15}{4}.\frac{J}{kT}) + 2.(\frac{1}{2}).(\frac{3}{2}).2.\exp(-\frac{3}{4}.\frac{J}{kT})}{4.\exp(-\frac{15}{4}.\frac{J}{kT}) + 2.2.\exp(-\frac{3}{4}.\frac{J}{kT})}\right] + TIP \qquad [10]$$

After several mathematical treatments and putting x = (J/kT) and multiplying through by $x^{15/4}$, and putting $Ng^2\beta^2/3kT = K$, we get the following expression

$$\chi_M = \frac{3K}{4T}\left[\frac{5+x^3}{1+x^3}\right] + TIP \qquad [11]$$

The advantage of this vector coupling method is that it is possible to perform non linear regression on two different exchange integrals (J values) independently which is not possible in the software MAGMUN 4.1. However, the major disadvantage of this method is that for large systems writing exchange equations is very difficult. That is why the fitting of variable temperature magnetic data for larger systems, such as the octanuclear $Cu(II)_8$ pinwheels, was carried out far more conveniently using the software MAGMUN 4.1. The calculations of spin states and the corresponding energies are done using the routines embedded within the software.

A2: Magnetic model, OW01.ini files, and * spk files

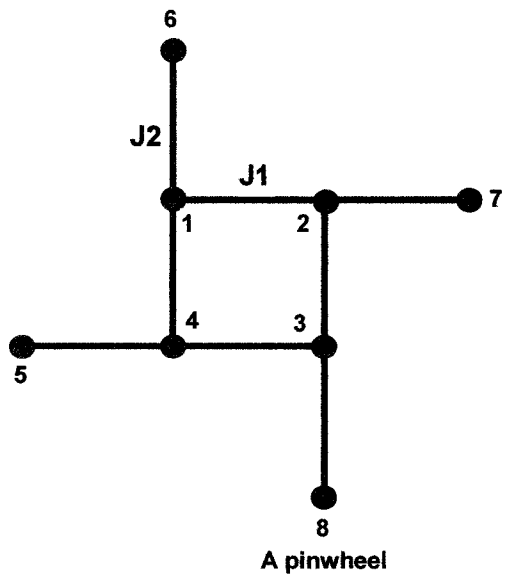

Fig. A2-1 A pinwheel model.

The exchange Hamiltonian for an octanuclear Cu_8 pinwheel complex with two different J values ($J1$ being the coupling constant within the central core and $J2$ being the coupling between the central core and the external copper (II) centers) would be

$$\boldsymbol{H_{ex}} = -J1\,[\hat{S}_1.\hat{S}_2 + \hat{S}_2.\hat{S}_3 + \hat{S}_3.\hat{S}_4 + \hat{S}_4.\hat{S}_1] - J2\,[\hat{S}_1.\hat{S}_6 + \hat{S}_2.\hat{S}_7 + \hat{S}_3.\hat{S}_8 + \hat{S}_4.\hat{S}_5]$$

If the two exchange integrals are same then $J1 = J2 = J$, and the input in the OW01.ini file would be

Spins: 1 1 1 1 1 1 1 1
Coupling: 12 23 34 41 16 27 38 45
Strengths: -1 -1 -1 -1 -1 -1 -1 -1
Output: Cu8pinwheel-single J

The *spk file generated by the OW01.ini file would be:

MDA 01.00 SPK 00
#PROGRAM:
Program OW0L, (c) Oliver Waldmann,
Version 11.5.01
#HAMILTONIAN:
Heisenberg Hamiltonian
#SYSTEM:
Spins = 1/2 1/2 1/2 1/2 1/2 1/2 1/2 1/2
Couplings = 1-2 2-3 3-4 4-1 1-5 2-6 3-7
4-8
#PARAMETER:
Strengths = -1 -1 -1 -1 -1 -1 -1 -1
Emin = -3.46716625452677
#COMMENT:
sorted spectrum with classification
#DATA: (Column 1 is the relative energy,
column 2 is 2S'+1)

0	0	0
0.4352118386	2	0
0.8496005729	2	1
0.8496005729	2	2
1.121004724	4	0
1.220186651	0	1
1.612528575	2	3
1.647414962	0	2
1.760059473	0	3
1.760059473	0	4
1.835647006	2	4
1.835647006	2	5
1.941479134	4	1
1.953381756	2	6
2.015560292	2	7
2.323043449	4	2
2.323043449	4	3
2.381016361	2	8
2.381016361	2	9
2.467166255	2	10
2.467166255	0	5
2.612528575	4	4
2.664366643	4	5
2.708931467	0	6
2.825544582	2	11
2.825544582	2	12
2.849132266	6	0
2.870197971	2	13
2.912208122	0	7
3.03015023	4	6
3.03015023	4	7
3.064134538	2	14
3.174273036	0	9
3.174273036	0	8
3.269965866	4	8
3.299689836	2	15
3.299689836	2	16
3.311787285	2	17
3.467166255	0	10
3.467166255	4	9
3.467166255	2	18
3.467166255	0	11
3.725818277	4	10
3.760059473	6	1
3.760059473	6	2
3.789232983	2	19
3.789232983	2	20
3.870197971	4	11
3.904182279	4	12
3.904182279	4	13
3.918772217	2	21
4.151371466	2	22
4.151371466	2	23
4.168284139	2	24
4.26910399	0	12
4.321803934	2	25
4.467166255	6	3
4.467166255	4	14
4.512318589	0	13
4.605227229	2	26
4.605227229	2	27
4.61128906	4	15
4.61128906	4	16
4.734201353	4	17
4.813327785	4	18
4.918772217	4	19
5.085200243	6	4
5.174273036	6	5
5.174273036	6	6
5.467166255	8	0

A plot of distribution of S′ values with respect to the energy is shown in figure A2-2.

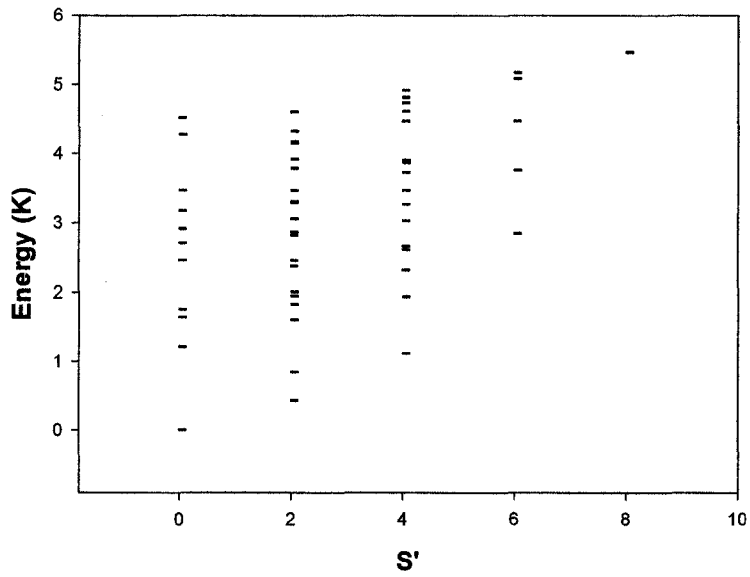

Fig. A2-2 Distribution of S′ versus energy

In cases where *J1* and *J2* are unequal, individual *J* values cannot be evaluated independently within the current package of MAGMUN 4.1. However, for such systems, the second *J* value can be represented as an appropriate ratio of the first one. If *J1* is twice *J2*, such that *J1*/*J2* = 2, then the OW01.ini input file would be

Spins: 1 1 1 1 1 1 1 1
Coupling: 12 23 34 41 16 27 38 45
Strengths: -1 -1 -1 -1 -0.5 -0.5 -0.5 -0.5
Output: Cu8pinwheelJ1byJ2-2

The *spk output file would have a similar format as shown above but spin states and energies would be different.

In order to find out the best ratio for J1/J2 for a complex, the variable temperature magnetic data were fitted with the aid of MAGMUN 4.1 for a series of ratios ranging from 0.8, 1.11, 1.25, 1.43, 1.66, 2.0, 2.5, 3.33, 4, 5, 8, 10. During each of the fitting procedures, the temperature independent paramagnetism parameter (TIP) was kept constant to 500 x 10^{-6} cm^3. mol^{-1} (a reasonable value for eight copper (II) ions). The other parameters such as g, J, θ and ρ were allowed to vary independently. In the second step Goodness of Fit (GOF) parameter (R^2) was calculated for each ratios of J1/J2 and plotted against the J1/J2 ratio. GOF parameter is the squared value of R ($R = [\Sigma(\chi_{obs} - \chi_{calcd})^2 / \Sigma\chi_{obs}^2]^{1/2}$.

Data for the calculation of R used for the octanuclear complex **1** (Chapter 5) are provided below. The graph in Figure 5.10, Chapter 5, was plotted using these values.

J1/J2	R	R^2			
			2	3.700022	13.69016
10	3.976528	15.81278	1.6	3.708	13.74926
8	3.839053	14.73832	1.43	3.708	13.74926
5	3.763886	14.16684	1.25	3.712	13.77894
4	3.754315	14.09488	1.11	3.723	13.86073
3.33	3.723298	13.86294	1	3.739	13.98012
2.5	3.705735	13.73247	0.8	3.764961	14.17493

The plot of R^2 against *J1/J2* gave a trough like graph with the minimum at J1/J2 ~ 2.0. The best ratio for *J1/J2* was chosen as the one with least R^2 values. The variable

temperature magnetic data were fitted to the appropriate equations with the new ratio. The fitted value for the exchange integral J was later translated into the internal coupling constant ($J1$) and the external coupling constant ($J2$) by multiplying it with the best fitted ratio.